Technische Universität München

Precise top and bottom quark masses from pair production near threshold in e^+e^- collisions

Dissertation

by

Thomas Johannes Georg Rauh

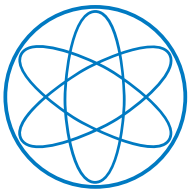

Lehrstuhl für theoretische Elementarteilchenphysik T31

Fakultät für Physik

Technische Universität München

Physik Department T31

Precise top and bottom quark masses from pair production near threshold in e^+e^- collisions

Thomas Johannes Georg Rauh

Vollständiger Abdruck der von der Fakultät für Physik der Technischen Universität München zur Erlangung des akademischen Grades eines

Doktors der Naturwissenschaften

genehmigten Dissertation.

Vorsitzender:		Prof. Dr. Stephan Paul
Prüfer der Dissertation:	1.	Prof. Dr. Martin Beneke
	2.	Priv.-Doz. Dr. Antonio Vairo
	3.	Prof. Andrzej Czarnecki (schriftliche Beurteilung)

Die Dissertation wurde am 09.08.2016 bei der Technischen Universität München eingereicht und durch die Fakultät für Physik am 06.09.2016 angenommen.

Abstract

In this thesis we present a dedicated study of heavy-quark pair production near threshold in e^+e^- collisions. Precise theory predictions for this process allow the extraction of the top and bottom quark masses from experimental data. Besides the conceptual importance of the accurate determination of the fundamental parameters in nature, there are also significant phenomenological benefits.

The calculation is organized with potential non-relativistic QCD (PNRQCD) and Unstable-Particle Effective Theory. We review the notion of a heavy-quark mass and the effective field theory framework in detail. We then compute electroweak and non-resonant corrections to the cross section at next-to-next-to-leading order (NNLO) and P-wave and Higgs corrections at NNNLO. Together with the recently completed NNNLO calculation in pure QCD, this provides full NNNLO QCD plus NNLO electroweak accuracy for the cross section near threshold.

Based on this prediction we discuss the physics potential of a threshold scan of top-pair production at a future lepton collider. In addition to the extraction of the top-quark mass with an estimated uncertainty of just 50 MeV, it also provides accurate determinations of the strong coupling constant and the top-quark width and Yukawa coupling.

Furthermore, we present the first complete NNNLO determination of the bottom-quark mass from non-relativistic sum rules, which was performed in the context of this dissertation. Our result for the mass in the $\overline{\text{MS}}$ scheme is given by $m_b^{\overline{\text{MS}}}(m_b^{\overline{\text{MS}}}) = 4.203^{+0.016}_{-0.034}\,\text{GeV}$. We then demonstrate that our approach is completely insensitive to non-perturbative corrections.

Zusammenfassung

In dieser Arbeit präsentieren wir eine ausführliche Studie der Paarproduktion schwerer Quarks in e^+e^- Kollisionen nahe der Produktionsschwelle. Präzise Theorievorhersagen für diesen Prozess ermöglichen die Extraktion der Top- und Bottomquarkmasse aus experimentellen Daten. Neben der konzeptionellen Relevanz der präzisen Bestimmung der fundamentellen Naturkonstanten gibt es auch erheblichen phänomenologischen Nutzen.

Die Rechnungen wurden in potentieller nicht-relativistischer QCD (PNRQCD) und der Effektiven Theorie Instabiler Teilchen durchgeführt. Wir bieten einen Überblick über die Definitionen von Quarkmassen und das effektive Feldtheoriegerüst. Dann werden elektroschwache und nichtresonante Korrekturen zum Wirkungsquerschnitt in nächst-nächst-führender Ordnung (NNLO), sowie P-Wellen- und Higgskorrekturen in NNNLO berechnet. Zusammen mit der kürzlichen Vervollständigung der NNNLO-Rechnung in reiner QCD erhalten wir eine Vorhersage für den Wirkungsquerschnitt nahe der Produktionsschwelle, die sämtliche NNNLO QCD und NNLO elektroschwache Korrekturen beinhaltet.

Anhand dieser Vorhersage diskutieren wir das Physikpotential einer Schwellenabtastung des Toppaarproduktionswirkungsquerschnitts an einem zukünftigen Leptonenkollider. Zusätzlich zu der Extraktion der Topquarkmasse mit einer geschätzten Unsicherheit von nur 50 MeV ermöglicht sie auch die akkurate Bestimmung der starken Kopplungskonstante und der Zerfallsbreite und Yukawakopplung des Topquarks.

Weiterhin stellen wir die erste Bestimmung der Bottomquarkmasse aus nichtrelativistischen Summenregeln mit vollständiger NNNLO Genaugkeit vor, die im Rahmen dieser Dissertation durchgeführt wurde. Unser Ergebnis im $\overline{\text{MS}}$ Schema lautet $m_b^{\overline{\text{MS}}}(m_b^{\overline{\text{MS}}}) = 4.203^{+0.016}_{-0.034}\,\text{GeV}$. Anschließend demonstrieren wir die Unabhängigkeit dieser Herangehensweise von nichtperturbativen Korrekturen.

Publications within the context of this dissertation

- [1]: M. Beneke, J. Piclum and T. Rauh, *P-wave contribution to third-order top-quark pair production near threshold*, Nucl. Phys. B **880** (2014) 414 [arXiv:1312.4792 [hep-ph]].
- [2]: M. Beneke, A. Maier, J. Piclum and T. Rauh, *The bottom-quark mass from non-relativistic sum rules at NNNLO*, Nucl. Phys. B **891** (2015) 42 [arXiv:1411.3132 [hep-ph]].
- [3]: T. Rauh, *The bottom-quark mass from Υ sum rules at NNNLO*, PoS FWNP (2014) 017.
- [4]: M. Beneke, A. Maier, J. Piclum and T. Rauh, *Higgs effects in top anti-top production near threshold in e^+e annihilation*, Nucl. Phys. B **899** (2015) 180 [arXiv:1506.06865 [hep-ph]].
- [5]: M. Beneke, A. Maier, J. Piclum and T. Rauh, *Non-QCD contributions to top-pair production near threshold*, PoS EPS **-HEP2015** (2015) 315 [arXiv:1511.00801 [hep-ph]].
- [6]: M. Beneke, A. Maier, J. Piclum and T. Rauh, *NNNLO determination of the bottom-quark mass from non-relativistic sum rules*, arXiv:1601.02949 [hep-ph].
- M. Beneke, A. Maier, T. Rauh and P. Ruiz-Femenía, *Electroweak NNLO contributions to top anti-top production near threshold in e^+e^- annihilation*, in preparation.

Further publications

- [7]: M. Bobrowski, A. Lenz and T. Rauh, *Short distance D-Dbar mixing*, arXiv:1208.6438 [hep-ph].
- [8]: A. Lenz and T. Rauh, *D-meson lifetimes within the heavy quark expansion*, Phys. Rev. D **88** (2013) 034004 [arXiv:1305.3588 [hep-ph]].
- [9]: F. Krinner, A. Lenz and T. Rauh, *The inclusive decay $b \to c\bar{c}s$ revisited*, Nucl. Phys. B **876** (2013) 31 [arXiv:1305.5390 [hep-ph]].

Contents

1. Introduction

The first years of operation of the Large Hadron Collider (LHC) have been an astonishing success story for the Standard Model (SM) of elementary particles, culminating in the discovery of the Higgs boson in 2012 [10,11]. Since then a plethora of analyses has revealed no statistically significant deviation from the SM. There is, however, observational evidence for physics beyond the SM from the baryon asymmetry of the universe, neutrino oscillations and dark matter. Their common drawback is that they cannot be associated with a specific new physics scale, since it has been demonstrated that new physics from well below the electroweak scale all the way up to the Planck scale constitute possible explanations. Most prominent models of new physics therefore invoke additional guiding principles like minimality, naturalness or similar notions of aesthetics.

The LHC and the next generation of collider experiments will provide an extremely stringent test of these models and the respective assumptions. Therefore, it is paramount that the high precision on the experimental side is matched by theory predictions within the SM. The complete automatization of next-to-leading order (NLO) QCD corrections for hadron collider processes [12], the first computation of NNLO QCD corrections to a $2 \to 2$ process with all external particles being colored [13–15] and even NNNLO QCD corrections to Higgs boson production in gluon fusion [16] are merely some select highlights of the tremendous theory effort employed towards this goal in recent years.

The most straightforward way to further improve theory predictions is to achieve the highest possible precision for SM parameters. Often parametric uncertainties are of comparable size than scale uncertainties, which are used to estimate missing higher order perturbative corrections. For processes involving colored external particles, the most important are the strong coupling constant α_s and the quark masses m_q, where the present uncertainties are of the order of 1%. This thesis focuses mainly on the determination of the top-quark and bottom-quark masses. Their current status and the importance for phenomenology will be discussed in the following.

Currently, the top quark is the heaviest known elementary particle with a mass that is about 185 times that of the proton. Thus, it plays a unique role in the SM. It is of particular importance for the Higgs sector due to its large Yukawa coupling. The precise measurements of its properties, that are possible at a future linear collider, are an essential probe of the SM and its extensions. So far, the most precise determination of the top-quark mass $m_t^{\mathrm{MC}} = 173.34 \pm 0.76$ GeV was achieved from the direct reconstruction of top quarks from their decay products at the TeVatron and LHC experiments [17]. Unfortunately, this value has to be taken with a grain of salt because it corresponds to a so-called Monte-Carlo mass whose relationship to a proper short-distance mass scheme contains an unknown non-perturbative contribution, that is estimated to be of the order

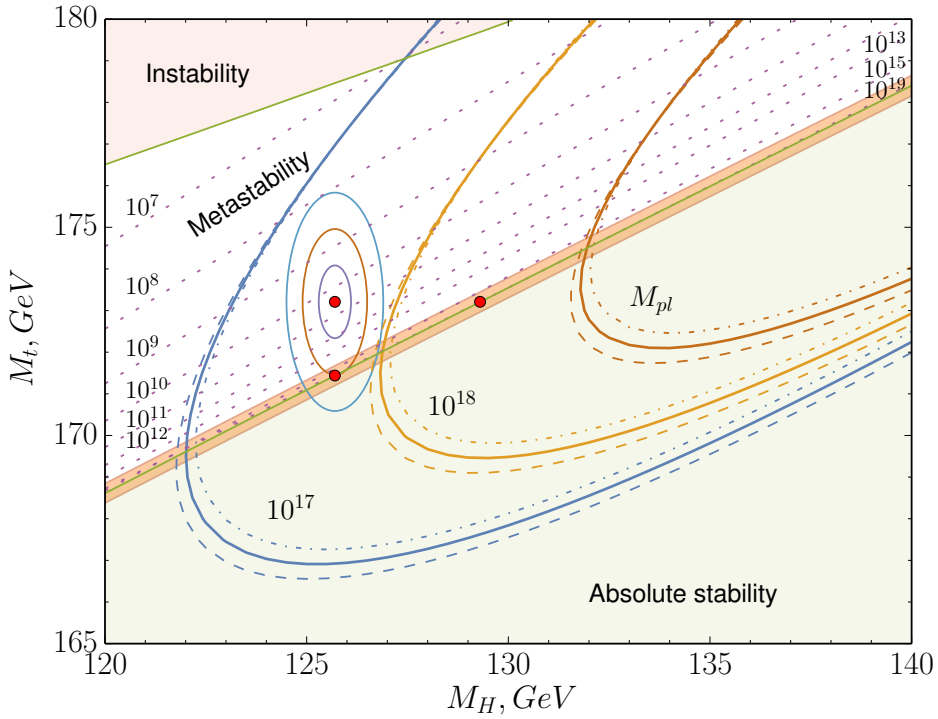

Figure 1.1.: The shaded areas show the regions of absolute stability (green), metastability (white) and instability (red) of the electroweak vacuum in the $m_H - m_t$ parameter space. The upper left red point shows the current values of the Higgs mass and top Monte-Carlo mass with the ellipses denoting the 1,2 and 3 σ contours. The authors of [23] find that this is compatible with absolute stability at the level of only 1.3σ, when the additional uncertainty in the relation of the pole and Monte-Carlo masses is ignored. Figure from [23].

of 1 GeV [18]. Even worse, the concept of a Monte Carlo mass is not universal, as different Monte Carlo generators can correspond to different Monte Carlo mass schemes. Alternatively, it is possible to directly extract the top-quark pole mass from the measured total top-pair production cross section [19–21] or from a fit to electroweak precision data and flavor observables [22]. This, however, comes at the cost of an increased uncertainty at the level of $2 - 3$ GeV. In reverse, the observables considered for these fits obviously benefit from a precise independent determination of the top-quark mass. The most striking example for the importance of the top-quark mass is related to the destabilization of the electroweak vacuum due to the effects of top-quark loops on the renormalization group evolution (RGE) of the quartic Higgs coupling. The size of this effect depends crucially on the Higgs and top-quark masses and the most recent results show a scenario that is intriguingly close to the absolute stability bound [23], see Figure 1.1.

In the field of B physics many important experimental results are expected in the coming years from the LHCb and Belle II collaborations. The precise knowledge of the bottom-quark mass is highly important for theory predictions of B-meson decay rates. For example, the total lifetime of B mesons depends on the fifth power of the bottom-quark mass. It is also of considerable importance for Higgs branching ratios. In the SM the dominant decay channel $H \to b\bar{b}$ scales as m_b^2, whereas the other channels exhibit at most a mild m_b dependence. Therefore, the parametric uncertainty for the branching ratios is given by

$$\frac{[\delta \operatorname{Br}(H \to X)]_{m_b}}{\operatorname{Br}(H \to X)} = \operatorname{Br}(H \to b\bar{b}) \frac{2\delta m_b}{m_b}. \tag{1.1}$$

The present PDG average of the bottom-quark $\overline{\text{MS}}$ mass is $\overline{m}_b(\overline{m}_b) = 4.18 \pm 0.03$ GeV [24]. Thus, the branching ratios of all Higgs decay channels apart from $b\bar{b}$ are plagued by a 1% parametric uncertainty, which dominates for most tree-level decay channels assuming an eventual uncertainty of 100 MeV for the Higgs mass from 300 fb^{-1} of data [25].

To understand the challenges that are associated with the precise determination of heavy-quark masses, it is crucial to first understand their nature. The key point is that they aren't physical observables, but constitute renormalization scheme and, in general, renormalization scale dependent quantities. Just like e.g. the strong coupling constant, heavy-quark masses are parameters in the Lagrangian of the SM and can't be predicted in the framework of the SM. Thus, they can only be determined by comparing predictions for a physical observable, made using the heavy-quark mass in a specific renormalization scheme and at a specific scale, with experimental results. To obtain an accurate result the considered observable has to satisfy three necessary conditions. First of all, it has to be experimentally clean, which suggests considering lepton collisions since there the partonic center-of-mass energy is known and backgrounds are significantly smaller. Secondly, it must be theoretically well understood and the computation of higher-order perturbative corrections must be possible. This suggests inclusive processes with as few external particles as possible. Thirdly, the observable has to depend strongly on the parameter that is to be determined. For heavy-quark masses this suggests considering a processes near the threshold, where a new channel including the heavy quark opens up.

For the top-quark mass, the three criteria are fulfilled by the total inclusive cross section for the production of top pairs in electron positron collisions $e^+e^- \to t\bar{t}X$ for center-of mass energies near the top threshold $s \approx 4m_t^2$. Experimentally, this threshold scan is possible at a future linear collider within about one year of running. The results of a simulation [26], assuming the design of the ILC, and the estimated statistical uncertainties for the simultaneous extraction of the top-quark mass and the strong coupling constant are shown in Figure 1.2. The dependence on variations of the top-quark mass δm_t manifests as a shift of the shape of the cross section by $2\delta m_t$, as depicted by the blue dashed curves. This facilitates the determination of m_t and α_s with a statistical uncertainty of only 27 MeV and 0.0008, respectively [26]. To achieve a theory uncertainty in the same ballpark, the prediction for the cross section must be very precise. NNLO QCD corrections have been computed at the end of the 90's by various groups and turned out to be large [27]. Thus, it

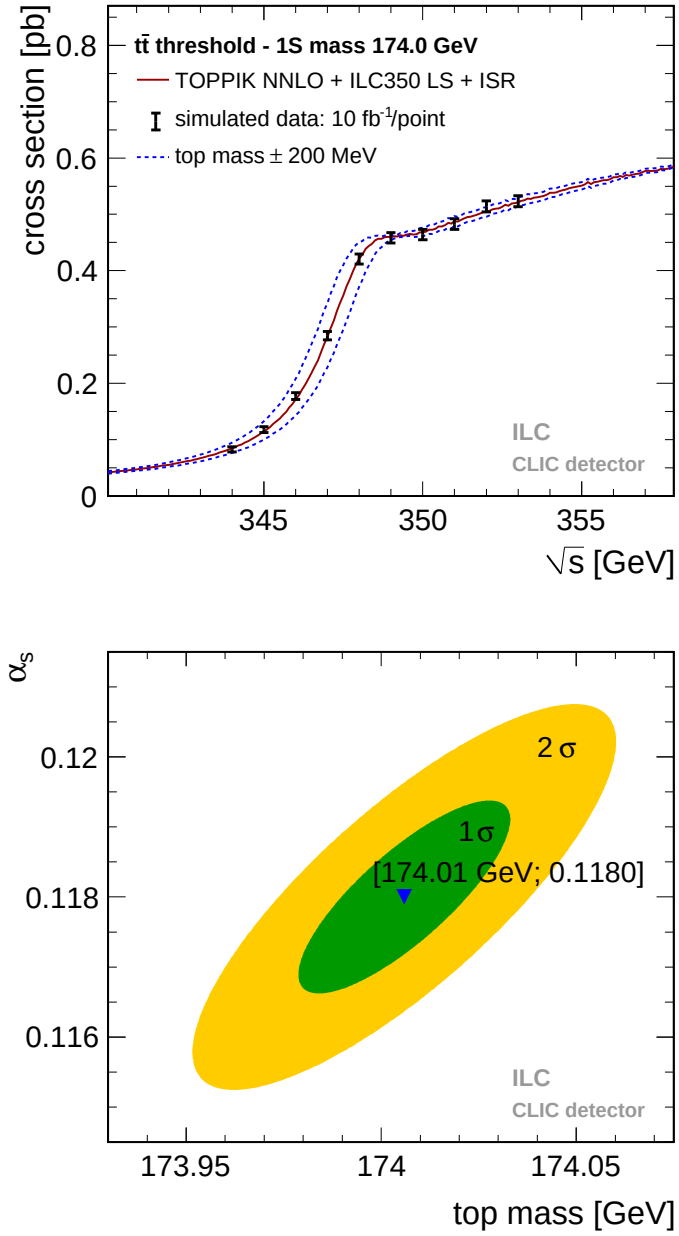

Figure 1.2.: The upper plot shows simulated data points (black error bars) for the top-pair production cross section near threshold together with the theory prediction (red line). The blue dashed lines show the theory prediction using an input mass that is shifted by ±200 MeV. There is a large sensitivity to the top-quark mass in the region, where the slope of the cross section is biggest. The lower plot shows the statistical uncertainty of the top-quark mass and strong coupling constant extracted from the simulated data in a simultaneous fit. Figures from [26].

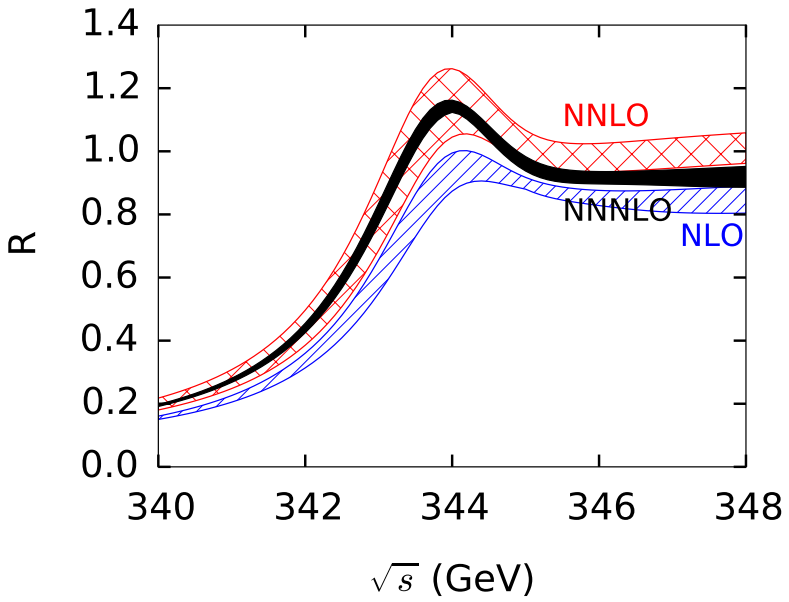

Figure 1.3.: The top-pair production cross section near threshold, normalized to the muon-pair production cross section, $R(s) = \sigma(t\bar{t}X)/\sigma_0(\mu^+\mu^-)$ at NLO (blue), NNLO (red) and NNNLO (black). The bands are spanned by variation of the renormalization scale in the range from 50 GeV to 350 GeV. Figure from [28].

was necessary to further improve the accuracy of the computation. Following a tremendous effort from a large collaboration, the computation of the full NNNLO QCD contributions has been completed recently [28] and is now available in the form of the public code `QQbar_Threshold` [29]. The corrections proved to be small and the scale uncertainty is greatly reduced with respect to the NNLO result and now at the level of just $\pm 3\%$, thus proving that strong dynamics are under control, see Figure 1.3. The computation of subleading non-QCD contributions to the cross sections is described in this thesis. The corrections are larger than the remaining QCD uncertainties and affect the determination of the top-quark mass significantly. The sensitivity of the threshold scan to the top width, top Yukawa coupling and the strong coupling constant will also be discussed.

It is not possible to determine the bottom-quark mass from the direct comparison of the shape of the bottom-pair production cross section near threshold with experimental data, because of the presence of very large non-perturbative corrections in this region. It was originally proposed in [30, 31] to consider moments

$$\mathcal{M}_n = \int_0^\infty ds \, \frac{R_b(s)}{s^{n+1}} \tag{1.2}$$

of the normalized cross section

$$R_b(s) = \frac{\sigma(e^+e^- \to b\bar{b} + X)}{\sigma(e^+e^- \to \mu^+\mu^-)} \tag{1.3}$$

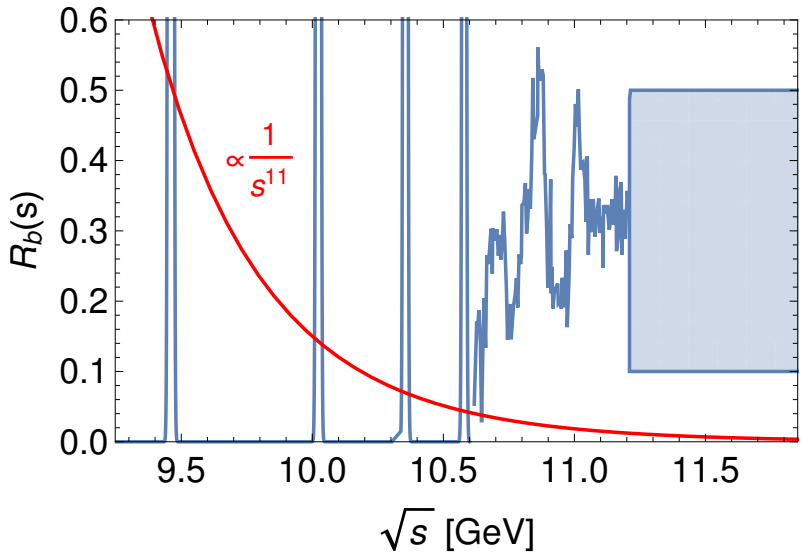

Figure 1.4.: The blue curve shows the experimental data for the normalized cross section R_b in the threshold region from the Υ resonances [24] (left), the BaBar collaboration [32], including corrections for initial state QED radiation from [33], and the assumption $R_b = 0.3 \pm 0.2$ for higher center-of-mass energies (right). The red line shows the weight factor in the integral (1.2) for the tenth moment.

instead. They are much less sensitive to infrared QCD contributions than the cross section itself and, therefore, provide the possibility of a very clean determination of m_b by making use of the results from [28]. The available experimental data on R_b comes from measurements of the properties of the Υ resonances [24] and from the BaBar collaboration for center of mass energies between 10.6178 GeV and 11.2062 GeV [32] and is depicted in Figure 1.4. Data for higher energies is not available so far and the conservative assumption $R_b(\sqrt{s} > 11.2062\,\text{GeV}) = 0,3 \pm 0.2$ is made in the following. The experimental uncertainty of the moments thus decreases for larger n because the sensitivity to the poorly known energy region is reduced by the weight factor $1/s^{n+1}$ in the integral. In addition, the mass dependence of the moments is increased for larger n because, for dimensional reasons, $\mathcal{M} \sim m_b^{-2n}$. However, for arbitrarily large n the moments are completely dominated by the $\Upsilon(1S)$ resonance and non-perturbative contributions can no longer be ignored. A good compromise is reached by values of n near 10. The first full NNNLO analysis for the bottom-quark mass from moments in this range was obtained in the course of this thesis and will be described here in detail.

The methods used for the determination of the top and bottom-quark masses rely on the precise computation of the respective pair production cross sections near the partonic thresholds $\sqrt{s} = 2m_q + E$ with $E \sim m_q\alpha_s^2 \ll m_q$ and $q = t, b$. For kinematic reasons, the heavy quarks are non-relativistic, i.e. have a small velocity $v = (E/m_q)^{1/2} \sim \alpha_s \ll 1$. The presence of so-called Coulomb corrections, which scale as $(\alpha_s/v)^n \sim 1$, causes the break-

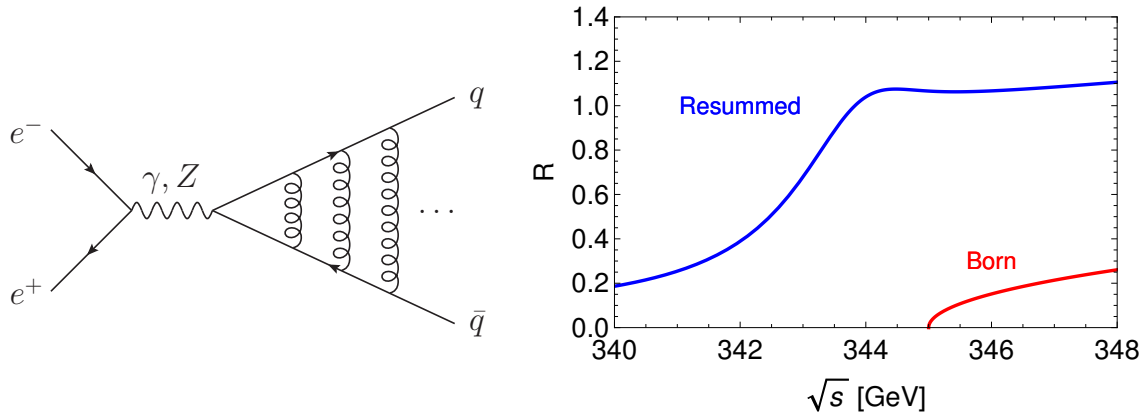

Figure 1.5.: Ladder diagram contributing to the $e^-e^+ \to q\bar{q}$ amplitude (left). The effect of Coulomb resummation is shown on the right for top quarks. The red curve is the Born cross section and the blue curve the resummed result at LO.

down of the conventional perturbative expansion in α_s. The responsible class of Feynman diagrams is shown in Figure 1.5, where each additional gluon exchange yields another factor of α_s/v. It is, therefore, necessary to resum this kind of contributions to obtain a realistic prediction for the cross section. The dramatic effect of this resummation is shown in Figure 1.5. This introduces narrow Coulomb bound-state resonances below threshold (cf. Figure 1.4), which are smeared out in the top-pair production cross section by the sizeable decay width of the top quarks. At higher orders in the resummed perturbation theory, the remnant of the 1S toponium resonance is visible as a distinct peak as shown in Figure 1.3. The comparison with the Born result in Figure 1.5 demonstrates that the cross section is also substantially enhanced above the production threshold. The resummation can be achieved with an effective field theory called potential non-relativistic QCD (PNRQCD) [34–38]. In this theory, the ladder exchanges of gluons are described by an instantaneous, but spatially non-local, color-Coulomb potential, which constitutes a leading order effect in the non-relativistic power counting $\alpha_s \sim v \ll 1$ and is therefore treated non-perturbatively. PNRQCD provides a framework in which higher-order corrections in α_s and v around the resummed solution can be computed in a systematic fashion. The consistent treatment of the large top-quark width requires an extension to Unstable Particle Effective Theory [39, 40], which also accounts for the non-resonant production of the decay products of the top pair. Higgs and general electroweak corrections can be described in the same framework.

The structure of this thesis is as follows. In Chapter 2, we discuss various heavy quark mass schemes and their properties. The effective field theory framework upon which all computations in this thesis are based is described in Chapter 3. Since it is clearly impossible to cover all the aspects in depth, the purpose of these review chapters is to serve as a pedagogical introduction to the concepts and to the respective literature. The computation of the non-resonant and resonant contributions is performed in Chapter 4 and 5,

respectively. In Chapter 6, we study the phenomenological implications on the top threshold scan at a future linear collider. The determination of the bottom-quark mass from non-relativistic sum rules is discussed in Chapter 7. We then present some preliminary and previously unpublished results on non-perturbative gluon-condensate corrections to bottomonium sum rules and bound states in Chapter 8. We conclude in Chapter 9.

2. Heavy quark mass definitions

The first step towards a determination of heavy quark masses must necessarily be their precise definition. This is already a subtle point due to the confining nature of QCD. In the bare QCD Lagrangian, bare quark masses $m_{q,0}$ appear as the coefficient of a local operator, just like the strong coupling constant. As such, they are subject to renormalization $m_{q,0} = Z_{m_q} m_q$, which induces a scheme dependence of the renormalized masses m_q, since the mass renormalization constants Z_{m_q} must absorb the divergences, but are otherwise arbitrary. Masses defined in different schemes are related by $\tilde{m}_q = (Z_{m_q}/\tilde{Z}_{m_q}) m_q$. When physical observables are expressed in terms of m_q, this scheme dependence cancels at the considered order in perturbation theory. The convergence of the perturbative expansion can however differ substantially in different mass schemes. Thus, to determine a heavy quark mass precisely, it is crucial to choose a mass scheme that leads to the best possible behaviour for the considered observable.

The most common definitions are the pole and $\overline{\text{MS}}$ masses. The pole mass scheme is convenient for analytical computations, since expressions usually take a simpler form. We make use of this in later chapters, where the index for the pole mass is dropped, $m_q \equiv m_q^{\text{pole}}$, whereas m_q without a superscript denotes a generic quark mass in this chapter. However, it has severe shortcomings, as discussed in Section 2.1, and therefore it is not used for the determination of the masses.

In the $\overline{\text{MS}}$ scheme, $Z_{m_q}^{\overline{\text{MS}}}$ is defined as a minimal subtraction of divergences after the shift $\mu^2 \to \tilde{\mu}^2 \equiv \mu^2 (e^{\gamma_E}/(4\pi))$ is applied. The $\overline{\text{MS}}$ mass is well suited for a wide range of observables. However, threshold processes involve small energies $E^{\text{pole}} \equiv \sqrt{s} - 2m_q^{\text{pole}} \sim m_q \alpha_s^2$ and the use of the $\overline{\text{MS}}$ mass interferes with the power counting because $\Delta m_q \equiv m_q^{\text{pole}} - m_q^{\overline{\text{MS}}} \sim m_q \alpha_s$ and thus

$$E^{\overline{\text{MS}}} \equiv \sqrt{s} - 2m_q^{\overline{\text{MS}}} = E^{\text{pole}} + 2\Delta m_q \sim m_q \alpha_s \gg m_q \alpha_s^2 \sim E^{\text{pole}}. \tag{2.1}$$

For the threshold production of heavy quarks, one therefore requires a mass definition that only differs from the pole mass by terms of the order $m_q \alpha_s^2$ and that does not have the shortcomings of the pole mass. We will discuss a scheme that fulfills these specifications in Section 2.2.

2.1. The pole mass

The pole mass of a heavy quark is defined, at any given order in perturbation theory, as the real part of the location of the pole of the full heavy quark propagator. Its IR finiteness and

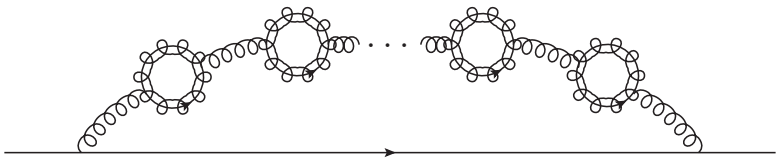

Figure 2.1.: Leading contribution to the quark self energy in the large β_0 limit. The bubbles correspond to insertions of the total one-loop gluon vacuum polarization and are summed to all orders.

gauge independence have been proven in [41]. Thus, from a purely technical point of view, it fulfills all criteria for a sound mass definition. However, the pole mass definition refers to a free heavy quark, i.e. to an unphysical object due to confinement. This implies an inherent uncertainty of the order of the confinement scale $\Lambda_{\rm QCD}$ in the definition of the pole mass, which manifests in the perturbative expansion as an IR renormalon ambiguity [42–44].

To understand this issue in more detail, we consider the relation between the pole and $\overline{\rm MS}$ mass in the large β_0 limit, i.e. an expansion in $\alpha_s \ll 1$ while counting $\beta_0\alpha_s \sim 1$. There is a powerful machinery for computations in this limit, which allows us to study the large order behaviour of the expansion coefficients in this approximation. Assuming that the exact perturbative expansion follows the same basic patterns, strong statements are possible.

The leading contribution in the large β_0 approximation is given by the diagram shown in Figure 2.1. Each bubble insertion counts as $\alpha_s\beta_0 \sim 1$ and the chain with an arbitrary number of insertions must be summed. This yields [45]

$$\Delta m(\mu) \equiv m_{\rm pole} - m_{\overline{\rm MS}}(\mu) = -4\pi i C_F \tilde{\mu}^{2\epsilon} \int \frac{d^dk}{(2\pi)^d} \alpha_s(ke^{-5/6}) \frac{\gamma^\mu(\not{k}+\not{p}+m)\gamma_\mu}{k^2[(k-p)^2-m^2]}\bigg|_{p^2=m^2}, \tag{2.2}$$

where

$$\alpha_s(ke^{-5/6}) = \frac{\alpha_s(\mu)}{1+\Pi(k^2)} = \frac{\alpha_s(\mu)}{1-\alpha_s(\mu)\beta_0\log(k^2e^{-5/6}/\Lambda^2)}, \tag{2.3}$$

and it is understood that the UV divergence of the integral is subtracted in the $\overline{\rm MS}$ scheme. The beta function in the convention of (2.3) is given by

$$\beta(\alpha_s) = \frac{1}{\mu^2}\frac{\partial\alpha_s}{\partial\mu^2} = \beta_0\alpha_s^2 + \beta_1\alpha_s^3 + \ldots, \tag{2.4}$$

$$\beta_0 = -\frac{1}{4\pi}\left(\frac{11N_c}{3} - \frac{2n_f}{3}\right). \tag{2.5}$$

Eq. (2.2) has the exact same form as the one-loop result in conventional perturbation theory, but with the strong coupling constant evaluated at the momentum running in the

loop. We compute it following the procedure introduced in [46]. The first step consists in introducing the dispersion relation

$$\frac{1}{1+\Pi(k^2)} = \frac{1}{\pi}\int_0^\infty d\lambda^2 \frac{1}{k^2-\lambda^2}\frac{\text{Im }\Pi(\lambda^2)}{|1+\Pi(\lambda^2)|^2} + \int_{-\infty}^\infty d\lambda^2 \frac{1}{k^2-\lambda^2}\frac{\lambda_L^2\delta(\lambda^2-\lambda_L^2)}{-\beta_0\alpha_s}, \tag{2.6}$$

where the second term is localized at the Landau pole

$$\lambda_L^2 = -\mu^2 \exp\left(\frac{1}{\beta_0\alpha_s}+\frac{5}{3}\right). \tag{2.7}$$

Using partial fractioning for $1/(k^2(k^2-\lambda^2))$, (2.2) can be written as a dispersion integral over the one-loop self energy with a massive gluon

$$\Delta m(\mu) = \frac{m\alpha_s C_F}{4\pi}\int_{-\infty}^\infty \frac{d\lambda^2}{\lambda^2}\left(\frac{\theta(\lambda^2)\text{Im }\Pi(\lambda^2)}{\pi|1+\Pi(\lambda^2)|^2} + \frac{\lambda_L^2\delta(\lambda^2-\lambda_L^2)}{-\beta_0\alpha_s}\right)\left(r_0(\lambda^2)-r_0(0)\right), \tag{2.8}$$

where

$$r_0(\lambda^2) = -\frac{(4\pi)^2}{m} i\tilde{\mu}^{2\epsilon}\int \frac{d^dk}{(2\pi)^d}\frac{\gamma^\mu(\not{k}+\not{p}+m)\gamma_\mu}{[k^2-\lambda^2][(k-p)^2-m^2]}\bigg|_{p^2=m^2}. \tag{2.9}$$

The difference $\Delta r_0(\lambda^2) \equiv r_0(\lambda^2) - r_0(0)$ is obtained by a straightforward computation

$$\Delta r_0(\lambda^2) = x - \frac{x^2}{2}\log x - \frac{\sqrt{x}(8+2x-x^2)}{\sqrt{4-x}}\left[\arctan\frac{2-x}{\sqrt{x(4-x)}} + \arctan\frac{\sqrt{x}}{\sqrt{4-x}}\right], \tag{2.10}$$

where $x \equiv \lambda^2/m^2$. After integration by parts, (2.8) becomes

$$\Delta m(\mu) = \frac{m\alpha_s C_F}{4\pi}\left[\int_0^\infty d\lambda^2 \Phi(\lambda^2)\Delta r_0'(\lambda^2) + \frac{\Delta r_0(\lambda_L^2)}{-\beta_0\alpha_s}\right], \tag{2.11}$$

where $\Delta r_0'(\lambda^2) = (d/d\lambda^2)\Delta r_0(\lambda^2)$ and

$$\Phi(\lambda^2) = \frac{1}{\pi\alpha_s\beta_0}\arctan\left[\frac{-\pi\alpha_s\beta_0}{1-\alpha_s\beta_0\log(\lambda^2 e^{-5/3}/\mu^2)}\right] + \frac{\theta(-\lambda_L^2-\lambda^2)}{\alpha_s\beta_0}. \tag{2.12}$$

The first term in (2.11) can be interpreted as an integral over the contribution $\Delta r_0'(\lambda^2)$ from gluons with virtuality of the order λ^2 weighted with an effective charge $\Phi(\lambda^2)$. The effective charge $\Phi(\lambda^2)$ is a monotonous function, that approaches $\Phi(0) = 1/(\beta_0\alpha_s)$ and $\Phi(\lambda^2 \to \infty) \to 0$ logarithmically. The contribution from the Landau pole of the strong coupling has been absorbed into the second term $\Delta r_0(\lambda_L^2)/(-\beta_0\alpha_s)$. The function $\Delta r_0'(\lambda^2)$ has the asymptotic behaviour

$$\Delta r_0'(\lambda^2\to 0) = -\frac{\pi}{\sqrt{m^2\lambda^2}} + \frac{3}{m^2} - \frac{9\pi}{8m^2}\sqrt{\frac{\lambda^2}{m^2}} + \left(\frac{7}{6}-\log\frac{\lambda^2}{m^2}\right)\frac{\lambda^2}{m^4} + \ldots, \tag{2.13}$$

$$\Delta r_0'(\lambda^2\to\infty) = -\frac{3}{\lambda^2} - \frac{\left(20-12\log\frac{\lambda^2}{m^2}\right)m^2}{3\lambda^4} - \frac{\left(51-36\log\frac{\lambda^2}{m^2}\right)m^4}{2\lambda^6} + \ldots. \tag{2.14}$$

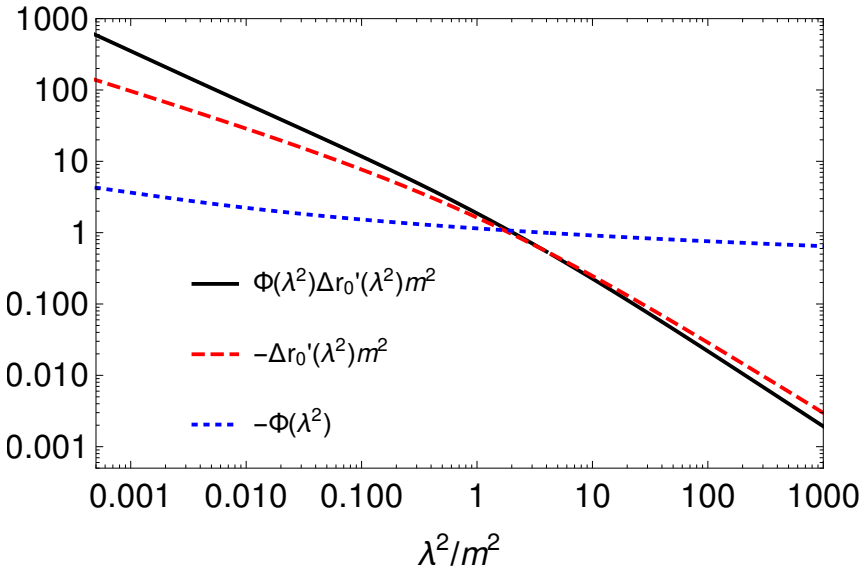

Figure 2.2.: The integrand of (2.11) for $\mu^2 = m^2$.

The behaviour of the complete integrand is shown in Figure 2.2. We observe that the integral is not saturated by contributions from virtualities λ^2 near the physical scale m^2 of the problem, but receives large contributions from the IR and UV regions $\lambda^2 \ll m^2$ and $\lambda^2 \gg m^2$. This property is the core of the renormalon contributions. For a more precise formulation we define the Borel transform $B[\Delta m]$ of Δm (stripped of the prefactor $(m\alpha_s C_F)/(4\pi)$)

$$\Delta m \equiv \frac{m\alpha_s C_F}{4\pi} \sum_{n=0}^{\infty} r_n (-\beta_0 \alpha_s)^n \quad \Rightarrow \quad B[\Delta m](u) \equiv \sum_{n=0}^{\infty} r_n \frac{u^n}{n!}. \tag{2.15}$$

It was computed exactly in [42]

$$B[\Delta m](u) = \left(\frac{\mu^2}{m^2}\right)^u e^{\frac{5u}{3}} 6(1-u) \frac{\Gamma(u)\Gamma(1-2u)}{\Gamma(3-u)} + \frac{\tilde{G}_0(u)}{u}, \tag{2.16}$$

where $\tilde{G}_0(u)$ is a subtraction term for the UV divergence in (2.2) and is specified in [42]. The Borel transform $B[\Delta m](u)$ can be used as a generating function for the expansion coefficients

$$r_n = \frac{d^n}{du^n} B[\Delta m](u)|_{u=0}. \tag{2.17}$$

Numerical results for the coefficients at $\mu = m$ are shown in Table 2.1. We observe that the perturbative expansion of Δm has a vanishing radius of convergence due to the factorial growth of the coefficients. However, it can be summed by making use of the Borel transform (2.16), which converges for $|u| < 1/2$ due to the additional $1/n!$ in the series

n	r_n	IR(1/2)	IR(3/2)	UV(−1)	UV(−2)
0	4	9.2039	−6.09125	−0.755502	0.160533
1	18.7446	18.4078	−4.06083	0.755502	−0.080267
2	70.4906	73.6312	−5.41444	−1.511	0.080267
3	439.435	441.787	−10.8289	4.53301	−0.1204
4	3495.7	3534.3	−28.877	−18.1321	0.240799
5	35358.7	35343.	−96.2567	90.6603	−0.601999
6	423257.	424116.	−385.027	−543.962	1.806
7	5939874	5937622	−1796.79	3807.73	−6.32099
8	94962946	95001956	−9582.89	−30461.9	25.2839

Table 2.1.: Coefficients $r_n(\mu = m)$ for the pole-$\overline{\text{MS}}$ relation as defined in (2.15). For comparison, the contributions from the leading and next- to-leading IR and UV renormalons are given as well.

expansion. The Borel integral

$$\widetilde{\Delta m} = \frac{m\alpha_s C_F}{4\pi} \int\limits_0^\infty du\, e^{-u/(-\beta_0\alpha_s)} \frac{B[\Delta m](u)}{(-\beta_0\alpha_s)} \tag{2.18}$$

has the same series expansion as the original function and may therefore be used to assign a numerical value to the divergent series.[1] In doing so, we have to shift the contour up or down by an infinitesimal amount in the complex u plane because the Borel transform (2.16) has poles for real positive u. As a result, the Borel integral acquires an imaginary part

$$\text{Im}\left(\widetilde{\Delta m}\right) = \pm\pi \frac{m\alpha_s C_F}{4\pi} \sum_{u_i} e^{-u_i/(-\beta_0\alpha_s)} \frac{\text{Res}_{u_i} B[\Delta m](u)}{(-\beta_0\alpha_s)}, \tag{2.21}$$

where the sum picks up all residues from poles on the positive real axis and the sign depends on the way the contour is deformed. Poles in the Borel transform are usually referred to

[1] For a convergent series $S(z) = \sum_{n=0}^\infty a_n z^n$ this is easy to show. We insert factors of one in the sum and obtain

$$S(z) \equiv \sum_{n=0}^\infty a_n z^n = \sum_{n=0}^\infty \left(\int\limits_0^\infty dt \frac{t^n e^{-t}}{n!} \right) a_n z^n = \int\limits_0^\infty du \frac{e^{-u/z}}{z} B[S](u), \tag{2.19}$$

with $u = tz$ and the Borel transform

$$B[S](u) = \sum_{n=0}^\infty \frac{a_n}{n!} u^n. \tag{2.20}$$

In the last step of (2.19) we used the convergence of $S(z)$ to change the order of summation and integration. It was generalized to a larger class of functions [47], which does however not encompass the pole-$\overline{\text{MS}}$ relation (2.2), whose Borel transform has poles on the positive real axis.

as renormalons and the dependence of (2.21) on the choice of the contour is called a renormalon ambiguity.[2] The poles in (2.16) originate from the asymptotic behaviour of the integrand in (2.11). The Borel transform of (2.11) is [46,48] (ignoring additional terms required for quantities, that require renormalization, see [46,48])

$$-\frac{\sin(\pi u)}{\pi u}\int\limits_0^\infty d\lambda^2 \left(\frac{\lambda^2}{\mu^2}e^{-5/3}\right)^{-u} \Delta r_0'(\lambda^2). \tag{2.22}$$

For illustrational purposes, we split this integral into three parts by introducing cut-offs $\xi^2_{\rm IR} \ll m^2$ and $\xi^2_{\rm UV} \gg m^2$. In the IR region $0 \le \lambda^2 \le \xi^2_{\rm IR}$ the expansion (2.13) for the integrand can be used to reproduce the poles and residues of (2.16) at positive half-integer and integer values of u, which are therefore called IR renormalons. Similarly, using (2.14) in the UV region $\xi^2_{\rm UV} \le \lambda^2 \le \infty$ gives the poles and residues at negative integer values or UV renormalons. Note that the pole at 0 is canceled by the subtraction term $\tilde{G}_0(u)/u$ in (2.11). The poles and their residues are independent of the artificial parameters $\xi_{\rm IR/UV}$. The intermediate region only yields a regular contribution.

Poles related to higher order terms in (2.13) and (2.14) yield renormalon poles that are further away from $u = 0$. Consequently, the poles closest to $u = 0$ will be called the leading, next-to leading, ... renormalons. The contributions to the coefficients $r_n(m)$ from the leading and next-to leading IR and UV renormalons are also shown in Table 2.1. We observe that the IR renormalons lead to same sign divergent behaviour of the coefficients and UV renormalons to sign-alternating divergences. Therefore, the UV renormalons are Borel summable and do not cause any ambiguities, whereas the IR renormalons are not naively Borel summable. This property is characteristic of the confining nature of QCD. In QED the beta function has opposite sign and the definition of the Borel sum (2.18) must be changed, such that the exponent is negative. This implies that the IR and UV renormalon behaviour is interchanged in QED.

The coefficients r_n of the large-β_0 expansion are quickly dominated by the first IR renormalon contribution. The exact expansion coefficients of the pole-$\overline{\rm MS}$ relation have recently been computed up to four-loop order [49]. The comparison shows that the r_n are indeed a good approximation to the full result already at relatively low orders, with the precise size of the deviations depending on the heavy quark flavour through the number of light quarks n_f (see Table 2.2 for the bottom mass). Thus, the exact expansion coefficients are also dominated by the leading IR renormalon contribution.

[2] The same ambiguity appears in the "direct computation." In (2.2), the order of the loop integration and summation over bubble contributions was interchanged. The sum was then evaluated, which results in the change of the argument of the strong coupling constant. Since the summation is divergent, this is not mathematically justified and also leads to an ambiguity. The real part of the result (2.11) of the "direct computation" is identical to the principal part of the Borel integral (2.18). (2.11) also gets an imaginary part from the Landau-pole term $\Delta r_0(\lambda_L^2)/(-\beta_0\alpha_s)$ due to a branch cut in Δr_0 along the negative real axis. It agrees with (2.21), see [46].

Renormalon ambiguities indicate the presence of power corrections. They scale as

$$e^{-u_i/(-\beta_0\alpha_s)} = e^{u_i \log \frac{\Lambda_{\rm QCD}^2}{\mu^2}} = \left(\frac{\Lambda_{\rm QCD}^2}{\mu^2}\right)^{u_i}. \tag{2.23}$$

When they appear in physical observables, they are expected to cancel with contributions from higher-dimensional operators. Thus, renormalon ambiguities are not a shortcoming of QCD, but rather of applying perturbation theory to QCD without also accounting for power corrections. The leading ambiguity of the pole-$\overline{\rm MS}$ mass relation from the $u = 1/2$ IR renormalon is of the order $\Lambda_{\rm QCD}$. Since the $\overline{\rm MS}$ mass involves only a minimal subtraction of UV divergences, the renormalon ambiguity is part of the pole mass. Since the heavy quark pole mass refers to an unphysical object, it is not clear how its definition could be generalized beyond perturbation theory. Thus, its IR renormalon ambiguity cannot be canceled by including non-perturbative corrections. Parametrically, the concept of a pole mass can therefore not be made more precise than the confinement scale $\Lambda_{\rm QCD}$. A recent study [50] found that size of the ambiguity for the top-quark mass is around 70 MeV. This is larger than the estimated accuracy in a threshold scan and thus demonstrates that the pole mass is not suited for this kind of application. Instead a different mass definition will be used, where the leading IR renormalon is canceled in the perturbative expansion.

2.2. The potential subtracted mass

We discuss the potential subtracted (PS) mass [51] as an example for a mass definition that only differs from the pole mass by terms of order $m_q\alpha_s^2$ and does not contain an IR renormalon at $u = 1/2$. Other examples for mass definitions, that comply with these specifications are the $1S$-mass [52], the kinetic mass [53] and the renormalon subtracted mass [54].

The definition of the PS mass is inspired by the observation that the total energy $E_{\rm static}(\mathbf{r}) = 2m_q^{\rm pole} + V_C(\mathbf{r})$ of a static heavy-quark pair $q\bar{q}$ separated by a distance $r \ll 1/\Lambda_{\rm QCD}$ is an observable and therefore unambiguous [51, 55]. Since the static energy receives no $\mathcal{O}(\Lambda_{\rm QCD})$ power corrections, this implies that the leading ambiguity of the pole mass must be canceled by an opposite ambiguity in the static potential. Below, we demonstrate this cancellation explicitly in the large-β_0 limit. The ambiguities in the mass and potential can be removed by a redefinition of both quantities by an opposite mass shift.[3]

The large-β_0 approximation for the Coulomb potential in momentum space is given by

$$\tilde{V}_C(\mathbf{q}^2) = -\frac{4\pi\alpha_s C_F}{\mathbf{q}^2}\frac{1}{1+\Pi(-\mathbf{q}^2)}. \tag{2.24}$$

We now consider its Fourier transform and repeat the same steps as for the pole-$\overline{\rm MS}$ mass

[3] The $1S$ mass is based on the same idea, but considers a different observable, the mass of the $\Upsilon(1S)$ resonance.

relation

$$V_C(\mathbf{r}) = \int \frac{d^3\mathbf{q}}{(2\pi^3)} e^{i\mathbf{q}\cdot\mathbf{r}} \tilde{V}_C(\mathbf{q}^2)$$
$$= -4\pi\alpha_s C_F \left[\int_0^\infty d\lambda^2 \Phi(\lambda^2) d_0'(\lambda^2) + \frac{d_0(\lambda_L^2) - d_0(0)}{-\beta_0\alpha_s} \right], \tag{2.25}$$

where $d_0(\lambda^2) = e^{-\lambda|\mathbf{r}|}/(4\pi|\mathbf{r}|)$ is the Yukawa potential in position space. We are only interested in the leading IR renormalon. Thus, we expand the integral in (2.25) in $\lambda^2|\mathbf{r}|^2$

$$V_C(\mathbf{r}) = \frac{\alpha_s C_F}{2} \int_0^{\xi_{\rm IR}^2} d\lambda^2 \Phi(\lambda^2) \left(\frac{1}{\sqrt{\lambda^2}} - |\mathbf{r}| + \dots \right) + \dots . \tag{2.26}$$

In the comparison of (2.26) with (2.11) and (2.13) we observe that the leading $1/\sqrt{\lambda^2}$ contribution is independent of the distance $|\mathbf{r}|$ and indeed cancels in the large-β_0 approximation for the static energy of a heavy quark pair. This suggests introducing a subtraction term to also remove the leading IR renormalon from the mass definition and the potential separately. The result is a subtracted potential

$$V_C(\mathbf{r}, \mu_f) = V_C(\mathbf{r}) + 2\delta m(\mu_f) \tag{2.27}$$

and the potential subtracted mass

$$m_q^{\rm PS}(\mu_f) = m_q^{\rm pole} - \delta m(\mu_f), \tag{2.28}$$

where

$$\delta m(\mu_f) \equiv -\frac{1}{2} \int_{|\mathbf{q}|<\mu_f} \frac{d^3\mathbf{q}}{(2\pi)^3} \tilde{V}_C(\mathbf{q}^2). \tag{2.29}$$

It is clear from (2.26) that only the leading term in an expansion of the factor $e^{i\mathbf{q}\cdot\mathbf{r}} = 1 + \mathcal{O}(\mathbf{q}\cdot\mathbf{r})$ is required in (2.29) to achieve the cancellation of the pole at $u = 1/2$. The subtraction scale μ_f introduced in the definitions above is assumed to be of the order $m_q\alpha_s$. This assures that the PS mass has the scaling required for threshold problems.

We define the Borel transform of $\delta m(\mu_f)$ in the large β_0 approximation by

$$\delta m^{(\beta_0)} \equiv \frac{\mu_f \alpha_s C_F}{4\pi} \sum_{n=0}^{\infty} h_n (-\beta_0\alpha_s)^n \quad \Rightarrow \quad B[\delta m^{(\beta_0)}](u) \equiv \sum_{n=0}^{\infty} h_n \frac{u^n}{n!}. \tag{2.30}$$

We obtain

$$B[\delta m^{(\beta_0)}](u) = 4e^{5u/3} \left(\frac{\mu^2}{\mu_f^2} \right)^u \frac{1}{1-2u}, \tag{2.31}$$

which only has one IR renormalon pole at $u = 1/2$. The coefficients h_n are obtained from its derivatives at $u = 0$. In Table 2.2, we show a comparison of the perturbative

n	$\Delta m_b^{(\beta_0)}$	$\Delta m_b^{(\text{exact})}$	$\delta m_b^{(\beta_0)}$	$\delta m_b^{(\text{exact})}$	$(\Delta m_b - \delta m_b)^{(\beta_0)}$	$(\Delta m_b - \delta m_b)^{(\text{exact})}$
0	0.40107	0.40107	0.19099	0.19099	0.21009	0.21009
1	0.28043	0.19988	0.14677	0.11942	0.13366	0.08046
2	0.15735	0.14537	0.12980	0.11342	0.02755	0.03194
3	0.14636	0.135(2)	0.13605	0.13628	0.01032	−0.001(2)
4	0.17372		0.17172		0.00201	
5	0.26219		0.26060		0.00159	
6	0.46829		0.46866		−0.00038	
7	0.98057		0.97997		0.00060	
8	2.33909		2.33995		−0.00087	

Table 2.2.: The terms in the perturbative expansion of the pole-$\overline{\text{MS}}$ (Δm_b), the pole-PS (δm_b) and the PS-$\overline{\text{MS}}$ ($\Delta m_b - \delta m_b$) mass relation are shown for the bottom quark in the large β_0 approximation and exactly, where available. We use $m_b^{\overline{\text{MS}}}(m_b^{\overline{\text{MS}}}) = 4.2$ GeV, $\mu = 4.2$ GeV, $\alpha_s(\mu) = 0.225$ and $\mu_f = 2$ GeV as inputs and neglect all light-quark masses.

expansions of the pole-$\overline{\text{MS}}$, the pole-PS and the PS-$\overline{\text{MS}}$ mass relation for the bottom quark. We observe that both the pole-$\overline{\text{MS}}$ and the pole-PS mass relation start to diverge from the order α_s^5 ($n = 4$). The exact expansion is known up to order α_s^4 and we see that already for $n = 2, 3$ the large β_0 approximation reproduces the full result up to $\mathcal{O}(10\%)$ corrections. The PS-$\overline{\text{MS}}$ mass relation is much better behaved. The minimal term is reached for $n = 6$, where the contributions from the leading UV renormalon begin to dominate. Recall that UV renormalons are naively Borel summable and do not cause ambiguities. The remaining renormalon ambiguity is due to the pole at $u = 3/2$ in (2.16) and of the order $\Lambda_{\text{QCD}}^3/m_b^2 \sim 1$ MeV, which is completely negligible compared to other uncertainties. Thus, the PS mass is ideally suited for threshold problems. Furthermore, it can lead to improved convergence with respect to the $\overline{\text{MS}}$ scheme in observables where a heavy quark is close to its mass shell like inclusive B decays. Comparisons of different mass schemes in this context can be found in [9, 56].

3. Effective field theory setup

In this chapter we describe the effective field theory setup, that all computations in this thesis are based upon. In Section 3.1, we discuss the basic scaling properties of the threshold production of heavy quarks. Section 3.2 discusses how loop integrals can be systematically expanded according to these scaling rules prior to the loop integration. Rather than performing expansions on a diagrammatic level, it is beneficial to construct an effective field theory, whose Feynman rules directly give the expanded form of the contributions. It is provided by PNRQCD, as described in Section 3.3. Finally, Section 3.4 shows how the setup can be generalized to also account for the decays of the top quarks. The procedure introduces spurious divergences in the resonant and non-resonant contributions to the full cross section, which cancel when they are treated in a consistent way. We therefore devote Section 3.5 to a detailed description of the organization of the computation.

3.1. Kinematics and basic structure

We consider the production of a top pair in e^+e^- collisions by the s-channel exchange of a photon. The tree-level diagram for this process is shown in Figure 3.1. The threshold region for this process is defined by $s = q^2 \approx 4m_t^2$, or more precisely in the center-of-mass frame by $q = (2m_t + E, \mathbf{0})$ with $E \sim m_t\alpha_s^2$. The top quarks can be off-shell by a small

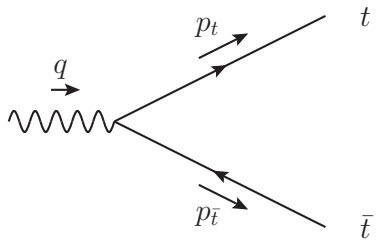

Figure 3.1.: Tree-level diagram for the production of a top pair from a s-channel photon.

amount determined by their width $\Gamma_t \sim m_t\alpha$. Our counting for the coupling constants is $\alpha \sim \alpha_s^2$, which is numerically well justified. We parametrize the top-quark momentum by small fluctuations around them being at rest, $p_t = (m_t, \mathbf{0}) + p$ and $p_{\bar{t}} = (m_t, \mathbf{0}) + \bar{p}$. The condition

$$p_t^2 - m_t^2 \sim m_t\Gamma_t \sim m_t^2\alpha_s^2 \tag{3.1}$$

gives the following scaling for the top momentum

$$p^0 \sim m_t \alpha_s^2, \qquad \mathbf{p} \sim m_t \alpha_s, \tag{3.2}$$

and the same for the anti-top. We observe that, near threshold, the tops are non-relativistic with a small velocity of the order of the strong coupling constant

$$v \equiv \sqrt{E/m_t} \sim \alpha_s \ll 1. \tag{3.3}$$

This implies that threshold production involves three different scales, which are the hard scale, set by the top mass m_t, the soft scale, set by the spatial top momentum $\mathbf{p} \sim m_t v \sim m_t \alpha_s$, and the ultrasoft scale, set by the kinetic energy $p^0 \sim m_t v^2 \sim m_t \alpha_s^2$ of the tops. The presence of multiple scales makes the computation of higher order corrections very challenging and it requires sophisticated methods, which will be described in Sections 3.2 and 3.3.

First however, let us consider the expansion of the diagram in Figure 3.1 in the small velocity v. For non-relativistic systems it is convenient to use the Dirac basis

$$u(p_t) = \sqrt{2m_t + p^0} \begin{pmatrix} \xi \\ \frac{\boldsymbol{\sigma}\cdot\mathbf{p}}{2m_t + p^0}\xi \end{pmatrix}, \tag{3.4}$$

$$v(p_{\bar{t}}) = \sqrt{2m_t + \bar{p}^0} \begin{pmatrix} \frac{\boldsymbol{\sigma}\cdot\bar{\mathbf{p}}}{2m_t + \bar{p}^0}\eta \\ \eta \end{pmatrix}, \tag{3.5}$$

$$\gamma^0 = \begin{pmatrix} \mathbf{1} & \mathbf{0} \\ \mathbf{0} & -\mathbf{1} \end{pmatrix}, \tag{3.6}$$

$$\gamma^i = \begin{pmatrix} \mathbf{0} & \boldsymbol{\sigma}^i \\ -\boldsymbol{\sigma}^i & \mathbf{0} \end{pmatrix}. \tag{3.7}$$

The two-spinors are normalized according to $\xi^\dagger \xi = \eta^\dagger \eta = 1$. Due to the ward identity $q^\mu \Gamma_\mu = 0$, the zero component of the vertex vanishes in the center-of-mass frame. The spatial components are simply

$$\bar{u}\gamma^i v = 2m_t \xi^\dagger \sigma^i \eta + \mathcal{O}(v^2), \tag{3.8}$$

where the missing terms are only relevant at NNLO in the non-relativistic power counting $v \sim \alpha_s$. We now consider the virtual one-loop correction shown in Figure 3.2. In the threshold region, real radiation is restricted to very small momenta $k \sim m_t v^2$ by momentum conservation and is therefore strongly suppressed. Thus, it will not be considered here. Instead of the whole loop diagram integrated over all momentum regions, we focus only on the part where the top quarks inside the loop are also non-relativistic. This implies that the loop momentum k also scales like (3.2). The expansion of the numerator in this region yields

$$\begin{aligned} &\bar{u}\gamma_\alpha(\not{k} + \not{p}_t + m_t)\gamma^i(\not{k} - \not{p}_{\bar{t}} + m_t)\gamma_\alpha v \\ &= m_t^2 \bar{u}\gamma_\alpha(1+\gamma^0)\gamma^i(1-\gamma^0)\gamma_\alpha v + \dots \\ &= -8m_t^3 \xi^\dagger \sigma^i \eta + \mathcal{O}(\epsilon) + \mathcal{O}(v^2), \end{aligned} \tag{3.9}$$

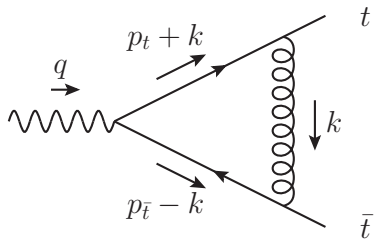

Figure 3.2.: One-loop diagram for the production of a top pair from a s-channel photon.

which has the same structure as the tree-level result (3.8). When the same expansion is also applied to the denominators, one obtains

$$\begin{aligned}
&i\int\frac{d^dk}{(2\pi)^d}\frac{1}{k^2[(k+p_t)^2-m_t^2][(k-p_{\bar{t}})^2-m_t^2]}\\
&=i\int\frac{d^dk}{(2\pi)^d}\frac{1}{[-\mathbf{k}^2][2m_t(k^0+p^0)-(\mathbf{k}+\mathbf{p})^2][2m_t(E-k^0-p^0)-(\mathbf{k}+\mathbf{p})^2]}+\dots\\
&=\frac{1}{4m_t}\int\frac{d^{d-1}\mathbf{k}}{(2\pi)^{d-1}}\frac{1}{[-\mathbf{k}^2][m_tE-(\mathbf{k}+\mathbf{p})^2]}+\dots\\
&=\frac{1}{4m_t}\frac{\Gamma(1/2+\epsilon)}{(4\pi)^{3/2-\epsilon}}\int_0^1\frac{dx}{[x(1-x)\mathbf{p}^2-xm_tE]^{1/2+\epsilon}}+\dots\sim\frac{1}{m_t^2v}+\dots.
\end{aligned}\tag{3.10}$$

In the second step the contour in the k^0 plane has been closed in the upper half-plane and the residue of the pole at $k^0 = E - p^0 - (\mathbf{k}+\mathbf{p})^2/(2m_t) + i0$ has been picked up. The remaining integral over the spatial components of the loop momenta is straightforward. We can already see from its Feynman parametrization that it scales like $1/v$ because both $\mathbf{p}^2$ and m_tE are of the order $m_t^2v^2$. It may seem odd that the integrand is expanded non-relativistically, whereas the integration is performed over the whole domain of loop momenta. In the framework of the expansion by regions, discussed in the next section, this will turn out to be a well-defined contribution to the complete loop integral expanded in v. For now, we are mainly concerned with the scaling of the integral and note that it could also have been obtained from applying the power counting $k^0 \sim m_tv^2$, $\mathbf{k}\sim m_tv$ to the integration measure $d^dk = dk^0d^{d-1}\mathbf{k}\sim m_t^4v^5$ and the denominators, which all scale like $m_t^2v^2$. In conclusion, the considered contribution from the one-loop correction is proportional to the same structure $\xi^\dagger\sigma^i\eta$ as the leading order result and has the relative scaling α_s/v. Since $v\sim\alpha_s$, this contribution is not suppressed relative to the tree-level one. This generalizes to arbitrary loop orders, which can be demonstrated by applying the power counting to the type of diagrams shown in Figure 3.3, which scale like $(\alpha_s/v)^n\sim 1$. Additional gluons do not change the structure of the numerator (3.9). Thus, the Dirac algebra is trivial at LO in the non-relativistic regime. The scaling of the ladder diagrams demonstrates the

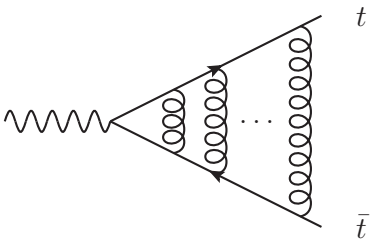

Figure 3.3.: Ladder type diagram for the production of a top pair from a s-channel photon.

breakdown of conventional perturbation theory in α_s for threshold problems. To obtain a reliable prediction, it is necessary to sum these ladder type contributions to all orders.

We note that a naive power counting analysis leads to the fallacy that other structures with an equal number of propagators are also unsuppressed, e.g. ladders with crossing rungs or with vertex corrections to rungs. It is simple to show that these examples vanish because the poles in the zero component of one of the loop momenta lie on the same side of the contour, which can thus be closed without picking up either of the residues. However, it is difficult to generalize these arguments to all possible contributions, especially when higher orders in the expansion are considered. Clearly, a more formal approach is required.

3.2. Expansion by regions

The threshold production of top quarks is governed by a hierarchy of three scales. They are set by the mass m_t, the spatial momentum $m_t v$ and the non-relativistic energy $m_t v^2$ and denoted as the hard, soft and ultrasoft scale, respectively. Having three different scales makes the exact evaluation of multiloop integrals particularly difficult. Instead of attempting to solve the integrals exactly, the large hierarchy between the scales makes it possible to expand in their ratios, which is equivalent to an expansion in the small velocity v. This can be done prior to the loop integration by a method denoted as expansion by regions [57–59]. The relevant momentum regions for threshold problems are

$$\begin{array}{lll} \text{hard region (h):} & k^0 \sim m_t, & \mathbf{k} \sim m_t, \\ \text{soft region (s):} & k^0 \sim m_t v, & \mathbf{k} \sim m_t v, \\ \text{potential region (p):} & k^0 \sim m_t v^2, & \mathbf{k} \sim m_t v, \\ \text{ultrasoft region (us):} & k^0 \sim m_t v^2, & \mathbf{k} \sim m_t v^2. \end{array} \tag{3.11}$$

The recipe to obtain the expansion of a given one-loop integral is

$$\mathcal{T}_v \int d^d k f(k) = \int d^d k \mathcal{T}_{(\mathrm{h})} f(k) + \int d^d k \mathcal{T}_{(\mathrm{s})} f(k) + \int d^d k \mathcal{T}_{(\mathrm{p})} f(k) + \int d^d k \mathcal{T}_{(\mathrm{us})} f(k), \tag{3.12}$$

where $\mathcal{T}_v$ corresponds to a Taylor expansion of the loop integral with respect to the velocity and $\mathcal{T}_{(\mathrm{r})}$ to a Taylor expansion of the integrand with respect to the scaling (3.11)

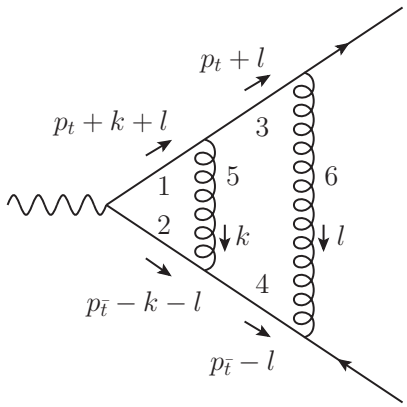

Figure 3.4.: Two-loop example for the expansion by regions.

of the region r for the loop momentum k. It is assumed that the parametrization of the loop momentum satisfies what is called "canonical routing" in [57]. This means that the large external momenta of heavy quarks are routed through the heavy quark lines in the loop as well. The formulation (3.12) of the threshold expansion is for example not valid for Figure 3.2 with the reparametrization $k \to k - p_t$. A reparametrization-independent formulation in terms of subgraphs of different momentum regions can be found in [57].

The expanded integrands are integrated over the whole domain and all scaleless integrals are set to zero. In general, this procedure leads to additional divergences in the individual integrals, that cancel in the sum over regions. It was proven that there is no multiple counting associated with the fourfold integration over the whole domain in [59]. This relies on the use of dimensional regularization for the integrals and the homogeneous scaling in the small parameter v of all the regions. In general, the expansion by regions can be formulated including so-called overlap contributions, which account for multiple counting. In the application to threshold production these overlap integrals are all scaleless and vanish. The formalism of [59] also assures that no regions are missed. Any additional regions one might introduce only yield scaleless integrals.

The ad hoc treatment used in the previous section for the diagram in Figure 3.2 corresponds to the leading contribution from the potential region. Section 4 of [59] shows how the expansion of the full result for the scalar integral of the diagram in Figure 3.2 is reproduced by the expansion by regions in a mathematically rigorous way.

The expansion by regions can also be applied to multiloop integrals. In this case a formulation in terms of subgraphs is mandatory because, in a given parametrization (even for "canonical routing"), there can, for example, be contributions, where the loop momenta k and l are hard, but a certain linear combination of them is potential. This is the case in Figure 3.4 with k and l hard, but $k + l$ potential. The proper description is that the subgraph involving the lines 3, 4, 5, and 6 is hard and the remainder potential. Loosely speaking, the full result is obtained by taking the sum over all possible assignments of

regions to subgraphs. Since the procedure is very intuitive, we refrain from describing the algorithm for obtaining the result for a general diagram in the expansion by regions meticulously and refer to [57] instead.

3.3. Non-relativistic and potential non-relativistic QCD

The expansion by regions provides a method to expand an individual loop integral in a small parameter. At higher orders in perturbation theory, the number of diagrams grows rapidly. For applications at NNNLO, it is therefore advantageous to perform this expansion at the Lagrangian level by introducing effective field theories. The corresponding Feynman rules provide a way to obtain the terms of a certain order in the expansion by regions directly, without referring to diagrams in the full theory. This section only deals with QCD and the discussion of electroweak effects is postponed to Section 3.4. The complete setup necessary for the NNNLO QCD computation is described in detail in [60] (see also [61,62] for additional reviews). We restrict our discussion to the basic concepts and refer to the literature for detailed results.

The production of a top pair in e^+e^- annihilation proceeds via the exchange of photons and Z bosons. The coupling of photons to fermions is vector-like and the Z boson couples to vector currents and axial-vector currents with the respective strengths

$$v_f = \frac{T_3^f - 2e_f \sin^2\theta_w}{2\sin\theta_w\cos\theta_w}, \qquad a_f = \frac{T_3^f}{2\sin\theta_w\cos\theta_w}, \tag{3.13}$$

where θ_w is the weak mixing angle, e_f the electric charge and T_3^f the third component of the weak isospin of the fermion f.

We define the ratio $R = \sigma_{t\bar{t}X}/\sigma_0$ as the inclusive $t\bar{t}$ production cross section $\sigma_{t\bar{t}X} = \sigma(e^+e^- \to t\bar{t}X)$ normalized to the high-energy limit of the $\mu^+\mu^-$ production cross section $\sigma_0 = 4\pi\alpha_{\text{em}}^2/(3q^2)$. The optical theorem can be used to relate the R-ratio to the imaginary part of the spectral functions $\Pi^{(v,a)}$ of vector and axial-vector currents

$$\begin{aligned} R = 12\pi\ \text{Im}\Bigg[& e_t^2\Pi^{(v)}(q^2) - \frac{2q^2}{q^2-M_Z^2} v_e v_t e_t \Pi^{(v)}(q^2) \\ & + \left(\frac{q^2}{q^2-M_Z^2}\right)^2 (v_e^2+a_e^2)(v_t^2\Pi^{(v)}(q^2) + a_t^2\Pi^{(a)}(q^2))\Bigg]. \end{aligned} \tag{3.14}$$

The spectral functions are defined as

$$\begin{aligned} \Pi_{\mu\nu}^{(X)}(q^2) &= i\int d^dx\, e^{iq\cdot x} \left\langle 0 \,\middle|\, T\left[j_\mu^{(X)}(x) j_\nu^{(X)}(0)\right] \,\middle|\, 0\right\rangle \\ &= (q_\mu q_\nu - q^2 g_{\mu\nu})\,\Pi^{(X)}(q^2) + q_\mu q_\nu \Pi_L^{(X)}(q^2). \end{aligned} \tag{3.15}$$

for the vector current $j_\mu^{(v)} = \bar{t}\gamma_\mu t$ and the axial-vector current $j_\mu^{(a)} = \bar{t}\gamma_\mu\gamma_5 t$. We want to determine the cross section in the non-relativistic expansion $\alpha_s \sim v \ll 1$. Including

the all-order summation of the ladder graphs in Figure 3.3 (Coulomb resummation), the counting is

$$R \sim v \sum_k \left(\frac{\alpha_s}{v}\right)^k \times \begin{cases} 1 & \text{LO} \\ \alpha_s, v & \text{NLO} \\ \alpha_s^2, \alpha_s v, v^2 & \text{NNLO} \\ \alpha_s^3, \alpha_s^2 v, \alpha_s v^2, v^3 & \text{NNNLO} \end{cases} . \tag{3.16}$$

The prefactor v comes from the phase-space, which is suppressed near threshold. We describe below, how the Coulomb resummed cross section can be computed using effective field theories.

The construction of the effective field theory makes use of the large scale hierarchy. The hard and soft scale can be integrated out because external particles with these large momentum modes cannot appear as final states in the threshold region due to kinematic restrictions (see Section 3.1). The full theory, QCD, contains heavy quarks Q and massless particles g (gluons, light quarks and ghost are abbreviated here with g for simplicity of notation) of all momentum regions. However, heavy quarks cannot be ultrasoft. This is equivalent to the statement that all terms with an ultrasoft heavy quark line lead to scaleless integrals. The procedure consists of two steps:

$$\begin{array}{ll} \mathcal{L}_{\text{QCD}}[Q(\text{h,s,p}), g(\text{h,s,p,us})] & \mu > m \\ \Big\downarrow & \\ \mathcal{L}_{\text{NRQCD}}[Q(\text{s,p}), g(\text{s,p,us})] & mv < \mu < m \\ \Big\downarrow & \\ \mathcal{L}_{\text{PNRQCD}}[Q(\text{p}), g(\text{us})] & \mu < mv \end{array} \tag{3.17}$$

In the first step, non-relativistic QCD (NRQCD) [63–65] is constructed by integrating out the hard scale. In the process hard subgraphs are contracted to local vertices. In the spectral function, the hard subgraph can either contain both external currents, one of them or neither one. In the first case, the imaginary part vanishes since there are no on-shell cuts involving hard modes. Hard subgraphs, that contain one external current, are absorbed into hard Wilson coefficients c_v, d_v and c_a of the non-relativistic currents

$$j^{(v)k} = c_v \psi^\dagger \sigma^k \chi + \frac{d_v}{6m^2} \psi^\dagger \sigma^k \mathbf{D}^2 \chi + \ldots , \tag{3.18}$$

$$j^{(a)k} = \frac{c_a}{2m_t} \psi^\dagger \left[\sigma^k, (-i)\boldsymbol{\sigma} \cdot \mathbf{D}\right] \chi + \ldots , \tag{3.19}$$

where $\psi(\chi)$ are the non-relativistic heavy quark (anti-quark) fields, which can be either soft or potential. The Wilson coefficients can be computed in perturbation theory through a matching computation. The NNLO corrections to c_v are known since the 90's [66,67] and

the full NNNLO result required for the third-order cross section was computed recently [68–70]. The coefficient d_v multiplies the subleading term in the non-relativistic expansion of the vector current, which is suppressed by $v^2 \sim \alpha_s^2$. Thus, it is only required up to NLO [60]. The axial-vector current is of order $v \sim \alpha_s$. The interference contribution of a vector and axial-vector current vanishes when integrated over phase-space and, therefore, c_a is also only needed at NLO. It is known up to NNLO [70].

Last but not least, hard subgraphs, that do not contain either one of the external currents, are represented by local operators in the NRQCD Lagrangian. The NRQCD Lagrangian contains only the non-relativistic degrees of freedom indicated in (3.17). The matching computations, that are relevant for the NNNLO cross section, were performed in [60], where the Lagrangian and the Feynman rules can be found.

The spectral functions in NRQCD take the form

$$\Pi^{(v)}(q^2) = \frac{1}{(d-1)q^2}\,\Pi_{ii}^{(v)}(q^2) = \frac{N_c}{2m_t^2}\,c_v\left[c_v - \frac{E}{m}\left(c_v + \frac{d_v}{3}\right)\right] G(E) + \ldots, \tag{3.20}$$

$$\Pi^{(a)}(q^2) = \frac{1}{(d-1)q^2}\,\Pi_{ii}^{(a)}(q^2) = \frac{N_c c_a^2}{2m_t^4}\,\frac{d-2}{d-1}\,G^P(E) + \ldots, \tag{3.21}$$

where the dots stand for terms that are beyond NNNLO. The expressions G and G^P are non-relativistic S-wave and P-wave Green functions

$$G(E) = \frac{i}{2N_c(d-1)}\int d^dx e^{iEx^0}\left\langle 0\,\middle|\,T\left([\psi^\dagger\sigma^k\chi]^\dagger(x)[\psi^\dagger\sigma^k\chi](0)\right)\,\middle|\,0\right\rangle_{\text{NRQCD}}, \tag{3.22}$$

$$G^P(E) = \frac{i}{8N_c(d-2)}\int d^dx e^{iEx^0}\left\langle 0\,\middle|\,T\left([\psi^\dagger\Gamma^k\chi]^\dagger(x)[\psi^\dagger\Gamma^k\chi](0)\right)\,\middle|\,0\right\rangle_{\text{NRQCD}}, \tag{3.23}$$

where $\Gamma^k = (-i)\left[\sigma^k, \boldsymbol{\sigma}\cdot\mathbf{D}\right]$. They must be evaluated with the NRQCD Lagrangian.

In the second step of (3.17), the soft modes and massless potential modes are integrated out. If the soft subgraph connects to both external currents, there are again no on-shell cuts. If it connects to one external current, it gives a contribution to the soft Wilson coefficients for the external current. However, it was demonstrated in [60] that the soft matching for the external currents is trivial, since all integrals are scaleless. Soft subgraphs, that do not connect to the external currents, are absorbed into the Lagrangian of an effective field theory called potential non-relativistic QCD (PNRQCD) [34–38]. It has the form

$$\begin{aligned}\mathcal{L}_{\text{PNRQCD}} = {}& \psi^\dagger\left(i\partial_0 + \frac{\boldsymbol{\partial}^2}{2m} + g_s A_0(t,\mathbf{0}) - g_s\mathbf{x}\cdot\mathbf{E}(t,\mathbf{0}) + \frac{\boldsymbol{\partial}^4}{8m^3}\right)\psi \\ & + \chi^\dagger\left(i\partial_0 - \frac{\boldsymbol{\partial}^2}{2m} + g_s A_0(t,\mathbf{0}) - g_s\mathbf{x}\cdot\mathbf{E}(t,\mathbf{0}) - \frac{\boldsymbol{\partial}^4}{8m^3}\right)\chi \\ & + \int d^{d-1}\mathbf{r}\left[\psi_a^\dagger\psi_b\right](x+\mathbf{r})V_{ab;cd}(\mathbf{r},\partial)\left[\chi_c^\dagger\chi_d\right](x).\end{aligned} \tag{3.24}$$

In PNRQCD, the heavy quark fields are purely potential and the gluon field is purely ultrasoft. Thus, they have a manifest power-counting in the velocity v. The counting

$\psi \sim (mv)^{3/2}$ for the heavy quark fields can be deduced from the expansion of the full theory propagator

$$\langle 0 \,|\, Tq(x)\bar{q}(y) \,|\, 0\rangle = \int \frac{d^4p}{(2\pi)^4} \frac{i(\not{p}+m)}{p^2-m^2+i0} e^{-ip\cdot(x-y)} \tag{3.25}$$

in the non-relativistic region, where

$$\frac{i(\not{p}+m)}{p^2-m^2+i0} = \frac{im(1+\gamma^0)}{2mp^0-\mathbf{p}^2+i0} + \cdots \sim \frac{1}{mv^2} \tag{3.26}$$

and $d^4p \sim m^4v^5$. The $i\partial_0$ and $\boldsymbol{\partial}^2/(2m)$ terms in (3.24) have the same counting in v because they act on a potential mode with $p^0 \sim mv^2$ and $\mathbf{p} \sim mv$. The leading order kinetic term of the heavy quarks has the typical structure for non-relativistic modes and is of the order m^4v^5. The non-relativistic quark and anti-quark fields interact via potentials $V_{ab;cd}$. The leading effect is the color Coulomb potential given by

$$V_{ab;cd}(\mathbf{r},\partial) = -\frac{\alpha_s}{|\mathbf{r}|} T^A_{ab} T^A_{cd}, \tag{3.27}$$

which comes from integrating out potential gluon exchange. Counting $r = |\mathbf{r}| \sim 1/(mv)$, the LO potential term in (3.24) is of the same order m^4v^5 as the kinetic terms. Thus, it must be treated non-perturbatively, which accounts for the Coulomb resummation in the cross section. Contrary to most field theories, the LO approximation of PNRQCD does not describe the propagation of free particles, but the propagation of heavy quark-antiquark pairs, that interact via the instantaneous LO color Coulomb potential.

The effective theory described by (3.24) is local in time, but non-local in space due to the appearance of the potentials. This may seem peculiar, but can be understood in a very simple way. The first step in the construction of an effective field theory is to integrate out certain particles or momentum modes. This does not rely on any hierarchies whatsoever. Any modes, that do not appear externally, can be integrated out in principle, which always yields a nonlocal action. The size of the non-localities is determined by the typical distance, over that the modes were propagating, i.e. they are of the size $x_{\rm nl} \sim 1/m$ for the hard modes integrated out in the first step in (3.17). In the construction of NRQCD, one then exploits that the remaining modes are at most soft, which means that they only fluctuate significantly over distances of the order $x_{\rm fluc} \sim 1/(mv)$ or larger. The hierarchy $x_{\rm nl} \ll x_{\rm fluc}$ enables us to perform an operator product expansion (OPE) [71] to obtain a local effective theory. The physical picture corresponding to the expansion is that the wavelength of the remaining modes is much larger than the size of the non-localities, which implies that they cannot be resolved and non-local operator products appear point-like.

In the second step of (3.17), soft modes and massless potential modes are integrated out. From the expansion of the propagator, we observe that massless potential modes only propagate in the spatial components. Thus, integrating out these modes yields non-localities of the order $t_{\rm nl} \sim |\mathbf{x}_{\rm nl}| \sim 1/(mv)$. The remaining potential heavy quark fields fluctuate significantly over time differences of the order $t_{\rm fluc} \sim 1/(mv^2)$ and spatial distances

of the order $|\mathbf{x}_{\rm fluc}| \sim 1/(mv)$. Fluctuations of the ultrasoft modes occur over similar or larger scales $t_{\rm fluc} \sim |\mathbf{x}_{\rm fluc}| \sim 1/(mv^2)$. We observe that there is a hierarchy between the size of the non-localities and of the remaining fluctuations in the time component $t_{\rm nl} \ll t_{\rm fluc}$, but not in the spatial components $|\mathbf{x}_{\rm nl}| \sim |\mathbf{x}_{\rm fluc}|$. Thus, an expansion in the time component can be performed to render the effective theory local in time, but the non-localities in the spatial components remain. This explains the structure of PNRQCD.

Similar scaling arguments also demonstrate why the ultrasoft gluon field has to be multipole expanded in (3.24). The ultrasoft gluon field can resolve the temporal, but not the spatial fluctuations of potential heavy quark modes. Thus, the ultrasoft gluon fields are multipole expanded in their spatial components in the interaction terms with heavy quarks in (3.24). The multipole expansion in position space corresponds to the strict expansion by regions in momentum space, which renders all terms homogeneous in v. Details on the origin of the ultrasoft gluon interaction terms can be found in [56].

The leading term in the multipole expansion $g_s A_0(t, \mathbf{0})$ couples to the net color charge of the heavy quark pair. Since the initial state is colorless the net color charge vanishes and the $g_s A_0(t, \mathbf{0})$ coupling does not contribute. Technically, this can be demonstrated by performing a field redefinition involving a Wilson line of the A_0 field

$$\psi(x) \to \bar{P} \exp\left[-ig_s \int_0^\infty dt A_0(x + (t, \mathbf{0}))\right] \psi(x), \tag{3.28}$$

and analogously for the anti-quark field [72]. The symbol $\bar{P}$ stands for anti-path ordering of the exponential. The redefinition (3.28) removes the $g_s A_0(t, \mathbf{0})$ term from the Lagrangian. It introduces a Wilson line in the couplings to $g_s \mathbf{x} \cdot \mathbf{E}(t, \mathbf{0})$, which modifies the Lagrangian only beyond NNNLO.

The chromoelectric dipole term $g_s \mathbf{x} \cdot \mathbf{E}(t, \mathbf{0})$ is of the order $m^4 v^{13/2}$, i.e. suppressed by $v^{3/2}$. It contributes at NNNLO because two insertions are required to obtain a non-vanishing effect. The ultrasoft corrections due to the chromoelectric dipole operator have been computed in [73, 74].

The Coulomb resummed cross section is obtained by evaluating the non-relativistic Green functions (3.22) and (3.23) in PNRQCD. Due to the triviality of the soft matching of the external currents, they are given by the expressions (3.22) and (3.23) with the only difference that the matrix elements have to be evaluated within PNRQCD instead of NRQCD. Derivations of the PNRQCD Feynman rules can be found in [38, 60]. Barring ultrasoft effects, PNRQCD perturbation theory works exactly like time-independent perturbation theory in quantum mechanics and the particle numbers of the heavy quark and anti-quark are separately conserved. The crucial difference with respect to quantum mechanics is that the potentials are not phenomenological, but follow directly from a matching procedure to the full theory, QCD. Furthermore, PNRQCD also describes "vacuum fluctuation" effects in a systematic way. For example, its cousin PNRQED provides a completely linear derivation of the Lamb shift [35], without any complications like the need to introduce an artificial photon mass [75]. It is therefore also an ideal framework for some precision calculations in atomic physics, see e.g. [76].

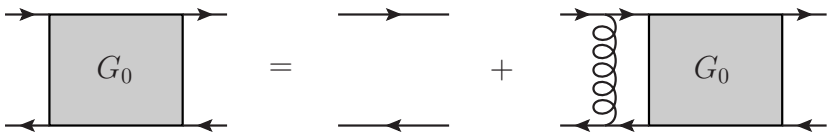

Figure 3.5.: Graphical representation of the Lippmann-Schwinger equation.

The Coulomb resummed propagator for a heavy quark pair in a color singlet state is given by a non-relativistic Green function and higher order potentials are treated perturbatively

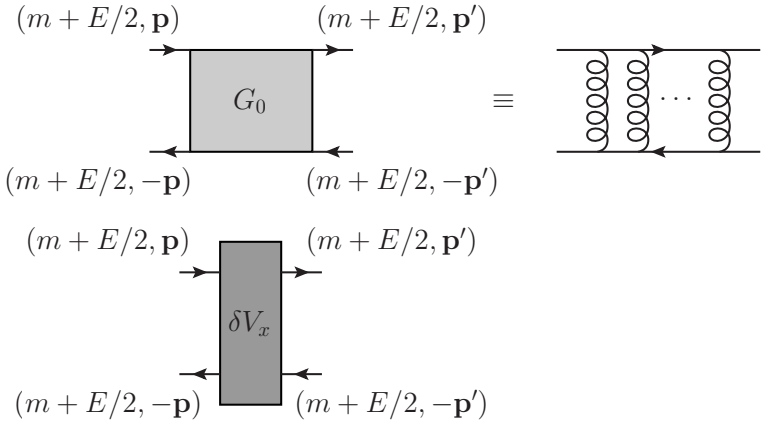

(3.29)

The Green function $\tilde{G}_0(\mathbf{p},\mathbf{p}';E)$ satisfies the d-dimensional Lippmann-Schwinger equation

$$\left(\frac{\mathbf{p}^2}{m_t}-E\right)\tilde{G}_0(\mathbf{p},\mathbf{p}';E)-\tilde{\mu}^{2\epsilon}\int\frac{d^{d-1}\mathbf{k}}{(2\pi)^{d-1}}\frac{4\pi C_F\alpha_s}{\mathbf{k}^2}\,\tilde{G}_0(\mathbf{p}-\mathbf{k},\mathbf{p}';E) \\ =(2\pi)^{d-1}\delta^{(d-1)}(\mathbf{p}-\mathbf{p}'), \tag{3.30}$$

where $\tilde{\mu}=\mu\left[e^{\gamma_E}/(4\pi)\right]^{1/2}$ has been chosen such that the minimal subtraction of $1/\epsilon$ poles corresponds to the $\overline{\text{MS}}$ instead of the MS scheme. The equation (3.30) has the structure shown in Figure 3.5, which comes from splitting the sum over arbitrary number of gluon exchanges into zero exchanges and the sum over at least one exchange. The tilde is used to indicate that the Green function is given in momentum space. Its Fourier transform

$$G_0(\mathbf{r},\mathbf{r}';E)=\int\frac{d^{d-1}\mathbf{p}}{(2\pi)^{d-1}}\int\frac{d^{d-1}\mathbf{p}'}{(2\pi)^{d-1}}\,e^{i\mathbf{p}\cdot\mathbf{r}}e^{-i\mathbf{p}'\cdot\mathbf{r}'}\tilde{G}_0(\mathbf{p},\mathbf{p}';E) \tag{3.31}$$

is the solution to a Schrödinger equation

$$\left(-\frac{\nabla^2_{(r)}}{m_t}-\frac{C_F\alpha_s}{r}-E\right)G_0(\mathbf{r},\mathbf{r}';E)=\delta^{(3)}(\mathbf{r}-\mathbf{r}') \tag{3.32}$$

in four dimensions. Representations for the Green function are only known in $d=4$ dimensions [77–80]. It is convenient to decompose the Green function in terms of partial

waves

$$G_0(\mathbf{r},\mathbf{r}';E)=\sum_{l=0}^{\infty}(2l+1)\,P_l\!\left(\frac{\mathbf{r}\cdot\mathbf{r}'}{rr'}\right)\,G_{[l]}(r,r';E), \tag{3.33}$$

where l is the quantum number of the angular momentum of the quark pair and $P_l(z)$ are the Legendre polynomials. We will make use of the integral representation from [77],

$$\begin{aligned}G_{[l]}(r,r';E)=&\frac{m_t p}{2\pi}\frac{(2pr)^l(2pr')^l}{\Gamma(l+1+\lambda)\Gamma(l+1-\lambda)}\\&\times\int_0^1 dt\int_1^\infty ds\,[s(1-t)]^{l+\lambda}\,[t(s-1)]^{l-\lambda}\exp\left\{-p\left[r'(1-2t)+r(2s-1)\right]\right\},\end{aligned} \tag{3.34}$$

valid for $r'<r$ and a sum representation from [79, 80],

$$G_{[l]}(r,r';E)=\frac{m_t p}{2\pi}(2pr)^l(2pr')^l e^{-p(r+r')}\sum_{s=0}^{\infty}\frac{s!L_s^{(2l+1)}(2pr)L_s^{(2l+1)}(2pr')}{(s+2l+1)!(s+l+1-\lambda)}, \tag{3.35}$$

with the Laguerre polynomials

$$L_s^{(\alpha)}(z)=\frac{e^z z^{-\alpha}}{s!}\left(\frac{d}{dz}\right)^s\left[e^{-z}z^{s+\alpha}\right]. \tag{3.36}$$

We have also defined

$$\begin{aligned}p&=\sqrt{-m_t E},\\ \lambda&=\frac{m_t\alpha_s C_F}{2p}.\end{aligned} \tag{3.37}$$

The non-relativistic correlators (3.22) and (3.23) can now be evaluated in the resummed perturbation theory. The Feynman diagrams up to NNLO are shown in Figure 3.6. The higher order potentials have been determined in [37, 81–87] and can be found in [60]. For the computation of the P-wave contribution, we require only the colour-singlet projection

$$V(\mathbf{p},\mathbf{p}')=\frac{1}{N_c}\delta_{bc}\delta_{da}V_{ab;cd}(\mathbf{p},\mathbf{p}') \tag{3.38}$$

of the general potential up to NLO. It is given by

$$V(\mathbf{p},\mathbf{p}')=-\frac{4\pi C_F\alpha_s}{\mathbf{q}^2}\left[\mathcal{V}_C^{(0)}+\frac{\alpha_s}{4\pi}\mathcal{V}_C^{(1)}+\mathcal{O}(\alpha_s^2)\right]+\ldots, \tag{3.39}$$

where the coefficients of the LO and NLO Coulomb potential in d dimensions are

$$\mathcal{V}_C^{(0)}=1, \tag{3.40}$$

$$\mathcal{V}_C^{(1)}=\left[\left(\frac{\mu^2}{\mathbf{q}^2}\right)^{\epsilon}-1\right]\frac{\beta_0}{\epsilon}+\left(\frac{\mu^2}{\mathbf{q}^2}\right)^{\epsilon}a_1(\epsilon), \tag{3.41}$$

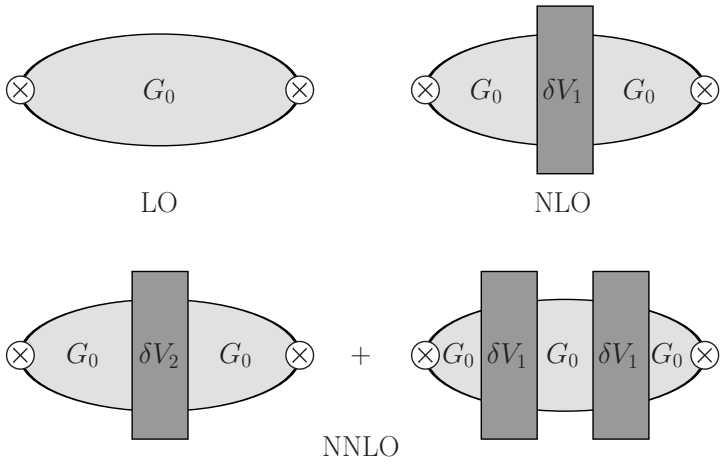

Figure 3.6.: The Green functions (3.22) and (3.23) in PNRQCD perturbation theory. The vertices correspond to the insertion of the non-relativistic currents given in (3.18) and (3.19).

with

$$a_1(\epsilon) = \Big(C_A[11-8\epsilon] - 4T_F n_f\Big)\frac{e^{\gamma_E\epsilon}\Gamma(1-\epsilon)\Gamma(2-\epsilon)\Gamma(\epsilon)}{(3-2\epsilon)\Gamma(2-2\epsilon)} - \frac{\beta_0}{\epsilon}, \tag{3.42}$$

and

$$\beta_0 = \frac{11C_A}{3} - \frac{4T_F n_f}{3}, \tag{3.43}$$

where $C_A = 3$, $T_F = 1/2$ and n_f is the number of massless quarks. Using the Feynman rules (3.29) for the non-relativistic correlators (3.22) and (3.23) at NLO, we obtain

$$\begin{aligned} G(E) &= \frac{i}{2N_c}\int d^dx e^{iEx^0}\left\langle 0\left|\, T\left([\psi^\dagger\chi]^\dagger(x)[\psi^\dagger\chi](0)\right)\right|0\right\rangle_{\text{PNRQCD}} \\ &= G_0(E) + \delta_1 G(E) + \dots \\ &= \tilde{\mu}^{4\epsilon}\int\frac{d^{d-1}\mathbf{p}}{(2\pi)^{d-1}}\int\frac{d^{d-1}\mathbf{p}'}{(2\pi)^{d-1}}\Bigg[G_0(\mathbf{p},\mathbf{p}';E) \\ &\quad + \tilde{\mu}^{4\epsilon}\int\frac{d^{d-1}\mathbf{p}_1}{(2\pi)^{d-1}}\int\frac{d^{d-1}\mathbf{p}_2}{(2\pi)^{d-1}}\,G_0(\mathbf{p},\mathbf{p}_1;E)\,i\left(-\frac{\alpha_s^2 C_F}{(\mathbf{p}_1-\mathbf{p}_2)^2}\mathcal{V}_C^{(1)}\right)iG_0(\mathbf{p}_2,\mathbf{p}';E) \\ &\quad + \dots\Bigg], \end{aligned} \tag{3.44}$$

$$\begin{aligned} G^P(E) &= \frac{i}{2N_c}\int d^dx e^{iEx^0}\left\langle 0\left|\, T\left([\psi^\dagger iD^k\chi]^\dagger(x)[\psi^\dagger iD^k\chi](0)\right)\right|0\right\rangle_{\text{PNRQCD}} \\ &= G_0^P(E) + \delta_1 G^P(E) + \dots \\ &= \tilde{\mu}^{4\epsilon}\int\frac{d^{d-1}\mathbf{p}}{(2\pi)^{d-1}}\int\frac{d^{d-1}\mathbf{p}'}{(2\pi)^{d-1}}\,\mathbf{p}\cdot\mathbf{p}'\times\Bigg[G_0(\mathbf{p},\mathbf{p}';E) \end{aligned}$$

$$+\tilde{\mu}^{4\epsilon}\int\frac{d^{d-1}\mathbf{p}_1}{(2\pi)^{d-1}}\int\frac{d^{d-1}\mathbf{p}_2}{(2\pi)^{d-1}}\,G_0(\mathbf{p},\mathbf{p}_1;E)\,i\left(-\frac{\alpha_s^2C_F}{(\mathbf{p}_1-\mathbf{p}_2)^2}\mathcal{V}_C^{(1)}\right)iG_0(\mathbf{p}_2,\mathbf{p}';E)$$
$$+\ldots\Big]. \tag{3.45}$$

We have used the spin independence of the NLO potential (3.39) to evaluate the spin algebra once and for all in the first step. The leading order terms $G_0(E)$ and $G_0^P(E)$ of the non-relativistic correlator for the vector and axial-vector current project out the S-wave and P-wave component of the full Green function (3.33), respectively. The arguments are $r = r' = 0$ because the quark pair is produced and annihilated by a hard process, which is represented by a local operator in the effective theory. Using the four-dimensional representation (3.34), we see that the Green functions are divergent for $r, r' \to 0$. These divergences will be regulated dimensionally. The result for the LO S-wave Green function in dimensional regularization is

$$G_0(E) = \frac{m_t^2\alpha_sC_F}{4\pi}\left[\frac{1}{4\epsilon}+L_\lambda^w+\frac{1}{2}-\frac{1}{2\lambda}-\hat{\psi}(1-\lambda)+\mathcal{O}(\epsilon)\right], \tag{3.46}$$

expressed through $L_\lambda^w = \log(\lambda\mu_w/(m_t\alpha_sC_F))$, and $\hat{\psi}(x) = \gamma_E + \psi(x)$, where ψ is the logarithmic derivative of the gamma function. We distinguish between the renormalization scale μ_r, which appears in (3.46) only implicitly as the argument of the strong coupling constant $\alpha_s \equiv \alpha_s(\mu_r)$, and the scale μ_w, which is introduced together with the spurious divergences (cf. Section 3.2) by the splitting of loop integrals into different momentum regions. We note that the imaginary part of (3.46) is independent of the scale μ_w. The μ_w dependence of the pair production cross section first appears at NNLO and only when the decay width of the heavy quark is taken into account. The consistent treatment of the heavy-quark decays, which we describe in Section 3.4 and 3.5, guarantees the cancellation of the spurious divergences and the related μ_w dependence.

Results for the S-wave Green function up to NNNLO were computed in [60, 74, 88, 89]. We have evaluated the P-wave Green function up to NLO in [1], which will be reviewed in Section 5.2. Some earlier results are available as well [90–93], but none of them were obtained in dimensional regularization and, thus, they cannot be combined consistently with the rest of the computation.

The resummation of the Coulomb exchanges produces bound-state poles in the Green function. The locations and residues of these poles correspond to the bound-state energies and the wave functions at the origin of the vector resonances, respectively. Explicitly, the exact Green function contains single poles of the form

$$G(E) \overset{E\to E_n}{=} \frac{|\psi_n(0)|^2}{E_n-E-i0}+\text{regular} \tag{3.47}$$

$$= \frac{|\psi_n^{(0)}(0)|^2(1+F_n^{(1)}+\ldots)}{(E_n^{(0)}+E_n^{(1)}+\ldots)-E-i0}+\text{regular}, \tag{3.48}$$

where at LO

$$E_n^{(0)} = -\frac{m\alpha_s^2 C_F^2}{4n^2}, \qquad |\psi_n^{(0)}(0)|^2 = \frac{1}{\pi}\left(\frac{m\alpha_s C_F}{2n}\right)^3, \tag{3.49}$$

and $E_N^{(i)}$ and $F_N^{(i)}$ describe perturbative corrections to the energy levels and wave functions, respectively. When computing higher-order corrections, we however obtain the Green function in its perturbatively expanded form

$$G(E) \overset{E\to E_n}{=} \frac{|\psi_n^{(0)}(0)|^2}{E_n^{(0)} - E - i0} + \left[\frac{-|\psi_n^{(0)}(0)|^2 E_n^{(1)}}{(E_n^{(0)} - E - i0)^2} + \frac{|\psi_n^{(0)}(0)|^2 F_n^{(1)}}{E_n^{(0)} - E - i0}\right] + \cdots + \text{regular}. \tag{3.50}$$

Due to the different structure, the perturbative and exact Green functions differ numerically in the vicinity of the resonances. This can be cured by performing a pole resummation, where we subtract (3.50) from the perturbative result for the Green function and add back the exact form of the poles (3.48). To do so, it is necessary to determine the perturbative corrections to the energy levels and wave functions, which can be read off from the expansion of the Green function around the bound-state poles. We do this for all contributions and it is implied that pole resummation is used throughout. For the P-wave contributions, it is done explicitly in Section 5.2.3.

3.4. Top decays and generalization to Unstable Particle Effective Theory

Previously, we have treated the heavy quarks as stable particles. The decay width of the bottom quark is of the order $\Gamma_b \sim m_b^5\alpha/m_W^4$, not counting an additional CKM suppression. With respect to the lowest scale of the threshold production process, the energy $E \sim m_b\alpha_s^2$, it is suppressed by $(m_b/M_W)^4 \sim 10^{-5}$. Thus, it is perfectly justified to neglect the decays of the bottom quarks. The top width is, however, of the order $\Gamma_t \sim m_t\alpha$, which is the ultrasoft scale. Consequently, the decays of the top quarks cannot be factorized in the sense of a narrow-width approximation and modify the cross section near threshold in a non-perturbative way. Thus, the top-quark pair production cross section is ill-defined near threshold. Instead one should consider the inclusive production cross section for its decay products $Xb\bar{b}W^+W^-$ in the same kinematic region.[1] This final state can also be produced without an intermediate non-relativistic top pair, i.e. non-resonantly. Physically, these contributions cannot be distinguished. Thus, they must be summed to get a well-defined result for the $Xb\bar{b}W^+W^-$ cross section near the top-pair production threshold.

This structure is also reflected by divergences, that appear separately in both parts. In the resonant contribution, they come from the UV limit of the loop momenta, where the virtuality of the top quarks becomes large, although being small parametrically. In the non-resonant contribution, the situation is reversed. The virtuality of the top-quarks

[1] We will however continue to also use the phrase top-pair production near threshold with the understanding that it really refers to the production of $Xb\bar{b}W^+W^-$ in the kinematic region $s \approx 4m_t^2$.

is parametrically large and divergences arise from the IR region of loop momenta, where the tops are numerically close to on-shell. These divergences cancel in the sum over both contributions, which renders the cross section well-defined.

The inclusion of electroweak effects requires a generalization of the effective field theory framework described above. The required steps for the construction of Unstable Particle Effective Theory have been described in detail for a toy model in [39, 40]. The setup was then used to compute the cross section for the process $e^-e^+ \to \mu^-\bar{\nu}_\mu u\bar{d}X$ in the resonant W^+W^- region at NLO [94, 95] and N$^{3/2}$LO [96] in the power counting $\alpha \sim v^2 \sim \alpha_s^2$. For top-pair production, NLO [97] and partial NNLO [98–100] results are known. A review of Unstable Particle Effective Theory and its applications can be found in [101]. Below, we describe the setup that is required for the full NNLO electroweak corrections.

Let us begin by studying the momentum regions, that are relevant for the additional particles. In the center-of-mass frame, the incoming electrons and positrons are very energetic, but close to their mass shell. We can use the direction of the electron momentum to define a light-like vector n. With a second light-like vector $\bar{n}$, that satisfies the relation $n \cdot \bar{n} = 2$, one can perform a light-cone decomposition of momenta

$$k^\mu = \frac{1}{2}\,(\bar{n}\cdot k)\,n^\mu + \frac{1}{2}\,(n\cdot k)\,\bar{n}^\mu + k_\perp^\mu, \tag{3.51}$$

where $n \cdot k_\perp = \bar{n} \cdot k_\perp = 0$. A natural choice for $\bar{n}$ would be the direction of the incoming positron. The region collinear to n is defined as

$$n\text{-collinear:} \qquad \bar{n}\cdot k \sim m_t, \qquad n\cdot k \sim m_t\alpha_s^2, \qquad k_\perp \sim m_t\alpha_s. \tag{3.52}$$

This implies that collinear momenta have small virtuality $k^2 \sim m_t^2\alpha_s^2$. The interactions of such modes with massless gauge bosons can be described within Soft-Collinear Effective Theory (SCET) [102–106]. We refrain from giving an introduction to SCET here and refer to the very nice review [107], that has appeared recently.

Hard modes can appear from interactions of collinear modes with different directions. E.g. a hard photon can be produced from the annihilation of the incoming collinear electron and positron. In addition a collinear electron can radiate either a collinear or an ultrasoft photon, while preserving its collinear scaling. The latter region is usually denoted as the soft region in the SCET literature, but we stick with our convention and call it ultrasoft to avoid any ambiguities between soft in the sense of SCET and PNRQCD. Of course, photons can also be soft or potential, when they couple to the non-relativistic modes in the PNRQCD sector of the final state and electrons soft in the vacuum polarization of potential photons.

Electroweak $W^\pm, Z$ and Higgs bosons have masses that are of the same order as the top-quark mass. Thus, they can only be hard.[2] The bottom-quark mass will be neglected here. Bottom quarks are singled out from other massless fermions because they are produced by the decay $t \to bW^+$. Bottom quarks produced by this decay or other electroweak processes

[2]The non-relativistic modes of the top quark are only present because the experimental setup is tuned to the top threshold. Thus, they need not be considered for the electroweak bosons.

are always hard because they have large energy and no direction is distinguished in the inclusive cross section, i.e. they are not described by collinear modes. They can also have momenta in other regions, e.g. when they appear in the context of a sum over all light quarks in the vacuum polarization of the gluon, but this contribution is not specific to the quark flavour and we assume it is already taken into account as part of generic massless modes.

To sum up, we have to take the following additional regions into account:

$$\begin{array}{cl} e^{\pm}, \gamma & \text{hard, collinear, ultrasoft; soft; potential photons,} \\ W^{\pm}, Z, H & \text{hard,} \\ b & \text{hard (when produced in electroweak processes).} \end{array} \tag{3.53}$$

Unstable Particle Effective Theory is constructed in the same manner as PNRQCD, by integrating out all hard, soft and massless potential modes. Consequently, it is formulated in terms of the same dynamical modes as PNRQCD with the addition of collinear electrons and collinear and ultrasoft photons. We note that it is also possible to integrate out collinear modes that differ from the external states by a collinear momentum, and to only keep so-called external-collinear modes for the electron field [39, 40]. While this has clear advantages for the production of a single resonant particle, it is not essential for our treatment of top-pair production and will not be discussed.

Let us consider the imaginary part of the forward scattering amplitude $\mathcal{A}$. Similar to before, hard subgraphs can either connect to both the incoming and outgoing collinear electron and positron, only one side, or none. Now however, the first type yields a non-vanishing contribution because, unlike $t\bar{t}$, cuts like $t\bar{b}W^-$ and $\bar{t}bW^+$, corresponding to the final state $b\bar{b}W^+W^-X$, are kinematically possible in the hard region. Integrating out such a hard subgraph gives production-annihilation operators $\mathcal{O}_{4e}^{(k)}$ with the field content $\mathcal{O}_{4e}^{(k)} \sim (\bar{e}_{c_1}\Gamma_1 e_{c_2})(\bar{e}_{c_2}\Gamma_2 e_{c_1})$, where Γ_i are shorthands for a combination of Dirac matrices, c_1 and c_2 are the directions of the incoming electron and positron and e_{c_i} the respective collinear fields. The respective Wilson coefficients $C_{4e}^{(k)}$ are complex now and the imaginary part corresponds to the non-resonant contribution to the cross section.

Integrating out hard subgraphs, that only connect to the incoming or the outgoing collinear states, gives production or annihilation operators $\mathcal{O}_{p}^{(k)}$ with the field content $\mathcal{O}_{p}^{(k)} \sim (\bar{e}_{c_1}\Gamma_1 e_{c_2})(\psi^\dagger\Gamma_2\chi)$. They replace the external currents in the pure-QCD framework since the collinear electron field is now also part of the effective theory. The respective Wilson coefficients $C_p^{(k)}$ acquire an imaginary part from cuts over full-theory diagrams like those shown in Figure 3.7. Only cuts that correspond to the inclusive $b\bar{b}W^+W^-X$ final state must be taken into account. These contributions describe the interference of the resonant and non-resonant production mechanisms. To the left of the cuts in Figure 3.7, the final state $\bar{t}bW^+$ is produced in a hard tree level process, i.e. non-resonantly. On the right, it is created from a non-relativistic top pair through the decay $t \to bW^+$, i.e. resonantly. These contributions are attributed to the resonant part because they contain the propagation of a non-relativistic top pair.

Last but not least, integrating out the remaining hard subgraphs yields the sum of the SCET and NRQCD Lagrangians, which contain additional terms from the electroweak

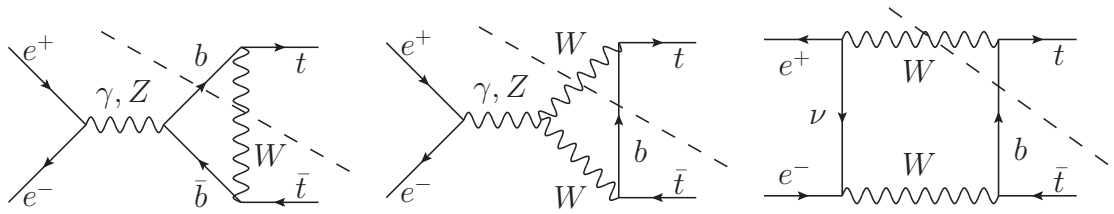

Figure 3.7.: Examples for full theory diagrams that contribute to the imaginary part of the Wilson coefficients $C_p^{(k)}$.

sector. After soft and massless potential modes are also integrated out, one obtains the effective Lagrangian

$$\mathcal{L}_{\text{eff}} = \mathcal{L}_{\text{PNRQCD}} + \delta_{\text{EW}}\mathcal{L}_{\text{PNRQCD}} + \mathcal{L}_{c_1} + \mathcal{L}_{c_2}. \tag{3.54}$$

The PNRQCD Lagrangian was shown in (3.24), supplementary terms due to electroweak effects will be given in (3.67) below and

$$\mathcal{L}_{c_i} = \bar{e}_{c_i}\left(in\cdot D + i\not{D}_{\perp c_i}\frac{1}{i\bar{n}\cdot D_{c_i}+i0}i\not{D}_{\perp c_i}\right)\frac{\not{\bar{n}}}{2}e_{c_i} - \frac{1}{4}F_{c_i\mu\nu}F_{c_i}^{\mu\nu} + \dots \tag{3.55}$$

is the SCET Lagrangian for the c_i-collinear sector, where indices c_i refer to c_i-collinear fields and the covariant derivative with no index includes couplings to the ultrasoft and c_i-collinear photon field.

On the whole, one obtains the master formula [40] for the forward scattering amplitude

$$\begin{aligned} i\mathcal{A} = &\sum_{k,l} C_p^{(k)} C_p^{(l)} \int d^4x \, \langle e^-e^+|\mathrm{T}[i\mathcal{O}_p^{(k)\dagger}(0)\, i\mathcal{O}_p^{(l)}(x)]|e^-e^+\rangle \\ &+ \sum_k C_{4e}^{(k)} \langle e^-e^+|i\mathcal{O}_{4e}^{(k)}(0)|e^-e^+\rangle\,, \end{aligned} \tag{3.56}$$

where the first line corresponds to the resonant contribution and the second line to the non-resonant part. The matrix elements must be evaluated with the effective Lagrangian (3.54), describing the interactions of the collinear as well as the non-relativistic sector. However, in the resonant part, no collinear lines may cross from the incoming collinear sector to the outgoing collinear sector, as this is kinematically forbidden.

We briefly recapitulate the expressions for the LO cross section in this new notation. We have

$$\sigma^{\text{LO}} = \sigma_{\text{res}}^{\text{LO}} = \sigma_0 \frac{24\pi N_c}{s}\left[C^{(v)^2} + C^{(a)^2}\right] \mathrm{Im}\left[G_0(E)\right], \tag{3.57}$$

where $\sigma_0 = 4\pi\alpha^2/(3s)$ is the high-energy limit of the muon pair production cross section

at leading order and $E = \sqrt{s} - 2m_t$.

$$C^{(v)} = e_e e_t + v_e v_t \frac{s}{s - m_Z^2}, \tag{3.58}$$

$$C^{(a)} = -a_e v_t \frac{s}{s - m_Z^2}, \tag{3.59}$$

$$C^{(v)}_{\text{P-wave}} = -v_e a_t \frac{s}{s - m_Z^2}, \tag{3.60}$$

$$C^{(a)}_{\text{P-wave}} = a_e a_t \frac{s}{s - m_Z^2} \tag{3.61}$$

are the leading order Wilson coefficients of the production operators

$$\mathcal{O}^{(v)} = \frac{4\pi\alpha}{s} \bar{e}_{c_2} W_{c_2} \gamma_k W^\dagger_{c_1} e_{c_1} \psi^\dagger \sigma^k \chi, \tag{3.62}$$

$$\mathcal{O}^{(a)} = \frac{4\pi\alpha}{s} \bar{e}_{c_2} W_{c_2} \gamma_k \gamma^5 W^\dagger_{c_1} e_{c_1} \psi^\dagger \sigma^k \chi, \tag{3.63}$$

$$\mathcal{O}^{(v)}_{\text{P-wave}} = \frac{4\pi\alpha}{s} \bar{e}_{c_2} W_{c_2} \gamma_k W^\dagger_{c_1} e_{c_1} \psi^\dagger \frac{\left[\sigma^k, (-i)\boldsymbol{\sigma}\cdot\mathbf{D}\right]}{2m_t} \chi, \tag{3.64}$$

$$\mathcal{O}^{(a)}_{\text{P-wave}} = \frac{4\pi\alpha}{s} \bar{e}_{c_2} W_{c_2} \gamma_k \gamma^5 W^\dagger_{c_1} e_{c_1} \psi^\dagger \frac{\left[\sigma^k, (-i)\boldsymbol{\sigma}\cdot\mathbf{D}\right]}{2m_t} \chi, \tag{3.65}$$

where $\psi(\chi)$ is the non-relativistic top (anti-top) field and e_c denotes a collinear electron field in the light-like direction c. The directions c_1 and c_2 are set by the electron and positron beams, respectively. The collinear Wilson lines

$$W_{c_i}(x) = \mathrm{P}\ \exp\left[ig \int_{-\infty}^{0} dt \bar{c}_i \cdot A_c(x + \bar{c}_i t)\right] \tag{3.66}$$

have been introduced to make the operators invariant under covariant gauge transformations. The factor of $4\pi\alpha/s$ is absorbed into the operators to render the coefficients dimensionless and of order one. The P-wave production operators and Wilson coefficients will be required below. The non-relativistic Green function at LO is the same as before, see (3.46).

The additional electroweak terms in the PNRQCD Lagrangian up to NNLO are

$$\begin{aligned}\delta_{\text{EW}}\mathcal{L}_{\text{PNRQCD}} = {} & \psi^\dagger \left[e_t e A_0^{(\gamma)}(t, \mathbf{0}) - \frac{\Delta}{2} - \frac{\Delta \boldsymbol{\partial}^2}{4m_t^2} + \frac{\Delta^2}{8m_t} + \dots \right] \psi \\ & + \chi^\dagger \left[e_t e A_0^{(\gamma)}(t, \mathbf{0}) + \frac{\Delta}{2} + \frac{\Delta \boldsymbol{\partial}^2}{4m_t^2} - \frac{\Delta^2}{8m_t} + \dots \right] \chi \\ & + \int d^{d-1}\mathbf{r} \left[\psi^\dagger \psi\right](x + \mathbf{r}) \delta V_{\text{QED}}(\mathbf{r}) \left[\chi^\dagger \chi\right](x).\end{aligned} \tag{3.67}$$

The leading coupling to the ultrasoft photon field $A_0^{(\gamma)}$ does not contribute and can be removed in the same way as the respective gluon coupling. The QED Coulomb potential

$$\delta V_{\mathrm{QED}}(r) = -\frac{e_t^2 \alpha}{r} \tag{3.68}$$

is a NLO effect and other electroweak potentials only appear at NNNLO. Δ is a short-distance coefficient, that can be determined by matching the renormalized full theory propagator to the effective theory as described in the following.

First we review the pole mass and width definitions for unstable fermions following loosely [108]. The renormalization constants are defined through

$$m_{t,0} = m_t + \delta m_t, \tag{3.69}$$

$$t_{L/R,0} = Z_{L/R}^{1/2} t_{L/R} = (1 + \delta Z_{L/R}/2 + \dots) t_{L/R}, \tag{3.70}$$

where the index 0 denotes the bare mass and bare fields. We parametrize the renormalized top self energy[3] as

$$\Sigma(\not{p}_t) = \not{p}_t \left(\Sigma_L(p_t^2) P_L + \Sigma_R(p_t^2) P_R\right) + m_t \Sigma_S(p_t^2), \tag{3.71}$$

with the left and right-handed projectors $P_{L/R} = (1 \mp \gamma^5)/2$. The coefficients have the form

$$\Sigma_{L/R}(p_t^2) = \Sigma_{L/R}^{\mathrm{bare}}(p_t^2) + \delta Z_{L/R}, \tag{3.72}$$

$$\Sigma_S(p_t^2) = \Sigma_S^{\mathrm{bare}}(p_t^2) - \frac{\delta Z_L + \delta Z_R}{2} - \frac{\delta m_t}{m_t}. \tag{3.73}$$

To make the pole position in the renormalized propagator apparent, we complete the square

$$\frac{i}{\not{p}_t - m_t + \Sigma(\not{p}_t)} = \frac{i\left[\not{p}_t + m_t + \not{p}_t(\Sigma_L(p_t^2) P_L + \Sigma_R(p_t^2) P_R) - m_t \Sigma_S(p_t^2)\right]}{p_t^2[1 + \Sigma_L(p_t^2)][1 + \Sigma_R(p_t^2)] - m_t^2[1 - \Sigma_S(p_t^2)]^2}. \tag{3.74}$$

We obtain an implicit equation for the pole position $M_\star^2$ of the denominator

$$M_\star^2 = m_t^2 \frac{\left[1 - \Sigma_S(M_\star^2)\right]^2}{\left[1 + \Sigma_L(M_\star^2)\right]\left[1 + \Sigma_R(M_\star^2)\right]}. \tag{3.75}$$

Each of the coefficients in the self-energy can be expanded in the coupling order and around the mass shell

$$\Sigma_X(p_t^2) = \sum_{m,n} \Sigma_X^{(m,n)} \left(p_t^2 - m_t^2\right)^n, \tag{3.76}$$

[3] A pseudo-scalar contribution to the self-energy would violate CP [109] and is thus put to zero.

with $\Sigma_X^{(m,n)}$ of order α^m, i.e. m can also take half-integer values from QCD corrections. Since we focus on electroweak corrections here, we assume that the Σ_X are of order α. Then, we can solve (3.75) perturbatively

$$\begin{aligned} M_\star^2 = m_t^2 - m_t^2 \left[\Sigma_L^{[1]} + \Sigma_R^{[1]} + 2\Sigma_S^{[1]}\right] + m_t^2 \Big[&- \Sigma_L^{(2,0)} - \Sigma_R^{(2,0)} - 2\Sigma_S^{(2,0)} \\ &+ \Sigma_L^{(1,0)^2} + \Sigma_L^{(1,0)}\Sigma_R^{(1,0)} + \Sigma_R^{(1,0)^2} + \Sigma_S^{(1,0)^2} + 2(\Sigma_L^{(1,0)} + \Sigma_R^{(1,0)})\Sigma_S^{(1,0)} \\ &+ m_t^2 \left(\Sigma_L^{(1,0)} + \Sigma_R^{(1,0)} + 2\Sigma_S^{(1,0)}\right)\left(\Sigma_L^{(1,1)} + \Sigma_R^{(1,1)} + 2\Sigma_S^{(1,1)}\right)\Big] + \dots, \end{aligned} \tag{3.77}$$

with $\Sigma_X^{[1]} = \Sigma_X^{(1,0)} + \Sigma_X^{(3/2,0)}$. The complex pole is parametrized through the pole mass m_t and the pole width Γ_t via

$$M_\star^2 = m_t^2 - i m_t \Gamma_t. \tag{3.78}$$

We deduce that the on-shell renormalization conditions require the real part of the square brackets on the right-hand side of (3.77) to vanish. The pole width in perturbation theory is determined by the respective imaginary part. To perform the expansion of the full-theory renormalized top propagator in the non-relativistic region, we still need to determine the field renormalization constants. We require the residue of the renormalized propagator to be unity

$$\lim_{p_t^2 \to M_\star^2} \frac{i}{\not{p}_t - m_t + \Sigma(\not{p}_t)} = \frac{i}{\not{p}_t - M_\star}. \tag{3.79}$$

Keeping only the leading order terms in the expansion, this gives the conditions

$$\Sigma_L^{(1,0)} = \Sigma_R^{(1,0)}, \tag{3.80}$$

$$\frac{i\Gamma_t}{m_t} = \Sigma_L^{(1,0)} + \Sigma_R^{(1,0)} + 2\Sigma_S^{(1,0)}, \tag{3.81}$$

$$0 = \Sigma_L^{(1,0)} + \Sigma_R^{(1,0)} + 2m^2 \left(\Sigma_L^{(1,1)} + \Sigma_R^{(1,1)} + 2\Sigma_S^{(1,1)}\right). \tag{3.82}$$

With the restriction that δm is real, this fixes the top width and renormalization constants at order α as follows

$$\Gamma_t = m_t \,\mathrm{Im}\left[\Sigma_L^{\mathrm{bare},(1,0)} + \Sigma_R^{\mathrm{bare},(1,0)} + 2\Sigma_S^{\mathrm{bare},(1,0)}\right] + \dots, \tag{3.83}$$

$$\delta m_t = m_t \,\mathrm{Re}\left[\Sigma_L^{\mathrm{bare},(1,0)} + \Sigma_R^{\mathrm{bare},(1,0)} + 2\Sigma_S^{\mathrm{bare},(1,0)}\right] + \dots, \tag{3.84}$$

$$\delta Z_L = -\Sigma_L^{\mathrm{bare},(1,0)} - m_t^2 \left[\Sigma_L^{\mathrm{bare},(1,1)} + \Sigma_R^{\mathrm{bare},(1,1)} + 2\Sigma_S^{\mathrm{bare},(1,1)}\right] + \dots, \tag{3.85}$$

$$\delta Z_R = -\Sigma_R^{\mathrm{bare},(1,0)} - m_t^2 \left[\Sigma_L^{\mathrm{bare},(1,1)} + \Sigma_R^{\mathrm{bare},(1,1)} + 2\Sigma_S^{\mathrm{bare},(1,1)}\right] + \dots. \tag{3.86}$$

The expansion of the renormalized full theory propagator (3.74) with momentum $p_t =$

$(m_t, \mathbf{0}) + p$ in the potential region is

$$\begin{aligned}\frac{i}{\not{p}_t - m_t + \Sigma(\not{p}_t)} = &\left[\frac{i(1+\gamma^0)}{2\left(p^0 - \frac{\mathbf{p}^2}{2m_t} + \frac{i\Gamma_t}{2}\right)}\right]_{v^{-2}} + \left[\frac{-i\boldsymbol{\gamma}\cdot\mathbf{p}}{2m_t\left(p^0 - \frac{\mathbf{p}^2}{2m_t} + \frac{\Gamma_t}{2}\right)}\right]_{v^{-1}} \\ &+ \left[-\frac{i(1+\gamma^0)\left(\frac{\mathbf{p}^2}{2m_t} - \frac{i\Gamma_t}{2}\right)^2}{4m_t\left(p^0 - \frac{\mathbf{p}^2}{2m_t} + \frac{i\Gamma_t}{2}\right)^2} - \frac{i\frac{\mathbf{p}^2}{m_t^2}}{4\left(p^0 - \frac{\mathbf{p}^2}{2m_t} + \frac{i\Gamma_t}{2}\right)}\right. \\ &\left. - \frac{i(1-\gamma^0)}{4m_t} - \frac{i(1+\gamma^0)(\Sigma_L^{(1,0)}P_L + \Sigma_R^{(1,0)}P_R)}{2\left(p^0 - \frac{\mathbf{p}^2}{2m_t} + \frac{i\Gamma_t}{2}\right)}\right]_{v^0} + \ldots, \end{aligned} \tag{3.87}$$

where we have indicated the order in v of the various terms, but not expanded out higher-order terms in the top width to keep the expressions compact. The first two lines in (3.87) are reproduced by the EFT propagator multiplied by a factor

$$\frac{\not{p}_t + M_\star}{2E_{\mathbf{p}}} = \frac{1+\gamma^0}{2} - \frac{\boldsymbol{\gamma}\cdot\mathbf{p}}{2m_t} - \frac{\mathbf{p}^2}{4m_t^2} + \ldots, \tag{3.88}$$

which accounts for the different spin sum and normalization of states in the full and effective theory (cf. [40, 94]). The matching condition in the pole scheme becomes

$$\Delta = -i\Gamma, \tag{3.89}$$

where Γ is the pole width of the top quark. The first term in the third line does not contain a pole in the complex p^0 plane. Thus, it produces only scaleless integrals in the potential region[4] and can be dropped. The remaining term does not have the form of an operator insertion into the EFT propagator, but is a correction to the residue from the renormalized self-energy. It must be taken into account in the matching for the production and decay operators. By expressing the renormalized self energy through (3.72), (3.85) and (3.86) we observe that the correction to the residue is only related to derivatives of the self energies. Therefore, the structure of the expanded top propagator (3.87) exactly mirrors the one of the W propagator discussed in [94].

3.5. Organization of the computation

Because of the presence of divergences in the resonant and non-resonant part, it is mandatory to perform both calculations in the same computational scheme. We discuss in the following, how this can be done consistently including all effects up to NNLO.

In the master formula (3.56), the non-resonant contribution is expressed through the Wilson coefficients $C_{4e}^{(k)}$ of the four-electron operators, multiplying matrix elements which

[4]The p^0 contour can be closed in the upper half-plane such that the pole from the anti-top propagator is not picked up.

are trivial at NNLO. Thus, instead of computing $C_{4e}^{(k)}$ through a matching procedure, we determine the NNLO non-resonant contribution to the cross section directly. As discussed in [97, 98], it is equivalent to the sum of the NLO cross sections for the processes $e^+e^- \to \bar{t}W^+b$ and $e^+e^- \to tW^-\bar{b}$ at the center-of-mass energy $\sqrt{s} = 2m_t$.[5] Since the self-energy of the top quark is parametrically smaller than the off-shellness of the non-resonant top quarks $m_t\Sigma(\not{p}_t) \sim m_t^2\alpha \ll p_t^2 - m_t^2 \sim m_t^2$, they must be treated perturbatively. This renders the cross section singular at the endpoints of the phase space, where $(p_b + p_{W^+})^2 \to m_t^2$ or $(p_{\bar{b}} + p_{W^-})^2 \to m_t^2$. Consistency with the resonant computations demands that these divergences must be regularized dimensionally [97, 98]. They then cancel the finite width divergences present in the resonant part, as it has been demonstrated up to NNLO in [98].

We split the NNLO non-resonant contribution into separate parts, which are each evaluated using different methods or computational schemes. The set of endpoint singular diagrams in unitary gauge has been identified in [98]. We divide it into the $\mathcal{O}(\alpha_s)$ corrections to the diagram h_1 (see Figure 3.8) and the contributions h_{ia} with $i = 2, 3, 4$ (see the first row of Figure 3.9). The former is IR and UV finite and will be referred to as the squared contribution. The latter is also IR finite, but contains UV divergences from the loop integration. A closer look at the diagrams h_{ia} in Figure 3.9 reveals that they can be split into a UV finite, but endpoint divergent part and an endpoint finite, but UV divergent part.[6] Below, we will introduce artificial counterterms to subtract the UV divergences. The whole set of contributions in Figure 3.9 will be denoted as the interference contribution and is split into three parts

$$\sigma_{\text{interference}} = \sigma_{\text{interference}}^{(\text{EP})} + \sigma_{\text{interference}}^{(\text{UV})} + \sigma_{\text{interference}}^{(\text{c.t.})}. \tag{3.90}$$

This allows us to separate the non-resonant NNLO corrections into a completely finite part and an endpoint divergent, but UV and IR finite, part

$$\sigma_{\text{non-res}}^{\text{NNLO}} = \left(\sigma_{\text{non-res}}^{\text{NNLO}} - \sigma_{\text{squared}} - \sigma_{\text{interference}}^{(\text{EP})}\right)_{\text{finite}} + \left(\sigma_{\text{squared}} + \sigma_{\text{interference}}^{(\text{EP})}\right)_{\text{EP divergent}}. \tag{3.91}$$

The endpoint divergences in $\sigma_{\text{interference}}^{(\text{EP})}$ cancel with the part of the resonant contribution associated with the bare absorptive contribution to the matching coefficients $C^{(k)}$, discussed in Section 5.1.4. The endpoint divergences in σ_{squared} cancel with the remaining resonant contributions. Accordingly, we divide the resonant part in two contributions

$$\sigma_{\text{res}}^{\text{NNLO}} = \left(\sigma_{\text{res}}^{\text{NNLO}} - \sigma_{C_{\text{Abs,bare}}^{(k)}}\right) + \sigma_{C_{\text{Abs,bare}}^{(k)}}. \tag{3.92}$$

This allows us to decompose the full NNLO correction to the inclusive $b\bar{b}W^+W^-$ cross

[5] We do not consider the small contributions from the processes $e^+e^- \to W^+W^-H$ and $e^+e^- \to W^+W^-Z$ with $H \to b\bar{b}$ or $Z \to b\bar{b}$ because they can easily be removed on the experimental side by imposing invariant mass cuts on $b\bar{b}$.

[6] E.g. by performing a tensor decomposition of the loop integral. Only the scalar integral C_0 yields an endpoint divergence and only the tensor C_{00} yields a UV divergence. The other tensor structures, C_i and C_{ij} with $i, j = 1, 2$, give finite contributions and can be assigned arbitrarily to either part.

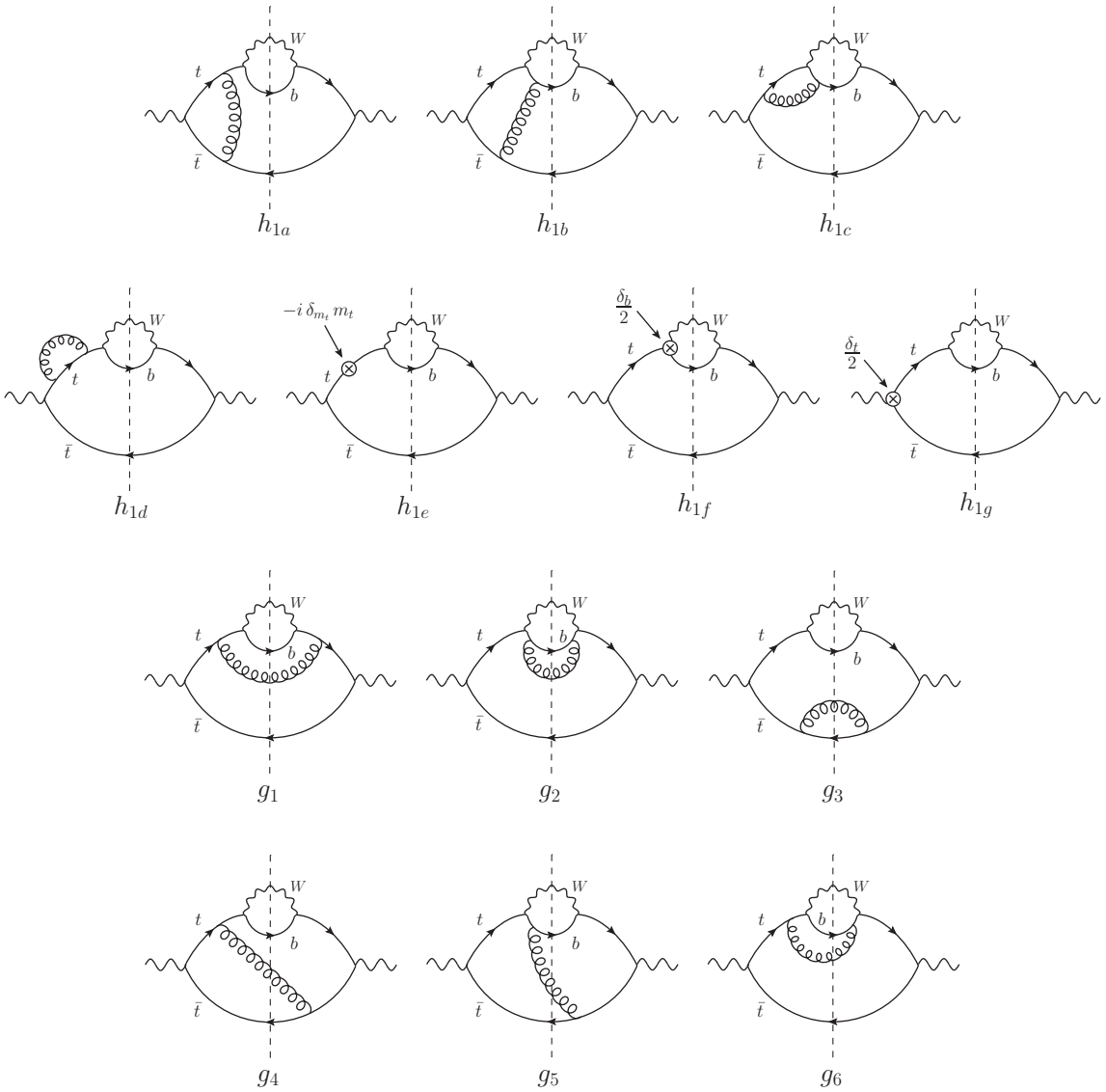

Figure 3.8.: Gluon corrections to the tree-level diagram h_1. This set of endpoint divergent diagrams is UV and IR finite and will be denoted as the squared contribution. Symmetric diagrams and diagrams with $tW^-\bar{b}(g)$ cuts are not displayed.

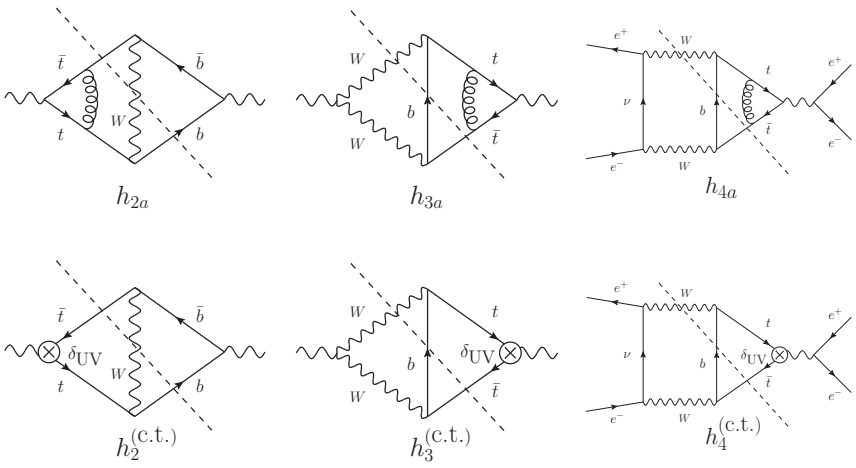

Figure 3.9.: Additional endpoint singular diagrams that contribute to the NNLO non-resonant part. We have introduced artificial UV counterterms (lower panel) to render the set of diagrams UV finite. It is denoted as the interference contribution. Symmetric diagrams and diagrams with $tW^-\bar{b}$ cuts are not displayed.

section (3.56) into three separately finite parts

$$\sigma^{\mathrm{NNLO}} = \left(\sigma_{\mathrm{squared}} + \sigma_{\mathrm{res}}^{\mathrm{NNLO}} - \sigma_{C^{(k)}_{\mathrm{Abs,bare}}}\right)_{\mathrm{finite}} \tag{3.93}$$

$$+ \left(\sigma^{(\mathrm{EP})}_{\mathrm{interference}} + \sigma_{C^{(k)}_{\mathrm{Abs,bare}}}\right)_{\mathrm{finite}} \tag{3.94}$$

$$+ \left(\sigma^{\mathrm{NNLO}}_{\mathrm{non\text{-}res}} - \sigma_{\mathrm{squared}} - \sigma^{(\mathrm{EP})}_{\mathrm{interference}}\right)_{\mathrm{finite}}, \tag{3.95}$$

We now have the freedom to choose a different computational scheme for each of the parenthesis (3.93), (3.94) and (3.95), as long as it is applied to all the parts, that are contained within.

The scheme for (3.93) is fixed by the existing QCD results for $\sigma_{\mathrm{res}}^{\mathrm{NNLO}}$. The resonant QCD cross section factorizes into a leptonic tensor L and a hadronic spectral function $\Pi(q^2)$. The former is evaluated in 4 dimensions and the latter completely in d dimensions and using the naive dimensional regularization scheme (NDR). The squared contribution also factorizes into the same leptonic tensor L and a hadronic tensor H and the same conventions must be applied. We compute this part in Section 4.2.1. The electroweak NNLO corrections to the resonant part must also abide by this description (apart from $\sigma_{C^{(k)}_{\mathrm{Abs,bare}}}$) and are discussed in Section 5.1.

It would be a natural choice to use the same scheme for the contribution (3.94). We can however simplify the computation of this part by performing the Dirac algebra and one of the loop integrations in 4 dimensions. The details of this scheme and the computation of $\sigma^{(\mathrm{EP})}_{\mathrm{interference}}$ and $\sigma_{C^{(k)}_{\mathrm{Abs,bare}}}$ are shown in Section 4.2.2 and 5.1.4, respectively.

The part (3.95) contains a large number of non-resonant diagrams, that are endpoint

finite. Thus, it is possible and beneficial to use automated programs for the most part of (3.95). For technical reasons, this requires a subdivision

$$(3.95) = \left(\sigma^{\text{NNLO}}_{\text{non-res}} - \sigma_{\text{squared}} - \sigma_{\text{interference}}\right)_{\text{finite, but scheme dependent}} \tag{3.96}$$

$$+ \left(\sigma^{(\text{UV})}_{\text{interference}} + \sigma^{(\text{c.t.})}_{\text{interference}}\right)_{\text{finite, but scheme dependent}} . \tag{3.97}$$

Both parts are finite, but must obviously use the same definition for the artificial counterterms introduced in Figure 3.9. In Section 4.1, we define the scheme and evaluate the automated part (3.96) using MadGraph [12] code with some minor modifications. The remainder (3.97) is computed in the same scheme in Section 4.2.2.

4. Non-resonant contribution to top-pair production near threshold at NNLO

Our main focus is the non-resonant NNLO correction to the full cross section $\sigma(e^+e^- \to b\bar{b}W^+W^-X)$, but we also present results in the presence of loose cuts on the invariant mass of the top and anti-top quark

$$(m_t - \Delta M_t)^2 \leq p_{t,\bar{t}}^2 \leq (m_t + \Delta M_t)^2. \tag{4.1}$$

The cut is considered to be loose when $\Delta M_t \gg \Gamma_t$. Thus, a loose cut never affects the resonant contribution to the cross section, where the off-shellness of the tops is parametrically of order Γ_t.[1] To describe the implementation of the cut, we consider an event that contributes to the full cross section, i.e. it contains reconstructed b and $\bar{b}$ jets and a reconstructed W^+ and W^-, as well as radiation with momenta $r_i, \ldots, r_N$. The event passes the cut, if, for at least one of the subsets s_I of $S = \{1, \ldots, N\}$, the conditions

$$\begin{aligned}
(m_t - \Delta M_t)^2 &\leq \left(p_b + p_{W^+} + \sum_{i \in s_I} r_i\right)^2 \leq (m_t + \Delta M_t)^2 \\
(m_t - \Delta M_t)^2 &\leq \left(p_{\bar{b}} + p_{W^-} + \sum_{i \in S \setminus s_I} r_i\right)^2 \leq (m_t + \Delta M_t)^2
\end{aligned} \tag{4.2}$$

are simultaneously fulfilled. If we apply this to the $e^+e^- \to \bar{t}W^+b$ or $e^+e^- \to \bar{t}W^+bg$ cross sections at threshold, the cut can be expressed as a single Heaviside function $\theta((p_b+p_{W^+})^2 - ym_t^2)$ or $\theta((p_b + p_{W^+} + p_g)^2 - ym_t^2)$, respectively. We have defined $y \equiv (m_t - \Delta M_t)^2/m_t^2$. The simplicity of the cut for the $\bar{t}W^+bg$ final state is due to the special kinematics near threshold, where (4.2) being fulfilled for $s_I = \{\}$ implies that (4.2) is also fulfilled for $s_I = \{1\}$. Thus, the gluon is always effectively combined with the bottom quark and W^+ boson, irrespective of whether it is considered as part of the bottom jet or not. This implies that the NNLO cross section with the cut (4.1) does not depend on the jet algorithm.

We don't support other cuts, but it is straightforward to implement them as long as they are loose. A general cut is a function $c(p_i)$ of the external momenta that evaluates to

[1] This argument also applies to the interference of the resonant and non-resonant production mechanisms, which is considered to be part of the resonant contribution. The loose cut is automatically fulfilled for kinematic configurations where the non-resonant amplitude has a non-vanishing overlap with the resonant one.

one if the event passes the cut and to zero otherwise. We define the complementary cut as $\bar{c}(p_i) = 1 - c(p_i)$. Assuming that $c(p_i)$ is loose, the non-resonant cross section $\sigma^{\bar{c}}_{\text{non-res}}$ in the presence of $\bar{c}(p_i)$ is finite and can be computed with automated NLO parton level event generators like MadGraph [12]. The non-resonant contribution with the original cut is given by subtracting $\sigma^{\bar{c}}_{\text{non-res}}$ from the total non-resonant cross section, where the cancellation of divergences between the resonant and non-resonant parts is already taken care of. This approach will also be exploited in Section 4.3 to perform a powerful check on our computation.

A generalization to tight cuts would affect the resonant contributions and is beyond the scope of this work. Recently however, first results of an implementation of the fully differential cross section with NLL accuracy near threshold matched to the NLO fixed order result have been presented [110].

4.1. The automated part

We first recall some aspects of MadGraph that are relevant to our definition of the computational scheme applied for (3.95).

1. IR singularities are subtracted before the phase-space integration using the FKS method [111, 112]. The phase-space integration is then always done in 4 dimensions.

2. In the virtual corrections, MadGraph uses rational R_2 terms [113] to absorb the (-2ϵ)-dimensional parts of the numerators. For a given diagram with the amplitude $\mathcal{C}$ the decomposition takes the form

$$\mathcal{C} \equiv \int d^d\bar{l} \frac{\bar{N}(\bar{l})}{\prod_i \bar{D}_i} = \int d^d\bar{l} \frac{N(l)}{\prod_i \bar{D}_i} + R_2, \tag{4.3}$$

   where $D_i = (\bar{l}+p_i)^2 - m_i^2$, quantities with a bar are $(4-2\epsilon)$-dimensional and quantities without a bar are 4-dimensional. The non-R_2 term can be written as a sum over 4-dimensional coefficients multiplying d-dimensional tensor integrals. The (-2ϵ)-dimensional parts related to the implementation of the 't Hooft-Veltman scheme [114] in MadGraph are all contained in the R_2 terms.

3. The amplitudes for the non-R_2 terms, the R_2 terms, the UV counterterms and the FKS subtraction terms are written as separate lists, each of them containing the coefficient of the $1/\epsilon^2$ pole, the $1/\epsilon$ pole and the finite part. Afterwards, only 4-dimensional operations are performed, i.e. the multiplication with the conjugated 4-dimensional born amplitude and the 4-dimensional phase-space integration. MadGraph will terminate, if the $1/\epsilon^2$ or $1/\epsilon$ pole of the renormalized and FKS subtracted squared amplitude does not vanish. This is why we have to introduce the counterterm diagrams in Figure 3.9 to cancel the UV divergences in $\sigma^{(\text{UV})}_{\text{interference}}$ and render the automated part finite.

Given the way that (3.96) is defined, we never have to modify the construction of an amplitude $\mathcal{A}_i$ and only have to remove certain contributions $\mathcal{A}_i\mathcal{A}_j^*$ in the squared amplitude $|\mathcal{A}|^2 = \sum_{i,j} \mathcal{A}_i\mathcal{A}_j^*$. All the contributions associated with the diagrams in Figure 3.8 have to be removed, i.e. also the R_2 parts, the UV counterterms and the FKS subtraction terms. There is however an ambiguity in the subtraction of the contributions in Figure 3.9, which determines the scheme in which (3.97) must be computed. We choose to only subtract the non-R_2 terms of h_{ia} with $i = 2, 3, 4$ and define the artificial counterterm contributions $\sigma^{(\text{c.t.})}_{\text{interference}}$ as a minimal subtraction of the UV divergences. Following the discussion of the items 1 and 2 above, this implies that (3.97) has to be computed by using dimensional regularization for the tensor integrals. All other steps in the computation of (3.97) are then performed in 4 dimensions and the UV divergence also has to be subtracted minimally.

In the following, we describe the steps we performed in MadGraph to obtain the contribution (3.96) in the scheme defined above. It is obvious that this can't be achieved by modifying the process generation because (3.96) does not correspond to a squared amplitude. Thus, we first generate the full process $e^+e^- \to \bar{t}W^+b$ including QCD corrections. By not invoking the complex mass scheme, we make sure that the self-energy insertions are treated perturbatively. Hence, the cross section diverges rapidly for center-of-mass energies approaching $\sqrt{s} = 2m_t$ from below. We remove the contribution from the endpoint divergent born diagram h_1, the diagrams shown in Figures 3.8 and the non-R_2 terms from Figure 3.9 by editing the code generated by MadGraph. The counterterm contribution in Figure 3.9 can be added by modifying the $1/\epsilon$ component of the existing field renormalization contributions, but leaving the respective finite part unchanged. The discussion under item 3 above implies that this indeed constitutes a minimal subtraction since the finite part is unaffected.

Finally, we have to deactivate some checks inside the code that are invalidated by the modifications. After the subtractions, the tree-level cross section and the real corrections are no longer the squared absolute value of an amplitude and, thus, no longer positive for all phase-space points. The positivity of these expressions is not necessary to make the code run properly, but only serves as an internal check [115]. Therefore, we can safely switch it off. The code can now be evaluated directly at the threshold $\sqrt{s} = 2m_t$. The desired contribution (3.96) is given by the difference of fixed order runs at NLO and LO, multiplied by a factor two to account for the $t\bar{b}W^-$ contribution, which gives the same result due to CP invariance.

4.2. The manual part

All the endpoint divergences are contained in this part of the computation. To understand the challenges associated with this contribution, we consider the phase-space integral of a virtual diagram h_{ix}, where the integrand f_{ix} is a Lorentz scalar, i.e. it only depends on scalar products of its arguments.

$$\int d\text{LIPS}_{e^+e^-\to\bar{t}W^+b} f_{ix}(p_{e^+}, p_{e^-}, p_{\bar{t}}, p_{W^+}, p_b)\theta\left((p_{W^+} + p_b)^2 - ym_t^2\right)$$

$$= \frac{m_t^2}{2\pi} \int\limits_y^1 dt \int d\text{LIPS}_{e^+e^-\to t\bar{t}} \int d\text{LIPS}_{t\to W^+b} f_{ix}(p_{e^+}, p_{e^-}, p_{\bar{t}}, p_{W^+}, p_b)$$

$$\equiv \int\limits_y^1 dt g_{ix}(t), \tag{4.4}$$

where $t \equiv (p_{W^+} + p_b)^2/m_t^2$. The Heaviside function accounts for the cut on the invariant mass of the top quark discussed in Section 4. The real corrections can be brought into the same form as (4.4) with the variable $t^* \equiv (p_{W^+} + p_b + p_g)^2/m_t^2$ instead of t. In [98], the leading terms in an expansion around $t \sim 1$ of the integrands $g_{ix}(t)$ have been obtained using the expansion by regions approach [57, 59]. The remaining t-integration for the expanded result is trivial

$$\int\limits_y^1 dt(1-t)^{-a-b\epsilon} = \frac{(1-y)^{1-a-b\epsilon}}{1-a-b\epsilon}. \tag{4.5}$$

The divergent integrals with $a \geq 1$ are regulated dimensionally by the $b\epsilon$ in the exponent. Negative powers of $(1-t)$ occur from top-quark propagators. At NNLO, endpoint divergent integrals with $a = 1, 3/2, 2$ contribute, but only those with $a = 1$ manifest as $1/\epsilon$ poles. This is related to the well-known artifact of dimensional regularization that it renders some formally divergent integrals finite for $\epsilon \to 0$.

It is obvious from (4.5) that the integrands $g_{ix}(t)$ must not be expanded in ϵ because it would spoil the dimensional regularization of the endpoint divergences. This implies that the loop integrals in Figures 3.8 and 3.9 can't be expanded in ϵ. Expressions for scalar one-loop integrals in general d dimensions with up to four external legs were obtained recently [116], but we have used a different strategy instead. We take the results for the endpoint divergent terms from [98] as subtractions to the complete integrand. The integrals (4.4) are decomposed as follows:

$$\int\limits_y^1 dt g_{ix}(t) = \int\limits_y^1 dt \left[g_{ix}(t) - \sum_{a=1,\frac{3}{2},2} \sum_b \frac{\hat{g}_{ix}^{(a,b)}}{(1-t)^{a+b\epsilon}} \right] + \sum_{a=1,\frac{3}{2},2} \sum_b \frac{\hat{g}_{ix}^{(a,b)}(1-y)^{1-a-b\epsilon}}{1-a-b\epsilon}, \tag{4.6}$$

where the required coefficients $\hat{g}_{ix}^{(a,b)}$ of the series expansion in $(1-t)$ are available from [98] up to order $\mathcal{O}(\epsilon^0)$. This renders the t-integration on the right-hand side finite and allows us to expand the subtracted expression in the square bracket in ϵ. Thus, the integral can be performed numerically. Additionally, we require the $\mathcal{O}(\epsilon)$ contributions to $\hat{g}_{ix}^{(1,b)}$ because the coefficients with $a = 1$ are multiplied with a $1/\epsilon$ pole in (4.6). They must be determined using the same conventions as their counterparts in the resonant part and are therefore treated differently, depending on whether they belong to (3.93) or (3.94).

4.2.1. The squared contribution

The squared contribution is fully contained in (3.93). The contributions from the individual diagrams to the hadronic tensor H are evaluated in d dimensions and are written in the form (4.6). The numerical t (or t^*) integral contains all terms with positive integer or half-integer powers of $(1-y)$. With the exception of h_{1b}, the subtracted integrands were all obtained in analytical form. The integrand for h_{1b} contains an additional numerical angular integral. The expressions for the integrands are rather lengthy and will not be given explicitly. The numerical integrals are plagued by integrable singularities involving $1/\sqrt{1-t}$ and $\log(1-t)$ terms, that cause numerical instabilities in the contributions from some diagrams. As a remedy, we computed additional terms in the expansion in $(1-t)$ analytically and used them as further subtractions.

The contributions corresponding to the second term in (4.6) are given by the sum of the respective expressions from [98] and terms from the $\mathcal{O}(\epsilon)$ contributions to $\hat{g}_{ix}^{(1,b)}$. The latter encapsulate the dependence of the squared contribution on the computational scheme and are therefore specified below. In the notation of [98] and the scheme for (3.93), we obtain

$$
\begin{aligned}
H_{1a} &= H_{1a}|_{\text{from [98]}} + N_\epsilon \Bigg[\left(-\frac{623+239x+1154x^2-192(2+2x+5x^2)\log\frac{1-x}{2}}{144(1-x)(1+2x)} \right) v_t^{\mathrm{L}} v_t^{\mathrm{R}} \\
&\quad - \left(\frac{2+3x}{2+4x} - \frac{1}{2}\log\frac{1-x}{2} \right) v_t^{\mathrm{L}} a_t^{\mathrm{R}} + \left(\frac{11+16x}{18+36x} - \frac{1}{3}\log\frac{1-x}{2} \right) a_t^{\mathrm{L}} a_t^{\mathrm{R}} \Bigg] + \mathcal{O}\left(\frac{\Lambda}{m_t}\right), \\
H_{1b} &= H_{1b}|_{\text{from [98]}} + N_\epsilon \Bigg[\left(\frac{1-2x+15x^2-3\,(1+x+2x^2)\log\frac{1-x}{2}}{2(1-x)(1+2x)} \right) v_t^{\mathrm{L}} v_t^{\mathrm{R}} \\
&\quad + \left(-\frac{17-28x-6(1-2x)\log\frac{1-x}{2}}{18(1+2x)} \right) v_t^{\mathrm{L}} a_t^{\mathrm{R}} \\
&\quad + \left(\frac{5-4x-6(1-2x)\log\frac{1-x}{2}}{18(1+2x)} \right) a_t^{\mathrm{L}} v_t^{\mathrm{R}} \Bigg] + \mathcal{O}\left(\frac{\Lambda}{m_t}\right),
\end{aligned}
\tag{4.7}
$$

with the prefactor

$$
N_\epsilon = \left(\frac{\mu^2}{m_t^2}\right)^{3\epsilon} m_t \Gamma_B N_c C_F \frac{\alpha_s}{4\pi}, \tag{4.8}
$$

and Γ_B is the tree-level top decay width in four dimensions. The other diagrams in Figure 3.8 do not contain $1/\epsilon_{\text{EP}}$ poles and, therefore, no terms of this type are present. The contribution of an individual diagram h_{ix} to the non-resonant part is

$$
\sigma_{ix} = -8\pi^2\alpha^2 n_s \sum_{L,R=\gamma,Z} \frac{v_e^L v_e^R + a_e^L a_e^R}{(s-m_L^2)(s-m_R^2)} \operatorname{Re}\left(H_{ix}\right), \tag{4.9}
$$

where n_s is a symmetry factor, that is either two for diagrams which are symmetric with respect to the cut, or four for diagrams which are not symmetric with respect to the cut.

The photon couplings are $v_f^\gamma = -e_f$ and $a_f^\gamma = 0$, where e_f is the fermion charge measured in units of the positron charge. The couplings of the fermions to Z bosons are given by

$$v_f^Z \equiv v_f = \frac{T_3^f - 2e_f s_w^2}{2 s_w c_w}, \qquad a_f^Z \equiv a_f = \frac{T_3^f}{2 s_w c_w}, \tag{4.10}$$

where T_3^f is the third component of the weak isospin of the fermion f and s_w and c_w are the sine and cosine of the Weinberg angle, respectively. The photon mass obviously vanishes, $m_\gamma = 0$.

In (4.9), $\mathcal{O}(\epsilon)$ terms in the leptonic tensor have been discarded, as discussed in Section 3.5. For our result, we have checked explicitly that IR and UV divergences cancel in the sum over the diagrams in the squared contribution.

4.2.2. The interference contribution

The interference contribution is split into $\sigma^{(\mathrm{EP})}_{\mathrm{interference}}$ and $\sigma^{(\mathrm{UV})}_{\mathrm{interference}} + \sigma^{(\mathrm{c.t.})}_{\mathrm{interference}}$. The latter is endpoint finite and the respective integrands $g_{ix}^{(\mathrm{UV+c.t.})}(t)$ can be expanded in ϵ without the necessity of introducing subtraction terms. It is computed in the scheme of (3.95) and only contributes at the order $\mathcal{O}(\Lambda/m_t)$ in the expansion used in [98]. For h_{4a} and $h_4^{(\mathrm{c.t.})}$, the contribution to the cross section could only be expressed as a two-dimensional numerical t and angular integral. The other parts are obtained as a 1-dimensional numerical integral over t. Again, we refrain from giving explicit expressions for the integrands due to their length. The integrable singularities are treated as described in Section 4.2.1.

The contribution $\sigma^{(\mathrm{EP})}_{\mathrm{interference}}$ is endpoint divergent and therefore treated in the fashion of (4.6). Again, the terms from the $\mathcal{O}(\epsilon)$ contributions to $\hat{g}_{ix}^{(\mathrm{EP}),(1,b)}$ contain the dependence on the computational scheme. In the notation of [98] and the scheme for (3.94), we obtain

$$\begin{aligned}
H_{2a}^{(\mathrm{EP})} &= H_{2a}|_{\text{from [98]}} + N_\epsilon \left(\frac{(1-5x-2x^2)\left(8 - 3\log\frac{\mu^2}{4m_t^2}\right)}{36(1+x)(1+2x)} \right) v_t^{\mathrm{L}}(v_b^{\mathrm{R}} + a_b^{\mathrm{R}}) + \mathcal{O}\left(\frac{\Lambda}{m_t}\right), \\
H_{3a}^{(\mathrm{EP})} &= H_{3a}|_{\text{from [98]}} + N_\epsilon \left(-\frac{(2+5x-2x^2)\left(8 - 3\log\frac{\mu^2}{4m_t^2}\right)}{36x(1+2x)} \right) I_{\mathrm{WW}}^{\mathrm{L}} v_t^{\mathrm{R}} + \mathcal{O}\left(\frac{\Lambda}{m_t}\right), \\
\Delta\sigma_{4a}^{(\mathrm{EP})} &= \Delta\sigma_{4a}|_{\text{from [98]}} + N_\epsilon \frac{\pi^2\alpha^2}{s_w^2}\frac{1}{s}\left(\frac{e_t e_e}{s} + \frac{v_t(v_e+a_e)}{s-M_Z^2}\right)\Bigg[-\left(2 - \log\frac{\mu^2}{4m_t^2}\right) \\
&\quad \times \frac{(1-x)(1-2x-23x^2) + 12x^2\log\left(\frac{2}{x}-1\right)}{3x(1-x)^3(1+2x)} \Bigg] + \mathcal{O}\left(\frac{\Lambda}{m_t}\right).
\end{aligned} \tag{4.11}$$

The contribution of h_{2a} and h_{3a} follows from equation (4.9) with $n_s = 4$ and the contribution of h_{4a} is given by (4.11), multiplied with the symmetry factor $n_s = 4$.

4.3. Consistency checks

Having performed the computation of the non-resonant part in the presence of the invariant mass cut (4.1), denoted by $c_{\Delta M_t}(p_i)$, allows us to perform a very powerful numerical consistency check. The non-resonant cross section $\sigma^{\bar{c}_{\Delta M_t}}_{\text{non-res}}$ in the presence of the complementary cut $\bar{c}_{\Delta M_t}(p_i) = 1 - c_{\Delta M_t}(p_i)$ is finite. Therefore, we can evaluate it using unedited MadGraph code. On the other hand, it can be obtained from our result by taking the difference $\sigma_{\text{non-res}} - \sigma^{c_{\Delta M_t}}_{\text{non-res}}$. The comparison for various values of the cut ΔM_t numerically tests the whole non-resonant result, with the exception of the contributions from the $\mathcal{O}(\epsilon)$ parts of the $\hat{g}^{(1,b)}_{ix}$ terms in (4.6), which originate from the $t^{(*)} \to 1$ region and are independent of the value of the cut, i.e. which are not present in $\sigma^{\bar{c}_{\Delta M_t}}_{\text{non-res}}$. The result is shown in Figure 4.1. We have performed the same check for the individual contributions of the diagrams h_{ia} with $i = 2, 3, 4$. In particular, this provides very welcome reassurance that the scheme dependence in (3.96) and (3.97) has been treated consistently. Additionally, it provides a strong test on the correctness of the actual computation, which is extremely important since a significant part of it has not been checked independently yet.

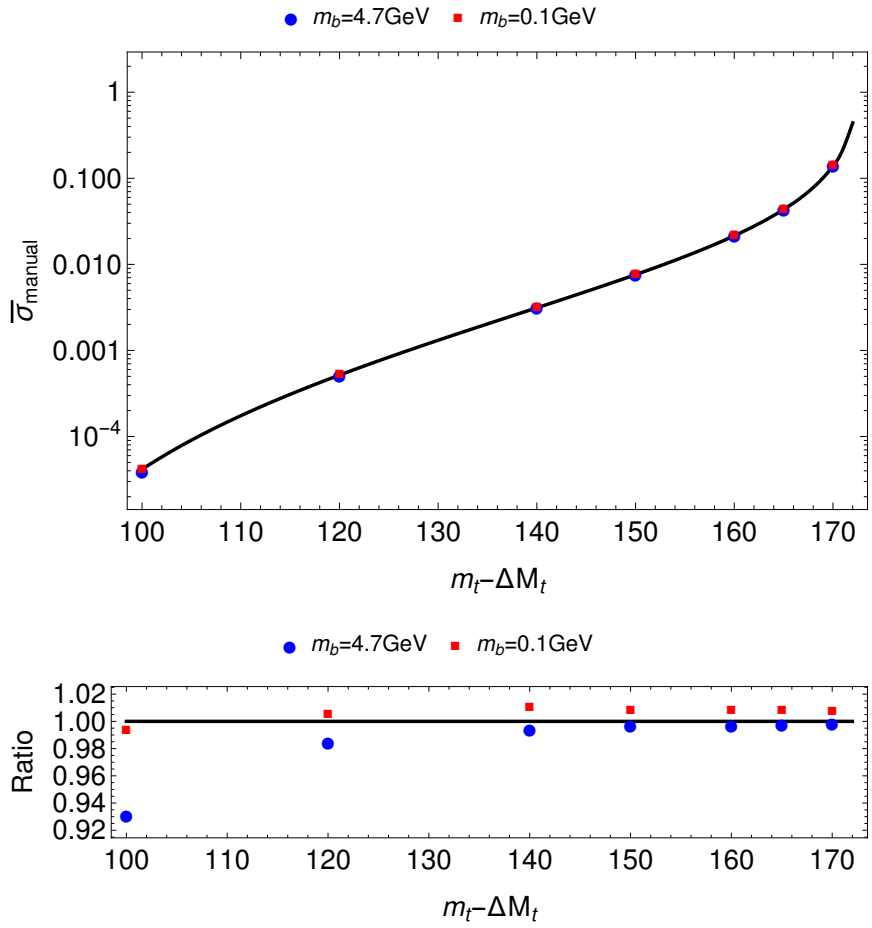

Figure 4.1.: Consistency check for various values for the complementary cut $p_t^2 \leq (m_t - \Delta M_t)^2$. The line in the upper panel is our result for the manual part $\sigma_{\text{manual}}^{\bar{c}_{\Delta M_t}}$ in pb, given by the sum of the contributions from the tree-level diagram h_1, the squared and the interference contributions. The points give the same quantity obtained from the difference of MadGraph runs with the unedited and edited code. The lower panel shows the same results normalized to ours. The MadGraph results have been obtained for the default value of the bottom-quark mass $m_b = 4.7\,\text{GeV}$ and a negligible value $m_b = 0.1\,\text{GeV}$. All points with the latter value agree with our result (obtained by neglecting the bottom-quark mass) within less than 1%, which is the estimated numerical uncertainty of our result. For the sake of this check, we have furthermore used the default values of MadGraph, $m_t = 173\,\text{GeV}$, $\mu = m_Z$, $\alpha_s(m_Z) = 0.118$ and $\alpha = 1/132.507$.

5. Resonant non-QCD contributions to top-pair production near threshold

5.1. Resonant contributions of electroweak origin

In this section, we discuss electroweak corrections to the resonant contribution up to NNLO. The contribution $\sigma_{C^{(k)}_{\text{Abs,bare}}}$ has been separated in (3.92). The remainder contains the following parts

$$\sigma_{\text{res}}^{\text{NNLO}} - \sigma_{C^{(k)}_{\text{Abs,bare}}} = \sigma_{\text{QCD}} + \sigma_{\text{P-wave}} + \sigma_H + \sigma_{\delta V_{\text{QED}}} + \sigma_\Gamma + \sigma_{C^{(k)}_{\text{EW}}} + \sigma_{C^{(k)}_{\text{Abs},Z_t}} + \sigma_{\text{IS}}^{\text{conv}}. \quad (5.1)$$

In the scheme of (3.93), the pure QCD S-wave contribution σ_{QCD} has been determined in [37,60,89] and top-pair production in a P-wave state $\sigma_{\text{P-wave}}$ is considered up to NNNLO in Section 5.2. Higgs contributions σ_H that only involve the top Yukawa coupling are taken into account up to NNNLO in Section 5.3. The effects $\sigma_{\delta V_{\text{QED}}}$ of the LO QED Coulomb potential $\delta V_{\text{QED}} = -4\pi\alpha e_t^2/\mathbf{q}^2$ have also been considered up to NNNLO [4]. At NNLO, top decays introduce additional contributions to the bilinear part of the PNRQCD Lagrangian, that yield an additional contribution σ_Γ to the non-relativistic Green function (see Section 5.1.1). Furthermore, there are electroweak corrections to the hard matching coefficients $C^{(k)}$, which yield a contribution $\sigma_{C^{(k)}_{\text{EW}}}$, see Section 5.1.3. They contain an imaginary part from cuts over all possible final states. However, only the part corresponding to the $\bar{t}W^+b$ ($tW^-\bar{b}$) final state contributes to the cross section [117]. It is split into a bare contribution $\sigma_{C^{(k)}_{\text{Abs,bare}}}$ (see Section 5.1.4) and a contribution from field renormalization $\sigma_{C^{(k)}_{\text{Abs},Z_t}}$ (see Section 5.1.2) because the two parts must be treated in different schemes. Finally, we consider effects from initial state radiation (ISR), $\sigma_{\text{IS}}^{\text{conv}}$, in Section 5.1.5.

From power counting one would also expect corrections to the color Coulomb potential from electroweak gauge bosons at NNLO, which however vanish in the on-shell scheme (see Section 5.1.2). Partial results for the mixed-QCD-electroweak corrections to the hard matching coefficients $C^{(k)}$ are available [118,119], but they only contribute at NNNLO and will not be considered here.

5.1.1. Contributions to the NNLO Green function

We consider the corrections to the NNLO Green function from the electroweak contributions to the PNRQCD Lagrangian given in (3.67). As argued in Section 3.4, there are no ultrasoft photon corrections at this order. The single insertion of the QED Coulomb

potential (3.68) constitutes a NLO effect. At NNLO, there is the double insertion of (3.68), as well as mixed QCD and QED Coulomb corrections. All insertions can be inferred from the computation of the QCD corrections in [89], even up to NNNLO. Thus, we include the effects of the QED Coulomb potential (3.68) up to third order, see [4].

The remaining terms depend on the top-quark decay width. At LO, it is required in d dimensions

$$\Gamma_0 = \frac{m_t \alpha}{16 s_w^2} \frac{(1-x)^2(1+2(1-\epsilon)x)}{x} \frac{\sqrt{\pi}}{2\Gamma(3/2-\epsilon)} \left(\frac{4\mu^2 e^{\gamma_E}}{m_t^2(1-x)^2} \right)^{\epsilon}, \tag{5.2}$$

with $x = m_W^2/m_t^2$. QCD corrections are only needed in 4 dimensions and are known up to NNLO [120, 121]. The term $(i\Gamma_0/2)(\psi^\dagger\psi - \chi^\dagger\chi)$ in (3.67) belongs to the LO Lagrangian and must be treated non-perturbatively. It leads to the replacement $E \to E + i\Gamma_0$, that has been used to *define* the QCD contribution. In the implementation of the top-pair production cross section [29] the width is treated as a parameter. This implies that higher order corrections to the width are also treated non-perturbatively through the replacement $E \to E + i\Gamma$. The $\mathcal{O}(\epsilon)$ terms in the width have not been considered there. They are however included in the non-resonant part and consistency requires that we also add them to the resonant part. This is done in (5.6) below. The remaining terms in (3.67) that contain the width are treated perturbatively. Only two simple insertions are required. We denote the correction to the Green function $G_0(E)$ from the terms $(X/2)(\psi^\dagger\psi - \chi^\dagger\chi)$ and $(X/2)(\psi^\dagger \boldsymbol{\partial}^2 \psi - \chi^\dagger \boldsymbol{\partial}^2 \chi)$ by $\delta_X G(E)$ and $\delta_{X\boldsymbol{\partial}^2} G(E)$, respectively. They are given by

$$\delta_X G(E) = X G_0'(E) = \frac{X}{m\alpha_s^2 C_F^2} \frac{m^2 \alpha_s C_F}{4\pi} \left[\lambda + 2\lambda^2 + 2\lambda^3 \psi_1(1-\lambda) \right], \tag{5.3}$$

$$\delta_{X\boldsymbol{\partial}^2} G(E) = -mX \frac{m^2 \alpha_s C_F}{4\pi} \left[-\frac{3}{4\lambda} + \frac{1}{2\epsilon} + \frac{1}{2} + 2L_\lambda^{(w)} - 2\hat{\psi}(1-\lambda) + \frac{\lambda}{2}\psi_1(1-\lambda) \right]. \tag{5.4}$$

The NNLO contribution to the Green function from top decays is

$$\delta_{2,\Gamma} G(E) = \left(\delta_X G(E)|_{X=-\frac{\Gamma^2}{4m_t}} \right) + \left(\delta_{X\boldsymbol{\partial}^2} G(E)|_{X=\frac{i\Gamma}{2m_t^2}} \right), \tag{5.5}$$

where we assume that Γ is a parameter, i.e. 4-dimensional. The additional contributions to the cross section from the $\mathcal{O}(\epsilon)$ terms in (5.2), that multiply finite width divergences in (5.5) and the pure QCD result, are added explicitly:

$$\begin{aligned} \delta_{\Gamma_\epsilon/\epsilon}\sigma = \sigma_0 \frac{m_t \Gamma_B \alpha_s C_F N_c}{s} \left[\frac{2(1+x)}{1+2x} + \log\frac{\mu_w^2}{m_t^2} - 2\log(1-x) \right] \\ \times \left[C^{(v)^2} + C^{(a)^2} + C^{(v)^2}_{\text{P-wave}} + C^{(a)^2}_{\text{P-wave}} \right], \end{aligned} \tag{5.6}$$

where Γ_B is the $\epsilon \to 0$ limit of (5.2). On the whole, we obtain

$$\sigma_\Gamma = \sigma_0 \frac{24\pi N_c}{s} \left[C^{(v)^2} + C^{(a)^2} \right] \mathrm{Im}\left[\delta_{2,\Gamma} G(E) \right] + \delta_{\Gamma_\epsilon/\epsilon}\sigma. \tag{5.7}$$

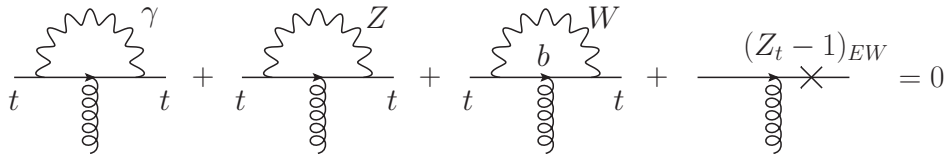

Figure 5.1.: Cancellation of the electroweak gtt vertex corrections in the on-shell scheme.

It is understood that we resum the top-width contributions to the poles in the Green function. They can be determined from the expansion of (5.5) around the resonances and are given by

$$\delta_\Gamma E_n^{(2)} = \frac{\Gamma^2}{4m_t} + \frac{i\Gamma\alpha_s^2 C_F^2}{8n^2}, \qquad \delta_\Gamma F_n^{(2)} = -\frac{3i\Gamma}{2m_t}, \tag{5.8}$$

in the notation of (3.48). We note that the bound-state poles are defined for stable quarks, i.e. with $\Gamma = 0$. Nevertheless, we can resum the higher-order poles of the form (3.50) from the width contribution to retain the structure (3.48), which contains only single poles.

5.1.2. Corrections to the Coulomb potential and field renormalization

Electroweak corrections to the gtt vertex are of order $\alpha \sim \alpha_s^2$ and contribute to the bare color Coulomb potential. With the external momenta in the potential region, it is straightforward to show, that only the hard region contributes to the loop integrals in Figure 5.1. This implies that the external momenta are expanded out of the loop integrals. The corrections to the Coulomb potential therefore effectively involve on-shell vertex corrections, which vanish in the on-shell scheme, see Figure 5.1.

The top-quark field renormalization also contributes to the hard matching coefficients $C^{(k)}$. At NNLO it becomes complex due to bW^+ loop corrections. The imaginary part contributes to the finite width divergence of the resonant part in (3.93). Thus, it has to be determined in d dimensions in accordance with the scheme used to evaluate the other components of (3.93). The other absorptive contributions to $C^{(k)}$ are, however, part of (3.94) and therefore have to be computed in 4 dimensions. Since the two parts are treated using different conventions, we find it convenient to separate them also in notation. Our convention for the Wilson coefficients up to NNLO is

$$C_{\text{full}}^{(k)} = C^{(k)}\left[1 + c_k^{(1)}\left(\frac{\alpha_s}{4\pi}\right) + c_k^{(2)}\left(\frac{\alpha_s}{4\pi}\right)^2 + \frac{y_t^2}{2}c_{vH}^{(2)} + \dots\right] + \left(C_{\text{EW}}^{(k)} + iC_{\text{Abs}}^{(k)}\right)\frac{\alpha}{4\pi} + \dots, \tag{5.9}$$

$$C_{\text{Abs}}^{(k)} = C_{\text{Abs},Z_t}^{(k)} + C_{\text{Abs,bare}}^{(k)}. \tag{5.10}$$

The bare result is computed in Section 5.1.4. The real electroweak corrections $C_{\text{EW}}^{(k)}$ do not yield any finite width divergences at NNLO. Thus, it is not necessary to split them as well.

We obtain

$$C^{(v)}_{\mathrm{Abs},Z_t} = \frac{\pi\Gamma_0}{m_t\alpha s_w^2(4c_w^2-x)(1-x)(1+2x(1-\epsilon))} \times\Big[(1+4e_e s_w^2)(2-\epsilon+x(2-5\epsilon+2\epsilon^2)+2x^2(1-\epsilon)^2) -2s_w^2 e_t(1+e_e(4-x))(3-2\epsilon)(1+x(1-2\epsilon)+2x^2(1-\epsilon))\Big], \tag{5.11}$$

$$C^{(a)}_{\mathrm{Abs},Z_t} = \frac{-\pi\Gamma_0}{m_t\alpha s_w^2(4c_w^2-x)(1-x)(1+2x(1-\epsilon))}\Big[2-\epsilon+x(2-5\epsilon+2\epsilon^2) +2x^2(1-\epsilon)^2-2e_t s_w^2(3-2\epsilon)(1+x(1-2\epsilon)+2x^2(1-\epsilon))\Big]. \tag{5.12}$$

The contribution to the NNLO cross section is given by

$$\sigma_{C^{(k)}_{\mathrm{Abs},Z_t}} = \sigma_0\,\frac{12\alpha N_c}{s}\left[C^{(v)}C^{(v)}_{\mathrm{Abs},Z_t}+C^{(a)}C^{(a)}_{\mathrm{Abs},Z_t}\right]\mathrm{Re}\left[G_0(E)\right], \tag{5.13}$$

where the finite terms from the multiplication of the $1/\epsilon$ divergence in the real part of the Green function (3.46) with the $\mathcal{O}(\epsilon)$ parts of (5.11) and (5.12) must be included. We stress again that this contribution, which is caused by the interference of the resonant and non-resonant amplitudes, is not affected by loose cuts.

5.1.3. Electroweak contribution to the hard matching coefficient

The real electroweak contributions to the NNLO matching coefficients $C^{(k)}$ have been computed in [122–124]. Pure QED corrections have been neglected there. Therefore, we split

$$C^{(k)}_{\mathrm{EW}} = C^{(k)}_{\mathrm{QED}} + C^{(k)}_{\mathrm{WZ}}, \tag{5.14}$$

where

$$C^{(v,a)}_{\mathrm{WZ}} = \frac{s}{\alpha^2}C^{\mathrm{ew}}_{V,A}(\nu=1) - C^{(v,a)}\,\frac{y_t^2}{2}\,c^{(2)}_{vH}, \tag{5.15}$$

with $C^{\mathrm{ew}}_{V,A}(\nu=1)$ given in [124]. The subtraction term is present because Higgs effects that only involve the top Yukawa coupling are treated separately. Corrections that involve Higgs couplings to gauge bosons or Goldstone bosons remain in (5.15).

There is no contribution from the box diagram involving two photons, since only its interference with the production of the top pair through the vector component of the s-channel γ or Z boson is of NNLO and the correlator of three vector currents vanishes [125]. The QED vertex correction to the γe^+e^- and Ze^+e^- vertices contains divergences, that cancel among initial state radiation contributions (see Section 5.1.5). Therefore, we consider it to be part of the ISR, to render both, $\sigma_{C^{(k)}_{\mathrm{EW}}}$ and σ_{IS} finite, separately. Then, the only pure QED effect is the photon vertex correction to the $\gamma t\bar{t}$ and $Zt\bar{t}$ currents, which is given by

$$C^{(v,a)}_{\mathrm{QED}} = -8e_t^2 C^{(v,a)}. \tag{5.16}$$

The contribution from the electroweak corrections to the hard matching coefficients of the production operators is given by

$$\sigma_{C^{(k)}_{\rm EW}} = \sigma_0 \, \frac{12\alpha N_c}{s} \left[C^{(v)} C^{(v)}_{\rm EW} + C^{(a)} C^{(a)}_{\rm EW}\right] {\rm Im}\left[G_0(E)\right]. \tag{5.17}$$

The matching coefficients given in [122–124] are expressed in terms of the fine-structure constant α. This scheme suffers from a large spurious dependence on the light fermion masses, that cancels explicitly with the self-energy corrections to the matching coefficients, when the fine-structure constant is expressed in terms of a less infrared-dependent definition of the electroweak coupling constant. We use the running on-shell coupling $\alpha(\mu_\alpha)$ [126], that coincides with the fine-structure constant for $\mu_\alpha \to 0$. The cross section can be expressed in this scheme with the simple replacements

$$\alpha \to \alpha(\mu_\alpha), \tag{5.18}$$

$$\Pi^{\rm AA'}(0) \to \Pi^{\rm AA}(\mu_\alpha^2)/\mu_\alpha^2. \tag{5.19}$$

The latter replacement rule for the photon self-energy insertion is written in the notation of [122] because the term $\Pi^{\rm AA'}(0)$ only appears in the electroweak contributions to the matching coefficients $C^{(k)}$. The derivative and the explicit factor $1/\mu_\alpha^2$ appear because [122] defines the photon vacuum polarization $\Pi^{\rm AA}$ as a dimensionfull quantity and do not imply a power-dependence of the cross section on the scale μ_α.

5.1.4. Absorptive contribution to the hard matching coefficient

The bare absorptive part of the matching coefficients $C^{(k)}_{\rm Abs,bare}$ is given by the contributions from the diagrams shown in Figure 3.7, which have an obvious correspondence with the interference contribution. In 4 dimensions, we find

$$\begin{aligned} C^{(v)}_{\rm Abs,bare} = -\frac{\pi}{24 s_w^4 x\,(1-x^2)\,(4c_w^2-x)} \Big[& (1-x)\left(5+44x+28x^2-4x^3-x^4\right) \\ & -(1-x)s_w^2\big[(e_e(1-x)^2\left(e_t(4-21x-3x^2+2x^3)-4+4x-4x^2\right) \\ & +e_t(1-x)^2(1-5x-2x^2)+4+48x+36x^2+8x^3\big] \\ & -12x(1+x)(4c_w^2-x){\rm arctanh}(1-x)\Big], \end{aligned} \tag{5.20}$$

$$\begin{aligned} C^{(a)}_{\rm Abs,bare} = \frac{\pi}{24 s_w^4 x\,(1-x^2)\,(4c_w^2-x)} \Big[& (1-x)\left(5+44x+28x^2-4x^3-x^4\right) \\ & -(1-x)s_w^2\big[e_t(1-x)^2(1-5x-2x^2)+4+48x+36x^2+8x^3\big] \\ & -12x(1+x)(4c_w^2-x){\rm arctanh}(1-x)\Big]. \end{aligned} \tag{5.21}$$

We have checked that, in the limit $\epsilon \to 0$, (5.10) reproduces the result in [117]. The contribution to the cross section in the scheme used for (3.94) is given by

$$\sigma_{C^{(k)}_{\rm Abs,bare}} = \sigma_0 \, \frac{12\alpha N_c}{s} \left[C^{(v)} C^{(v)}_{\rm Abs,bare} + C^{(a)} C^{(a)}_{\rm Abs,bare}\right] {\rm Re}\left[\frac{3}{3-2\epsilon} G_0(E)\right]. \tag{5.22}$$

We recall that at LO the Dirac structure of the top pair becomes trivial in the non-relativistic regime and only yields a prefactor $3-2\epsilon$. Thus, by introducing the factor $3/(3-2\epsilon)$ in front of the Green function in (5.22), we have adapted the expression to the correct scheme, which involves 4-dimensional Dirac algebra. The contribution (5.22) is not affected by loose cuts.

We have verified the correctness of (5.22) by computing the sum of the diagrams h_{2a}, h_{3a} and the resonant terms from the corresponding contributions of the absorptive matching conditions (left and middle diagram in Figure 3.7) in d dimensions in the NDR scheme. This combination is finite and the result agrees with the one obtained in the scheme of (5.22). This allows us to avoid the much harder evaluation of h_{4a} and the respective contribution to the absorptive matching coefficient in d dimensions.

5.1.5. Initial state radiation

Last but not least, we take into account effects from initial state radiation. The non-resonant part is only affected at NNNLO and will not be considered. With the exception of the hard region, all contributions are universal and the treatment closely follows the one for W pair production near threshold in [94–96].

We evaluate the contributions from different momentum regions separately. The contribution to the hard matching coefficients $C^{(v,a)}$ from the QED γ/Zee vertex correction makes up the hard part. We find

$$\begin{aligned} C^{(v,a)}_{\gamma/Zee} &= \mathrm{Re}\left[C^{(v,a)}\frac{\alpha}{4\pi}\left(\frac{\mu^2}{-4m_t^2-i0}\right)^{\epsilon}\left(-\frac{2}{\epsilon^2}-\frac{3}{\epsilon}-8+\frac{\pi^2}{6}\right)\right] \\ &= -C^{(v,a)}\frac{\alpha}{4\pi}\left(\frac{2}{\epsilon^2}+\frac{1}{\epsilon}\left(3+2\log\frac{\mu^2}{4m_t^2}\right)+\log^2\frac{\mu^2}{4m_t^2}+3\log\frac{\mu^2}{4m_t^2}+8-\frac{7\pi^2}{6}\right). \end{aligned} \tag{5.23}$$

We only kept the real part because the imaginary part comes from cuts that do not correspond to the final state $b\bar{b}W^+W^-$. The correction to the cross section from hard ISR is

$$\sigma^{(\mathrm{H})}_{\mathrm{IS}} = \sigma_0\,\frac{12\pi N_c}{s}\left[C^{(v)}C^{(v)}_{\gamma/Zee}+C^{(a)}C^{(a)}_{\gamma/Zee}\right]\mathrm{Im}\left[G_0(E)\right]. \tag{5.24}$$

The contributions from the ultrasoft momentum region are shown in Figure 5.2. Virtual ultrasoft corrections are scaleless. The diagram with the photon attached to incoming and outgoing electron vanishes because it is proportional to the square of the light-like direction c_1. No ultrasoft corrections that couple to the collinear and non-relativistic sector occur at NNLO because the leading ultrasoft photon coupling to the final state vanishes, as discussed in Section 5.1.1. Thus, the contribution to the cross section from the ultrasoft region is due to the right diagram in Figure 5.2 and reads

$$\sigma^{(\mathrm{US})}_{\mathrm{IS}} = \sigma_0\,\frac{24\pi N_c}{s}\left[C^{(v)^2}+C^{(a)^2}\right]\frac{\alpha}{4\pi}\frac{-8\sqrt{\pi}}{\epsilon\Gamma(1/2-\epsilon)}\left(\mu^2 e^{\gamma_E}\right)^{\epsilon}\mathrm{Im}\left[\int_0^\infty dk\frac{G_0(E-k)}{k^{1+2\epsilon}}\right]. \tag{5.25}$$

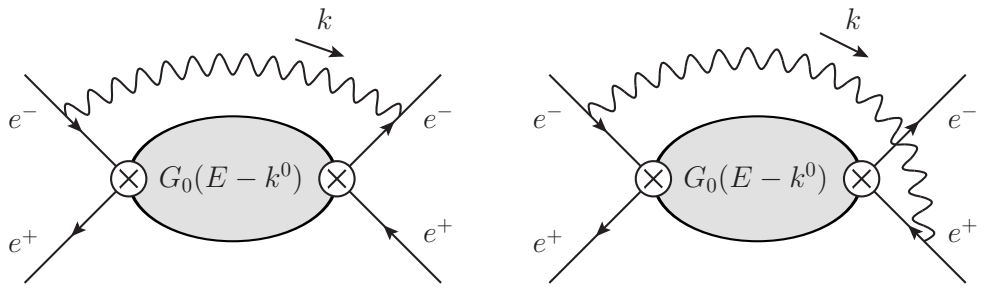

Figure 5.2.: Ultrasoft photon corrections to the resonant cross section. The symmetric diagrams, obtained by the interchange of electrons and positrons, are not shown.

Real collinear corrections are kinematically forbidden in the resonant part because they carry away a hard momentum fraction and push the top-pair off-shell. Virtual collinear corrections are scaleless.

Thus, when the small electron mass is neglected, the photon radiation corrections are given by the sum of (5.24) and (5.25). We observe that the $1/\epsilon^2$ pole cancels, but a collinear divergence remains because the cross section is not infrared safe for $m_e = 0$. This divergence can be regularized by a non-zero electron mass, which in turn yields large logarithms $\ln(s/m_e^2)$. They can be resummed into an electron distribution function, which accounts for collinear radiation off the incoming electron and positron. The cross section with resummed ISR is given by

$$\sigma(s) = \int_0^1 dx_1 \int_0^1 dx_2 \Gamma_{ee}^{\mathrm{LL}}(x_1)\Gamma_{ee}^{\mathrm{LL}}(x_2)\hat{\sigma}^{\mathrm{conv}}(x_1 x_2 s), \tag{5.26}$$

where the structure function $\Gamma_{ee}^{\mathrm{LL}}(x)$ describes the probability of finding an electron with momentum xp in the 'parent electron' with momentum p. Expressions for the structure function can be found in [127–130]. The superscript LL implies that terms of the form $(\alpha \ln(s/m_e^2)/\pi)^n$ have been resummed to all orders. The partonic cross section $\hat{\sigma}^{\mathrm{conv}}(x_1 x_2 s)$ is defined in a different scheme than the one used above. First, we need to change the regulator to a finite electron mass. Then, the $\mathcal{O}(\alpha)$ terms that appear in the convolution of the structure functions with the LO cross section have to be subtracted from the fixed order NNLO partonic cross section to avoid double counting.

The presence of an additional scale, given by the non-vanishing electron mass $m_e \ll m_t\alpha_s^2$, introduces additional regions

$$\begin{array}{lllll} n\text{-hard-collinear:} & \bar{n}\cdot k \sim m_t, & n\cdot k \sim \frac{m_e^2}{m_t}, & k_\perp \sim m_e, \\ n\text{-soft-collinear:} & \bar{n}\cdot k \sim m_t\alpha_s^2, & n\cdot k \sim \frac{m_e^2\alpha_s^2}{m_t}, & k_\perp \sim m_e\alpha_s^2, \end{array} \tag{5.27}$$

with $k^2 \sim m_e^2$ and $k^2 \sim m_e^2\alpha_s^4$, respectively. These regions yield only scaleless integrals for $m_e = 0$. The soft-collinear region contributes in the diagrams shown in Figure 5.2.

As before, the left diagram vanishes. For the right diagram, both the c_1-soft-collinear and c_2-soft-collinear regions must be taken into account. One finds

$$\sigma_{\rm IS}^{\rm (SC)} = \sigma_0 \, \frac{24\pi N_c}{s} \, [C^{(v)^2} + C^{(a)^2}] \frac{\alpha}{4\pi} 8\Gamma(\epsilon) \, \left(\frac{m_t^2}{m_e^2}\right)^{\epsilon} \left(\mu^2 e^{\gamma_E}\right)^{\epsilon} \, {\rm Im} \left[\int\limits_0^\infty dk \frac{G_0(E-k)}{k^{1+2\epsilon}} \right] . \quad (5.28)$$

The hard-collinear contribution comes from the c_1-hard-collinear and c_2-hard-collinear regions of the γ/Zee vertex correction diagram

$$\begin{aligned} \sigma_{\rm IS}^{\rm (HC)} &= \sigma_0 \, \frac{24\pi N_c}{s} \, [C^{(v)^2} + C^{(a)^2}] \, {\rm Im} \, [G_0(E)] \\ &\quad \times \frac{\alpha}{4\pi} \left[\frac{4}{\epsilon^2} + \frac{1}{\epsilon} \left(6 + 4 \ln \frac{\mu^2}{m_e^2} \right) + 2 \ln^2 \frac{\mu^2}{m_e^2} + 6 \ln \frac{\mu^2}{m_e^2} + \frac{\pi^2}{3} + 12 \right] . \end{aligned} \quad (5.29)$$

The collinear $1/\epsilon$ poles cancel in the sum of the hard and hard-collinear, and ultrasoft and soft-collinear contributions, separately. The collinear sensitivity is instead expressed through the large logarithms $\ln(4m_t^2/m_e^2)$. The remaining singularities cancel in the sum over all regions. To make the cancellation explicit, one can expand the factor $1/k^{1+2\epsilon}$ in the distribution sense:

$$\frac{1}{k^{1+2\epsilon}} = -\frac{a^{-2\epsilon}}{2\epsilon} \delta(k) + \frac{1}{[k]_{a+}} + \mathcal{O}(\epsilon), \quad (5.30)$$

where $a > 0$ is arbitrary and we have introduced the modified plus-distribution

$$\int\limits_0^\infty dk \frac{f(k)}{[k]_{a_+}} = \int\limits_0^\infty dk \frac{f(k) - f(0)\theta(a-k)}{k}. \quad (5.31)$$

With $z = m_e^2/(4m_t^2)$, we obtain

$$\begin{aligned} \sigma_{\rm IS} &= \sigma_{\rm IS}^{\rm (H)} + \sigma_{\rm IS}^{\rm (HC)} + \sigma_{\rm IS}^{\rm (US)} + \sigma_{\rm IS}^{\rm (SC)} \\ &= \sigma_0 \, \frac{24\pi N_c}{s} \, [C^{(v)^2} + C^{(a)^2}] \, \frac{\alpha}{4\pi} \left\{ -8 \ln(z) \int\limits_0^\infty dk \frac{{\rm Im} \, [G_0(E-k)]}{[k]_{a+}} \right. \\ &\quad \left. + \left[\frac{4\pi^2}{3} - 4 - 6\ln(z) - 4 \ln\left(\frac{a^2}{m_t^2}\right) \ln(z) \right] {\rm Im} \, [G_0(E)] \right\}, \end{aligned} \quad (5.32)$$

which is finite, such that the four-dimensional expression (3.46) for the LO Green function can be used. The a dependence cancels.

We determine the subtraction terms by expanding the convolution of the LO cross section with the structure function in the coupling constant. The perturbative expansion of the structure function is written as

$$\Gamma_{ee}^{\rm LL}(x) = \delta(1-x) + \Gamma_{ee}^{\rm LL(1)}(x) + \mathcal{O}(\alpha^2). \quad (5.33)$$

We take the expression for the electron structure function from [130] with $\beta_{\text{exp}} = \beta_{\text{S}} = \beta_{\text{H}} = -(2\alpha/\pi)(\ln(z)+1)$. The non-logarithmic term accounts for a subset of terms at NLL.[1] For the cross section near threshold, only the limit $x \to 1$ is important

$$\Gamma_{ee}^{\text{LL}(1)}(x) \xrightarrow{x\to 1} -\frac{\alpha}{4\pi}[\ln(z)+1]\left[\frac{4}{[1-x]_+} + 3\delta(1-x)\right]. \tag{5.34}$$

The $\mathcal{O}(\alpha)$ term in the convolution of the leading order partonic cross section with the structure functions is

$$\begin{aligned} 2\int_0^1 dx \Gamma_{ee}^{\text{LL}(1)}(x)\hat{\sigma}^{\text{LO}}(xs) = \sigma_0 \frac{24\pi N_c}{s}\left[C^{(v)^2} + C^{(a)^2}\right]\frac{\alpha}{4\pi}[\ln(z)+1] \\ \times\left\{-6\text{Im}\left[G_0(E)\right] - 8\int_0^{m_t} dk \frac{\text{Im}\left[G_0(E-k)\right]}{[k]_+}\right\}, \end{aligned} \tag{5.35}$$

where the non-relativistic Green function was evaluated at $\sqrt{xs} - 2m_t = E - m_t(1-x)$ and we have substituted $k = m_t(1-x)$. The partonic cross section in the conventional scheme for the electron structure function is given by (5.32) with (5.35) subtracted. We obtain

$$\begin{aligned} \sigma_{\text{IS}}^{\text{conv}} = \sigma_0 \frac{24\pi N_c}{s}\left[C^{(v)^2} + C^{(a)^2}\right]\frac{\alpha}{4\pi} \\ \times\left\{8\int_0^{m_t} dk \frac{\text{Im}\left[G_0(E-k)\right]}{[k]_+} + \left(\frac{4\pi^2}{3}+2\right)\text{Im}\left[G_0(E)\right]\right\}, \end{aligned} \tag{5.36}$$

where we have set $a = m_t$ and neglected the imaginary part of the Green function for non-relativistic energies $E < -m_t$. The photon radiation contribution to the cross section (5.36) in this scheme is finite and free of large logarithms of the electron mass.

The treatment of ISR presented here is complete at the NNLO plus LL level. We find, however, that it leads to a huge modification of the cross section at the level of $-(30-45)\%$. This clearly shows that the determination of the full NLL corrections is mandatory for the threshold scan, where a prediction for the cross section with an uncertainty at the level of a few % is required. This necessity is not specific to the top threshold scan, since the structure functions are universal and a future lepton collider will probe many processes with unprecedented precision. A crude estimate for the size of the NLL corrections can be obtained by comparing to the results with $\beta_{\text{exp}} = \beta_{\text{S}} = \beta_{\text{H}} = -(2\alpha/\pi)\ln(z)$ without the constant term. The difference is of the order of 2%, which is comparable to the overall scale uncertainty.

[1] For the resummation of ISR we adopt the usual counting conventions. N^{k}LL includes all terms of the order $\alpha^n \ln^{n-k}(z)$.

5.2. The P-wave contribution at NNNLO

In this section, we compute the axial-vector correlation function (3.21). The hard matching coefficient c_a in the naive anti-commuting (NDR) scheme for γ_5 is given by [131]

$$c_a = 1 - 4C_F \frac{\alpha_s}{4\pi}\left[1 - \epsilon \ln \frac{m_t^2}{\mu^2} + \mathcal{O}(\epsilon^2)\right] + \mathcal{O}(\alpha_s^2). \tag{5.37}$$

The P-wave Green function (3.45) up to NLO is determined below. In Section 5.2.4, the full result for the P-wave contribution to the cross section up to NNNLO is obtained.

5.2.1. Leading order Green function

We recall that already the leading-order S-wave Green function (3.46) contains a $1/\epsilon$ pole proportional to α_s, i.e. from the 2-loop contribution. The one-loop part is also divergent, but finite in dimensional regularization. The P-wave Green function contains an additional factor $\mathbf{p}\cdot\mathbf{p}'$ and simple power counting demonstrates that ladder diagrams with up to four loops are UV divergent. The knowledge of the 4-dimensional representations (3.34) and (3.35) for the leading order Green function is not sufficient for the computation of $G_0^P(0,0;E)$ in the $\overline{\text{MS}}$ scheme because the limit $r, r' \to 0$ diverges. In $d = 4$, but keeping the distance r as a regulator in (3.45), we obtain

$$\begin{aligned}
G_0^P(E)|_r &= \lim_{\mathbf{r},\mathbf{r}'\to 0} \langle \nabla_r \cdot \nabla_{r'} G_0(\mathbf{r},\mathbf{r}';E)\rangle \\
&= \lim_{\mathbf{r},\mathbf{r}'\to 0} \frac{1}{(4\pi)^2} \int d\Omega_{\mathbf{r}} \int d\Omega_{\mathbf{r}'} \nabla_r \cdot \nabla_{r'} G_0(\mathbf{r},\mathbf{r}';E) \\
&= \frac{m^4\alpha_s^3 C_F^3}{32\pi\lambda^3}\Bigg[\frac{\lambda}{(pr)^2} - \frac{1-2\lambda^2}{pr} + 2(\lambda-\lambda^3)\log(pr) \\
&\quad + 1 - \left(\frac{9}{2} - 4\gamma_E - 2\log(2)\right)\lambda - 3\lambda^2 + (3 - 4\gamma_E - 2\log(2))\lambda^3 \\
&\quad + 2(\lambda-\lambda^3)\psi(2-\lambda) + \mathcal{O}(pr)\Bigg].
\end{aligned} \tag{5.38}$$

The integrals over the directions of $\mathbf{r}$ and $\mathbf{r}'$ project out the P-wave component of the Green function. Consistent with our expectations, only terms with up to three powers of α_s in the expression (5.38) are singular for $r \to 0$.

To obtain $G_0^P(0,0;E)$ in $\overline{\text{MS}}$, we can split off the divergent diagrams, the sum of which is denoted by $G_0^{P(\leq 3ex)}$, and compute them in momentum space, using dimensional regularization and conventional loop methods. The remainder $G_0^{P(\geq 4ex)}$ is finite and regularization independent. Thus, it can be obtained by expanding (5.38) in α_s and subtracting all terms with three or less powers of α_s.

The contribution of a diagram with n gluon exchanges to the Green function in $d = 4-2\epsilon$ dimensions is given by

$$\begin{aligned} G_0^{P(nex)} &\equiv \int \prod_{j=1}^{n+1} \left[\frac{d^{d-1}\mathbf{p}_j}{(2\pi)^{d-1}}\right] \frac{(C_F g_s^2)^n m^{n+1} (\mathbf{p}_1 \cdot \mathbf{p}_{n+1})}{[\mathbf{p}_1^2 - Em](\mathbf{p}_1-\mathbf{p}_2)^2 \dots (\mathbf{p}_n - \mathbf{p}_{n+1})^2 [\mathbf{p}_{n+1}^2 - Em]} \\ &= \frac{(C_F g_s^2)^n m^{n+1}}{2(-Em)^{\frac{n-3}{2}+(n+1)\epsilon}} \int \prod_{j=1}^{n+1} \left[\frac{d^{d-1}\mathbf{k}_j}{(2\pi)^{d-1}}\right] \frac{(\mathbf{k}_1^2+1)+(\mathbf{k}_{n+1}^2+1)-2-(\mathbf{k}_1-\mathbf{k}_{n+1})^2}{[\mathbf{k}_1^2+1](\mathbf{k}_1-\mathbf{k}_2)^2 \dots (\mathbf{k}_n-\mathbf{k}_{n+1})^2[\mathbf{k}_{n+1}^2+1]}. \end{aligned} \tag{5.39}$$

where we have rescaled all momenta by $\mathbf{p}_i \to \sqrt{-mE}\mathbf{k}_i$. The numerator $\mathbf{k}_1 \cdot \mathbf{k}_{n+1}$ has been decomposed into irreducible terms. The first two give massless tadpoles in either $\mathbf{k}_{n+1}$ or $\mathbf{k}_1$ and therefore vanish. The other two can be reduced to known master integrals using integration by parts, which is described in detail in e.g. [132]. We used the package `FIRE` [133, 134] to perform this reduction. The required master integrals are known for general dimensions d [135] and have also been reproduced within more general calculations for the NLO contribution. The result is

$$G_0^{P(\leq 3ex)}(E) = \frac{m_t^4 C_F^3 \alpha_s^3}{32\pi\lambda^3} + 4\pi C_F \alpha_s \left[I_{\mathrm{P}}^{00}[1] + I_{\mathrm{P}}^{10}[1] + I_{\mathrm{P}}^{20}[1]\right], \tag{5.40}$$

where the contribution from the one-loop, zero-gluon exchange diagram is stated explicitly. Its scaling $1/\lambda^3 \sim E^{3/2} \sim v^3$ is characteristic for the threshold behaviour of the P-wave production. The notation $I_{\mathrm{P}}^{(n-1)0}[1]$ for the higher-loop integrals, corresponding to diagrams with n gluon exchanges, is explained in more detail in the context of the NLO calculation. Explicit results can be found in Appendix A.

The correlation function in dimensional regularization is given by the sum $G_0^{P(\leq 3ex)} + G_0^{P(\geq 4ex)}$ and takes the form

$$\begin{aligned} G_0^P(E) = \frac{m_t^4 C_F^3 \alpha_s^3}{32\pi\lambda^3} \Bigg[1 - \left(\frac{1}{2\epsilon} + 2L_\lambda^w + 4\right)\lambda - 3\lambda^2 + \left(\frac{1}{4\epsilon} + 2L_\lambda^w + \frac{7}{2}\right)\lambda^3 \\ + 2(\lambda - \lambda^3)\hat{\psi}(2-\lambda)\Bigg], \end{aligned} \tag{5.41}$$

where

$$L_\lambda^a = \ln\left(\frac{\lambda\mu_a}{m_t\alpha_s C_F}\right) = -\frac{1}{2}\ln\left(\frac{-4m_t E}{\mu_a^2}\right), \tag{5.42}$$

with $a \in \{r, w\}$. Minimal subtraction of the poles in (5.41) yields the result in the $\overline{\mathrm{MS}}$ scheme. We find that only the residue of the $1/\epsilon$ pole in the first line of (5.41) is complex for a non-zero width. The residue of the second pole is energy-independent and real. Thus, the finite-width divergence in (5.41) is purely due to the two-loop, one exchange contribution. It is in agreement with the result of [98, 136]. When the top width is neglected, the

imaginary part of the P-wave Green function is finite, and has the form

$$\begin{aligned}\mathrm{Im}\big[G_0^P(E)\big] &= \left(\frac{m_t C_F\alpha_s}{2}\right)^5 \sum_{n=2}^{\infty} \frac{n^2-1}{n^5}\,\delta(E-E_n) \\ &\quad + \frac{m_t^4}{4\pi}\left(\frac{E}{m_t}+\frac{C_F^2\alpha_s^2}{4}\right)\frac{\pi C_F\alpha_s}{1-e^{-C_F\alpha_s\pi/v}}\,\theta(E),\end{aligned} \tag{5.43}$$

where $v \equiv \sqrt{E/m_t}$. It contains an infinite number of narrow resonances below threshold with the bound-state energies $E_n = -(m_t C_F^2\alpha_s^2)/(4n^2)$ with $n \geq 2$. Above the threshold, the cross section is enhanced by the famous Sommerfeld factor. Our result (5.43) is in agreement with [90].

5.2.2. Next-to-leading order Green function

Following the same approach as the S-wave computation [89], one can define the single-insertion function

$$I_{\mathrm{P}}[x+u] = \int \left[\prod_{i=1}^{4} \frac{d^{d-1}\mathbf{p}_i}{(2\pi)^{d-1}}\right] \mathbf{p}_1\cdot\mathbf{p}_4\;\tilde{G}_0(\mathbf{p}_1,\mathbf{p}_2;E)\frac{1}{(\mathbf{q}_{23}^2)^x}\left(\frac{\mu^2}{\mathbf{q}_{23}^2}\right)^u \tilde{G}_0(\mathbf{p}_3,\mathbf{p}_4;E), \tag{5.44}$$

where $\mathbf{q}_{ij} = \mathbf{p}_i - \mathbf{p}_j$. The NLO correction to the P-wave Green function (3.45) can be expressed through this function as follows:

$$\delta_1 G^P(E) = C_F\alpha_s^2\left[\frac{\beta_0}{\epsilon}\Big(I_{\mathrm{P}}[1+\epsilon]-I_{\mathrm{P}}[1]\Big)+a_1(\epsilon)I_{\mathrm{P}}[1+\epsilon]\right]. \tag{5.45}$$

Again, the diagrams with up to four loops are UV divergent. We use the same approach as at LO and split the NLO correction into a divergent (a) and a finite part (b). Due to the insertion of the NLO Coulomb potential, this has a more complicated structure as indicated in Figure 5.3. Due to the non-zero top width, divergences of the type Γ_t/ϵ, arising from poles of the form E/ϵ, appear in the imaginary part of (a). Thus, in the computation of part (a), the NLO Coulomb potential (3.41) must not be expanded in ϵ before the loop integration. This differs from the S-wave [88], which has a finite imaginary part, and where the potential can be expanded. Similarly, the imaginary part of (b) is finite and, therefore, the potential can be expanded prior to the integration.

In the computation of $I_{\mathrm{P}}^{(b)}[1+u]$, it is simpler to perform the necessary subtractions of the divergent diagrams after some initial simplifications. Thus, we first consider the

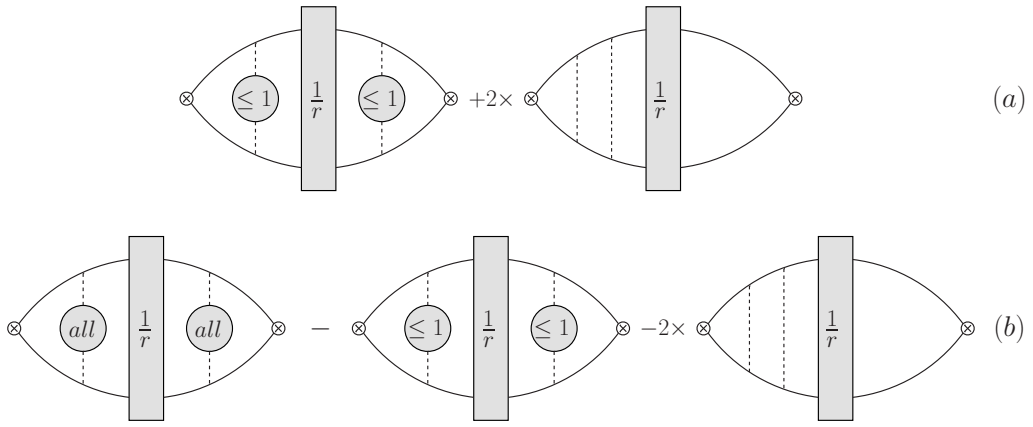

Figure 5.3.: We split the NLO correction to the Green function into a divergent part (a), that contains all diagrams with up to four loops, and the finite remainder (b).

complete $I_{\rm P}[1+u]$ in position space:

$$
\begin{aligned}
I_{\rm P}[1+u] &= \lim_{\mathbf{x},\mathbf{y}\to 0} \left\langle (\nabla_x \cdot \nabla_y) \int d^{d-1}\mathbf{r}\, G_0(\mathbf{x},\mathbf{r};E) \frac{\mu^{2u}\,(\mathbf{r}^2)^{u-\frac{1}{2}}}{4\pi\Gamma(1+2u)\cos(\pi u)} G_0(\mathbf{r},\mathbf{y};E) \right\rangle \\
&= \lim_{\mathbf{x},\mathbf{y}\to 0} \frac{9m_t^2(2p)^6\mu^{2u}}{(4\pi)^3\Gamma(1+2u)\cos(\pi u)\,\Gamma(2+\lambda)^2\Gamma(2-\lambda)^2} \\
&\quad \times \int_0^1 dt_1 \int_0^1 dt_2 \left[(1-t_1)(1-t_2)\right]^{1+\lambda} \left[t_1 t_2\right]^{1-\lambda} \int_1^\infty ds_1 \int_1^\infty ds_2 \left[s_1 s_2\right]^{1+\lambda} \left[(s_1-1)(s_2-1)\right]^{1-\lambda} \\
&\quad \times \left\langle (\nabla_x \cdot \nabla_y) \int d^{d-1}\mathbf{r}\, (\mathbf{x}\cdot\mathbf{r})\,(\mathbf{y}\cdot\mathbf{r})\,\left(\mathbf{r}^2\right)^{u-\frac{1}{2}} e^{-p[x(1-2t_1)+y(1-2t_2)+2r(s_1+s_2-1)]} \right\rangle .
\end{aligned}
\tag{5.46}
$$

The integral over $\mathbf{r}$ is straightforward:

$$
\int d^{d-1}\mathbf{r}\; r^i r^j\, r^{2u-1} e^{-2pr(s_1+s_2-1)} = \frac{\delta^{ij}}{d-1}\, \frac{2\pi^{(d-1)/2}\Gamma(d+2u)}{\Gamma((d-1)/2)} \left[2p(s_1+s_2-1)\right]^{-d-2u} .
\tag{5.47}
$$

After taking the derivatives and the limit $\mathbf{x},\mathbf{y}\to 0$, the integrations over t_1 and t_2 are simple and one obtains

$$
\begin{aligned}
I_{\rm P}[1+u] = \frac{m_t^2(2p)^{6-d-2u}\mu^{2u}}{4(4\pi)^3\Gamma(1+2u)\cos(\pi u)} \frac{2\pi^{(d-1)/2}\Gamma(d+2u)}{\Gamma((d-1)/2)} \\
\times \int_1^\infty ds_1 \int_1^\infty ds_2\, \frac{\left[s_1 s_2\right]^{1+\lambda}\left[(s_1-1)(s_2-1)\right]^{1-\lambda}}{(s_1+s_2-1)^{d+2u}} .
\end{aligned}
\tag{5.48}
$$

The α_s dependence of this expression is isolated in the exponents λ of the s_i and (s_i-1) factors. The necessary subtractions are the terms up to the order λ^3 in an expansion for

small λ. For the finite remainder (b), we can set $d = 4$. We find

$$I_{\mathrm{P}}^{(b)}[1+u] = \frac{m_t^2 p^2}{(4\pi)^2}\left(-\frac{\mu^2}{4m_t E}\right)^u j_{\mathrm{P}}(u), \tag{5.49}$$

where, after the substitution $t_i = s_i - 1$, we have

$$\begin{aligned} j_{\mathrm{P}}(u) = \frac{\Gamma(4+2u)}{\Gamma(1+2u)\cos(\pi u)} \int_0^\infty dt_1 \int_0^\infty dt_2 \frac{t_1 t_2 (1+t_1)(1+t_2)}{(1+t_1+t_2)^{4+2u}} \Bigg[\left(\frac{(1+t_1)(1+t_2)}{t_1 t_2}\right)^\lambda \\ - 1 - \lambda \log\left(\frac{(1+t_1)(1+t_2)}{t_1 t_2}\right) - \frac{\lambda^2}{2}\log^2\left(\frac{(1+t_1)(1+t_2)}{t_1 t_2}\right)\Bigg]. \end{aligned} \tag{5.50}$$

We can exploit the finiteness of part (b) and expand the Coulomb potential in ϵ. This yields the following simplification:

$$\begin{aligned} \delta_1 G^{P(b)}(E) &= C_F \alpha_s^2 \left[\beta_0 \frac{d}{du} I_{\mathrm{P}}^{(b)}[1+u]\Big|_{u=0} + a_1(0) I_{\mathrm{P}}^{(b)}[1]\right] \\ &= \frac{m_t^4 \alpha_s^4 C_F^3}{64\pi^2\lambda^2}\left[\beta_0\left(2 j_{\mathrm{P}}(0) L_\lambda + j'_{\mathrm{P}}(0)\right) + a_1(0) j_{\mathrm{P}}(0)\right]. \end{aligned} \tag{5.51}$$

In the first line, we have written the logarithm of $\mathbf{q}^2$ in the expanded potential as a derivative at zero u. This way, we do not require a solution of (5.50) for general u, but only its value and its first derivative at $u = 0$. We show the computation in Appendix A. The solution is

$$j_{\mathrm{P}}(0) = -1 + \left(\frac{\pi^2}{3} - 2\right)\lambda + 3\zeta(3)\lambda^2 + \left(1 - 3\lambda^2\right)\hat{\psi}(2-\lambda) + \left(\lambda^3 - \lambda\right)\psi_1(2-\lambda), \tag{5.52}$$

$$\begin{aligned} j'_{\mathrm{P}}(0) = \frac{\pi^2}{6} - \frac{50}{9} + \left[-4 + \frac{2\pi^2}{3} - 4\zeta(3)\right]\lambda + \left[\frac{34}{3} + \frac{\pi^2}{6} - \frac{\pi^4}{180} + 6\zeta(3)\right]\lambda^2 \\ + \left[4 + 6\lambda - 10\lambda^2\right]\hat{\psi}(2-\lambda) + \left(3\lambda^2 - 1\right)\left[\hat{\psi}(2-\lambda)^2 - 3\psi_1(2-\lambda)\right] \\ + \left(\lambda^3 - \lambda\right)\left[\left(\frac{22}{3} - 2\hat{\psi}(2-\lambda)\right)\psi_1(2-\lambda) + \psi_2(2-\lambda)\right] \\ + \frac{3}{2(\lambda-2)}\,{}_4F_3(1,1,4,4;5,5,3-\lambda;1), \end{aligned} \tag{5.53}$$

with $\psi_n(z)$ the nth derivative of the ψ function. The numerical evaluation of the hypergeometric function ${}_4F_3$ for complex values of λ requires an analytic continuation. This is briefly discussed in Appendix B, where the necessary formulas are given.

To compute the divergent part (a), we have to solve loop integrals like those in (5.39) with the exponent of one of the gluon propagators raised by u. Part (a) is given by (5.45) with I_P replaced by

$$I_{\mathrm{P}}^{(a)}[1+u] = I_{\mathrm{P}}^{00}[1+u] + 2I_{\mathrm{P}}^{10}[1+u] + 2I_{\mathrm{P}}^{20}[1+u] + I_{\mathrm{P}}^{11}[1+u], \tag{5.54}$$

where $I_{\mathrm{P}}^{nm}[1+u]$ is the contribution from the diagram with n potential gluon exchanges to the left and m to the right of the insertion of the NLO Coulomb potential. As at LO, the diagrams again have up to four loops, but with one propagator raised to a non-integer power. They must be calculated in dimensional regularization and we show the details and the results for the $I_{\mathrm{P}}^{nm}[1+u]$ in the second part of Appendix A. The final result for the NLO correction to the Green function in dimensional regularization is:

$$
\begin{aligned}
\delta_1 G^P(E) = &-\frac{m_t^4 \alpha_s^4 C_F^3}{64\pi^2\lambda^2} \\
&\times\Bigg\{\beta_0\Bigg[\left(-\frac{1}{12\epsilon^2}+\frac{59}{9}+\frac{5\pi^2}{72}+4L_\lambda^r+2L_\lambda^r L_\lambda^w-\left(L_\lambda^w\right)^2\right)+\left(9+6L_\lambda^r\right)\lambda \\
&\quad+\left(\frac{3}{40\epsilon^2}+\frac{1}{20\epsilon}-\frac{344}{15}-\frac{\pi^2}{8}-\frac{21}{2}L_\lambda^r+\frac{1}{2}L_\lambda^w-6L_\lambda^w L_\lambda^r+3\left(L_\lambda^w\right)^2\right)\lambda^2 \\
&\quad+\left[-4-6\lambda+10\lambda^2+2(3\lambda^2-1)L_\lambda^r\right]\hat{\psi}(2-\lambda) \\
&\quad+\left(\lambda-\lambda^3\right)\left[\psi_1(2-\lambda)\left(\frac{22}{3}+2L_\lambda^r-2\hat{\psi}(2-\lambda)\right)+\psi_2(2-\lambda)\right] \\
&\quad+\left(3\lambda^2-1\right)\left[3\psi_1(2-\lambda)-\hat{\psi}(2-\lambda)^2\right]+\frac{3}{4-2\lambda}\,{}_4F_3(1,1,4,4;5,5,3-\lambda;1)\Bigg] \\
&+a_1(\epsilon)\Bigg[\frac{1}{6\epsilon}+2+L_\lambda^w+3\lambda-\left(\frac{3}{10\epsilon}+\frac{26}{5}+3L_\lambda^w\right)\lambda^2+\left(3\lambda^2-1\right)\hat{\psi}(2-\lambda) \\
&\quad+\left(\lambda-\lambda^3\right)\psi_1(2-\lambda)\Bigg]\Bigg\}. \qquad (5.55)
\end{aligned}
$$

We have distinguished the renormalization scale μ_r and the scale μ_w related to finite width divergences as described in Appendix A. The scales can also be identified by demanding that the dependence on the renormalization scale cancels at NLO. By expanding the running coupling α_s in the leading order Green function, we can identify the logarithms of μ in (5.55), that are required for the cancellation, and assign them to μ_r. The remaining μ-dependence is related to the width, i.e. denoted by μ_w, and persists in the pure-QCD result. It will only cancel, when non-resonant effects are taken into account at NNNLO. One can see that the μ_w-dependence is polynomial in E and cancels in the imaginary part for $\Gamma_t = 0$. This is a further check for the consistency of the result.

5.2.3. Pole resummation

Due to the non-perturbatively strong color Coulomb interaction, the Green function develops bound-state poles below threshold. In the P-wave Green function they correspond to would-be toponium states with angular momentum $l = 1$. In conventional perturbation theory, these poles would never emerge. Accordingly, they are only present in the finite parts of the computation that sum over an infinite number of diagrams. In the formulas,

the poles appear in the polygamma and hypergeometric functions at positive integer values $\lambda \geq 2$.

When the exact Green function is expanded around the energy E_n^P of the nth P-wave bound state, it has the form

$$G^P(E) \overset{E\to E_n^P}{=} \frac{|\psi_n'(0)|^2}{E_n^P - E - i\epsilon} + \text{regular}, \tag{5.56}$$

where $\psi_n'(0)$ the derivative of the wave function of the nth bound state at the origin. Thus, the NLO Green function also contains the information necessary to determine the NLO corrections to the bound-state, parametrized by

$$E_n^P = E_n^{P(0)}\left(1 + \frac{\alpha_s}{4\pi}\, e_1^P + \mathcal{O}(\alpha_s^2)\right), \quad |\psi_n'(0)|^2 = |\psi_n'^{(0)}(0)|^2\left(1 + \frac{\alpha_s}{4\pi} f_1^P + \mathcal{O}(\alpha_s^2)\right). \tag{5.57}$$

The expansion of the perturbative result (3.45) for the Green function near the bound-state poles also contains higher poles because the energy-levels and wave functions in (5.56) are expanded

$$\begin{aligned} G^P(E) \overset{E\to E_n^{P(0)}}{=} & \frac{|\psi_n'^{(0)}(0)|^2}{E_n^{P(0)} - E - i\epsilon} + \frac{\alpha_s}{4\pi}\left(\frac{f_1^P |\psi_n'^{(0)}(0)|^2}{E_n^{P(0)} - E - i\epsilon} - \frac{e_1^P |\psi_n'^{(0)}(0)|^2 E_n^{P(0)}}{\left(E_n^{P(0)} - E - i\epsilon\right)^2}\right) \\ & + \mathcal{O}(\alpha_s^2) + \text{regular}. \end{aligned} \tag{5.58}$$

The results for the bound-states follow from an expansion of our results for the Green function for E near $E_n^{P(0)}$, or, equivalently, λ near positive integer n. Alternatively, the leading order terms can be read off from the imaginary part (5.43) of G_0^P:

$$E_n^{P(0)} = -\frac{m_t C_F^2 \alpha_s^2}{4n^2}, \qquad |\psi_n'^{(0)}(0)|^2 = \frac{1}{\pi}\left(\frac{m_t C_F \alpha_s}{2}\right)^5 \frac{n^2-1}{n^5}. \tag{5.59}$$

The expansion of (5.55) is

$$\begin{aligned} \delta_1 G^P(E) \overset{\lambda\to n}{=} & \frac{m_t^4 \alpha_s^4 C_F^3}{4(4\pi)^2} \\ & \times\Bigg\{ \frac{n^2-1}{n^2(n-\lambda)}\left[2\beta_0\left(2L_n^r + 4 + \frac{3}{n-1} - \frac{4n^2}{n^2-1}\hat{\psi}(n+2) - 2n\psi_1(n+2)\right) + 2a_1\right] \\ & + \frac{n^2-1}{n(n-\lambda)^2}\left[2\beta_0(L_n^r + \hat{\psi}(n+2)) + a_1\right] + \text{regular}\Bigg\}. \end{aligned} \tag{5.60}$$

Comparing this to (5.58), we find:

$$e_1^P = 2a_1 + 4\beta_0\left[L_n^r + \hat{\psi}(n+2)\right], \tag{5.61}$$

$$f_1^P = 5a_1 + 2\beta_0\left[5L_n^r + 4 + \frac{3}{n-1} - \frac{n^2+3}{n^2-1}\hat{\psi}(n+2) - 2n\psi_1(2+n)\right], \tag{5.62}$$

with $L_n^r = \ln(n\mu_r/(m_t C_F \alpha_s))$. This is in agreement with the results of [91, 92].

With these expressions, it is possible to resum the singular bound-state terms in (5.58) into the form (5.56), which contains only single poles. This defines the pole-resummed Green function

$$G^P_{\rm PR}(E) = G^P(E) + \sum_{n=2}^{\infty} \left\{ \left[\frac{|\psi_n'(0)|^2}{E_n^P - E - i\epsilon} \right]_{\rm unexpanded} - \left[\frac{|\psi_n'(0)|^2}{E_n^P - E - i\epsilon} \right]_{\rm expanded} \right\}. \quad (5.63)$$

Obviously, one can't take the sum up to infinity in the numerical evaluation. Fortunately, it is sufficient to apply a rather small cutoff due to the $1/n^3$ behaviour of the square of the derivative of the wave function at the origin. In practice, only the poles up to $n = 6$ are resummed.

5.2.4. P-wave contribution to the cross section

We recall from Section 3.5 that the correct treatment of finite terms, that arise from finite width divergences, is crucial for the consistent combination of the resonant and non-resonant part. Our prescription for the P-wave contribution is that the spectral function (3.21) is computed completely in d dimensions and the leptonic tensor in 4 dimensions. This implies that finite terms from the finite width divergences in the Green function multiplying the d-dimensional prefactor $(d-2)/(d-1) \times c_a^2$ in (3.21) must be taken into account. We parametrize the short-distance coefficient (5.37) in the form $c_a = 1 + [c_a^{(1)} + \epsilon c_a^{(1\epsilon)}] + \mathcal{O}(\alpha_s^2)$, where the scale μ in the logarithm in $c_a^{(1\epsilon)}$ should be identified with μ_w, and the Green function at LO (5.41) and NLO (5.55) as

$$G_0^P(E) = \frac{1}{\epsilon} G_{0,\rm div} + G^P_{0,\overline{\rm MS}}, \qquad \delta_1 G^P(E) = \frac{1}{\epsilon^2} \delta_1 G_{\rm div2} + \frac{1}{\epsilon} \delta_1 G_{\rm div1} + \delta_1 G^P_{\overline{\rm MS}}. \quad (5.64)$$

In terms of these expressions, the NLO result for the spectral function $\Pi^{(a)}(q^2)$ in the $\overline{\rm MS}$ scheme with the NDR treatment of γ^5 is given by $\Pi^{(a)}(q^2) = \Pi_0^{(a)}(q^2) + \delta_1 \Pi^{(a)}(q^2)$ with

$$\begin{aligned} {\rm Im}\,[\Pi_0^{(a)}(q^2)] &= \frac{N_c}{2m_t^4} \frac{2}{3} {\rm Im}\,[G^P_{0,\overline{\rm MS}}(E)] - \frac{2}{9} \frac{N_c}{32\pi} \frac{\alpha_s C_F \Gamma_t}{m_t}, \quad (5.65) \\ {\rm Im}\,[\delta_1 \Pi^{(a)}(q^2)] &= \frac{N_c}{2m_t^4} \frac{2}{3} {\rm Im}\,[\delta_1 G^P_{\overline{\rm MS}}(E)] + 2c_a^{(1)} {\rm Im}\,[\Pi_0^{(a)}(q^2)] \\ &\quad + 2c_a^{(1\epsilon)} \frac{2}{3} \frac{N_c}{32\pi} \frac{\alpha_s C_F \Gamma_t}{m_t} + \left(\frac{\beta_0}{81} - \frac{a_1(0)}{27} \right) \frac{N_c}{32\pi^2} \frac{\alpha_s^2 C_F \Gamma_t}{m_t}, \quad (5.66) \end{aligned}$$

where the finite terms proportional to the top width Γ_t have been worked out explicitly. We observe that they do not depend on the energy because they stem from poles that cancel with the non-resonant part, which is also energy independent. In (5.66), we have assumed that the width Γ_t is treated as a parameter, i.e. that it is not expanded in perturbation theory and it is 4-dimensional. In the non-resonant part, analytical expressions for the width are used. For a consistent combination, also the finite terms from $\mathcal{O}(\epsilon)$ terms in the

analytic expression for Γ_t must be taken into account. These terms are attributed to σ_Γ and were discussed in Section 5.1.1. The result for the P-wave contribution to the NNNLO cross section is given by

$$\sigma_{\text{P-wave}} = 12\pi\sigma_0 \left(C^{(v)^2}_{\text{P-wave}} + C^{(a)^2}_{\text{P-wave}} \right) \text{Im}\,[\Pi_0^{(a)}(q^2) + \delta_1\Pi^{(a)}(q^2)]. \tag{5.67}$$

5.3. Higgs effects at NNNLO

In this section we consider the effects of the Higgs boson up to NNNLO. At this point, only Higgs contributions which exclusively contain the top Yukawa coupling are taken into account. Corrections that also involve Higgs-gauge boson interactions are considered a general electroweak effect and treated as part of $\sigma_{C^{(k)}_{\text{EW}}}$ in Section 5.1.3.

The Higgs contribution involves two new parameters, the Higgs mass m_H, and top-quark Yukawa coupling y_t. The power counting of the Higgs mass is crucial for the structure of the contributions, as we argue below. It has been considered to be hard in Section 3.4, $m_H \sim m_t$, which is numerically well justified. In earlier analyses [137], before the Higgs boson discovery, it was implicitly assumed that the Higgs boson mass is of the order of the soft scale $m_t\alpha_s$. Higgs exchange contributions have been described by a Yukawa potential $\exp(-m_H r)/r$. Counting the Higgs mass as hard, the exponent in the Yukawa potential scales like $1/v$ and the potential becomes non-analytic in the velocity expansion. This is clearly inconsistent and violates the spirit of the effective field theory approach, where all terms should have an unambiguous scaling. Thus, the results of [137] can't be used in the light of the physical Higgs mass. Instead, one has to perform a proper matching with the correct scaling, in which case a local interaction $\delta^{(3)}(\mathbf{r})/m_H^2$ is obtained. This directly follows from the Higgs propagator $1/(\mathbf{q}^2 + m_H^2)$ in momentum space, where our counting implies that $\mathbf{q}^2 \sim m_t^2 v^2$ can be expanded out with respect to m_H^2. The leading Higgs potential in momentum space is therefore simply

$$\delta_H V = -\frac{y_t^2}{2m_H^2}. \tag{5.68}$$

With $m_H \sim m_t v$, both terms in the Higgs propagator would be of the same order and the Yukawa potential would be retained.

On the other hand, the counting of the top-quark Yukawa coupling merely determines at which order in perturbation theory the contributions appear. The standard model Yukawa coupling is related to the other parameters by the relation

$$y_t^2 = \frac{2m_t^2}{v^2} = \frac{2\pi\alpha m_t^2}{m_W^2 s_w^2}. \tag{5.69}$$

Our choice to consider $m_W \sim m_t$ as hard in Section 3.4 implies the counting $y_t^2 \sim \alpha_{\text{EW}} \sim \alpha_s^2$, that will be used here. Alternatively, one might take treating $y_t^2 \sim \alpha_s$ into consideration because of the large value of the top-quark mass. Below, we compare the actual size of

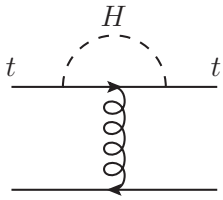

Figure 5.4.: One-loop Higgs correction to the colour Coulomb potential.

the Higgs corrections to QCD terms of the same order and show that our approach is appropriate.

The Higgs corrections appear in two ways. Firstly, there are contributions to the hard-matching coefficient of the external vector current or the production operators, respectively. Being a hard corrections, this is only suppressed by the coupling constant, which is given by y_t^2. In our counting, it constitutes a NNLO effect. At NNNLO, we also have to consider mixed Higgs-QCD contributions of this type. They are discussed in Section 5.3.1. The second effect is the Higgs potential (5.68). With respect to the leading QCD Coulomb potential $\alpha_s/\mathbf{q}^2$, it is a NNNLO effect. The correction to the non-relativistic correlation function is calculated in Section 5.3.2.

Naive power counting suggests that NNLO corrections to the colour Coulomb potential, as shown in Figure 5.4, are present. Only the hard loop momentum region is relevant for $m_H \sim m_t$. However, the external momenta are potential and must be expanded out in the loop integral. Thus, one obtains an $\mathcal{O}(y_t^2)$ correction to the $\psi^\dagger\psi A^0$ top-quark-gluon coupling of the NRQCD Lagrangian at zero momentum transfer. In the on-shell scheme this contribution is canceled by the top-quark field renormalization because the vertex is effectively on-shell (cf. Section 5.1.2).

5.3.1. Short-distance effects

The NNLO Higgs contributions to the hard-matching coefficient of the vector current have been computed in [122–124]. Here we only consider terms that contain the square of the top-Yukawa coupling. Other Higgs boson corrections are tiny and taken into account at NNLO in Section 5.1.3. For the mixed Higgs and QCD corrections at NNNLO, the leading six terms in expansions $m_H \approx m_t$ or $m_H \gg m_t$ have been determined in [118]. It was found that the NNNLO coefficient is IR divergent. The divergence was absorbed into the renormalization constant

$$\widetilde{Z}_v = 1 + [\text{pure QCD}] + \frac{\alpha_s C_F}{4\pi}\frac{y_t^2 m_t^2}{2m_H^2}\frac{1}{4\epsilon}. \tag{5.70}$$

for the vector current. We write the renormalized hard matching coefficient in the form

$$c_v = 1 + [\text{pure QCD}] + \frac{y_t^2}{2}\left[c_{vH}^{(2)} + \frac{\alpha_s}{4\pi}c_{vH}^{(3)}\right] + \dots. \tag{5.71}$$

In our convention, the results of [118] read

$$c_{vH}^{(2)} = \frac{1}{\pi^2}\left[\frac{3z-1}{12z} - \frac{2-9z+12z^2}{48z^2}\ln z + \frac{2-5z+6z^2}{24z}\Psi(z)\right], \tag{5.72}$$

with $z = m_t^2/m_H^2$ and

$$\Psi(z) = \begin{cases} \dfrac{\sqrt{4z-1}}{z}\arctan\sqrt{4z-1}, & z \geq 1/4, \\ \dfrac{\sqrt{1-4z}}{2z}\ln\dfrac{1-\sqrt{1-4z}}{1+\sqrt{1-4z}}, & z < 1/4. \end{cases} \tag{5.73}$$

$$c_{vH}^{(3)} = \frac{4C_F}{\pi^2}\Big[\frac{\pi^2}{8}(1-y)\ln\frac{m_t^2}{\mu^2} - 5.760 + 5.533y - 0.171y^2 + 0.0124y^3 + 0.0304y^4 + 0.0296y^5 + \ldots\Big], \tag{5.74}$$

with $y = 1 - z$. The approximate result $1b$ from [118] has been used for $c_{vH}^{(3)}$. It converges quickly for the physical Higgs boson mass and we neglect the truncation error, which we estimate to be well below one percent.

We can now compare the size of these corrections to the QCD contributions to assess the appropriateness of the power counting $y_t \sim \alpha_s$. The numerical result for the hard matching coefficient is given by

$$c_v = 1 - 0.103|_{\alpha_s} - 0.022|_{\alpha_s^2} + 0.031|_{y_t^2} - 0.070|_{\alpha_s^3} - 0.019|_{y_t^2\alpha_s} + \ldots, \tag{5.75}$$

where we have used $\alpha_s(\mu = 80\ \text{GeV}) = 0.1209$. The coupling orders for the various contributions are shown explicitly. The power counting is obviously justified here. Additionally, the Higgs potential (5.68) can be compared to its natural QCD counter-part, the local QCD contribution to the potential. This is the spin-projected QCD NNLO Darwin potential $\delta V_D = 8\pi\alpha_s C_F/(3m_t^2) = 1.35/m_t^2$, where we have used the numerical value for α_s from above. The Higgs potential $\delta_H V = -0.98/m_t^2$ is only slightly smaller, but we believe that our counting is valid because the Darwin potential itself is only a small correction compared to the overall NNLO QCD effect.

5.3.2. Potential contributions

The NNNLO correction to the non-relativistic S-wave Green function due to the Higgs potential (5.68) has the form

$$\delta_H G(E) = \langle \mathbf{0}|\, \hat{G}_0(E)\, i\delta_H V\, i\hat{G}_0(E)\, |\mathbf{0}\rangle = -\delta_H V\, G_0(E)^2, \tag{5.76}$$

where $G_0(E)$ is the LO Green function (3.46), evaluated at $\mathbf{r} = \mathbf{r}' = 0$. The Green function $G_0(\mathbf{r}, \mathbf{r}', E)$ describes the propagation of a non-relativistic top-pair in the presence of the

leading order Coulomb potential. The square of G_0 appears in (5.76) because the top pair is produced by a local current, then interacts via the local Higgs potential, i.e. is produced and annihilated at zero spatial separation, and is finally annihilated by a local current.

The real part of the LO Green function (3.46) contains a $1/\epsilon$ pole of UV origin from the one-gluon exchange diagram. This implies that G_0^2 contains a pole in the imaginary part. Explicitly, the divergence in the imaginary part of the Higgs correction reads

$$\mathrm{Im}\left[\delta_H G(E)\right]\big|_{\mathrm{div}} = \frac{y_t^2}{m_H^2}\frac{m_t^2\alpha_s C_F}{16\pi\epsilon}\,\mathrm{Im}\left[G_0(E)\right]. \tag{5.77}$$

We note that, as it stands, (5.77) also contains an unknown finite part from the $\mathcal{O}(\epsilon)$ terms in the imaginary part of G_0. However, in the Higgs contribution to the spectral function the combination $\mathrm{Im}[(c_v\widetilde{Z}_v^{-1})^2 G(E)]$ appears and the divergence (5.77) is canceled by the renormalization constant (5.70). This cancellation also extends to the unknown finite terms mentioned above. In the NNLO QCD part, an analogous cancellation happens between the divergent part of the single insertion of the QCD Darwin potential and part of the two-loop QCD contribution to the renormalization constant of the vector current $\widetilde{Z}_v$. Thus, it is sufficient to consider the minimally subtracted Green function

$$\delta_H G_{\mathrm{fin}}(E) = \frac{y_t^2}{2m_H^2}\left(\frac{m_t^2\alpha_s C_F}{4\pi}\left[L_\lambda + \frac{1}{2} - \frac{1}{2\lambda} - \hat{\psi}(1-\lambda)\right]\right)^2, \tag{5.78}$$

and the renormalized hard matching coefficient.

Similar to our discussion for the P wave in Section 5.2.3, one can resum the Higgs contributions to the poles of the S-wave Green function, which correspond to ${}^3S_1$ toponium bound states. Near these poles, the S-wave Green function has the form

$$G(E) \overset{E\to E_n}{\longrightarrow} \frac{|\psi_n(0)|^2}{E_n - E - i\epsilon}, \tag{5.79}$$

with the energy levels E_n and squared wave functions at the origin $|\psi_n(0)|^2$. We parametrize Higgs corrections in the following way:

$$\begin{aligned} E_n &= E_n^{(0)}\left(1 + [\text{pure QCD}] + \frac{\alpha_s}{4\pi}\frac{y_t^2}{2}e_H\right), \\ |\psi_n(0)|^2 &= |\psi_n^{(0)}(0)|^2\left(1 + [\text{pure QCD}] + \frac{\alpha_s}{4\pi}\frac{y_t^2}{2}f_H\right), \end{aligned} \tag{5.80}$$

where

$$E_n^{(0)} = -m_t\left(\frac{\alpha_s C_F}{2n}\right)^2, \qquad |\psi_n^{(0)}(0)|^2 = \frac{1}{\pi}\left(\frac{m_t\alpha_s C_F}{2n}\right)^3. \tag{5.81}$$

As described in Section 5.2.3, the higher order perturbative corrections to the Green function contain knowledge of the corrections to the bound state. We can determine e_H, f_H

from a comparison of the expansions of (5.78) and (5.79) around the bound-state energies, or equivalently an expansion for λ near positive integer values n. We obtain

$$\delta_H G_{\rm fin}(E) = \frac{y_t^2}{2m_H^2}\frac{m_t^4\alpha_s^2 C_F^2}{16\pi^2}\left[\frac{1}{(n-\lambda)^2}+\frac{2}{n-\lambda}\left(L_n+\frac{1}{2}-\frac{1}{2n}-\hat{\psi}(n)\right)+\ldots\right], \quad (5.82)$$

where $L_n = \log(n\mu/(m_t\alpha_s C_F))$ and regular terms in the limit $\lambda \to n$ have been discarded. We find

$$e_H = \frac{m_t^2 C_F}{m_H^2}\frac{2}{n}, \qquad f_H = \frac{m_t^2 C_F}{m_H^2}\left(2L_n+1+\frac{4}{n}-2S_1(n)\right), \quad (5.83)$$

where $S_1(n) = \sum_{k=1}^n k^{-1}$ is the nth harmonic number of order one. Our expressions agree with the results for the energy levels and the $\Upsilon(1S)$ wave function in [118].

5.3.3. Combined Higgs effects

Having collected all the parts, we can give expressions for the complete NNNLO Higgs corrections to the cross section, with the exception of the tiny corrections involving Higgs-gauge boson couplings. The NNLO correction to the vector correlation function (3.20) reads

$$\delta_{2H}\Pi^{(v)} = \frac{3}{2m_t^2} y_t^2 c_{vH}^{(2)} G_0(E), \quad (5.84)$$

and the NNNLO correction is given by

$$\delta_{3H}\Pi^{(v)} = \frac{3}{2m_t^2}\left[\frac{\alpha_s}{4\pi} y_t^2 (c_{vH}^{(3)} + c_{vH}^{(2)} c_1) G_0(E) + y_t^2 c_{vH}^{(2)} \delta_1 G(E) + \delta_H G_{\rm fin}(E)\right]. \quad (5.85)$$

It also contains mixed NNLO Higgs and NLO QCD terms. The NLO QCD contributions to the Green function and the hard-matching coefficient have been written in the usual parametrization $G(E) = G_0(E) + \delta_1 G(E) + \ldots$ and $c_v = 1 + \alpha_s c_1/(4\pi) + \ldots$. The Higgs contribution to the top-pair production cross section has the form

$$\sigma_H = 12\pi\sigma_0 \left(C^{(v)^2} + C^{(a)^2}\right) \mathrm{Im}\left[\delta_{2H}\Pi^{(v)}(q^2) + \delta_{3H}\Pi^{(v)}\right]. \quad (5.86)$$

6. Phenomenology of top-pair production near threshold

In this section, we present a phenomenological survey of the threshold scan of top-pair production from a theory perspective. Several experimental simulations [26, 138, 139] have found that the statistical uncertainties are tiny in realistic running scenarios at future linear colliders. First results from an experimental study [140] based on the theory prediction available in `QQbar_threshold` [29] have recently become available and have given a first combined account of the achievable accuracy. Therefore, we focus solely on the theory prediction and its uncertainty.

To avoid the IR renormalon ambiguities discussed in Section 2, we exclusively employ the PS Shift (PSS) mass scheme throughout this section. It is defined by

$$\sigma^{\rm PSS}(\sqrt{s}, m_t^{\rm PS}) = \sigma^{\rm pole}(\sqrt{s}, m_t^{\rm PS} + \delta m_t), \tag{6.1}$$

where the order of the pole-PS mass relation δm_t is correlated with the order of the prediction. One could also expand the right-hand side in $\delta_i m_t \sim m_t \alpha_s^{2+i}$ with $i \geq 1$, which defines the PS Insertion (PSI) scheme introduced in [89]. As discussed there, this leads to unphysical behaviour close to threshold and is therefore not considered below. It is mandatory to resum the resonance poles in the Green function to achieve renormalon cancellation in the PSS scheme. We do this for the first six poles following the procedure outlined in Section 3.3.

For the numerical evaluation we adopt the input values

$$\begin{array}{lll} m_t^{\rm PS} = 171.5\,{\rm GeV}, & \alpha_s(m_Z) = 0.1184, & \alpha(m_Z) = 1/128.944 \\ m_H = 125\,{\rm GeV}, & m_Z = 91.1876\,{\rm GeV}, & m_W = 80.385\,{\rm GeV}, \\ \Gamma_t = 1.33\,{\rm GeV}, & \mu_r = 80\,{\rm GeV}, & \mu_w = 350\,{\rm GeV}, \end{array} \tag{6.2}$$

where the running electroweak coupling is taken from [126], see the discussion in Section 5.1.3.

6.1. Analysis of non-QCD contributions

We first consider the P-wave contribution to the total cross section. Our results at LO and NLO are shown in Figure 6.1. Compared to the S-wave, the overall effect is below 1% in the threshold region because on top of the v^2 suppression of the P-wave, the ratio of the

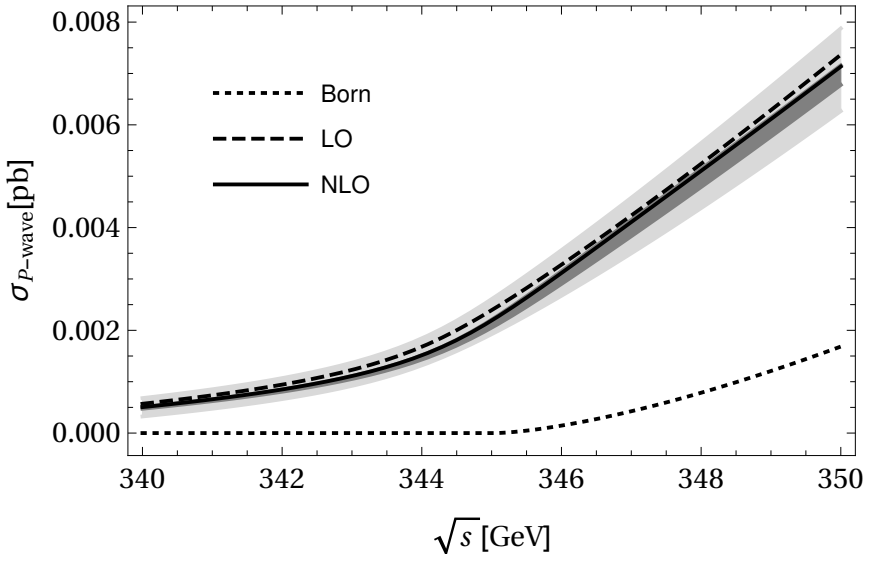

Figure 6.1.: The P-wave contribution to the cross section in pb. We used the PSS scheme with the parameter values of (6.2). The dashed and solid lines are the LO and NLO results, respectively. Due to the v^2 suppression of the P-wave, they contribute at NNLO and NNNLO to the total cross section. The shaded regions indicate the respective uncertainties from variation of μ_r between 50 GeV and 350 GeV. The dotted line denotes the Born-level result, where the Coulomb singularities are not resummed.

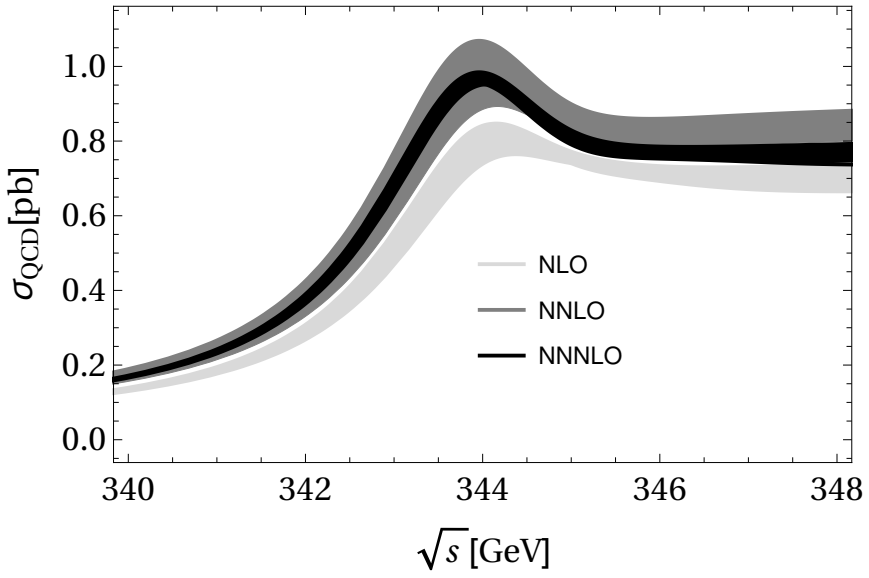

Figure 6.2.: The full QCD cross section up to NNNLO, including the small P-wave contribution. The bands are spanned by variation of μ_r between 50 GeV and 350 GeV.

couplings $(v_e^2 + a_e^2)a_t^2/e_t^2 \approx 0.28$ is small.[1] The shaded bands are determined by variation of the renormalization scale μ_r between 50 GeV and 350 GeV, while keeping $\mu_w = 350\,\text{GeV}$ fixed. The μ_w dependence is related to uncanceled finite-width divergences in the pure-QCD result and will be discussed below.

There is very good convergence between the LO and NLO P-wave results and the dependence on the renormalization scale is greatly reduced. Thus, we can conclude, that perturbation theory works well already at low orders for the P-wave contribution. The comparison with the Born result (dotted curve in Figure 6.1) shows the importance of Coulomb resummation, similar to the observation made for the S-wave result in Figure 1.5. However, the P-wave does not develop a visible resonance peak because the sizeable top-quark width completely smears out the small residue of the lowest $n = 2$ P-wave bound state.

We define a reference QCD prediction by adding the small P-wave contribution to the S-wave result of [28]. The result is shown in Figure 6.2, where the uncertainty bands are again due to variation of the renormalization scale. The conclusions of [28] are unchanged by this. On the basis of this reference QCD result, we show the effect of non-QCD corrections in Figure 6.3.

In the top-panel we show the relative effect of the Higgs contribution σ_H at NNLO and NNNLO. At NNLO there is an almost constant relative shift because only the hard-matching coefficient $c_{vH}^{(2)}$ is present. At NNNLO, it is partially compensated by the negative mixed Higgs-QCD corrections like $c_{vH}^{(3)}$. Furthermore, there is a contribution from the local Higgs potential, which modifies the position of the peak. Due to the attractive nature of the potential, the binding energy is increased and the peak is shifted to the left. At the same time the Higgs corrections increase the cross section by $4 - 8\%$, depending on the value of $\sqrt{s}$, and make the peak more pronounced.

The effects from the remaining electroweak contributions $\sigma_{\delta V_{\text{QED}}}$, σ_Γ, $\sigma_{C_{\text{EW}}^{(k)}}$ and $\sigma_{C_{\text{Abs,bare}+Z_t}^{(k)}}$ to the "partonic" resonant cross section are shown in the middle panel. The dashed line corresponds to the correction from the QED Coulomb potential only. It is attractive and therefore leads to an increase of the cross section by $2 - 8\%$ and a shift of the peak towards a smaller center-of-mass energy. The solid line shows the full correction. The width contribution σ_Γ changes the cross section by only $(-0.6) - (0.4)\%$. Including the real part of the electroweak matching coefficient leads to an almost constant relative shift of about -4%. The absorptive part of the matching coefficient multiplies the real part of the non-relativistic Green function, which has a broad peak, roughly centered around the point where the imaginary part has its maximal slope, on top of a smooth background. Thus, the absolute contribution has only a mild energy dependence and is of the order of $-(6-8)\%$ near and above the peak. However, it becomes even more important below the peak, where the cross section is small and it modifies the result by up to -18%.

The lower panel illustrates the behaviour of the non-resonant contribution to the total cross section. Its absolute size is nearly energy-independent. Thus, the shape of the curves

[1] However, it may be possible to extract the P-wave contribution experimentally using different beam polarizations, see [93].

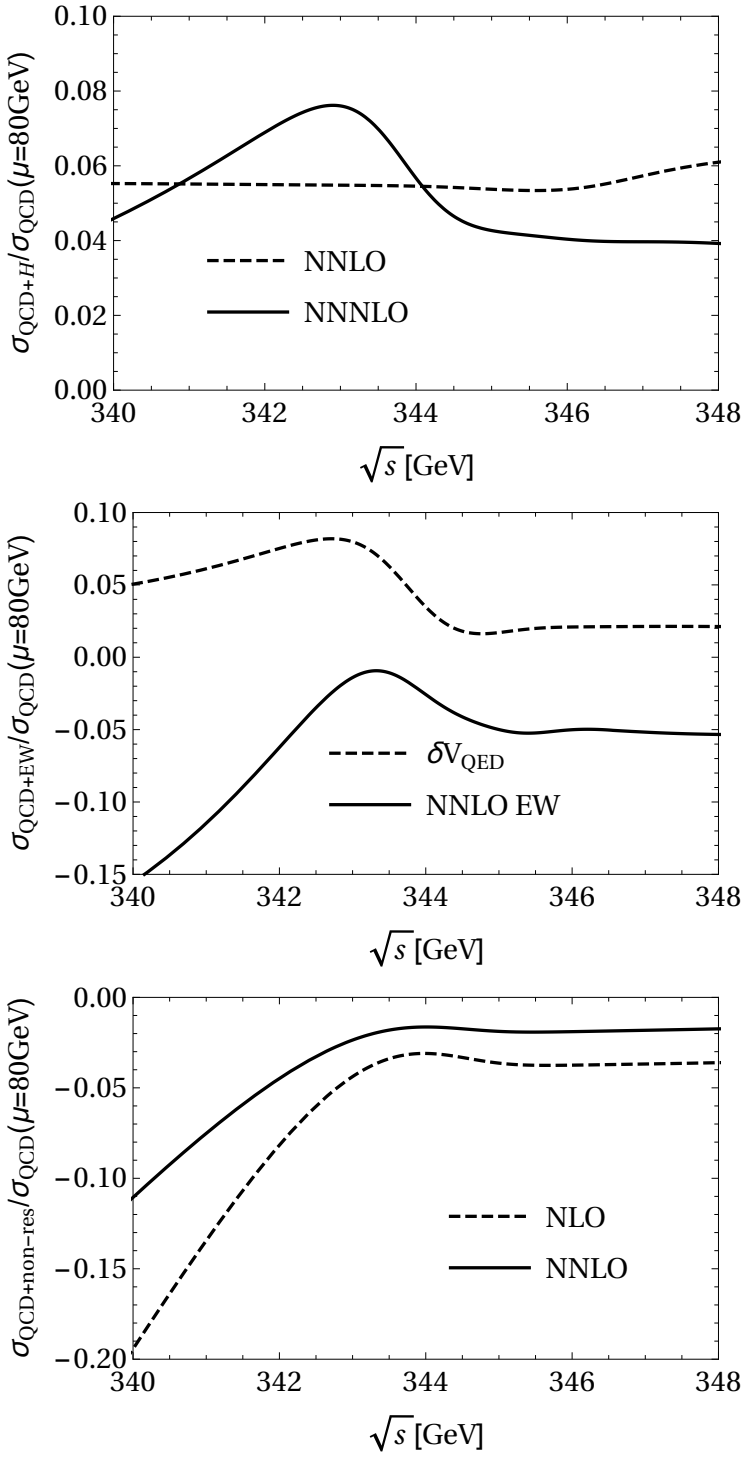

Figure 6.3.: Relative corrections to the QCD cross section from Higgs effects (top), electroweak effects (middle) and the non-resonant contribution (bottom).

is given by the inverse of the QCD cross section. At NLO, the effect is of the order $-(3-4)\%$ near and above the peak and reaches up to -20% for low center-of-mass energies, where the resonant cross section becomes small. The NNLO corrections compensate about half of the NLO result. This is in contrast to the findings of [98,99], where an enhancement of the negative non-resonant correction from an approximate NNLO result was observed. The apparent discrepancy is, however, entirely explained by the vastly different scale choices made in [98, 99] ($\mu_w = 30\,\text{GeV}$) and here ($\mu_w = 350\,\text{GeV}$). The dependence of the full result on μ_w is very mild as discussed below and, thus, mainly the size of the individual contributions (most notably the non-resonant correction and the one from the absorptive part of the hard matching coefficients) is affected.

The net effect of all the corrections barring ISR is shown in Figure 6.4. The non-QCD effects chisel out the peak, whose height is slightly increased and which moves towards smaller center-of-mass energies. Above the peak the cross section is slightly decreased by $-(2-3\%)$. The largest effect is observed below the peak, where the absorptive parts of the matching coefficients and the non-resonant contribution dominate the non-QCD corrections. Here, the bands cease to overlap at around $\sqrt{s} = 341.5\,\text{GeV}$. The size of the uncertainty band is slightly increased and now reaches almost $\pm 5\%$ directly below the peak, where the uncertainty estimate for the QCD result is $\pm 3.8\%$. In the remaining regions it is however of the size of $\pm 3\%$. The increase of the scale uncertainty is mainly due to the Higgs potential insertion.

We recall that the bands only include the variation of the renormalization scale between 50 GeV and 350 GeV, while the scale $\mu_w = 350\,\text{GeV}$ is kept fixed. The dependence on the scale μ_w cancels exactly between all contributions of a given order. We show the μ_w dependence of the resonant cross section and the full cross section in Figure 6.5. For the resonant-only cross section, it is mild near and above the peak, but is significantly larger than the renormalization scale dependence blow the peak. The sensitivity to μ_w is greatly reduced for the full cross section, where the variation by a factor of 14 considered in the plots only yields a $\pm 0.3\%$ effect near and above the peak and only a mild $\pm 2\%$ below the peak. The remaining μ_w dependence is of NNNLO, where the full QCD corrections, but only a few electroweak effects are considered and therefore no full cancellation is achieved.

We have discussed the possibility of imposing loose cuts, which only affect the non-resonant part of the cross section, in Section 4. The dependence on the cut defined in (4.2) is shown in Figure 6.6, where the dotted and solid lines denote the NLO and NNLO non-resonant contribution. Very loose cuts with $\Delta M_t \geq 30\,\text{GeV}$ have only a mild influence on the cross section. More tight cuts $\Delta M_t = (30, 20, 10, 5)\,\text{GeV}$ reduce the cross section by $(0.007, 0.014, 0.038, 0.086)\,\text{pb}$. We observe that for ΔM_t around 4 GeV the NNLO non-resonant contribution becomes as large as the NLO one. Here, the assumption that the cut is loose is no longer appropriate and our description breaks down. It is however unimpaired for $\Delta M_t \gtrsim 6\,\text{GeV}$.

The dashed line in Figure 6.6 shows the approximate NNLO result [98], which includes only the endpoint divergent terms, for comparison. It describes the dependence on the cut very well, since the endpoint divergent terms are most sensitive to it, but it is shifted by -0.006 pb for the full cross section and up to -0.009 pb in the presence of invariant mass cuts.

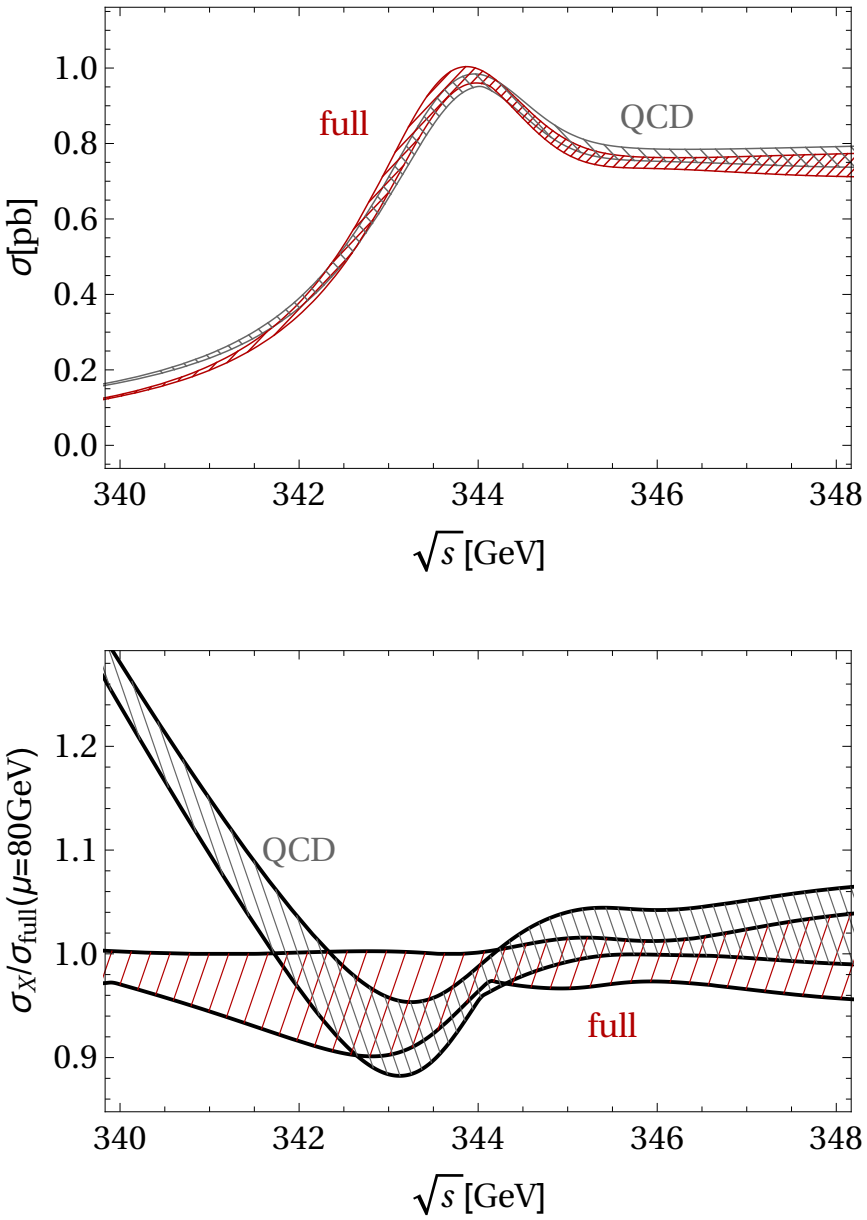

Figure 6.4.: The cross section including the corrections from Figure 6.3 (red hatched band) and in pure QCD (gray hatched band). The bands represent the uncertainty from scale variation. The upper panel shows the cross section in pb and the lower panel shows the results normalized to the full one for the central scale $\mu_r = 80\,\text{GeV}$.

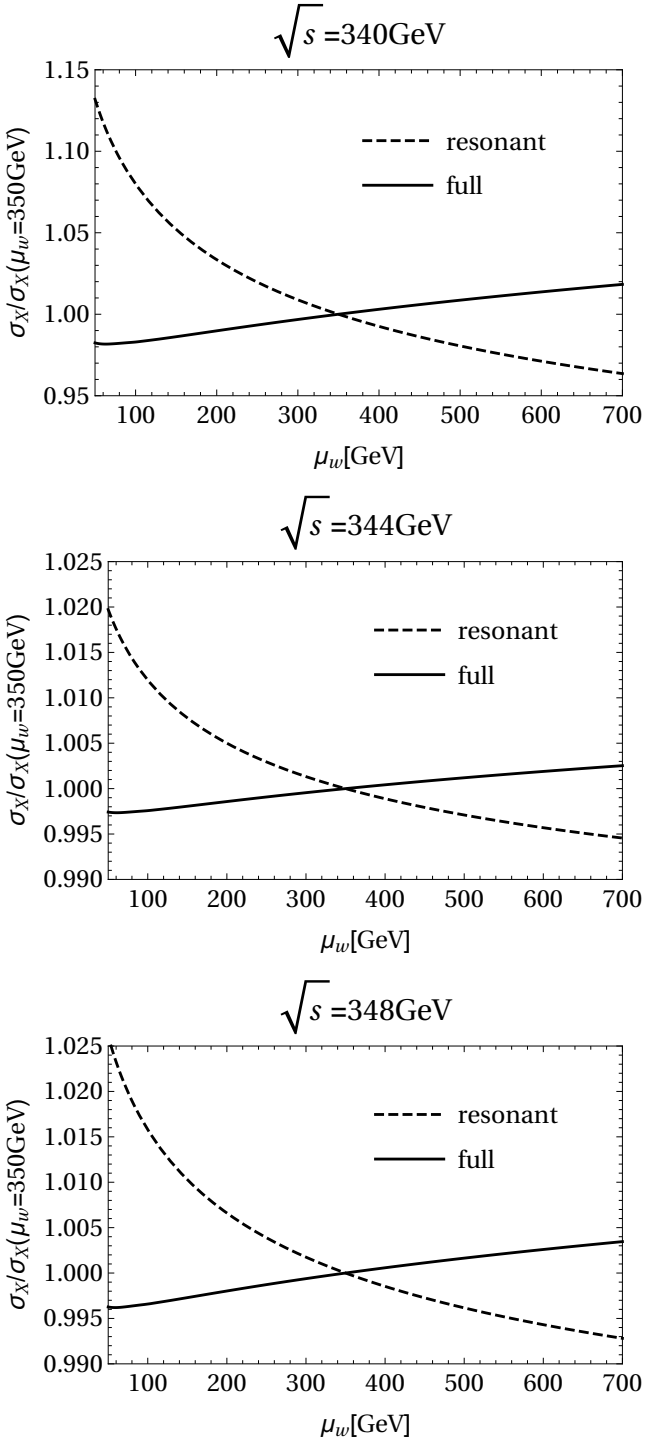

Figure 6.5.: Dependence of the resonant-only and full cross section on the scale μ_w normalized to the one at $\mu_w = 350\,\text{GeV}$ for $\sqrt{s} = 340\,\text{GeV}$ (top panel), $\sqrt{s} = 344\,\text{GeV}$ (middle panel) and $\sqrt{s} = 348\,\text{GeV}$ (bottom panel).

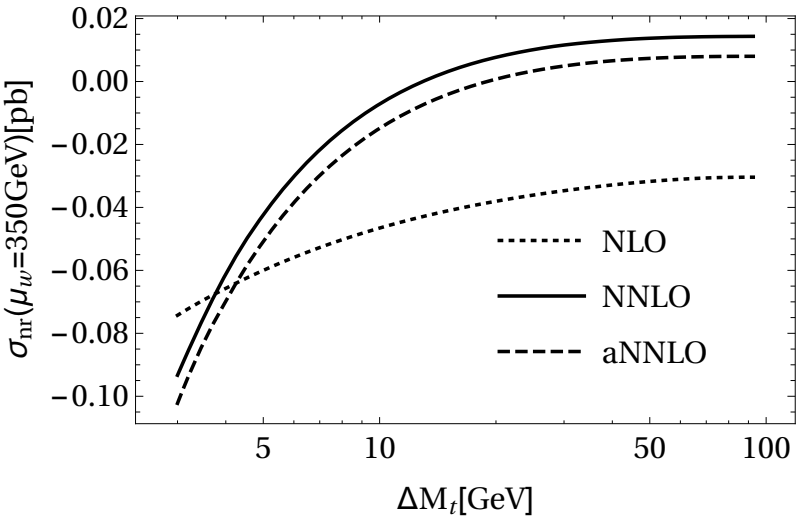

Figure 6.6.: The dependence of the non-resonant contribution to the cross section on the invariant mass cut (4.2). The dotted line shows the result at NLO and the solid line the NNLO correction (without the NLO terms). The dashed line denotes the approximate NNLO result from [98]. The full cross section corresponds to $\Delta M_t = m_t - m_W$.

In the absence of any cuts the exact result corresponds to a 75% correction with respect to the approximate NNLO result. We note, however, that for the scale choice of [98] and in the range of loose, but not too loose, cuts $\Gamma_t \ll \Delta M_t \ll m_t$ the approximation is much better.

We finally discuss the effects of initial state QED radiation, which have so far only been taken into account in the experimental studies. Figure 6.7 shows the overall effect from $\sigma_{\rm IS}^{\rm conv}$ and the convolution with the electron structure functions. The former is a small effect of the order $-(0.4 - 1.5)\%$. For the latter we have not used (5.26), but the numerically less expensive relation

$$\sigma(s) = \int_0^1 dx \left(\Gamma_{ee}^{\rm LL}(x)\big|_{\beta\to 2\beta} \right) \hat{\sigma}^{\rm conv}(xs) \tag{6.3}$$

from [128, 130], which is LL accurate. The black band is spanned by four different implementations of the convolution of the full NNNLO QCD plus NNLO EW cross section according to (6.3). This involves an extrapolation of the cross section for energy values outside of the range of the grids available in `QQbar_Threshold` [29]. We either use the shape of the LO cross section below $\sqrt{s} = 328\,\text{GeV}$, rescaled to match the full result at $\sqrt{s} = 328\,\text{GeV}$, or an alternative implementation that interpolates linearly between $\sigma(\sqrt{s} = 320\,\text{GeV}) = 0\,\text{pb}$ and our result at $\sqrt{s} = 328\,\text{GeV}$. Numerically, we find a small difference of 0.2% near and above the peak, which goes up to 1.3% at $\sqrt{s} = 340\,\text{GeV}$. For both implementations we consider the structure functions with and without the constant

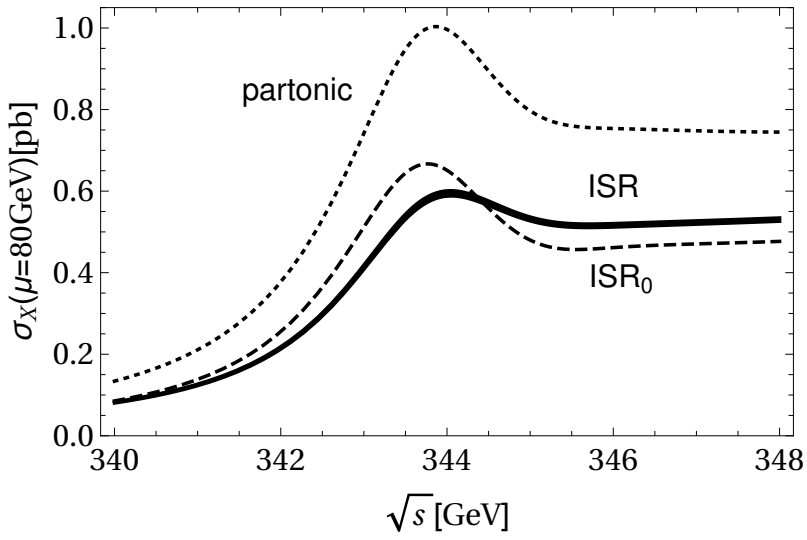

Figure 6.7.: The effect of initial state QED radiation on the cross section. The dotted curve shows the full partonic result. The solid band (ISR) is the envelope of results obtained by convoluting the full partonic result with the structure functions with different systematics (see text). The dashed line (ISR_0) is obtained by convoluting only the leading order partonic cross section with the structure function and adding the full partonic corrections on top.

term in $\beta_{\mathrm{exp}} = \beta_{\mathrm{S}} = \beta_{\mathrm{H}} = -(2\alpha/\pi)(\ln(z)+1)$. As discussed in Section 5.1.5, the difference yields a rough estimate for the order of the missing NLL terms. It is in the range of $1.3 - 2.2\%$, but we cannot exclude larger corrections.

For comparison we furthermore show the result

$$\sigma_{\mathrm{ISR}_0}(s) = \hat{\sigma}^{\mathrm{full}}(s) - \hat{\sigma}^{\mathrm{LO}}(s) + \int_0^1 dx \left(\Gamma_{ee}^{\mathrm{LL}}(x)\big|_{\beta\to 2\beta}\right) \hat{\sigma}^{\mathrm{LO}}(xs) \tag{6.4}$$

denoted by the dashed line. Formerly, the difference is a $\mathrm{N}^{1/2}\mathrm{LL}$ effect. Due to the sizeable higher-order corrections to the cross section it is, however, substantial. Thus, it is mandatory to evaluate (6.3) for the full partonic result.

The effects of ISR are huge, reducing the cross section by $30 - 45\%$. It also leads to a significant modification of the shape. The peak is shifted by almost 200 MeV to the right and smeared out considerably. Its height is reduced by about 40%. This emphasizes the need for a full NLL treatment of ISR and a proper analysis of the convergence and remaining uncertainty, which is of universal importance for e^+e^- collider processes, but is beyond the scope of this work.

6.2. Sensitivity to SM parameters

The comparison of the theoretical prediction for the top-quark pair production cross section to the experimental results from a future lepton collider can be used to extract precise values for several standard model parameters. The most characteristic features are the steep rise and peak of the cross section. Figure 6.8 shows the impact of the non-QCD corrections on the peak (upper panel) and maximum slope (lower panel). However, we do not take the effects of ISR into account for the discussion in this section since the important NLL corrections are presently unknown. The error bar is obtained by adding the uncertainties from renormalization scale variation between 50 GeV and 350 GeV and variation of $\alpha_s(m_Z)$ by ± 0.001 in quadrature, while the inner bar only captures the uncertainty from the strong coupling.

The Higgs contributions shift the peak by $-35\,\text{MeV}$ and increase its height by 6%. The remaining electroweak corrections cause an additional shift of $-50\,\text{MeV}$. The QED Coulomb potential enhances the height of the peak, but is overcompensated by the negative electroweak contribution to the matching coefficients of the production and annihilation operators, such that the height is reduced by -1.9%. The non-resonant contribution is nearly energy-independent and therefore leaves the position of the peak unchanged, while reducing its height by -1.6%. The effect of the non-QCD effects on the extracted value of the top-quark mass is essentially determined by half of the shift of the peak position, which yields $-42\,\text{MeV}$. This is of the same order as the expected theory uncertainty and demonstrates the importance of taking these contributions into account. Overall the corrections enhance the absolute height of the peak only marginally, but they also decrease the normalization of the "background", such that the peak becomes more pronounced.

The position of maximal slope experiences almost the same shifts as the peak. The maximal slope is however increased by 9.7%, mainly due to the Higgs contribution. The non-resonant contribution has no influence on the slope, since it is nearly energy-independent.

The top mass and width dependence of the cross section is shown in more detail in Figure 6.9. The upper panel demonstrates the effects due to variation of the top-quark PS mass by ± 50 and $\pm 100\,\text{MeV}$. The shape of the corresponding curves corresponds mainly to a shift of the cross section by $2\delta m_t$ in $\sqrt{s}$. The cross section is most sensitive to the mass about 1.5 GeV below the peak, where we observe a change of $\pm 7\%$ for $\delta m_t^{\text{PS}} = \mp 50\,\text{MeV}$. Since the respective scale uncertainty is slightly below $\pm 5\%$, we may expect that the theory uncertainty on the top-quark mass determination is even below $\pm 50\,\text{MeV}$.

The sensitivity to the top width is considered in the lower panel, where we study shifts $\delta\Gamma_t$ of $\pm 100\,\text{MeV}$. Since the top width is responsible for the "smearing" of the would-be toponium resonances, the peak becomes narrower and more pronounced for a decrease of Γ_t. The opposite happens for an increase in the width. The variation by $\pm 100\,\text{MeV}$ leads to curves well outside of the uncertainty band, which shows that the expected theory uncertainty on the determination of the top-quark width is significantly below 100 MeV.

The threshold scan further offers an important consistency check for the SM from the measurement of the top-quark mass and Yukawa coupling in the same process. In the SM the fermion masses and Yukawa couplings are connected by $y_f = \sqrt{2} m_f / v$. Any significant

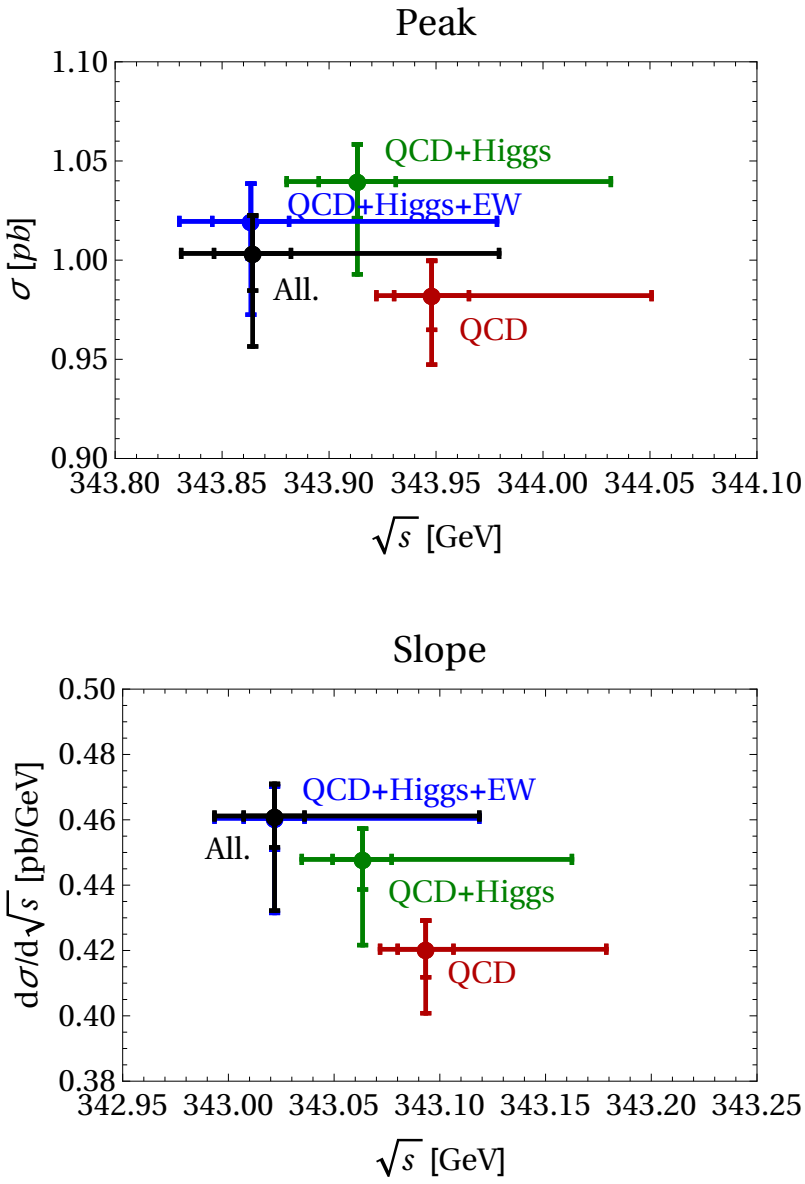

Figure 6.8.: The peak position and peak height (upper panel) of the cross section for QCD-only (red), QCD+Higgs (green), QCD+Higgs+EW (blue) and including all contributions barring ISR (black). The uncertainty is determined by the quadratic sum of the errors from renormalization scale variation and variation of $\alpha_s(m_Z)$ by ± 0.001. The size of the latter is indicated by the inner error bars. The lower panel shows the maximum slope using the same conventions.

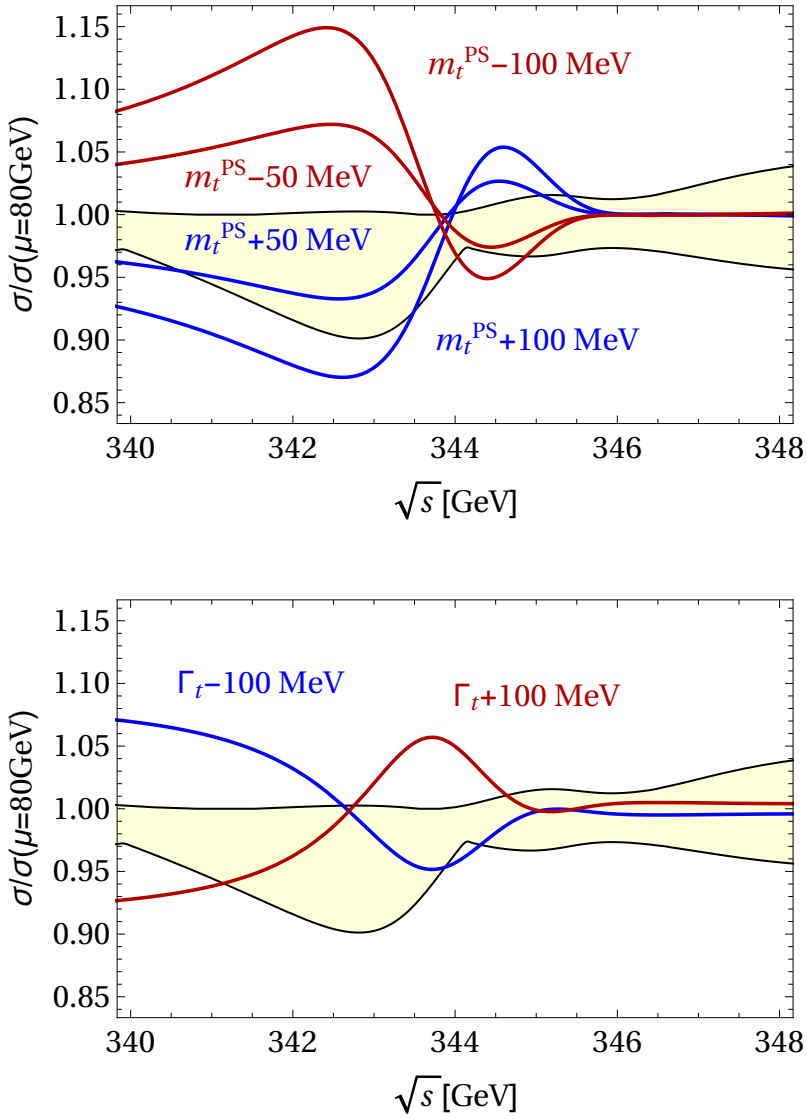

Figure 6.9.: The cross section for the input values (6.2) up to variations of the top mass (top panel) and top width (bottom panel) is shown in comparison to the uncertainty band from scale variation (cf. Figure 6.4). The prediction is normalized to the full cross section with (6.2).

deviation from this relation would be an unambiguous signal for new physics and provide important insight into the mechanism of electroweak symmetry breaking in nature. This is particularly interesting for the top quark because it is by far the most massive fermion in the SM and many new-physics explanations have been invoked to try to explain this happenstance. Such a deviation can, for example, be caused in the model-independent[2] framework of the dimension-six effective Lagrangian [141, 142]. To demonstrate this, we consider the operator

$$\Delta\mathcal{L} = -\frac{c_{\mathrm{NP}}}{\Lambda^2}(\phi^\dagger\phi)(\bar{Q}_3\widetilde{\phi}t_R) + \mathrm{h.c.}, \tag{6.5}$$

where $\widetilde{\phi} = i\sigma^2\phi^*$, c_{NP} is a new dimensionless coupling and $\Lambda \gg v$ is the scale of new physics. For simplicity, we have assumed that only the third generation is affected. After electroweak symmetry breaking, the operator yields corrections to the mass term and Yukawa term of the top,

$$\Delta\mathcal{L} \supset -\frac{c_{\mathrm{NP}}v^2}{2\sqrt{2}\Lambda^2}\left(v\bar{t}_Lt_R + 3h\bar{t}_Lt_R\right) + \mathrm{h.c.}, \tag{6.6}$$

where h denotes the physical Higgs field. The coefficients of the two terms differ by a factor three, which breaks the SM relation. We parametrize the correction with

$$\kappa_t \equiv \frac{y_t}{\sqrt{2}m_t/v} = 1 + \frac{c_{\mathrm{NP}}}{\Lambda^2}\frac{v^3}{\sqrt{2}m_t}, \tag{6.7}$$

where

$$m_t = \frac{v}{\sqrt{2}}\left(y_t^{\mathrm{SM}} + \frac{c_{\mathrm{NP}}v^2}{2\Lambda^2}\right) \quad \text{and} \quad y_t = y_t^{\mathrm{SM}} + \frac{3c_{\mathrm{NP}}v^2}{2\Lambda^2}. \tag{6.8}$$

The SM relation is recovered for $\kappa_t = 1$. We observe that this naturally leads to the κ-formalism that has been widely used to study Higgs couplings. It has also been demonstrated in [143] that there is a rigorous effective field theory justification for this formalism in general. The cross section is obviously also sensitive to other operators in the dimension-six Lagrangian – in particular those that cause further anomalous top couplings, e.g. to gluons. A complete treatment of these contributions is beyond the scope of this work.

We now apply our approach to study the sensitivity of the cross section to a rescaling of the Yukawa coupling y_t in the Higgs potential (5.68) and hard matching coefficients by non-unity values of κ_t. This is equivalent to the assumption that the top-quark mass and Yukawa coupling are independent parameters. The curves obtained for different values of κ_t are shown in Figure 6.10 in comparison to the scale uncertainty of the SM result. The results are normalized to the full cross section with $\mu_r = 80$ GeV. The overall normalization of the cross section changes due to the modification of the strength of the attractive Higgs potential, while the effect on the shape of the cross section is rather mild. Explicitly, we find an increase of the cross section by 5–10% for $\kappa_t = 1.5$ and a decrease of 3–5% for $\kappa_t = 0.5$, as well as shifts in the position of the peak by $-44\,\mathrm{MeV}$ and $+27\,\mathrm{MeV}$, respectively.

[2] Assuming new physics are heavy!

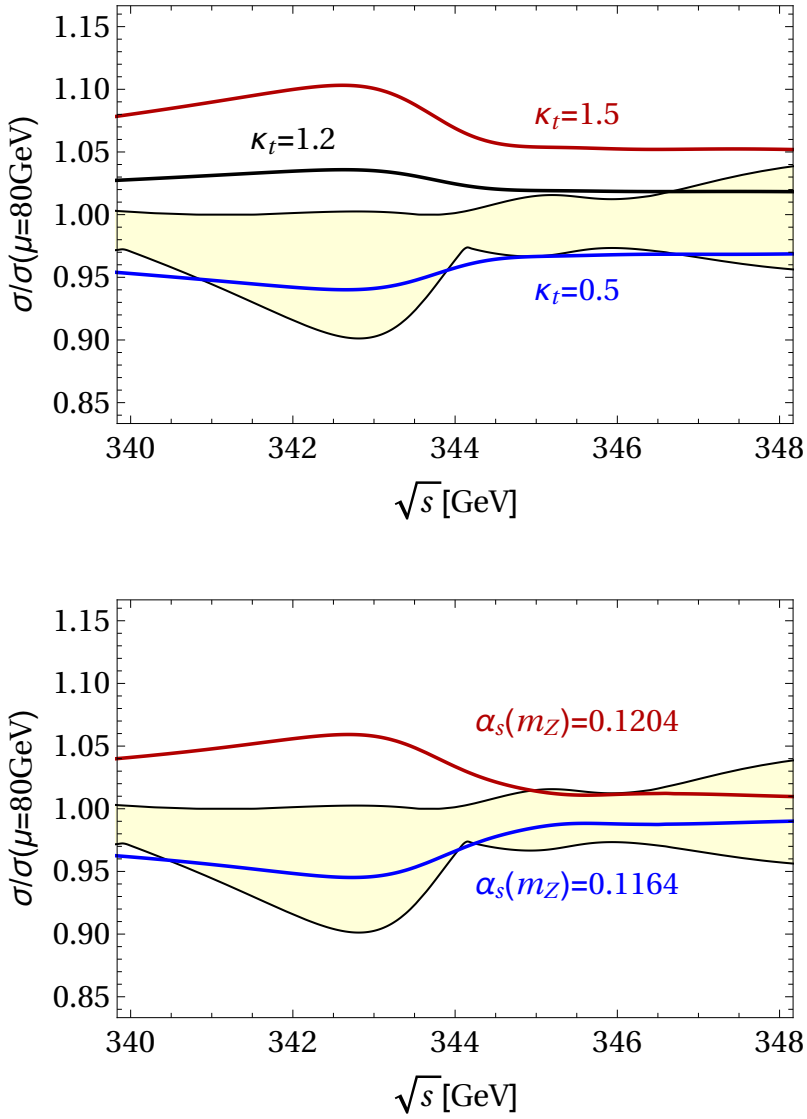

Figure 6.10.: The sensitivity of the cross section to variations of the Yukawa coupling (upper panel) and the strong coupling (lower panel). The uncertainty band is the same as in Figure 6.9. The prediction is normalized to the full cross section with the input values (6.2).

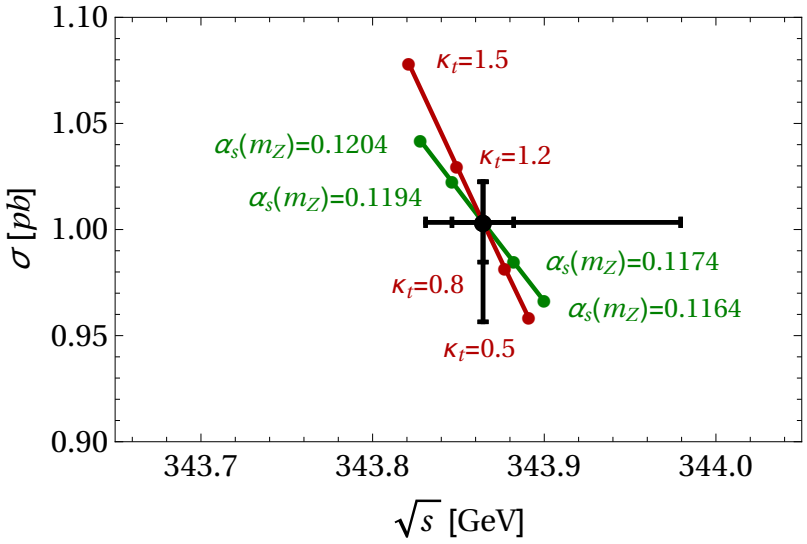

Figure 6.11.: The effect of the variation of the Yukawa coupling (red line) and the strong coupling (green line) on the position and height of the peak. The outer error bar is obtained by adding the uncertainties from the renormalization scale and variation of $\alpha_s(m_Z)$ by ± 0.001 in quadrature, while the inner bar shows only the latter contribution (cf. upper plot in Figure 6.8).

We can get a first estimate for the theoretical uncertainty in a determination of y_t by comparing the effect of the variations of κ_t to the theory uncertainty from variation of the renormalization scale μ_r. The curves lie only outside the band for rather large deviations from the SM Yukawa coupling of roughly $+20\%$ or -50%. A more detailed analysis that also takes the shape of the curve into account may however reveal that there is better sensitivity.

We note that the variation of the strong coupling constant shown in the lower panel of Figure 6.10 has a very similar effect as the variation of κ_t, although the energy dependence of the effect is somewhat different. The red curve, corresponding to $\alpha_s(M_Z) = 0.1204$, lies $1-6\%$ above our central prediction and the blue curve, corresponding to $\alpha_s(M_Z) = 0.1164$, lies $-(1-5)\%$ below. The partial degeneracy of the two effects is also apparent for the position and height of the peak as shown in Figure 6.11. Without a full-fledged analysis of the energy dependence it remains unclear to what degree the effects can be disentangled. Thus, it is also not settled to which degree the measurement of the top-quark Yukawa coupling and the strong coupling from a simultaneous fit is impaired by the degeneracy. One may however use $\alpha_s(m_Z)$ from other sources as an input and determine y_t in this way. Even with the present uncertainty of the order of ± 0.001, the $\alpha_s(m_Z)$ uncertainty is significantly smaller than the scale uncertainty. Assuming an improvement by a factor of two by the time a linear collider becomes available, we find that the added uncertainty on the determination of y_t is marginal.

The authors of [139] conclude that the top Yukawa coupling can be determined with

a statistical uncertainty of only 4.2% in a threshold scan. Their analysis is based on the assumption that the SM Higgs effects lead to an energy-independent increase of the cross section by 9%, which is somewhat at odds with our findings based on a rigorous treatment. Both the theoretical uncertainty of the cross section and the correlation with the strong coupling constant have not been considered in [139]. Our discussion shows that it is unlikely that the Yukawa coupling can be obtained with such high accuracy in a threshold scan. At a future linear collider, it can however also be determined from the cross section for $t\bar{t}h$ with an estimated uncertainty of 10% or 4% at $\sqrt{s} = 500\,\text{GeV}$ or $\sqrt{s} = 1\,\text{TeV}$, respectively [144], in which case the extraction of the Yukawa coupling from a threshold scan would still provide an important independent check.

6.3. Top-pair production in photon collisions

Our results for the P-wave Green function are also of interest beyond their tiny contribution to the total cross section for top-pair production in e^+e^- collisions. It is for example possible to produce top pairs in a pure P-wave state in photon collisions by adjusting their helicities to be opposite. A lepton collider can be converted into a high-energy photon collider via the back-scattering method [145]. This idea was considered in the Technical Design Report for TESLA [146] and is also discussed as an option for the ILC (see Sec. 12.6 of [147]). With opposite photon helicities, the cross section takes the form [91, 92]

$$\sigma_\gamma^{+-} \equiv \sigma_{\gamma\gamma\to t\bar{t}X}^{+-} = \frac{32\pi N_c e_t^4}{m_t^4}\, C_h^{+-}(\alpha_s)\,\text{Im}\left[G^P(E)\right], \tag{6.9}$$

near threshold. The hard matching coefficient is only known in four dimensions

$$C_h^{+-}(\alpha_s) = 1 - 16 C_F \frac{\alpha_s}{4\pi}. \tag{6.10}$$

Therefore, we subtract the finite-width divergences minimally in the P-wave Green function. The corresponding scheme and scale dependence can be cured by taking non-resonant effects into account.

Our results in the PSS scheme are shown in Figure 6.12. The cross section is larger than the P-wave contribution in e^+e^- collisions by an order of magnitude because of the different size of the involved couplings and numerical prefactors. Otherwise, its features are very similar. In particular, the substantial reduction of the scale uncertainty at NLO is also observed here, which is apparent from the (hardly visible) width of the dark-shaded band in Figure 6.12. Due to the different hard matching coefficient the NLO correction to the cross section is somewhat larger here, but the NLO band is still completely contained in the LO one.

The cross section (6.9) has previously been computed in [91, 92], where the scheme-dependent finite-width terms have been determined by matching the resonant contribution to the full theory diagram with an off-shell top decay. This approach captures the part of the non-resonant contributions, that dominates the respective non-resonant contribution

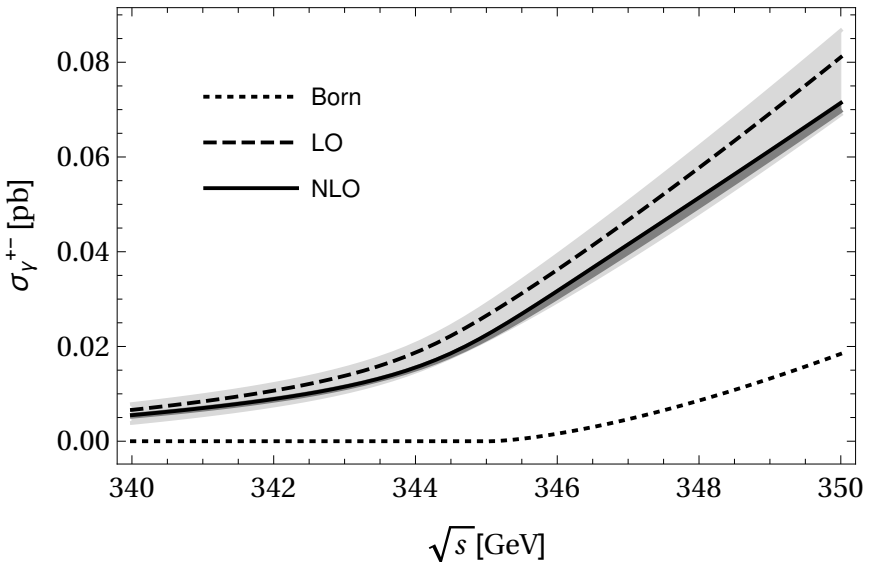

Figure 6.12.: The top-pair production cross section σ_γ^{+-} in collisions of photons with opposite helicities at LO (dashed) and NLO (solid). We adopt the same coding as in Fig. 6.1.

in e^+e^- collisions, but is technically not complete at LO. If a high-energy photon collider becomes available, the computation of the non-resonant contributions to the process $\gamma\gamma \to W^+W^-b\bar{b}$ with opposite photon helicities must be performed. We have compared our expressions for the LO P-wave Green function to the result of [91, 92] and found complete agreement for the scheme-independent terms. The NLO P-wave Green function is also determined in [91, 92], but is given only as a sum representation, which makes the symbolic comparison of even the scheme-independent terms difficult. There is, however, good numerical agreement between our results and the plots presented in [91, 92], if we set the scale in the hard matching coefficient and the finite-width scale and μ_w to the hard scale.

6.4. Stop-pair production at lepton and hadron colliders

The pair production of stops, the scalar supersymmetric partners of the top quark, has been studied extensively at both hadron and e^+e^- colliders. At hadron colliders it is very challenging to exclude the complete parameter space for light stops. A lepton collider can, however, exclude all electrically charged particles with masses up to half its center-of-mass energy. The stop-pair production cross section near threshold in e^+e^- collisions can also be determined in the effective field theory framework described in Chapter 3. It was first studied in [90]. The stops are produced in a P wave since the coupling of squarks to photons and Z bosons contains a derivative. We consider only the lighter mass eigenstate $\tilde{t} \equiv \tilde{t}_1 = \tilde{t}_L \cos\theta_{\tilde{t}} + \tilde{t}_R \sin\theta_{\tilde{t}}$, and assume the other mass eigenstate $\tilde{t}_2$ to be sufficiently

heavy that it cannot be pair produced close to the $\tilde{t}_1$ threshold. The cross section is given by

$$\sigma_{\tilde{t}\bar{\tilde{t}}X} = 12\pi\,\sigma_0 \left(e_{\tilde{t}}^2 - \frac{2q^2}{q^2 - M_Z^2} v_e z_{\tilde{t}} e_{\tilde{t}} + \left(\frac{q^2}{q^2 - M_Z^2} \right)^2 (v_e^2 + a_e^2) z_{\tilde{t}}^2 \right) \mathrm{Im}\left[\Pi^{(\partial)}(q^2) \right], \quad (6.11)$$

where $z_{\tilde{t}}$ denotes the coupling constant for the $Z\tilde{t}\bar{\tilde{t}}$ vertex and $\Pi^{(\partial)}(q^2)$ the spectral function of the derivative current. In NRQCD the derivative current matches to

$$j^{(\partial)k} = \frac{1}{m_{\tilde{t}}}\,\psi^*\, i\partial^k \chi^*, \quad (6.12)$$

where ψ and χ are the stop and anti-stop fields in the non-relativistic normalization $\psi \sim \chi \sim m_{\tilde{t}}^{3/2}$. Up to NLO, the spectral function takes the form

$$\Pi^{(\partial)}(q^2) = \frac{N_c}{4(d-1)m_{\tilde{t}}^4}\, c_\partial^2\, G^P(E), \quad (6.13)$$

with the hard matching coefficient of the current $j^{(\partial)k}$ [148]

$$c_\partial = 1 - 4C_F\,\frac{\alpha_s}{4\pi} + \mathcal{O}(\alpha_s^2), \quad (6.14)$$

and the P-wave Green function

$$G^P(E) = \frac{i}{N_c} \int d^dx\, e^{iEx^0} \left\langle 0 \,\middle|\, T\left([\chi i\partial^k \psi](x) [\psi^* i\partial^k \chi^*](0) \right) \,\middle|\, 0 \right\rangle_{\mathrm{PNRQCD}}. \quad (6.15)$$

The results for the cross section (6.11) depend strongly on the SUSY parameters, most notably the stop mass and decay width. For generic stops with a large decay width $\Gamma_{\tilde{t}} \gg \Lambda_{\mathrm{QCD}}$ the cross section has the same qualitative features as the P-wave contributions to top-pair production. In particular, it can be fully described within perturbative QCD as observed in [90]. This implies that the stop properties could be determined similar to the top threshold scan from a measurement of the cross section. In some regions of parameter space the stop can be long-lived and a different approach, similar to the one used for the determination of the bottom-quark mass in Chapter 7, would be required.

The P-wave Green function is also required for the resummation of Coulomb effects in the production of stop pairs in the quark-anti-quark channel at hadron colliders. For the light-flavored squarks the t-channel gluino exchange diagram dominants the pair production cross section. The respective stop-pair production diagram is negligible because it is suppressed by the minuscule top parton distribution function in the proton. Therefore, the dominant contribution in this channel is from s-channel gluon exchange, which creates stop pairs in a colour-octet P-wave state. The stop-pair production mechanism in gluon fusion is not flavour sensitive and can be taken over from the respective squark-pair production results.

A formalism for the combined resummation of soft and Coulomb corrections in the production of pairs of heavy colored particles in a S-wave state was derived at next-to-next-to-leading logarithmic order (NNLL) in [72] and was applied to the production of squarks and gluinos in [149]. The approach was extended to stop-pair production in [150, 151]. While the formal proof was only done at NLL the arguments presented there strongly suggest that the factorization formula is still valid at NNLL. The dominant missing part of the potential function J^{R_α} in the factorization formula is given by the potential NLO corrections to P-wave color-octet Green function, which accounts for NNLL terms beginning with α_s^2/β. They can be obtained from our result for the color singlet by a simple replacement of the color factor $-C_F \to D_8 = 1/(2N_c)$ in (3.41). To achieve full NNLL accuracy one also needs terms beginning with $\alpha_s^2 \log \beta$ [152], which arise from contributions of the non-Coulomb potentials.

7. Determination of the bottom-quark mass from non-relativistic sum rules at NNNLO

The extraction of the top-quark mass in a threshold scan relies on the direct comparison of the experimentally measured shape of the cross section with the theory prediction within perturbation theory. This approach is valid because the hadronization time $t_{\text{had}} \sim 1/\Lambda_{\text{QCD}} \sim 2 \cdot 10^{-24} s$ of the top quarks is much larger than their average lifetime $T_t \sim 1/\Gamma_t \sim 5 \cdot 10^{-25} s$. Thus, non-perturbative hadronization effects never become relevant for the cross section. A somewhat more formal formulation of this observation is that the large top width provides an IR cutoff and, therefore, protects the top quark from the non-perturbative regime of QCD, that is responsible for confinement.

The bottom quark, on the other hand, has a lifetime of the order of $T_b \sim 1.5 \cdot 10^{-12} s$, and is not protected against non-perturbative hadronization effects. At any order, perturbation theory predicts the production of free quarks and gluons and cannot be expected to reproduce the cross section measured by experiments, which involves only hadrons. To salvage the situation, one must find a way to introduce an artificial IR cutoff in analogy to the top-quark case, where the role is played by the width. In [153] it was demonstrated that smearing the cross section

$$\overline{R}(s, \Delta) = \frac{\Delta}{\pi} \int_0^\infty \frac{ds' R(s')}{(s' - s)^2 + \Delta^2} \tag{7.1}$$

with a Breit-Wigner shape of width Δ, effectively works as an IR cutoff, similar to a natural decay width of the order $\Delta/\sqrt{s}$. For sufficiently large Δ, one may therefore assume that the smeared theory prediction and smeared experimental result agree, which is known as quark-hadron duality. Consequently, it is possible to extract the bottom-quark mass in a similar fashion as the top-quark mass, but with the cross section averaged over an appropriate energy range. The smearing mechanism must provide a compromise between retaining the most information on the bottom-quark mass and suppressing the non-perturbative corrections. The most prominent approach is provided by the so-called moments $\mathcal{M}_n$, which are defined through a sum rule, first introduced in [30, 31]. We will review this idea in the following. Afterwards, we discuss the first full NNNLO bottom-quark mass determination from non-relativistic sum rules, provided by us in [2, 3, 6].

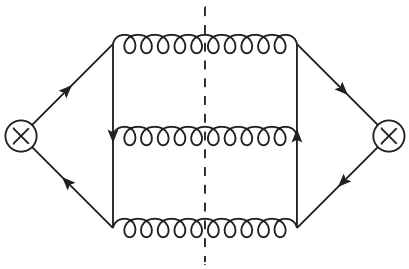

Figure 7.1.: Three gluon cut in the correlator of two heavy-quark vector currents at $\mathcal{O}(\alpha_s^3)$.

7.1. The sum rule

The sum rule [30, 31] is based on the analytic properties of the spectral function $\Pi_b(s)$ in the complex s plane. Its singularities correspond to physical states. In non-relativistic perturbation theory, including the effects of Coulomb resummation, they are given by an infinite number of isolated poles for real s below threshold, corresponding to $b\bar{b}$ bound states, and a branch cut on the real axis above the threshold, which represents the open $b\bar{b}$ continuum. At higher orders, subtleties, like a branch cut starting from $s = 0$ due to the three gluon cut shown in Figure 7.1, appear [154]. These cuts must be subtracted from the spectral function. The $b\bar{b}$ cuts of the same diagram can be described through a NNNLO contribution to the hard matching coefficient c_v or are of higher order [60]. Heavy quark radiation from light quarks is even more suppressed in the threshold region [60].

It is assumed that the analytic structure does not change qualitatively in the presence of non-perturbative effects, i.e. the pole positions can move by a small amount on the real axis, but no new singularities are generated. In the vicinity of the singularities, non-perturbative effects become important because the physical states are very sensitive to the IR properties of QCD. On the other hand, far away from the singularities, the bottom-pair state has a large virtuality, that acts as an IR cutoff. Thus, the spectral function can be computed as an operator product expansion (OPE) [71] in the ratio of the QCD scale over the virtuality, including non-perturbative effects. Clearly, this OPE breaks down in the vicinity of the singularities, where the bottom-quark pair is near its mass shell. We study the non-perturbative terms in the OPE approach in Section 8. Anticipating these results we can demonstrate this behaviour explicitly. For example, the smeared cross section (7.1) is proportional to the difference $\Pi_b(s+i\Delta)-\Pi_b(s-i\Delta)$ of the spectral function. We show the relative correction to the smeared cross section from the leading dimension four condensate as a function of the center-of-mass energy and the smearing width Δ in Figure 7.2. For Δ large enough, the hadronic effects are insignificant. On the other hand the OPE clearly breaks down where the absolute value of the ratio exceeds one, which happens for energies close to threshold and small smearing width.[1] We observe that, even for $\Delta \to 0$, the

[1] In fact the non-perturbative contribution also contains a perturbative suppression by v^2, cf. the discussion in Section 8.4.1. This implies that the breakdown of the OPE already occurs for smaller values of the ratio of the order $v^2 \ll 1$.

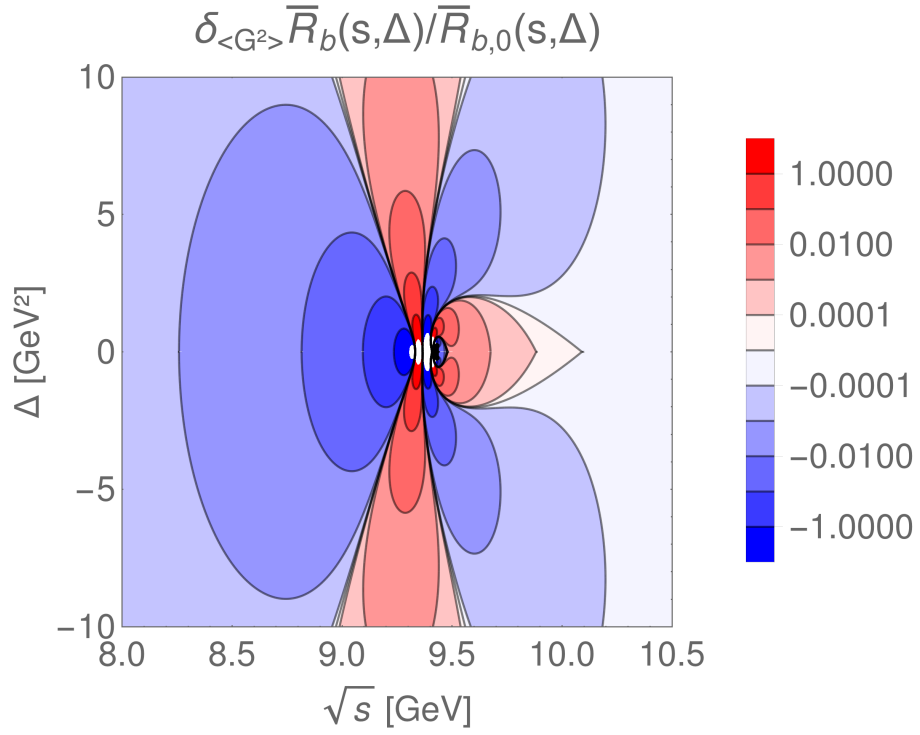

Figure 7.2.: The ratio $\delta_{\langle G^2\rangle}\overline{R}_b(s,\Delta)/\overline{R}_{b,0}(s,\Delta)$ as a function of $\sqrt{s}$ and Δ. The input values are the same as in Table 8.1.

corrections are small for energies above the threshold. This happens because the velocity becomes large, i.e. of order one, and the non-perturbative corrections are suppressed by powers of $\Lambda_{\rm QCD}/m_b$.

We now choose a complex momentum $s = Q^2$, which is supposed to be far away from the singularities, but otherwise arbitrary. The analytic properties can be exploited to relate $\Pi_b(Q^2)$ to the physical cross section, i.e. the imaginary part of the spectral function at the physical cut. We use Cauchy's theorem

$$\Pi_b(Q^2) = \frac{1}{2\pi i}\oint\limits_C dz \frac{\Pi_b(z)}{z-Q^2} \tag{7.2}$$

to express $\Pi_b(Q^2)$ through the contour integral indicated in Figure 7.3. The contour can then be deformed in the indicated way with the radius going to infinity without crossing any singularities. With $\Pi_b(s+i\epsilon) - \Pi_b(s-i\epsilon) = 2i\ \mathrm{Im}\ \Pi_b(s)$, we obtain

$$\Pi_b(Q^2) = \frac{1}{\pi}\int\limits_{s_0}^{\infty} ds \frac{\mathrm{Im}\ \Pi_b(s)}{s-Q^2} + \frac{1}{2\pi i}\oint\limits_{\bigcirc} dz \frac{\Pi_b(z)}{z-Q^2}. \tag{7.3}$$

This dispersion relation still contains a non-zero integration over the circle at infinity. It

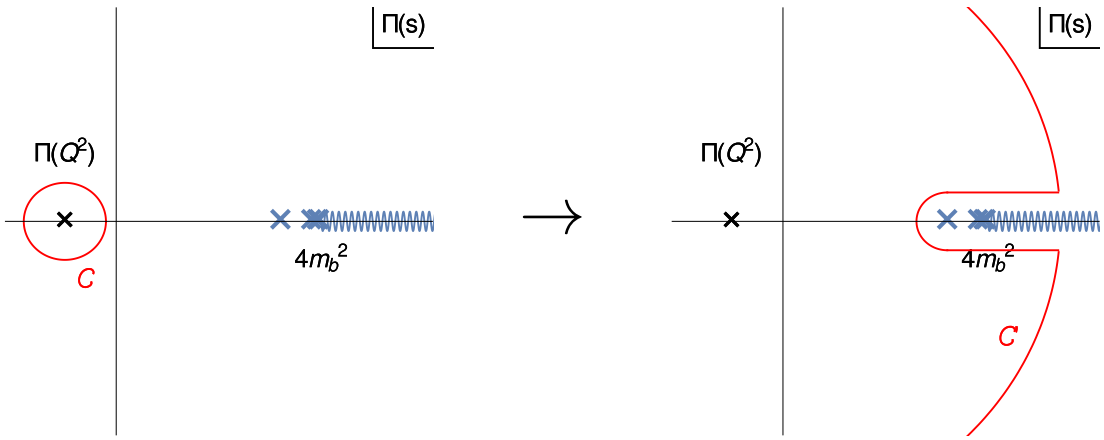

Figure 7.3.: Deformation of the contour in the complex s plane. The crosses and wiggly line on the real axis represent the bottomonium bound states and open $b\bar{b}$ continuum, respectively.

can be removed by taking derivatives in s. With $Q^2 = 0$, we obtain the sum rule

$$\mathcal{M}_n = \int_0^\infty ds\, \frac{R_b(s)}{s^{n+1}} = \frac{12\pi^2}{n!}\left(\frac{d}{dq^2}\right)^n \Pi_b(q^2)\Big|_{q^2=0} . \tag{7.4}$$

The sum rule can be used to determine experimental moments $\mathcal{M}_n^{\text{exp}}$ from the integral over the measured cross section. At the same time, theory moments $\mathcal{M}_n^{\text{th}}$ can be computed as an OPE in $\Lambda_{\text{QCD}}/(m_b/n)$, through derivatives of the spectral function. The scale m_b/n is the effective smearing range for the n'th moment and the breakdown of the OPE prohibits the applicability of the sum rule to arbitrarily large moments. On dimensional grounds, the theory moments are strongly dependent on the bottom-quark mass $\mathcal{M}_n^{\text{th}} \sim m_b^{-2n}$. Quark-hadron duality allows us to determine the bottom-quark mass from the condition $\mathcal{M}_n^{\text{th}}(m_b) = \mathcal{M}_n^{\text{exp}}$.

Note that we use a different convention for Π_b in this section, than the one introduced in Section 3. Electroweak effects are suppressed by the small mass ratio $m_b^2/m_{W,Z,H}^2$ and are therefore neglected. Since this removes the s-channel Z-exchange contribution, it is convenient to absorb the global factor e_b^2 from the photon coupling into Π_b.

For small values of n, the suppression of the large-energy region $s \gtrsim 4m_t^2$ through the factor $1/s^{n+1}$ in the integral is mild and the moments receive contributions from a large energy range. Thus, conventional perturbation theory is adequate and can be applied to calculate the moments directly from the derivatives of the spectral function. With increasing n, the convergence of the fixed-order perturbative approach deteriorates and it breaks down around $n = 10$ [155, 156].

At these larger values of $n \sim 10$, the integral is saturated by the threshold region [157, 158], where the characteristic velocity of the bottom-quarks is in the non-relativistic regime $v \sim 1/\sqrt{n} \ll 1$. Thus, the moments must be computed in non-relativistic perturbation theory, where the velocity of the bottom quarks is counted as the strong coupling $v \sim \alpha_s \ll$

1 and Coulomb singularities $(\alpha_s/v)^n$ are unsuppressed. This implies that the methods and results discussed in Section 3 can be used. The mass determination from large-n moments profits from lower experimental uncertainties and higher sensitivity of the moments to the mass. This comes at the cost of an increased IR sensitivity, which implies a larger theory uncertainty.

7.2. Experimental moments

The experimental moments $\mathcal{M}_n^{\text{exp}}$ contain contributions from the $\Upsilon(1S)$ to $\Upsilon(4S)$ resonances and the continuum. For the former, the narrow width approximation is applied. We obtain

$$\mathcal{M}_n^{\text{exp}} = 9\pi \sum_{N=1}^{4} \frac{1}{\alpha(M_{\Upsilon(NS)})^2} \frac{\Gamma_{\Upsilon(NS)\to l^+l^-}}{M_{\Upsilon(NS)}^{2n+1}} + \int_{s_{\text{cont}}}^{\infty} ds\, \frac{R_b(s)}{s^{n+1}}\,. \tag{7.5}$$

The masses $M_{\Upsilon(NS)}$ and leptonic widths $\Gamma_{\Upsilon(NS)\to l^+l^-}$ of the resonances are taken from the PDG [159]. A universal value $\alpha(2m_b) \approx 1.036\,\alpha$ [126] is used for the running QED coupling at the bound-state energies.

Data for the continuum cross section is only available in the region between $\sqrt{s_{\text{cont}}} = 10.6178\,\text{GeV}$ and $11.2062\,\text{GeV}$ [32]. We use the inputs from [33], where corrections for initial state radiation have been applied. The sensitivity of the large moments to the unknown cross section at higher energies is greatly suppressed. This allows us to make a very conservative estimate $R_b = 0.3 \pm 0.2$ without forfeiting the precision of the result. In analyses, that involve small n, much more aggressive assumptions have commonly been applied [33,160]. We determine the uncertainty of a given experimental moment by adding in quadrature the errors induced by uncertainties in the Υ masses and leptonic widths, the BaBar data [32] and our estimate in the high-energy region.

Our results for the experimental moments (7.5) are summarized in table 7.1. We observe that the continuum contribution is indeed subleading for $n \sim 10$ and the uncertainty from the continuum with respect to the resonances is not excessive for $n = 7-9$ and even small for $n \gtrsim 10$.

7.3. Theory moments

In practice, we do not compute the theory moments from derivatives of the spectral function, but use the dispersion relation (7.5) and calculate the integral over the normalized cross section R_b instead. At NNNLO in non-relativistic perturbation theory, the cross section is given by (see Section 3)

$$R_b = 12\pi e_b^2\, \text{Im}\left[\frac{N_c}{2m_b^2}\left(c_v\left[c_v - \frac{E}{m_b}\left(c_v + \frac{d_v}{3}\right)\right]G(E) + \dots\right)\right]. \tag{7.6}$$

The Green function contains an infinite number of poles below threshold, that correspond to narrow S-wave $b\bar{b}$ bound states. Their binding energies E_N and wave functions at the

n	6	7	8	9	10
resonances	0.1861(20)	0.2004(22)	0.2166(24)	0.2351(27)	0.2560(29)
continuum	0.0240(85)	0.0182(58)	0.0140(41)	0.0110(29)	0.0088(21)
total	0.2101(88)	0.2185(62)	0.2307(47)	0.2461(39)	0.2648(36)

n	11	12	13	14	15
resonances	0.2797(33)	0.3064(36)	0.3364(40)	0.3702(45)	0.4081(50)
continuum	0.0070(15)	0.0057(11)	0.0046(8)	0.0038(6)	0.0031(4)
total	0.2867(36)	0.3120(38)	0.3410(41)	0.3740(45)	0.4112(50)

Table 7.1.: The experimental moments $\mathcal{M}_n^{\text{exp}}$ in units of $(10\,\text{GeV})^{-2n}$. The individual contributions from the Υ resonances and the continuum are shown as well.

origin $\psi_N(0)$ can be determined from the expansion of the Green function around these poles. Like the experimental moments (7.5), the theory moments may therefore be split into bound-state and continuum contributions

$$\mathcal{M}_n^{\text{th}} = \frac{12\pi^2 N_c e_b^2}{m_b^2} \sum_{N=1}^{\infty} \frac{Z_N}{(2m_b + E_N)^{2n+1}} + \int_{4m_b^2}^{\infty} ds\, \frac{R_b(s)}{s^{n+1}}. \tag{7.7}$$

The residues

$$Z_N = c_v \left[c_v - \frac{E_N}{m_b} \left(c_v + \frac{d_v}{3} \right) \right] |\psi_N(0)|^2 + \dots . \tag{7.8}$$

are the squared absolute values of the amplitude for a lepton pair forming a $\Upsilon(NS)$ bound state. They also have a direct correspondence to the leptonic decay rate $\Gamma(\Upsilon(NS) \to l^+l^-)$ [86]. Thus, the Z_N are physical quantities and scale and scheme independent at the considered order in perturbation theory.

The following ingredients are required for the moments (7.7) at NNNLO:

- The hard matching coefficient c_v for the leading non-relativistic current at order α_s^3 [68] and d_v for the subleading current at order α_s [161].
- The NNNLO corrections to the $\Upsilon(NS)$ energy levels E_N [88, 162, 163], to the wave functions at the origin $|\psi_N(0)|^2$ [88, 163, 164], and to the continuum Green function $G(E)$ [88, 89] from insertions of the potentials up to NNNLO [60, 83–87].
- Ultrasoft corrections to the energy levels [165], wave functions [73] and Green function [74].

These quantities are available for top-pair production, where the energy is shifted in the complex plane by $i\Gamma$. The numerical evaluation for bottom quarks sometimes requires that the expressions are analytically continued in the limit $\Gamma \to 0$, i.e. for complex energies approaching the branch cut. Details of this step have been described in [2] and will not be recapitulated here.

7.4. Scheme definitions

We have discussed the shortcomings of the pole mass in depth in Section 2. Here, we describe the mass schemes we employ in the determination of the bottom-quark mass and other conventions related to the treatment of terms that are formerly beyond NNNLO.

The ambiguities, that are inherent in the pole mass scheme, can be removed by the use of a renormalon free mass definition like the PS mass [51] or the $\overline{\text{MS}}$ mass. Their relation to the pole mass is parametrized by

$$m_b = m_b^M + \sum_{i=0}^{\infty} \delta m_i^M \,, \tag{7.9}$$

where $M = \text{PS}, \overline{\text{MS}}$. At NNNLO terms up to $i = 3$ are required. The expressions for the PS and $\overline{\text{MS}}$ mass can be found in [88] and [49, 166, 167], respectively. In the PNRQCD Lagrangian, this introduces additional terms

$$\mathcal{L}_{\delta m} = \sum_{i=0}^{\infty} \delta m_i^M \, \left(\psi^\dagger \psi - \chi^\dagger \chi\right). \tag{7.10}$$

We observe that the leading order term in (7.10) in the $\overline{\text{MS}}$ mass scheme is of order v^4 and enhanced with respect to the kinetic terms in the non-relativistic power counting. Thus, the naive use of the $\overline{\text{MS}}$ scheme is inconsistent. In the PS scheme, the leading order term in (7.10) is of the same order v^5 as the kinetic terms and must be treated non-perturbatively. A consistent scheme, denoted PS-insertion (PSI) in [89], can be defined by strictly expanding the cross section in δm_i^{PS} up to the considered order. However, this introduces unphysical behaviour near threshold [89]. It was observed there that this behaviour can be cured by treating the complete mass shift non-perturbatively, which defines the PS-shift (PSS) scheme. To maintain the cancellation of renormalons, the factor $(2m_b + E_N)^{-(2n+1)}$ in equation (7.7) must not be expanded in the PSS scheme. This is equivalent to the pole resummation in the cross section, that we have already discussed for top-pair production.

To compute the N^{k}LO moments in the PSS scheme for a given PS mass m_b^{PS}, we first determine the respective pole mass $m_b^{[k]}$ from the relation (7.9), truncated after the kth term. In the resonance contribution to the moments (7.7), the residues (7.8) are truncated after the kth order, but the denominators are left unexpanded. The continuum part is not affected by the pole resummation and the N^{k}LO cross section R_b in the pole mass scheme with $m_b^{[k]}$ is used (cf. [89]).

The same procedure can also be applied starting from a $\overline{\text{MS}}$ mass, which defines the MSS scheme. Despite of the issues with the $\overline{\text{MS}}$ mass in threshold processes, this scheme is consistent because the $\overline{\text{MS}}$-pole mass relation is not expanded and the renormalons cancel.

In the expressions (7.6), (7.7) and (7.8), a prefactor $1/s$ in the spectral function has been expanded according to the non-relativistic counting and is therefore treated in a different way as the factor $1/s^{n+1}$ in the moment integral (7.7) in the shift schemes. This is the source of a renormalon ambiguity, which is suppressed by $1/n$ compared to the ambiguity

in the pole mass scheme. We define alternative moments $\widetilde{\mathcal{M}}_n^{\text{th}}$, where this factor is kept unexpanded, through

$$\widetilde{R}_b = 12\pi e_b^2 \,\text{Im}\left[\frac{2N_c}{s}\left(c_v\left[c_v - \frac{E}{m_b}\frac{d_v}{3}\right]G(E) + \dots\right)\right], \tag{7.11}$$

$$\widetilde{Z}_N = c_v\left[c_v - \frac{E_N}{m_b}\frac{d_v}{3}\right]|\psi_N(0)|^2 + \dots, \tag{7.12}$$

$$\widetilde{\mathcal{M}}_n^{\text{th}} = 48\pi^2 N_c e_b^2 \sum_{N=1}^{\infty} \frac{\widetilde{Z}_N}{(2m_b + E_N)^{2n+3}} + \int_{4m_b^2}^{\infty} ds\, \frac{\widetilde{R}_b(s)}{s^{n+1}}\,. \tag{7.13}$$

The difference is formerly of higher order, but we find that numerically it is of similar size as the other theory uncertainties. Without a careful analysis, it is not clear which scheme should be preferred because the expansion in the kinetic energy is not the only source of subleading renormalons. Such an analysis is beyond the scope of this work. We find however in Section 7.6.3 that the masses extracted from different moments show better consistency when the $1/s$ prefactor is not expanded non-relativistically. Thus, the moments (7.13) will be used as our default scheme. The uncertainty due to the scheme ambiguity is not taken into account for our result, but we make sure that the mass values obtained with the moments (7.7) lie within our quoted theory uncertainty.

7.5. Charm-quark mass effects

In Section 7.3, we listed the necessary ingredients for the moments, which are available from the NNNLO top-pair production cross section. These results assume the light quarks to be massless, which is well justified there due to the large hierarchy between the top-quark and light-quark masses. The mass of the charm quark is however of the same order as the inverse Bohr radius $m_b\alpha_s \sim m_b v$ of the Bottomonium system, which sets the soft scale for the bottom cross section. Thus, the effects from a non-vanishing charm-quark mass have to be taken into account as well. An analysis of charm-mass effects at NNLO [168] found a sizeable shift of about $-30\,\text{MeV}$ in the extracted $\overline{\text{MS}}$ bottom-quark mass.

However, the results of [168] are only available for moments, where the factor $1/s^{n+1}$ is expanded non-relativistically and cannot be incorporated in our expressions (7.7) and (7.13). We discuss how a non-zero charm-quark mass contributes and determine its effects on the cross section at NNLO. This way, the corrections can be adopted to any scheme one might employ for the moments.

We recall from Section 3 that the computation of the cross section can be organized in three steps. These are the hard matching, the soft matching and the calculation of the spectral function in the effective theory. The soft charm-quark mass is expanded out in the hard matching. Consequently, the effects must be analytic in $m_c^2/m_b^2 \sim \alpha_s^2$ and enter only at subleading order. Inserting a charm-quark loop into a gluon line thus yields a relative suppression $\alpha_s m_c^2/m_b^2 \sim \alpha_s^3$ and is beyond NNNLO.

The charm quark is integrated out in the soft matching procedure. It has been demonstrated in [60] that the soft Wilson coefficient of the external vector current is trivial, as long as the light quarks are considered to be massless because the associated loop integrals are scaleless. A soft charm-quark mass introduces a scale in the soft loops and this statement must be reconsidered. However, charm-quark contributions only enter at two loops and must vanish in the limit $m_c \to 0$. Since the only other scale in the soft matching of the current is m_b, there must be an additional suppression of at least $m_c/m_b \sim \alpha_s$, which implies that this is a higher-order effect.[2] Thus, only the Coulomb potential is affected at NNLO. We split off the difference V_{m_c} between a massive and a massless charm quark in the potential, such that we obtain

$$V = V_{\text{massless}} + V_{m_c}, \tag{7.14}$$

where V_{m_c} vanishes for $m_c \to 0$.[3] The correction V_{m_c} has been computed up to NNLO in [169, 170]. We use the convenient representations from [168], which can be found in Appendix C.1.

It remains to compute the contributions to the spectral function from the charm-quark correction to the Coulomb potential V_{m_c}. The single insertion of $V_{m_c}^{(1)}$ contributes at NLO. At NNLO, one requires the single insertion of $V_{m_c}^{(2)}$, the double insertions of $V_{m_c}^{(1)}$ and the mixed double insertion of $V_{\text{massless}}^{(1)}$ and $V_{m_c}^{(1)}$. Details on the computation of the NLO correction to the Green function can be found in Appendix C.3. In Appendix C.4, the full results for the NNLO charm-quark mass effects on the energy levels E_N and the wave functions $|\psi_N(0)|^2$ are given. The parts that are available in the literature [168,171] coincide numerically with our expressions.

The effects of a non-zero charm-quark mass also have to be taken into account in the conversion from the PS or $\overline{\text{MS}}$ mass to the pole mass, that is needed for the implementation of the PSS and MSS schemes discussed in Section 7.4. These corrections are known at order α_s^3 [172] for the relation between the pole and the $\overline{\text{MS}}$ scheme. We have computed the charm quark contributions to the relation between the PS and the pole mass at NNLO order and give results in Appendix C.2.

With these results, we can now discuss the impact of the non-zero charm-quark mass on the phenomenology of the sum rule analysis. The $\overline{\text{MS}}$ mass scheme, with μ_c set to the renormalization scale μ, is employed for the charm quark. The value of $m_c^{\overline{\text{MS}}}(\mu)$ is determined via 4-loop running from the input value $m_c^{\overline{\text{MS}}}(3\,\text{GeV}) = 0.986\,\text{GeV}$ [33].[4] The parametric uncertainty from the charm-quark mass is negligible in comparison to the missing NNNLO contributions.

The insertion of a charm-quark loop into a gluon line effectively provides an IR cutoff on the virtuality of the gluon. Thus, we expect the non-zero charm-quark mass effects to be significant for quantities with large infrared sensitivity, but small for observables with little

[2] We also checked through an explicit computation that there is no NNLO contribution.

[3] The effects on the running of α_s are included in the Coulomb potential. We use the same convention as [168], where the potential is defined for α_s evolving with $n_{l,\text{massless}} + 1$ flavors.

[4] The renormalization group evolution is performed with `RunDec` [173].

$N=1$	$2\delta m^{\rm PS}_{1,m_c}$	$2\delta m^{\rm PS}_{2,m_c}$	$E^{(1)}_{1,m_c}$	$E^{(2)}_{1,m_c}$	$f^{(1)}_{1,m_c}$	$f^{(2)}_{1,m_c}$
single insertion $\{m_c\}$	9.50	23.21	-6.82	-18.02	0.0335	0.0644
double insertions						
$\{m_c, \text{massless}\}$	–	–	–	-1.46	–	-0.0043
$\{m_c, m_c\}$	–	–	–	-0.02	–	-0.0001
$\sum$	9.50	23.21	-6.82	-19.50	0.0335	0.0600

Table 7.2.: The effects of a non-zero charm-quark mass on the binding energy $E^{(i)}_{1,m_c} = E^{(0)}_1 e^{(i)}_{1,m_c}$ and squared wave function at the origin $|\psi_1(0)|^2 = |\psi^{(0)}_1(0)|^2\big(1 + \sum_{i=1}^{\infty} f^{(i)}_1\big)$ of the $\Upsilon(1S)$ resonance. $f^{(i)}_{1,m_c}$ is the charm correction to $f^{(i)}_1$. The values were obtained in the pole-mass scheme with the inputs $m_b = 5$ GeV, $\mu = 5$ GeV, $\alpha_s(5\text{ GeV}) = 0.2135$ and $m_c(5\text{ GeV}) = 0.892$ GeV. Furthermore, we show results for the charm-quark mass corrections to the relation between the pole mass and the PS mass for $\mu_f = 2$ GeV. A significant cancellation in the $\Upsilon(1S)$ mass $M_{\Upsilon(1S)} = 2m_b + E_1 = 2m_b^{\rm PS} + 2\sum_{i=1}^{\infty}\delta m_i^{\rm PS} + E_1$ can be observed due to the reduced IR sensitivity in a short-distance mass scheme like the PS-scheme. The corrections to the mass shift $2\delta m^{\rm PS}_{i,m_c}$ and the binding energy $E^{(i)}_{1,m_c}$ are given in units of MeV, whereas $f^{(i)}_{1,m_c}$ is dimensionless.

IR sensitivity. This behaviour is illustrated in Table 7.2, which provides numerical results for the energy level and wave function at the origin of the $\Upsilon(1S)$ resonance. The individual charm-quark contributions to the mass shift and binding energy are big, but largely cancel against each other in the PS mass scheme. We can also show this cancellation analytically, by expanding the corrections in the limit of a small charm-quark mass. The linear terms in this expansion drops out in the sum of the corrections to the energy levels and the PS-pole mass relation (cf. [168]). The large IR sensitivity, that manifests itself through the linear charm-quark mass dependence, is related to the IR renormalon at $u = 1/2$ discussed in Section 2, which is absent in the PS-mass scheme.

In the following we analyze the effect of a non-zero charm-quark mass on the $\overline{\rm MS}$ bottom-quark mass determined from the tenth moment at NNNLO. Let us begin by only considering the corrections to the binding energies and the wave functions from single insertions. Including these effects up to NNLO (NLO) shifts the result for the bottom mass by $+16\,$MeV ($+4\,$MeV). As expected from the above discussion, we observe a significant cancellation when the charm effects in the PS-pole mass relation are also taken into account. The combined charm correction reduces to only $+0.5\,$MeV ($-0.5\,$MeV). Since both the PS and the $\overline{\rm MS}$ scheme are renormalon free, we expect the charm-effects in the conversion to be small. We find that the combined shift amounts to $-3.5\,$MeV ($-2\,$MeV) in the $\overline{\rm MS}$ bottom-quark mass.

As of yet, the effects due to double insertions and the continuum cross section have been neglected. The double insertions do not contribute to the linear term in the expansion

for small charm-quark masses and are found to be small compared to the single insertions (cf. [168]). They shift the extracted bottom-quark mass by only +0.5 MeV. The effect of the NLO corrections to the continuum contributions provided in Appendix C.3 amounts to less than 0.1 MeV, as expected from the large suppression of the overall continuum contribution to the tenth moment. Since the double insertions and the charm corrections to the continuum cross section are rather time-consuming and numerically negligible, we use them only to determine the central value of our analysis and switch them off when determining the theory uncertainty.

We observe that the perturbative corrections to the individual contributions considered above show no sign of convergence. The behaviour is however significantly improved for observables with reduced IR sensitivity like the $\Upsilon(1S)$ mass or the moments. The overall shift for the $\overline{\text{MS}}$ mass extracted from the tenth moment is $-3\,\text{MeV}$ ($-2\,\text{MeV}$) at NNLO (NLO), which suggests that the charm corrections converge. Nevertheless, we adopt the total size of the non-zero charm-quark mass effects for the bottom-quark mass obtained at NNLO as a conservative estimate for the missing higher order corrections.

We point out that there is a large discrepancy between our result of $-3\,\text{MeV}$ for the overall mass shift and the one from [168], which amounts to about $-30\,\text{MeV}$. According to our findings, this cannot be accounted for by the differences in the analyses, like the non-relativistic expansion of the factor $1/s^{n+1}$ in [168], the choices of the renormalization scale and the different values of the charm-quark mass. In particular, the claim of [168] that the effect on the 20th moment is as large as 50% appears suspicious to us. [168] employs the $1S$ mass scheme, where by definition charm effects cancel completely in the combination $2m_b^{1S} + 2\sum_{i=1}^{\infty} \delta m_i^{1S} + E_1 \equiv 2m_b^{1S}$. Since the moments for such large n are completely dominated by the contribution from the $\Upsilon(1S)$ state, only the charm corrections to the residue Z_1 are relevant. Our results show (cf. table 7.2) that they are significantly smaller than 50% and independent of n.

7.6. Numerical analysis

7.6.1. Choice of the renormalization scale

The adequate choice for the value of the renormalization scale is not obvious for observables that receive contributions from multiple physical scales, like the non-relativistic moments. In the NNLO analyses performed about 15 years ago, values for the renormalization scale at the soft scale were favored. E.g. [174] fixed the central value to $\mu = 2m_b/\sqrt{n}$ based on the observation that the logarithms $\log(\mu^2/(-4m_bE))$ vanish there for the characteristic energy $E = m_b/n$ of the nth moment.

We show the scale dependence of the tenth moment for μ between 2 GeV and 10 GeV at the available orders in perturbation theory in Figure 7.4. There is no overlap at all in this region between subsequent orders up to NNLO, which made it very difficult to estimate the uncertainties due to missing perturbative effects. It is also disconcerting that the NNLO corrections are significantly larger than the NLO ones. Both observations clearly

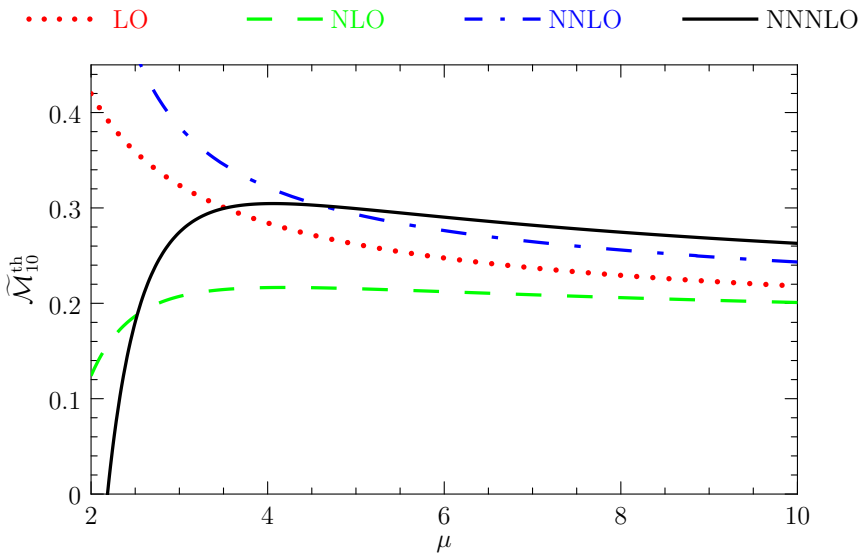

Figure 7.4.: Scale dependence of the tenth moment $\widetilde{\mathcal{M}}_{10}^{\rm th}$ in the PSS scheme (7.13) in units of $(10\,\text{GeV})^{-20}$ for $m_b^{\rm PS}(2\,\text{GeV}) = 4.5\,\text{GeV}$ and $\alpha_s(M_Z) = 0.1184$.

motivate the determination of NNNLO corrections. A possible explanation for the large NNLO corrections is that both relativistic corrections and non-Coulomb potentials first contribute at this order. The third order stands out because ultrasoft effects first appear there and all systematic types of contributions are considered.

Looking at Figure 7.4, one can indeed see a drastic improvement from the inclusion of third order corrections. For μ in the range from 3 GeV to 10 GeV, the NNNLO band is entirely contained in the NNLO one. Below 3 GeV however, there is no sign of convergence.[5] Therefore we use the central scale $\mu = m_b^{\rm PS}$ and estimate the perturbative uncertainty from variation of μ between 3 GeV and 10 GeV.

Further insight on the adequate choice of the renormalization scale can be obtained from resumming logarithms $\ln\sqrt{n}$ of the ratios of the different scales by applying renormalization group methods. We do not attempt this in our analysis because $\alpha_s \ln\sqrt{n} \approx 1.15\alpha_s \ll 1$ for $n \sim 10$. The available NNLL analyses [175, 176] show a significant stabilization of the results for low values of the renormalization scale and fairly small impact for larger scales. With our scale choice, we therefore expect that the resummation of logarithms would lead to a small reduction of the perturbative uncertainty due to better behaviour for $\mu \lesssim 3\,\text{GeV}$, but no no significant change of the central value.

7.6.2. Comparison to the fixed-order continuum

We have discussed the possibilities of using small and large n moments for the sum rule analysis as well as their particular advantages and disadvantages in Section 7.1. Ideally,

[5] The leptonic decay width of the $\Upsilon(1S)$ resonance [86] follows the same pattern.

one would like a unified description, that is valid in the complete range from $n = 1$ up to $n \approx 10$. It is a fair assumption that this could be achieved by merging the results for the cross section in non-relativistic perturbation theory and conventional perturbation theory. The latter is known analytically [177] up to order α_s and as a Padé approximation [178–180] at orders α_s^2 and α_s^3. The respective perturbative expansions miss terms, which scale as

$$\mathrm{Im}\left[\Pi^{\mathrm{NRPT}}_{>\mathrm{NNNLO}}\right] \sim v^5 \sum_{i=0}^{\infty}\left(\frac{\alpha_s}{v}\right)^i \sum_{j=0}^{\infty} v^j, \tag{7.15}$$

$$\mathrm{Im}\left[\Pi^{\mathrm{CPT}}_{>\mathrm{NNNLO}}\right] \sim \frac{\alpha_s^4}{v^3} \sum_{i=0}^{\infty}\left(\frac{\alpha_s}{v}\right)^i \sum_{j=0}^{\infty} v^j, \tag{7.16}$$

whereas the merged result would only lack the contributions

$$\mathrm{Im}\left[\Pi^{\mathrm{Merged}}_{>\mathrm{NNNLO}}\right] \sim v\alpha_s^4 \sum_{i=0}^{\infty}\left(\frac{\alpha_s}{v}\right)^i \sum_{j=0}^{\infty} v^j. \tag{7.17}$$

The merging relies on both approximations providing a good description in an intermediate region, where the hierarchy $\alpha_s \ll v \ll 1$ is fulfilled, i.e. both the assumptions $v \ll 1$ made in the non-relativistic expansion and $v \gg \alpha_s$ made in conventional perturbation theory are valid. Expanding (7.15) and (7.16) in this limit, we find that the leading missing contributions are roughly equal and of the order of $3 - 6\%$ for $v \sim 0.4 - 0.5$ based only on power counting. Applying the same approach to the merged result gives an estimate of only 0.2% for the missing higher-order terms. Thus, one would naively expect that the continuum NNNLO cross sections in PNRQCD and conventional perturbation theory agree at the level of about 10% in this region. Figure 7.5 depicts the respective predictions in the pole-mass scheme with $m_b = 5\,\mathrm{GeV}$, and keeping the factor $1/s$ in the polarization function unexpanded.

One finds good agreement at NLO and NNLO (upper panel) for velocities around $v \sim 0.4$. The NNNLO curves, however, miss each other completely (lower panel). It appears that this can mainly be attributed to the NNNLO PNRQCD curve, which lies considerably below its NNLO equivalent. The difference between consecutive orders of the PNRQCD result is much larger when going from NNLO to NNNLO compared to the step from NLO to NNLO. Furthermore, the dependence on the renormalization scale is significantly increased with respect to the NNLO result and even extends to unphysical negative values.[6]

On the other hand, the Padé approximation used for the prediction in conventional perturbation theory lacks some input from the naive threshold expansion of the NNNLO result. The missing terms scale like $v\alpha_s^3$ and can in principle be determined from the expansion of the NNNLO PNRQCD result in α_s. By construction, the behaviour of the Padé approximation follows the input of the naive threshold expansion for $v \to 0$. An example for a particularly large missing contribution is the product of the α_s^3 correction to

[6] In contrast to the continuum cross section, the $\Upsilon(1S)$ bound-state energy and leptonic decay rate have a much better behaved perturbative expansion and scale dependence at NNNLO [86].

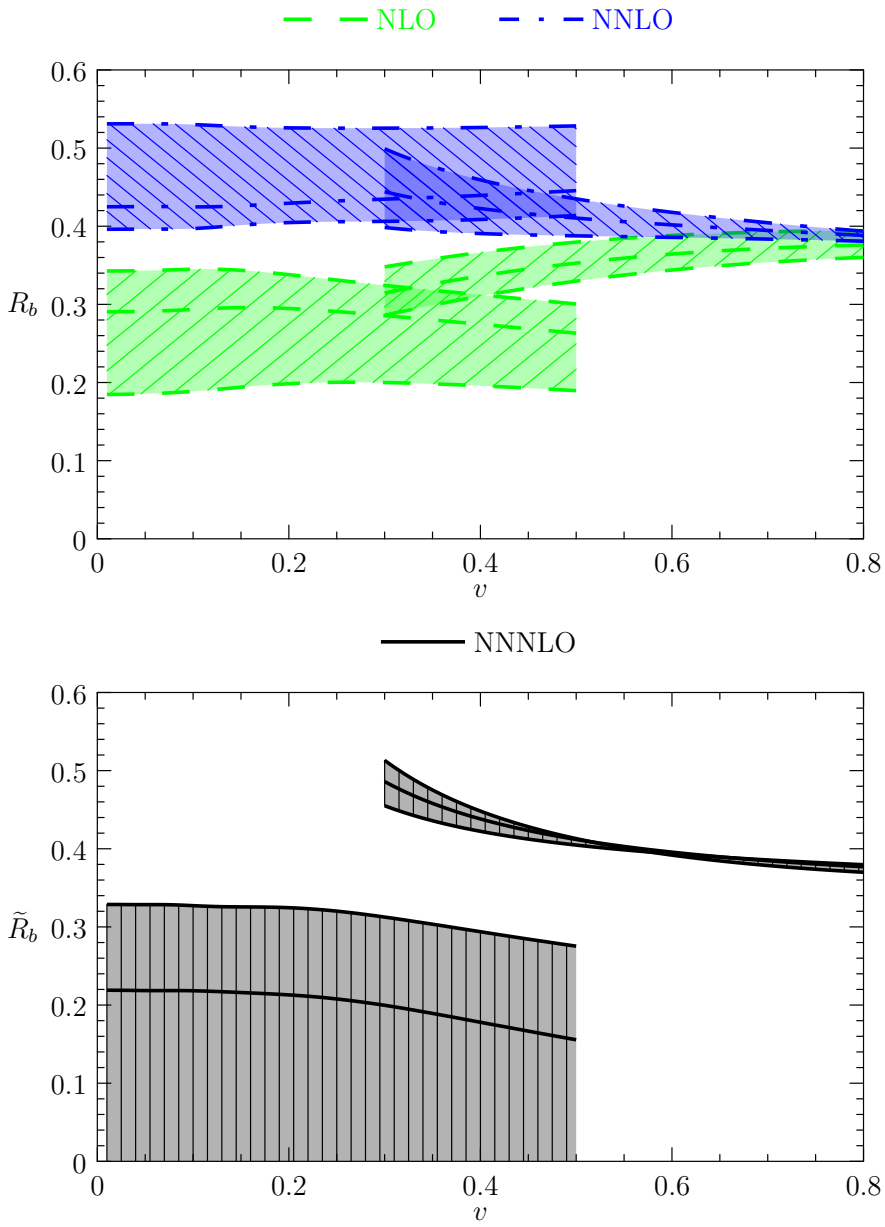

Figure 7.5.: Predictions for $\widetilde{R}_b$ as a function of $v = \sqrt{E/m_b}$ with a pole mass $m_b = 5\,\text{GeV}$ in non-relativistic perturbation theory (left curves) and conventional perturbation theory (right curves). The uncertainty from variations of the renormalization scale between 3 GeV and 10 GeV is illustrated by the shaded bands.

the hard matching coefficient of the vector current with the leading order Green function $G_0(E)$. In spite of the large parametric suppression, this term still shifts the normalized cross section R_b by ~ -0.2 for $v = 0.4$ due to the numerically large factor in the matching coefficient. This attribute persists at higher orders in conventional perturbation theory, e.g. the order $\alpha_s^4 v^0$ term from the product described above yields a further shift of -0.2 at $v = 0.4$. Thus, it may be possible that the discrepancy between predictions can be reconciled.

In practice, the determination of the potential contributions to the missing term is straightforward, but the complete extraction of the ultrasoft contribution appears to be rather involved and has not been attempted. The ultrasoft contributions to the logarithmic terms $v\alpha_s^3 \ln v$ and $v\alpha_s^3 \ln^2 v$ were however determined from the results of [73, 74]. One finds that neither the inclusion of the potential contributions nor of the full logarithmic terms can noticeably improve the behaviour of the Padé [181] or the analytical reconstruction of the polarization function based on the procedure developed in [182, 183]. The Padé becomes instable when partial contributions for the $v\alpha_s^3$ term are included and the result of the analytical reconstruction is hardly affected when only the logarithmic terms are included or breaks down when only the potential corrections are included.[7] We point out that the reconstructed results provide predictions for the missing coefficients based on the included input coefficients. The likely explanation for the instabilities appears to be that the reconstruction methods cannot accommodate inputs which show large discrepancy with respect to the predictions based on the lower order coefficients. We infer that the determination of the complete order $v\alpha_s^3$ coefficients is mandatory to settle the question, if the conventional perturbation theory result is affected significantly by the missing terms. Yet, even if the Padé result with complete input would join with the PNRQCD result for velocities $v \sim 0.4$, the issues with the behaviour of the PNRQCD expansion would remain.

The sum rule approach does, however, not depend on the behaviour of the continuum cross section by itself, but only on the moments, which are dominated by information on the $\Upsilon(NS)$ bound states. The moments are much less infrared sensitive than the continuum cross section, which must be due to cancellations between the continuum and resonance contributions. Therefore, one may also expect a partial cancellation of the scale dependence between the continuum and resonance part. In Figure 7.6, we show the continuum contribution to the tenth moment as a function of the renormalization scale $3\,\mathrm{GeV} < \mu < 10\,\mathrm{GeV}$ at different orders in PNRQCD perturbation theory. At NNNLO, the continuum contribution amounts to less than 5% for the central renormalization scale $\mu = m_b$ and about 15% for $\mu = 10\,\mathrm{GeV}$ and is significantly smaller than at lower orders. We find, however, that the inclusion of the continuum contribution reduces the renormalization scale dependence at each order as well as the difference between consecutive orders in perturbation theory. We conclude that the rather poor perturbative behaviour of the continuum cross section does not prohibit a determination of the bottom-quark mass from non-relativistic moments. Merging the non-relativistic and conventional perturbation theory does, however, not appear to be a viable option at NNNLO given the mismatch in the continuum

[7] This manifests by a wrong behaviour of the reconstructed polarization function in the limit $v \to 1$.

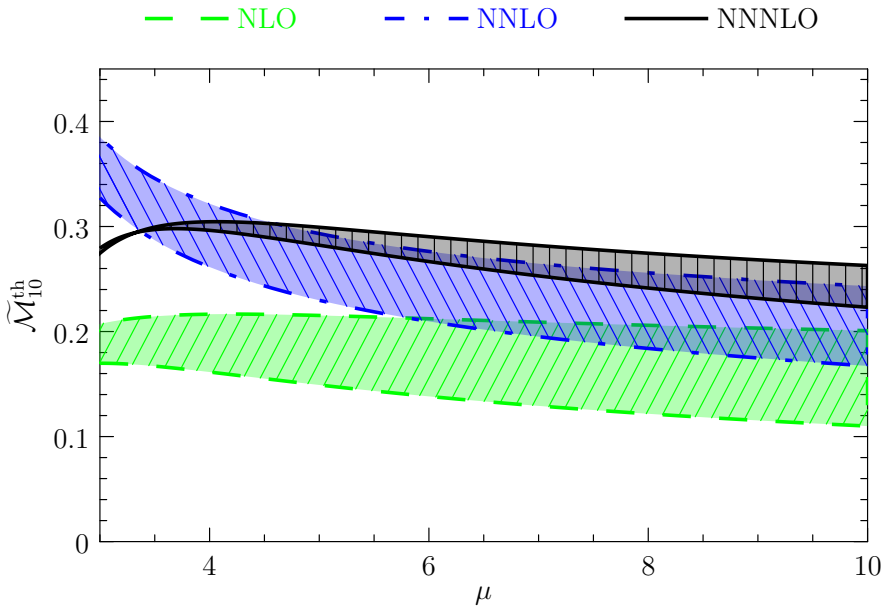

Figure 7.6.: The shaded bands show the continuum contribution to the tenth moment $\widetilde{\mathcal{M}}_{10}^{\rm th}$ in units of $(10\,\text{GeV})^{-20}$ for $m_b^{\rm PS}(2\,\text{GeV}) = 4.5\,\text{GeV}$ as a function of the renormalization scale. The lower boundaries of the bands are the resonance contributions, such that the upper boundaries correspond to the full moments.

cross section in Figure 7.5.

7.6.3. Determination of the bottom-quark mass

The bottom-quark mass can now be determined from the sum rule $\mathcal{M}_n^{\rm th}(m_b) = \mathcal{M}_n^{\rm exp}$ for moments with $n \approx 10$. We will first present results for the PS mass $m_b^{\rm PS}(\mu_f)$ obtained in the PSS scheme described in Section 7.4, which are then converted to the $\overline{\rm MS}$ scheme. The $\overline{\rm MS}$ mass is then also extracted directly in the MSS scheme.

We estimate the error on the extracted bottom-quark mass from a given moment $\mathcal{M}_n$ by adding the following sources of uncertainties in quadrature:

- Experimental uncertainty. As detailed in Section 7.2 we add in quadrature the uncertainties from the $\Upsilon(NS)$ masses and leptonic width, the BaBar data [32] and our estimate $R_b = 0.3 \pm 0.2$ for the continuum cross section at higher energies.

- Unknown higher-order corrections. We choose the PS mass itself as a renormalization scale for the extraction of the central value of $m_b^{\rm PS}$. Based on the discussion in Section 7.6.1, we estimate the error made by truncation of the theory moments at NNNLO in PNRQCD perturbation theory by varying the renormalization scale μ between 3 GeV and 10 GeV.

- Uncertainty in the strong coupling. We use $\alpha_s(m_Z) = 0.1184 \pm 0.0010$ as input for the strong coupling constant and evolve it down to the renormalization scale using four-loop running. The bottom quark is decoupled at $\mu_{\rm thr} = 2m_b$. Variations of the decoupling scale are numerically negligible.

- QED effects. Our analysis includes corrections from the leading order QED Coulomb potential, which formally modifies the moments at NLO in the counting $\alpha \sim \alpha_s^2$. The leading QED contribution is also taken into account in the conversion to the $\overline{\rm MS}$ scheme. The effect on the extracted bottom-quark mass amounts to less than 1 MeV in either scheme.

- Number of theoretical resonances. The infinite sum over the resonances in the theoretical moments (7.7), (7.13) is truncated after the sixth term. The corresponding error is approximated by the difference to the result, where only four resonances are considered.

- Scheme conversions. We determine PS masses for values of the subtraction scale μ_f between 1 GeV and 3 GeV. To determine the conversion error in the result for the PS mass $m_b^{\rm PS}(\mu_f = 2\,{\rm GeV})$, we convert the values to the PS mass at the central scale $\mu_f = 2\,{\rm GeV}$. The value for the PS mass is converted to the $\overline{\rm MS}$ mass $m_b^{\overline{\rm MS}}(\overline{\mu})$ at an intermediate scale $\overline{\mu}$, which is independent of the renormalization scale μ and varied between between 3 GeV and 10 GeV. This conversion is alway performed using the order α_s^4 relation, irrespective of the order of the moments. The scale-invariant mass $m_b^{\overline{\rm MS}}(m_b^{\overline{\rm MS}})$ is determined using renormalization group evolution at four-loop order. The small numerical uncertainty in the four-loop result for the pole-$\overline{\rm MS}$ mass relation [49] results in an error of just 2 MeV on the $\overline{\rm MS}$ mass. The overall scheme conversion error for the $\overline{\rm MS}$ bottom-quark mass is estimated by adding all uncertainties in quadrature.

- Charm-mass effects. The error due to missing third order charm-quark mass effects is estimated by taking the difference between the NNLO results with and without the corrections from a non-vanishing charm-quark mass (cf. Section 7.5).

- Non-perturbative effects. Following [158] (see also [184]), we estimate the size of non-perturbative corrections from the leading dimension-four gluon condensate correction in the operator product expansion (OPE) of the moments. The OPE is based on the hierarchy $m_b v^2 \sim m_b/n \gg \Lambda_{\rm QCD}$, which suggests a breakdown for moments with $n \sim 16$. Better insight on the validity of the OPE for the moments and the properties of the Υ resonances requires the calculation of higher-dimensional condensate corrections and α_s corrections to the dimension four condensate contribution. Some preliminary results are given in Section 8.

  Assuming the validity of the OPE for the tenth moment, we only find a tiny effect of less than 1 MeV on the value of the bottom-quark mass from the leading dimension

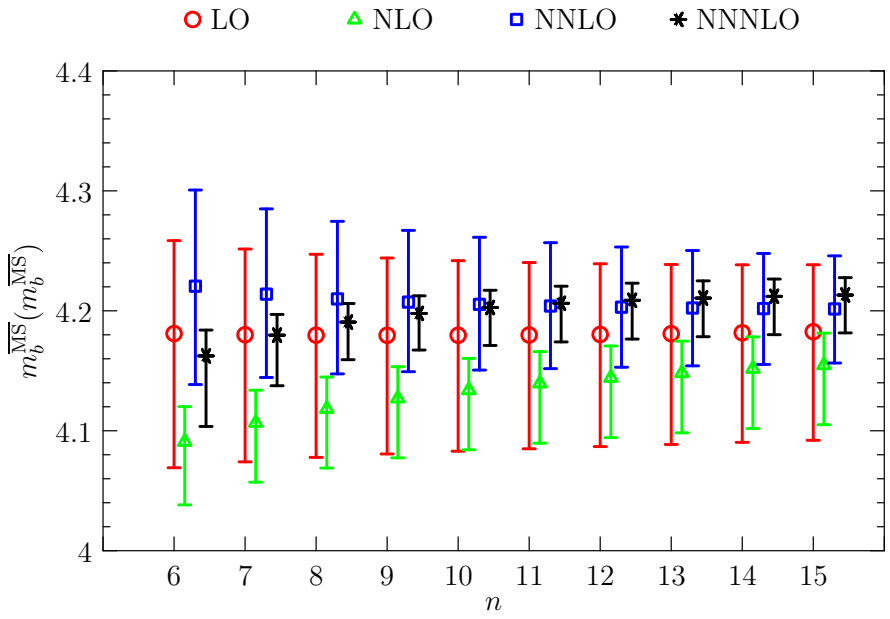

Figure 7.7.: Results for the $\overline{\rm MS}$ mass $m_b^{\overline{\rm MS}}(m_b^{\overline{\rm MS}})$ in units of GeV obtained from conversion of $m_b^{\rm PS}$ extracted from different moments $\widetilde{\mathcal{M}}_n$.

four condensate correction. This is rather surprising given that the respective corrections to the $\Upsilon(1S)$ are very large, when similar assumptions on the value of the gluon condensate and the scale choice are made (cf. the recent discussion in [86]). While the moments are constructed with cancellations of non-perturbative effects in mind, the extend of the cancellation is somewhat puzzling to us. The perturbative contribution from the $\Upsilon(1S)$ resonance makes up about 80% of the tenth moment, but the cancellation between non-perturbative effects on the $\Upsilon(1S)$ resonance contribution and the remainder is effective at about one part in 500. We therefore refrain from extending the sum rule rule analysis to values of n significantly larger than 10. A more detailed discussion of non-perturbative effects can be found in Section 8.

The $\overline{\rm MS}$ masses obtained from conversion of the PS mass extracted in the PSS scheme from unexpanded moments $\widetilde{\mathcal{M}}_n$ are shown in Figure 7.7 for $6 \leq n \leq 15$. The results from moments with $n \approx 10$ show good compatibility and there appears to be decent convergence of the values at different orders in perturbation theory. The behaviour becomes increasingly worse for lower values of n, where relativistic corrections are more important and the sensitivity to the poorly behaved continuum cross section (cf. section 7.6.2) is enhanced. Figure 7.8 demonstrates the decrease of the bottom mass values extracted from lower n, which can be attributed to an increased weight of the small NNNLO continuum cross section in the moments. The effect is even more pronounced for results obtained from expanded moments $\mathcal{M}_n$ (see lower panel).

It is apparent from Figure 7.8 that there is a sizeable difference between the masses

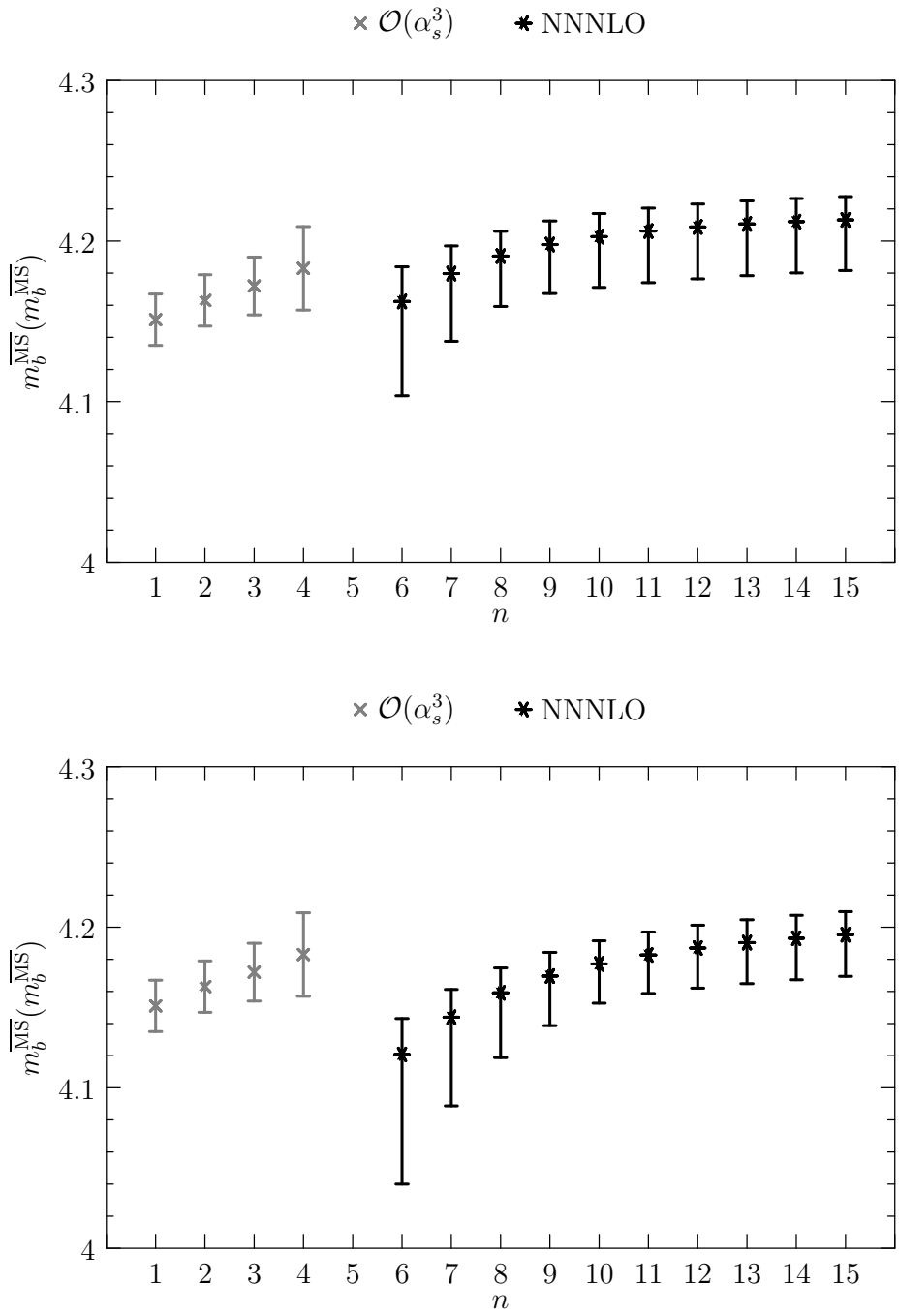

Figure 7.8.: NNNLO results for $m_b^{\overline{\rm MS}}(m_b^{\overline{\rm MS}})$ in units of GeV extracted from unexpanded moments $\widetilde{\mathcal{M}}_n^{\rm th}$ (upper panel) and expanded moments $\mathcal{M}_n^{\rm th}$ (lower panel) in the PSS scheme. We show the mass values from the relativistic moments with $n \leq 4$ as obtained in [33] for comparison.

determined from unexpanded moments $\widetilde{\mathcal{M}}_n^{\rm th}$ and expanded moments $\mathcal{M}_n^{\rm th}$. The expansion of the kinetic energy factor shifts the $\overline{\rm MS}$ mass, extracted from the tenth moment, by as much as $-26\,\text{MeV}$. This effect is however contained in our estimate for the perturbative uncertainty based on renormalization scale variation.

As stated in Section 7.4, we therefore use the unexpanded moments to determine our result and only consider scale variation to determine the perturbative uncertainty. Our final results for the PS and $\overline{\rm MS}$ masses are based on the tenth moment $\widetilde{\mathcal{M}}_{10}^{\rm th}$, which yields

$$\begin{aligned} m_b^{\rm PS}(2\,\text{GeV}) &= \big[4.532^{+0.002}_{-0.035}(\mu) \pm 0.010(\alpha_s)^{+0.003}_{-0}(\text{res}) \pm 0.001(\text{conv}) \\ &\quad \pm 0.002(\text{charm})^{+0.007}_{-0.013}(n) \pm 0.003(\text{exp})\big]\,\text{GeV} \\ &= 4.532^{+0.013}_{-0.039}\,\text{GeV}\,. \end{aligned} \tag{7.18}$$

$$\begin{aligned} m_b^{\overline{\rm MS}}(m_b^{\overline{\rm MS}}) &= \big[4.203^{+0.002}_{-0.031}(\mu) \pm 0.002(\alpha_s)^{+0.003}_{-0}(\text{res})^{+0.013}_{-0.004}(\text{conv}) \\ &\quad \pm 0.002(\text{charm})^{+0.006}_{-0.012}(n) \pm 0.003(\text{exp})\big]\,\text{GeV} \\ &= 4.203^{+0.016}_{-0.034}\,\text{GeV}\,. \end{aligned} \tag{7.19}$$

In these results, we have also taken into account an additional contribution to the uncertainty from the difference of the mass values obtained from $\widetilde{\mathcal{M}}_8^{\rm th}$ and $\widetilde{\mathcal{M}}_{12}^{\rm th}$ to the central result, which is denoted with the label (n). It is added in quadrature to the other sources of uncertainties discussed above. We observe that the uncertainty related to the value of the strong coupling constant is significantly reduced by the conversion from the PS to the $\overline{\rm MS}$ scheme.

Our result (7.19) for the $\overline{\rm MS}$ mass is compatible with other recent precision determinations from relativistic sum rules at NNNLO in conventional perturbation theory [33, 185] and partial NNNLO large-n sum rules [186]. We provide a more detailed comparison in Section 7.6.4.

We discussed the possibility to determine the bottom-quark $\overline{\rm MS}$ mass directly from the moments expressed in the MSS scheme in Section 7.4. Based on the tenth unexpanded moment we obtain the result

$$\begin{aligned} m_b^{\overline{\rm MS}}(m_b^{\overline{\rm MS}}) &= \big[4.204^{+0.000}_{-0.019}(\mu) \pm 0.002(\alpha_s)^{+0.003}_{-0}(\text{res})^{+0.002}_{-0.005}(\text{conv}) \\ &\quad \pm 0.002(\text{charm})^{+0.007}_{-0.013}(n) \pm 0.003(\text{exp})\big]\,\text{GeV} \\ &= 4.204^{+0.008}_{-0.024}\,\text{GeV}\,. \end{aligned} \tag{7.20}$$

The central value is (almost) unchanged with respect to (7.19), but the use of the MSS scheme leads to significantly smaller estimates for the perturbative and scheme conversion uncertainty. Since the difference between masses extracted from "unexpanded" and "expanded" moments is not covered, we feel that (7.19) better reflects the actual uncertainties in the non-relativistic sum rule approach and adopt it as our final result.

7.6.4. Comparison with previous works

Our result (7.19) for the bottom-quark $\overline{\rm MS}$ mass is in very good agreement with the PDG [24] average $m_b^{\overline{\rm MS}}(m_b^{\overline{\rm MS}})_{\rm PDG} = 4.18 \pm 0.03$ GeV. A comprehensive overview of results

Analysis	Central moment	Perturbative order	$m_b^{\overline{\rm MS}}(m_b^{\overline{\rm MS}})$ [GeV]
CKMMMSS [33]	$\mathcal{M}_2$	α_s^3	4.163 ± 0.016
DHM [185]	$\mathcal{M}_2$	α_s^3	4.176 ± 0.023
HRS [175]	$\mathcal{M}_{10}$	NNLO + NNLL	4.235 ± 0.055
PZ [186]	$\mathcal{M}_{15}$	approx. NNNLO	4.169 ± 0.009
This work	$\mathcal{M}_{10}$	NNNLO	$4.203^{+0.016}_{-0.034}$

Table 7.3.: Values of the scale invariant bottom-quark $\overline{\rm MS}$ mass obtained from recent sum rule analyses. We have added the experimental and theoretical errors quoted in the HRS analysis in quadrature.

for the bottom-quark mass can be found in [24]. We therefore focus on a detailed comparison to other recent precision determinations based on sum rules. The values shown in Table 7.3 are in decent agreement and we will discuss the differences in the analyses in the following.

Chetyrkin et al. (CKMMMSS) [33]

The analysis of CKMMMSS is based on relativistic moments $\mathcal{M}_n$ with $n \leq 4$, which are determined in conventional perturbation theory up to the order α_s^3. The determination of the experimental moments only differs in the estimate for the high-energy continuum. Due to the large sensitivity of the relativistic moments to the continuum, CKMMMSS must rely on stronger assumptions than we do. They assume that the perturbative QCD prediction is valid above 11.24 GeV and interpolate linearly between this region and the last BaBar data point at 11.2062 GeV. This leads to a peculiar jump between the BaBar data and the continuum and to a very small uncertainty estimate from the continuum region because the uncertainty of the perturbation theory result is tiny. In [160], CKMMMSS contemplate two options for relaxing the assumptions and smoothing out the jump. In particular, we find their Option A compelling, which assumes that the perturbative result is only valid above 13 GeV and interpolates linearly in between. This leads to an identical (up to 1 MeV) central value of $m_b^{\overline{\rm MS}}(m_b^{\overline{\rm MS}}) = 4.183\,\text{GeV}$ for the masses extracted for the moments with $n = 1, 2, 3$ and significantly better agreement with our result (7.19). However, CKMMMSS stick to their original result because "the shift (for $n = 2$) is (...) only slightly higher than the uncertainty of 16 MeV." [160]

To estimate the uncertainties from higher orders in perturbation theory, CKMMMSS fix the scale $\overline{\mu}$ for the $\overline{\rm MS}$ mass to the renormalization scale and vary them simultaneously between 5 GeV and 15 GeV. Our approach of varying the scales independently leads to a more conservative result, which makes direct comparison of the perturbative uncertainties difficult.

Dehnadi et al. (DHM) [185]

DHM have performed an analysis based on the same theoretical inputs as CKMMMSS, but applying different systematics and using other values for the experimental moments. For the latter a smooth fit between the BaBar data and the perturbative result for the continuum is performed, which coincides with the perturbative result for $\sqrt{s} \gtrsim 11.5\,\text{GeV}$. Thus, the experimental moments lie in between those of [33] and Option A of [160]. Similar to our approach, DHM vary the scale μ for the strong coupling constant and the scale $\overline{\mu}$ for the $\overline{\text{MS}}$ mass independently. DHM then argue that this might overestimate the error. Thus, the perturbative uncertainty estimate from independent variation is reduced by excluding a subset of $(\mu, \overline{\mu})$ values based on a convergence test. Through an extensive analysis, DHM demonstrate the stability of the result under modifications of the analysis strategy.

The final result of DHM has a larger error than CKMMMSS due to a more conservative estimate for the uncertainty of the experimental continuum and the independent scale variation. It is in good agreement with our result and the one of CKMMMSS. It is interesting that independent scale variation in the low-n moments leads to a basically identical overall error budget compared to our value, although the relativistic and non-relativistic sum rule analysis have completely different systematics.

Hoang, Ruiz-Femenía and Stahlhofen (HRS) [175]

The analysis of HRS uses moments $\mathcal{M}_n$ with $6 \leq n \leq 14$ and the default value of $n = 10$ in the framework of vNRQCD [187]. Besides Coulomb singularities $\alpha_s\sqrt{n}$, HRS also resum Coulomb logarithms $\alpha_s \ln \sqrt{n}$ to NNLO + (partial) NNLL accuracy. Like CKMMMSS and DHM, they estimate the unknown experimental high-energy continuum by the perturbative QCD prediction, but assume an uncertainty of 10%. Within the errors, their experimental moments are in agreement with ours.

HRS apply the sum rule to first extract a $1S$ mass and then convert to the bottom-quark $\overline{\text{MS}}$ mass with three-loop accuracy. The conversion error is estimated to be 15 MeV, which is about a factor two larger than what we find for the PS-$\overline{\text{MS}}$ conversion based on the four-loop relation. They also find an almost complete cancellation of the α_s dependence in the conversion from a threshold mass scheme to the $\overline{\text{MS}}$ mass.

Our central values for the $\overline{\text{MS}}$ mass at NNLO and NNNLO almost coincide, but are smaller by about 35 MeV and 70 MeV than the NNLL and NNLO results obtained by HRS. The two analyses differ in a number of aspects. As mentioned above, HRS extract the 1S instead of the PS mass before conversion to the $\overline{\text{MS}}$ scheme, which is done at three-loop accuracy. Furthermore, they expand the factor $1/s^{n+1}$ in the moments non-relativistically and expand the resonance poles, the 1S-pole mass relation and the kinetic factor $1/s$ in the vacuum polarization function. HRS use a moment-dependent renormalization scale $\mu = m_b(1/\sqrt{n} + 0.2)$ instead of our fixed $\mu = m_b$, but apply the hard scale for the matching coefficients of the vector current. Charm-mass effects are not included in the analysis of HRS because they are currently unknown in their renormalization group improved framework. When adopting our analysis to the NNLO one of HRS, we find that

the differences in central values are mainly due to the different scale choice. The precise size of the remaining changes in the analysis depends on the order in which they are implemented, but the effects are only moderate in size. We were able to reproduce the NNLO value obtained by HRS up to a negligible difference of 2 MeV.

Based on scale variation, HRS arrive at an estimate for the perturbative uncertainty at NNLO, which is about twice as large as ours. This originates from renormalization scale variations to lower values, where there appears to be a breakdown of non-relativistic fixed-order perturbation theory [88]. Based on the very good convergence of the successive perturbative approximations from NNLO to NNNLO at the scale $\mu = m_b$ (see figure 7.4), we believe that our assignment for the error due to truncation of the perturbative expansion is sufficiently conservative.

The resummation of logarithms performed by HRS reduces the scale dependence and leads to a stabilization of the result for lower scales in particular. Thus, the large difference in the bottom-quark masses at NNLO from the lower renormalization scale is partially compensated through the resummation and HRS obtain the value quoted in Table 7.3 as their final result at NNLL. Previously, a less complete renormalization group improved analysis obtained $m_b^{\overline{\rm MS}}(m_b^{\overline{\rm MS}}) = 4.19 \pm 0.06$ at NNLO + partial NNLL [176].

Penin and Zerf (PZ) [186]

The analysis of PZ also employs non-relativistic sum rules, but uses still higher moments with a central value of $n = 15$. The validity of the OPE, which is based on the hierarchy $n\Lambda_{\rm QCD}/m_b$, is dubious for these high values (see the discussion in Section 8). Assuming it is valid, the result for the bottom-quark $\overline{\rm MS}$ mass is increased by about 12 MeV when using $n = 15$ instead of $n = 10$.

For $n \sim 15$, the moments are dominated by the Υ resonances, which PZ exploit to neglect the experimental high-energy continuum. PZ compute the theory moments using the complete NNNLO PNRQCD prediction for the resonances, but employ an estimate of $R_b = \rho\, Z_1^{\rm NNNLO}/Z_1^{\rm NNLO} R^{\rm NNLO}$, $0.5 \le \rho \le 2$, to estimate the effects of the (then) unknown NNNLO contribution to the continuum. The comparison with our calculation shows that the true result lies somewhat below the range of values covered by variation of the auxiliary parameter ρ. Replacing the NNNLO continuum with the rescaled NNLO approximation increases the resulting mass value extracted from $\mathcal{M}_{15}$ by about 5 MeV. PZ however expand the factor $1/s$ in the polarization function (cf. Section 7.4), which lowers the mass by 17 MeV. PZ forgo the use of an intermediate threshold mass and directly extract the $\overline{\rm MS}$ mass. The effect on the final value is minimal, as can be seen from the comparison of (7.20) and (7.19). Based on the findings of [168], PZ apply an ad hoc mass shift of -25 ± 5 MeV to account for the effects of a non-vanishing charm-quark mass, while our computation yields a shift of only about -3 MeV (see the discussion in Section 7.5). In the absence of QED and charm-mass effects and using the estimate [54] for the four-loop contribution to the pole-$\overline{\rm MS}$ mass relation employed by PZ, the central values of PZ and our analysis coincide (4.194 GeV vs. 4.195 GeV).

PZ claim a strikingly small overall uncertainty of only 9 MeV in the value of the bottom-

quark mass. The three dominant sources of uncertainties considered by us (scale variation, scheme conversion and variation of n) are each similar in size or even exceed this value. The confrontation of their error estimate of 2.2 MeV for the scheme conversion with the shift of 13 MeV implied by the use of the exact four-loop pole-$\overline{\text{MS}}$ mass relation [49] demonstrates the severe underestimation of some sources of uncertainties. We believe that this is also the case for the perturbative uncertainty, where PZ assume 2.1 MeV.

8. Gluon condensate corrections

The key virtue of the sum rule approach is that non-perturbative effects can be included systematically by means of an OPE. In Section 7 we have only considered the perturbative contributions with the understanding that non-perturbative effects should be small for moderate $n \sim 10$. Here, we demonstrate that this is indeed the case and then discuss the spectroscopy and leptonic decays of the $\Upsilon(NS)$ states. The leading dimension four condensate contributions to Bottomonium states have first been evaluated in [80, 188]. This has been extended to the dimension six contribution in [189]. In the context of non-relativistic sum rules, the leading non-perturbative corrections were first discussed in [158]. For the relativistic moments, $\mathcal{O}(\alpha_s)$ corrections to the dimension four condensate correction [190,191], as well as contributions from higher-dimensional condensates [192,193] are known. We refer to [194–196] for more general reviews on condensate corrections.

The OPE relies on the QCD scale being small with respect to the hard, soft and ultrasoft scales that govern the perturbative evaluation of the moments. Accordingly, the gluon field in the PNRQCD Lagrangian can be split into two parts

$$A_\mu(t,\mathbf{x}) = A_\mu^{\mathrm{us}}(t,\mathbf{x}) + A_\mu^{\mathrm{bg}}(t,\mathbf{x}). \tag{8.1}$$

The superscripts denote the ultrasoft and the non-perturbative background gluon field. The latter can be multipole-expanded in the time and spatial components because it only fluctuates over scales of the order $1/\Lambda_{\mathrm{QCD}}$ and can neither resolve the dynamics of the potential heavy quark nor the ultrasoft massless fields. Thus, it behaves like a constant (in time and space) background field. A convenient gauge choice for background fields is given by Fock-Schwinger gauge

$$\mathbf{x}\cdot\mathbf{A}^{\mathrm{bg}}(t,\mathbf{x}) = 0, \qquad A_0^{\mathrm{bg}}(t,\mathbf{0}) = 0, \tag{8.2}$$

which removes the coupling of the heavy quarks to the A_0^{bg} field.[1] The PNRQCD Lagrangian then receives an additional term

$$\mathcal{L}_{\text{non-perturbative}} = \psi^\dagger\left(-g_s\mathbf{x}\cdot\mathbf{E}^{\mathrm{bg}}(0,\mathbf{0}) + \dots\right)\psi + \chi^\dagger\left(-g_s\mathbf{x}\cdot\mathbf{E}^{\mathrm{bg}}(0,\mathbf{0}) + \dots\right)\chi, \tag{8.3}$$

which is of the order $m_b^2 v^2 \Lambda_{\mathrm{QCD}}^2$ because the strong coupling at the QCD scale is counted as order one. This implies that the chromoelectric dipole coupling to the background field is suppressed by $v(\Lambda_{\mathrm{QCD}}/(m_b v^2))^2$ with respect to the leading order Lagrangian. The

[1] The gluon propagator in this gauge contains spurious singularities as discussed e.g. in [197]. Therefore this gauge will not be applied to the ultrasoft gluon modes, where its naive use can lead to inconsistencies as observed in [198].

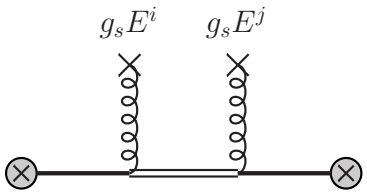

Figure 8.1.: Leading dimension four condensate contribution to the Green function. The single and double lines denote the LO color-singlet and color-octet Green functions, respectively.

multipole-expanded coupling of the background field to ultrasoft gluons is only relevant at higher orders. There is obviously no contribution from a single insertion of the chromomagnetic dipole operator (8.3) into the Green function because the vacuum expectation value of $\mathbf{E}^{\mathrm{bg}}$ vanishes, as can be seen for example by Lorentz invariance. The vacuum expectation value of the double insertion of (8.3) is therefore the leading non-perturbative correction. It can be related to the well-known gluon condensate by making use of Lorentz and $SU(3)_c$ invariance

$$\langle 0|E_i^A(0)E_j^B(0)|0\rangle = -\frac{1}{(N_c^2-1)d(d-1)}\delta^{AB}\delta^{ij}\langle 0|G^C_{\alpha\beta}(0)G^C_{\alpha\beta}(0)|0\rangle. \tag{8.4}$$

We evaluate this contribution in Section 8.1 and give some preliminary results for the dimension six condensate contribution and the $\mathcal{O}(\alpha_s)$ corrections to the dimension four contribution in Section 8.2 and 8.3, respectively. Finally, the phenomenological impact is studied in Section 8.4.

8.1. Dimension four contribution at leading order

The leading condensate contribution to the Green function comes from the diagram in Figure 8.1 and is given by

$$\begin{aligned}\delta_{\langle G^2\rangle}G(E) &= \langle \mathbf{0}|\hat{G}(E)i\hat{\mathcal{D}}i\hat{G}(E)i\hat{\mathcal{D}}i\hat{G}(E)|\mathbf{0}\rangle \\ &= \left(\frac{g_s}{2}\right)^2\langle 0|E_i^A(0)E_j^B(0)|0\rangle\langle \mathbf{0}|\hat{G}(E)\xi^A\hat{x}^i\hat{G}(E)\xi^B\hat{x}^j\hat{G}(E)|\mathbf{0}\rangle,\end{aligned} \tag{8.5}$$

where $\hat{\mathcal{D}}$ is the chromoelectric dipole operator from (8.3) and $\xi^A = T^{(3)A}\otimes 1^{(\bar{3})} - 1^{(3)}\otimes T^{(\bar{3})A}$. The hierarchy between the QCD scale and the perturbative scales has been used to factorize the physical state into a direct product of the quarkonium and the gluonic vacuum state. This is possible because interactions between the heavy quarks and gluons are treated as perturbations. With (8.4), the color identity $T^{(\bar{3})A}_{ab} = -T^{(3)A}_{ba}$ and the decomposition

$$\hat{G}(E) = \hat{G}^{(0)}(E)P_0 + \hat{G}^{(8)}(E)P_8, \tag{8.6}$$

with the color-singlet and color-octet projectors (with the color indices attached counterclockwise to the external legs of the Green function shown in Figure 3.29, starting at a for the outgoing quark, see also [60])

$$P_0 = \frac{1}{N_c}\delta_{bc}\delta_{da}, \qquad P_8 = 2T^A_{bc}T^A_{da}, \tag{8.7}$$

we obtain

$$\delta_{\langle G^2\rangle}G(E) = -\frac{2\langle 0|\pi\alpha_s G^2|0\rangle}{N_c d(d-1)}\langle \mathbf{0}|\hat{G}^{(0)}(E)\hat{x}^i\hat{G}^{(8)}(E)\hat{x}^i\hat{G}^{(0)}(E)|\mathbf{0}\rangle. \tag{8.8}$$

The superscripts (0) and (8) denote the color-singlet and color-octet Green function (see also [60]). The expression (8.8) is free of divergences and can be computed in $d = 4$ dimensions in configuration space (cf. [184])

$$\delta_{\langle G^2\rangle}G(E) = -\frac{\langle 0|\pi\alpha_s G^2|0\rangle}{18}\int d^3\mathbf{r}\int d^3\mathbf{r}'\,(\mathbf{r}\cdot\mathbf{r}')\,G^{(0)}(0,\mathbf{r};E)G^{(8)}(\mathbf{r},\mathbf{r}';E)G^{(0)}(\mathbf{r}',0;E), \tag{8.9}$$

We use the integral representation (3.34) for the color-singlet and the sum representation (3.35) for the color-octet Green function. In the latter, we have to replace λ by $\lambda^{(8)} = (D_8/(-C_F))\lambda = -\lambda/8$ to account for the different color factor $D_8 = C_A/2 - C_F$ instead of $-C_F$ in the LO Coulomb potential. The angular integrals in (8.9) project out the P-wave component of the color-octet Green function. We obtain

$$\delta_{\langle G^2\rangle}G(E) = -\frac{\pi^2}{18}K_4\frac{m^2\alpha_s C_F}{4\pi}\lambda^5\sum_{s=0}^{\infty}\frac{s!H_{\langle G^2\rangle}(s)^2}{(s+3)!(s+2+\lambda/8)}, \tag{8.10}$$

where

$$K_4 = \frac{\langle\frac{\alpha_s}{\pi}G^2\rangle}{m_b^4(\alpha_s C_F)^6}. \tag{8.11}$$

The coefficients can be integrated directly

$$\begin{aligned} H_{\langle G^2\rangle}(s) &= \int_0^\infty dt\left(\frac{1+t}{t}\right)^\lambda\int_0^\infty d\rho\rho^4 e^{-\rho(1+t)}L_s^{(3)}(\rho) \\ &= -\frac{(s+3)!}{s!}\lambda\frac{\Gamma(5)\Gamma(s-\lambda)}{\Gamma(5+s-\lambda)}. \end{aligned} \tag{8.12}$$

The sum in (8.10) yields

$$\begin{aligned}\delta_{\langle G^2\rangle}G(E) = -\frac{\pi^2}{18}K_4\frac{m^2\alpha_s C_F}{4\pi}\lambda^5\Bigg\{&\frac{8}{9(8-9\lambda)^2(16-9\lambda)^2(16+9\lambda)^2}\big(14155776+43024384\lambda\\&+212248576\lambda^2-136918656\lambda^3-607347072\lambda^4+444623094\lambda^5\\&+321157305\lambda^6-245939085\lambda^7-47534445\lambda^8+37200870\lambda^9\big)\\&+\frac{16\lambda^2\left(26624-101216\lambda^2+109935\lambda^4-25515\lambda^6\right)}{16384-25920\lambda^2+6561\lambda^4}\left(\psi_1(\lambda)-\frac{\pi^2}{\sin^2(\pi\lambda)}\right)\\&+\frac{134217728\lambda\left(64-\lambda^2\right)}{9\left(16384-25920\lambda^2+6561\lambda^4\right)^2}\left(\psi(1-\lambda)-\psi\left(2+\frac{\lambda}{8}\right)\right)\Bigg\}.\end{aligned} \tag{8.13}$$

The condensate corrections to the S-wave energy levels E_N and the wave functions at the origin $|\psi_N(0)|^2$ can be obtained from the expansion of (8.13) for λ near positive integer values N. We parametrize these corrections as

$$E_N = E_N^{(0)}\sum_{k,l=0}^{\infty} e_N^{(k,l)}, \tag{8.14}$$

$$|\psi_N(0)|^2 = |\psi_N^{(0)}(0)|^2\sum_{k,l=0}^{\infty} f_N^{(k,l)}, \tag{8.15}$$

where $e_N^{(k,l)}, f_N^{(k,l)}$ are the $(\Lambda_{\rm QCD}/(m_b\alpha_s^2))^k\alpha_s^l$ corrections to the Nth energy level and wave function, respectively. We obtain

$$e_N^{(4,2)} = -\frac{\pi^2}{18}K_4\frac{32N^6\left(25515N^6-109935N^4+101216N^2-26624\right)}{\left(6561N^4-25920N^2+163841\right)}, \tag{8.16}$$

$$\begin{aligned}f_N^{(4,2)} = \frac{\pi^2}{18}K_4&\frac{32N^6}{9\left(6561N^4-25920N^2+163841\right)^2}\\&\times\Big(4519905705N^{10}-36791660430N^8+101725313184N^6\\&-112065638400N^4+50981371904N^2-7583301632\Big),\end{aligned} \tag{8.17}$$

in agreement with the results from [80, 188].

8.2. Dimension six contribution

The dimension six contribution to the energy levels and wave functions has been determined in [189]. Unfortunately, the expressions for the correction to the Green function have not been given there (although they were computed), so we repeat the calculation here following [189].

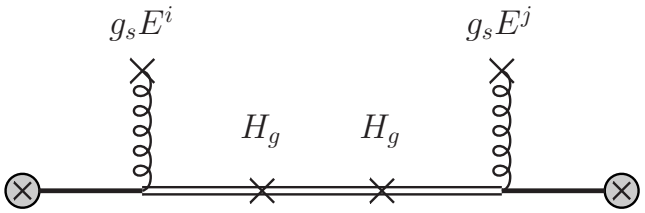

Figure 8.2.: Leading dimension six condensate contribution to the Green function.

At higher dimensions, the leading condensate corrections arise from insertions of the gluon Hamiltonian between the two insertions of the chromoelectric dipole operator [189]. These contributions are of the order $\alpha_s^2(\Lambda_{\rm QCD}/(m_b v^2))^{4+n_H}$, where n_H counts the insertions of the gluon Hamiltonian and must be even (cf. [189]). In comparison, additional insertions of (8.3) count as $\alpha_s^{n_\mathcal{D}}(\Lambda_{\rm QCD}/(m_b v^2))^{2n_\mathcal{D}}$, where $n_\mathcal{D} \geq 2$ is the number of dipole operators, and are thus subleading. The dimension six contribution shown in Figure 8.2 takes the form

$$\begin{aligned}\delta_6 G(E) &= \langle \mathbf{0}|\hat{G}(E) i\hat{\mathcal{D}} i\hat{G}(E) i\hat{\mathcal{H}}_g i\hat{G}(E) i\hat{\mathcal{H}}_g i\hat{G}(E) i\hat{\mathcal{D}} i\hat{G}(E)|\mathbf{0}\rangle \\ &= \frac{g_s^2}{4}\langle 0|E_i^A(0)\mathcal{H}_g\mathcal{H}_g E_j^B(0)|0\rangle\langle \mathbf{0}|\hat{G}(E)\xi^A\hat{x}^i\hat{G}(E)\hat{G}(E)\hat{G}(E)\xi^B\hat{x}^j\hat{G}(E)|\mathbf{0}\rangle,\end{aligned} \tag{8.18}$$

where $\mathcal{H}_g$ is the gluon Hamiltonian. The condensate has been worked out in [189]. We obtain

$$\delta_6 G(E) = O_1\langle \mathbf{0}|\hat{G}^{(0)}(E)\hat{x}^i\hat{G}^{(8)}(E)\hat{G}^{(8)}(E)\hat{G}^{(8)}(E)\hat{x}^i\hat{G}^{(0)}(E)|\mathbf{0}\rangle, \tag{8.19}$$

where in $d = 4$

$$O_1 = \frac{1}{108}\left[\frac{2^6}{3}\pi^2\alpha_s^2\langle 0|\bar{q}q|0\rangle^2 + \frac{3}{4}\langle G^3\rangle\right]. \tag{8.20}$$

The calculation is done in configuration space. Again, the angular integrals project out the P wave components of the color octet Green functions. We find

$$\begin{aligned}\delta_6 G(E) = K_6\frac{m^2\alpha_s C_F}{4\pi}\lambda^9\sum_{s_1=0}^{\infty}\sum_{s_2=0}^{\infty}\sum_{s_3=0}^{\infty}&\frac{s_1! H_{\langle G^2\rangle}(s_1)}{(s_1+3)!(s_1+2+\lambda/8)} \\ &\frac{s_2! K_1(s_1,s_2)K_1(s_2,s_3)}{(s_2+3)!(s_2+2+\lambda/8)}\frac{s_3! H_{\langle G^2\rangle}(s_3)}{(s_3+3)!(s_3+2+\lambda/8)},\end{aligned} \tag{8.21}$$

where

$$K_6 = \frac{O_1}{m_b^6(\alpha_s C_F)^{10}}. \tag{8.22}$$

and the function K_1 reads

$$\begin{aligned}K_1(a,b) &= \int_0^\infty d\rho\rho^4 e^{-\rho}L_a^{(3)}(\rho)L_b^{(3)}(\rho) \\ &= \frac{(\max(a,b)+3)!}{\min(a,b)!}\left[(2a+4)\delta_{a,b} - \delta_{a,b-1} - \delta_{a-1,b}\right].\end{aligned} \tag{8.23}$$

Since $K_1(a,b)$ is only non-vanishing for $|a-b| \leq 1$ the triple sum in (8.21) reduces to a single sum, which can be solved in terms of polygamma functions.

For the dimension six corrections to the energy levels and wave functions, we obtain

$$\begin{aligned} e_N^{(6,2)} &= K_6 \frac{4096N^{10}}{81\,(9N^2-64)\,(6561N^4-25920N^2+16384)^3} \\ &\quad \times\big[65241222927111N^{16}-1327743092409993N^{14}+10789755579716526N^{12} \\ &\quad -46158344158975776N^{10}+114216987240880128N^8-168309372752363520N^6 \\ &\quad +145600287615221760N^4-68153404341354496N^2+13295844358881280\big], \end{aligned} \tag{8.24}$$

$$\begin{aligned} f_N^{(6,2)} &= K_6 \frac{4096N^{10}}{81(64-9N^2)^2(1024-81N^2)(6561N^4-25920N^2+16384)^4} \\ &\quad \times\big[15602337339123058627 95N^{24}-6830286524297400399757 2N^{22} \\ &\quad +12578355878970418796814 66N^{20}-12922847845013954087408448N^{18} \\ &\quad +82659284132080163141376000N^{16}-34741428180504019854793113 6N^{14} \\ &\quad +98556319067506466530472755 2N^{12}-19060521046844362938258554 88N^{10} \\ &\quad +25046284234897074015499714 56N^8-21951178685012211125389885 44N^6 \\ &\quad +12270494955799097014715678 72N^4-39551953582322606859825971 2N^2 \\ &\quad +55919902706900903797981184\big]. \end{aligned} \tag{8.25}$$

The correction to the energy levels is identical to the result of [189]. Our result for the wave function correction however differs from the one in [189] in the coefficients in the square bracket that multiply factors of N. The constant term is in agreement. Numerically the difference is tiny, dropping from 3 permille for $N=1$ to 1.8 permille for $N=10$.

8.3. Dimension four contribution at NLO: Potential contributions

There is a number of effects that could possibly contribute to the $\mathcal{O}(\alpha_s)$ corrections to the dimension four condensate contribution to the Green function:

- An additional insertion of the NLO Coulomb potential, see Figure 8.3.
- An ultrasoft gluon correction from the color charge term $g_s A_0^{\mathrm{us}}(t,\mathbf{0})$ coupling to the color-octet state, see Figure 8.4.
- An α_s correction to the Wilson coefficient of the chromoelectric dipole operator (8.3). The Wilson coefficient was found to be trivial up to $\mathcal{O}(\alpha_s^2)$ in [199].
- $\mathcal{O}(m_b^2 v^3 \Lambda_{\mathrm{QCD}}^2)$ terms in the multipole expansion (8.3) of the gluon coupling to heavy quarks in the spatial components. They are identical to the multipole expansion of the coupling to the ultrasoft gluon field and were determined in [200], where they are

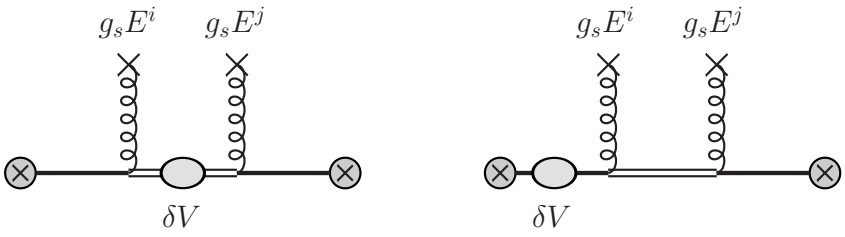

Figure 8.3.: Potential corrections to the dimension four condensate contribution to the Green function.

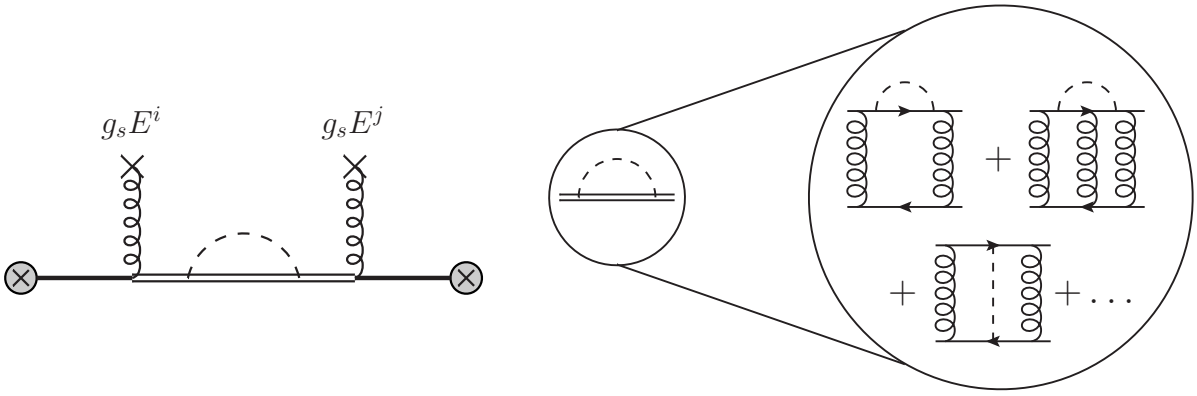

Figure 8.4.: Ultrasoft correction to the dimension four condensate contribution to the Green function.

denoted as $h_{SO}^{(1,0)}$. There is no contribution from these coupling because they either have vanishing tree level Wilson coefficients and are thus suppressed by an additional power of $\alpha_s \sim v$ or involve the chromomagnetic instead of the chromoelectric field, which only yields a vanishing condensate $\left\langle 0 \left| E_i^A B_j^B \right| 0 \right\rangle = 0$ at NLO.

- Contrary to the ultrasoft gluon-heavy quark coupling, the interactions of the background field must also be multipole expanded in the time component. The expansion of the A^0 component is trivial due to our gauge choice (8.2) and already the linear term $t(\partial^0 A^i)(0, \mathbf{0})$ in the expansion of the spatial component is only relevant at higher powers. Thus, no contributions of this type must be considered.

The potential corrections are determined below, whereas the ultrasoft contribution is postponed to future work. The color octet Coulomb potential required for the diagram on the left in Figure 8.3 in known up to NNNLO [201, 202]. At NLO only the global color factor must be adjusted.

The $\mathcal{O}(\alpha_s)$ potential corrections to the gluon condensate contribution to the Green func-

tion are expressed through two triple-insertion functions

$$\begin{aligned}\delta_{\langle G^2\rangle}G^{(1)}_{\rm pot}(E) &= \delta_{\langle G^2\rangle}G^{(1)}_{GVG}(E) + 2\delta_{\langle G^2\rangle}G^{(1)}_{GGV}(E)\\ &= \frac{\langle 0|\pi\alpha_s G^2|0\rangle}{18}\left[a_1+\beta_0\frac{d}{du}\right]\\ &\quad\left[(\alpha_s^2 D_8)I_{\langle G^2\rangle}[G,1+u,G] + 2(-\alpha_s^2 C_F)I_{\langle G^2\rangle}[G,G,1+u]\right]_{u=0}. \quad (8.26)\end{aligned}$$

Again the angular integrals project out the P wave Green function in the color octet states. The first triple insertion function takes the form

$$\begin{aligned}I_{\langle G^2\rangle}[G,1+u,G] &= \frac{1}{4\pi\Gamma(1+2u)\cos(\pi u)}\int d^3\mathbf{r}\int d^3\mathbf{r}'\int d^3\mathbf{r}''(\mathbf{r}\cdot\mathbf{r}'')G^{(0)}(0,\mathbf{r};E)\\ &\quad G^{(8)}(\mathbf{r},\mathbf{r}';E)r'^{-1+2u}G^{(8)}(\mathbf{r}',\mathbf{r}'';E)G^{(0)}(\mathbf{r}'',0;E)\\ &= \frac{\lambda^6}{(4\pi)^2m^2(\alpha_s C_F)^6}\sum_{s_1=0}^{\infty}\frac{s_1!H_{\langle G^2\rangle}(s_1)}{(s_1+3)!(s_1+2+\lambda/8)}\\ &\quad\sum_{s_2=0}^{\infty}\frac{s_2!H_{\langle G^2\rangle}(s_2)}{(s_2+3)!(s_2+2+\lambda/8)}K_V(u,s_1,s_2), \quad (8.27)\end{aligned}$$

where

$$K_V(u,s_1,s_2) = \frac{(\mu/2p)^{2u}}{\Gamma(1+2u)\cos(\pi u)}\int_0^{\infty}d\rho\rho^{3+2u}e^{-\rho}L_{s_1}^{(3)}(\rho)L_{s_2}^{(3)}(\rho). \quad (8.28)$$

For $u=0$ the integral gives

$$K_V^{(0)}(s_1,s_2)\equiv K_V(0,s_1,s_2) = \frac{(s_1+3)!}{s_1!}\delta_{s_1s_2}. \quad (8.29)$$

Its derivative at zero can be solved by applying the methods used for the Coulomb triple insertion in [89]. We obtain

$$K_V^{(1)}(s_1,s_2)\equiv\frac{d}{du}K_V(u,s_1,s_2)|_{u=0} = 2\left[(L_\lambda+\gamma_E)\frac{(s_1+3)!}{s_1!}\delta_{s_1s_2}+k_1(s_1,s_2)\right], \quad (8.30)$$

where

$$k_1(s_1,s_2) = \begin{cases}11+12s_1+3s_1^2+\frac{(s_1+3)!}{s_1!}\psi(1+s_1), & s_1=s_2\\ -\frac{(\min(s_1,s_2)+3)!}{\min(s_1,s_2)!|s_1-s_2|}, & \text{else.}\end{cases} \quad (8.31)$$

The second triple-insertion function yields

$$\begin{aligned} I_{\langle G^2\rangle}[G,G,1+u] &= \frac{1}{4\pi\Gamma(1+2u)\cos(\pi u)}\int d^3\mathbf{r}\int d^3\mathbf{r}'\int d^3\mathbf{r}''(\mathbf{r}\cdot\mathbf{r}')G^{(0)}(0,\mathbf{r};E) \\ &\quad G^{(8)}(\mathbf{r},\mathbf{r}';E)G^{(0)}(\mathbf{r}',\mathbf{r}'';E)r''^{-1+2u}G^{(0)}(\mathbf{r}'',0;E) \\ &= \frac{m^2}{4\pi}\frac{\lambda^6}{4\pi m^4(\alpha_s C_F)^6}\sum_{s_1=0}^{\infty}\frac{s_1!H_{\langle G^2\rangle}(s_1)}{(s_1+3)!(s_1+2+\lambda/8)} \\ &\quad \sum_{s_2=0}^{\infty}\frac{H(u,s_2+1)}{(s_2+1)(s_2+1-\lambda)}K_G(s_1,s_2), \end{aligned} \tag{8.32}$$

where

$$\begin{aligned} K_G(s_1,s_2) &= \int_0^{\infty} d\rho\rho^4 e^{-\rho}L_{s_1}^{(3)}(\rho)L_{s_2}^{(1)}(\rho) \\ &= \begin{cases} (-1)^{s_1+s_2}4!\frac{(s_1+3)!}{s_2!(s_1+3-s_2)!}\frac{(s_2+1)!}{s_1!(s_2+1-s_1)!}, & -1\le s_2-s_1\le 3 \\ 0, & \text{else,} \end{cases} \end{aligned} \tag{8.33}$$

and $H(u,k)$ is defined as in [89]. One requires

$$H^{(0)}(k)\equiv H(0,k)=\frac{k}{k-\lambda}, \tag{8.34}$$

$$H^{(1)}(k)\equiv\frac{\partial}{\partial u}H(u,k)|_{u=0}=\frac{2k}{k-\lambda}\left[L_\lambda-\hat{\psi}(k-\lambda)+\frac{\lambda}{k}\left(\hat{\psi}(1-\lambda)-\hat{\psi}(k+1-\lambda)\right)\right]. \tag{8.35}$$

The infinite sums in (8.27) and (8.32) converge quickly and can be truncated with negligible uncertainty at $s_i\sim 30$.

We briefly sketch what is required for the missing ultrasoft contribution of Figure 8.4. Power counting demonstrates that the ultrasoft correction is free of overall divergences. There are, however, UV subdivergences in the self-energy and vertex-correction diagrams shown on the right-hand side of Figure 8.4. Nevertheless, we proceed with the a priori ill-defined expressions for the ultrasoft diagram in $d=4$ dimension with the understanding that the necessary subtractions for the subdivergence must still be applied. We find

$$\begin{aligned} \delta_{\langle G^2\rangle}G^{(1)}_{\rm us}(E) &= \frac{\langle 0|\pi\alpha_s G^2|0\rangle}{6}g_s^2\int d^3\mathbf{r}\int d^3\mathbf{r}'\int d^3\mathbf{r}''\int d^3\mathbf{r}'''\,(\mathbf{r}\cdot\mathbf{r}''')\,G^{(0)}(0,\mathbf{r};E) \\ &\quad \times G^{(8)}(\mathbf{r},\mathbf{r}';E)i\int\frac{d^4k}{(2\pi)^4}\frac{G^{(8)}(\mathbf{r}',\mathbf{r}'';E-k^0)}{k^2+i0}G^{(8)}(\mathbf{r}'',\mathbf{r}''';E)G^{(0)}(\mathbf{r}''',0;E). \end{aligned} \tag{8.36}$$

We can proceed by closing the k^0 contour in the lower half plane, which picks up the residue

at $k^0 = |\mathbf{k}| - i0$ from the gluon propagator. This yields

$$\delta_{\langle G^2\rangle} G^{(1)}_{\rm us}(E) = \frac{\langle 0|\pi\alpha_s G^2|0\rangle}{6}\frac{\alpha_s}{\pi}\int d^3\mathbf{r}\int d^3\mathbf{r}'\int d^3\mathbf{r}''\int d^3\mathbf{r}'''\,(\mathbf{r}\cdot\mathbf{r}''')\,G^{(0)}(0,\mathbf{r};E) \qquad (8.37)$$
$$\times G^{(8)}(\mathbf{r},\mathbf{r}';E)\int\limits_0^\infty d|\mathbf{k}||\mathbf{k}|G^{(8)}(\mathbf{r}',\mathbf{r}'';E-|\mathbf{k}|)G^{(8)}(\mathbf{r}'',\mathbf{r}''';E)G^{(0)}(\mathbf{r}''',0;E),$$

where the angular integrals are only non-vanishing for the P-wave component of the color-octet Green functions. After simplifications one obtains

$$\delta_{\langle G^2\rangle} G^{(1)}_{\rm us}(E) = \frac{\pi^2 K_4}{6}\frac{\alpha_s}{\pi}\frac{m^2\alpha_s C_F}{4\pi}\lambda^9\sum_{s_1=0}^\infty\frac{s_1!H_{\langle G^2\rangle}(s_1)}{(s_1+3)!(s_1+2+\lambda/8)}\sum_{s_2=0}^\infty\frac{s_2!}{(s_2+3)!}$$
$$\sum_{s_3=0}^\infty\frac{s_3!H_{\langle G^2\rangle}(s_3)}{(s_3+3)!(s_3+2+\lambda/8)}\int\limits_0^\infty d\hat{k}\,\hat{k}\eta^3\frac{K_{\rm us}(\eta,s_1,s_2)K_{\rm us}(\eta,s_3,s_2)}{s2+2+\lambda/(8\eta)}, \qquad (8.38)$$

where we have defined $\eta = \sqrt{(E-|\mathbf{k}|)/E}$ and substituted $\hat{k} = |\mathbf{k}|/(m\alpha_s^2 C_F^2)$. The structure of the expression (8.38) is similar to the dimension six contribution (8.21), but complicated by the additional momentum integral. Unfortunately, the presence of the dimensionless variable η breaks the symmetry of $K_{\rm us}$ under exchange of its arguments and yields a rather complicated result

$$K_{\rm us}(\eta,a,b) = \int\limits_0^\infty d\rho\rho^4 e^{-\frac{1+\eta}{2}\rho}L_a^{(3)}(\rho)L_b^{(3)}(\eta\rho)$$
$$= 256\frac{(-1)^b(4+a+b)!}{a!b!(4+a)(4+b)}[2+a-(2+b)\eta]\frac{(\eta-1)^{a+b-1}}{(\eta+1)^{a+b+7}}$$
$$\times\left[a\eta\,{}_2F_1\left(1-a,-b,-4-a-b;\left(\frac{\eta+1}{\eta-1}\right)^2\right)\right.$$
$$\left.-(1+(2+a)\eta+\eta^2)\,{}_2F_1\left(-a,-b,-4-a-b;\left(\frac{\eta+1}{\eta-1}\right)^2\right)\right]. \qquad (8.39)$$

In contrast to (8.23), where only the diagonal and next-to-diagonal elements are non-vanishing, the matrix $K_{\rm us}$ has all non-zero entries and we cannot reduce the triple sum to a single sum. The subdivergence manifests through the divergence of the infinite sums.

The contributions to the energy levels and wave functions from the potential corrections can be extracted by expanding (8.27) and (8.32) for λ near positive integer values N. The

results are given by

$$e_N^{(4,3)} = \frac{\pi^2 K_4}{18}\,\frac{\alpha_s}{4\pi}\left[\frac{D_8}{C_F}\widetilde{e}_N^{\,\mathrm{GVG}} + \widetilde{e}_N^{\,\mathrm{GGV}} + \widetilde{e}_N^{\,\mathrm{us}}\right], \tag{8.40}$$

$$f_N^{(4,3)} = \frac{\pi^2 K_4}{18}\,\frac{\alpha_s}{4\pi}\left[\frac{D_8}{C_F}\widetilde{f}_N^{\,\mathrm{GVG}} + \widetilde{f}_N^{\,\mathrm{GGV}} + \widetilde{f}_N^{\,\mathrm{us}}\right], \tag{8.41}$$

$$\tag{8.42}$$

where $\widetilde{e}_{,N}^{\,\mathrm{GVG}}$, $\widetilde{e}_N^{\,\mathrm{GGV}}$, $\widetilde{e}_{,N}^{\,\mathrm{GVG}}$ and $\widetilde{f}_N^{\,\mathrm{GGV}}$ are given in Appendix D and the ultrasoft contributions $\widetilde{e}_N^{\,\mathrm{us}}$ and $\widetilde{f}_N^{\,\mathrm{us}}$ are still missing.

8.4. Size of non-perturbative corrections

The size of non-perturbative corrections to the moments and to the properties of the Upsilon resonances has been strongly disputed. Based on the leading dimension four condensate contribution Voloshin found that the relative corrections to the moments do not exceed about 1% for $n \leq 20$ [158]. On the other hand, the expansion parameter $n\Lambda_{\mathrm{QCD}}/m_b$ of the OPE is of order one for $n \sim 16$ indicating a much earlier breakdown.

The leading condensate correction to the $\Upsilon(1S)$ mass is of the order of 100 MeV and the applicability of the condensate expansion to excited states is doubtful. Nevertheless, it has been argued [203–205] that the $\Upsilon(1S)$ mass is in the perturbative domain. Intriguingly, the bottom-quark mass values obtained from the mass of the $\Upsilon(1S)$ state [203–205] are almost identical to ours, when the non-perturbative contribution to the bound-state energy is ignored. The leptonic decay width of the $\Upsilon(1S)$ resonance has been studied at NNNLO in [86] with the conclusion that the perturbative result stabilizes at NNNLO and makes up about 70% of the experimental value. Similar to the non-relativistic moments, there is however no sign of convergence for renormalization scales below about 3 GeV. On the other hand, the condensate corrections appear to only converge for considerably lower scales near the inverse Bohr radius [189]. Thus, it remained unclear whether the $\Upsilon(1S)$ state can be fully understood in the domain of the local condensate expansion.

Below, we attempt to gain some further insight into the condensate corrections from an analysis of the dimension six contribution and the partial NLO dimension four results. Unfortunately, we are mostly constrained to hierarchical statements because, firstly, the values of the condensates themselves are very uncertain. We use the estimates

$$\langle\frac{\alpha_s}{\pi}G^2\rangle = 0.012\,\mathrm{GeV}^4, \qquad O_1(\mu) = (3.13 + \alpha_s(\mu)\,7.41)\cdot 10^{-4}\,\mathrm{GeV}^6, \tag{8.43}$$

from [206] and [189], respectively.[2] Even worse, the expressions K_4 and K_6 in (8.11) and (8.22) contain large powers of α_s and are thus very sensitive to the renormalization scale.

[2] The gluon condensate is scale independent because the operator G^2 has vanishing anomalous dimension.

n	8	10	12	16	20	24
$\mathcal{M}_n^{\exp,\Upsilon(1S)}/\mathcal{M}_n^{\exp}$	0.738	0.803	0.850	0.913	0.948	0.969
$\widetilde{\mathcal{M}}_n^{\mathrm{pert},\Upsilon(1S)}/\widetilde{\mathcal{M}}_n^{\mathrm{pert}}$	0.769	0.814	0.849	0.899	0.932	0.953
$\widetilde{\mathcal{M}}_n^{\mathrm{pert,rest}}/\widetilde{\mathcal{M}}_n^{\mathrm{pert}}$	0.231	0.186	0.151	0.101	0.068	0.047
$\delta_{\Lambda^4}^{(0)}\widetilde{\mathcal{M}}_n^{\Upsilon(1S)}/\widetilde{\mathcal{M}}_n^{\mathrm{pert}}$	1.711	1.842	1.953	2.135	2.281	2.404
$\delta_{\Lambda^4}^{(0)}\widetilde{\mathcal{M}}_n^{\mathrm{rest}}/\widetilde{\mathcal{M}}_n^{\mathrm{pert}}$	-1.713	-1.845	-1.957	-2.144	-2.296	-2.427
$\delta_{\Lambda^4}^{(0)}\widetilde{\mathcal{M}}_n/\widetilde{\mathcal{M}}_n^{\mathrm{pert}}$	-0.002	-0.003	-0.005	-0.009	-0.015	-0.023
$\delta_{\Lambda^4}^{(1*)}\widetilde{\mathcal{M}}_n^{\Upsilon(1S)}/\widetilde{\mathcal{M}}_n^{\mathrm{pert}}$	*-5.322*	*-5.748*	*-6.118*	*-6.741*	*-7.263*	*-7.722*
$\delta_{\Lambda^4}^{(1*)}\widetilde{\mathcal{M}}_n^{\mathrm{rest}}/\widetilde{\mathcal{M}}_n^{\mathrm{pert}}$	*5.322*	*5.748*	*6.118*	*6.742*	*7.263*	*7.719*
$\delta_{\Lambda^4}^{(1*)}\widetilde{\mathcal{M}}_n/\widetilde{\mathcal{M}}_n^{\mathrm{pert}}$	*0.0003*	*0.0004*	*0.0004*	*0.0002*	*-0.0008*	*-0.003*
$\delta_{\Lambda^6}^{(0)}\widetilde{\mathcal{M}}_n^{\Upsilon(1S)}/\widetilde{\mathcal{M}}_n^{\mathrm{pert}}$	-8.402	-9.104	-9.723	-10.79	-11.71	-12.54
$\delta_{\Lambda^6}^{(0)}\widetilde{\mathcal{M}}_n^{\mathrm{rest}}/\widetilde{\mathcal{M}}_n^{\mathrm{pert}}$	8.402	9.104	9.723	10.79	11.71	12.54
$\delta_{\Lambda^6}^{(0)}\widetilde{\mathcal{M}}_n/\widetilde{\mathcal{M}}_n^{\mathrm{pert}}$	0.00002	0.00004	0.00008	0.0002	0.0005	0.001

Table 8.1.: We show the contribution of the $\Upsilon(1S)$ state and the remaining resonances combined with the continuum (rest) to the experimental moments and the perturbative and non-perturbative contributions to the moments, separately. We use the inputs $m_b^{\mathrm{PS}}(2\text{ GeV}) = \mu = 4.53$ GeV, $\alpha_s = 0.220486$, $m_c = 0$, and in K_4 and K_6 the condensates from (8.43) and the pole mass $m_b = 4.717$ GeV computed from $m_b^{\mathrm{PS}}(2\text{ GeV})$ at LO. The perturbative moments are evaluated at NNNLO in the PSS scheme, and the LO and partial NLO (denoted by a star and slanted numbers) dimension four contributions and the dimension six contribution in the pole scheme.

8.4.1. Non-relativistic moments

We can determine the condensate contributions to the moments through contour integration in the complex-energy plane. Contrary to the perturbative contribution, we may not split the condensate corrections into a resonance and continuum part, since both are separately divergent. The divergence in the resonance part appears in the sum over the principal quantum number because the dimension four and six contributions to the residues Z_N grow as N^5 and N^9 for $N \to \infty$. The continuum contribution is too singular for $E \to 0$. The corrections to the moments are however well-defined, since the moments only rely on the OPE in the Euclidean region.

It is also well-defined to split the condensate correction into the finite contribution from the $\Upsilon(1S)$ resonance and the rest. The corresponding values for the experimental and perturbative moments, as well as the LO and partial NLO dimension four and the LO dimension six condensate contributions are shown in Table 8.1.

Our first observation is that the $\Upsilon(1S)$ contribution obtained perturbatively is very close to the experimental one. It makes up the dominant contribution for the considered

n	8	10	12	16	20	24
$(n\Lambda_{\rm QCD}/m_b)_{\text{eff, dim 4}}$	0.357	0.431	0.505	0.649	0.790	0.927
$(n\Lambda_{\rm QCD}/m_b)_{\text{eff, dim 4}^*}$	*0.362*	*0.441*	*0.520*	*0.681*	*0.845*	*1.013*
$(n\Lambda_{\rm QCD}/m_b)_{\text{eff, dim 6}}$	0.231	0.277	0.321	0.408	0.493	0.575
$(n\Lambda_{\rm QCD}/m_b)_{\text{eff, dim 6}} \times 15^{1/6}$	0.363	0.434	0.504	0.641	0.774	0.904

Table 8.2.: Estimates for the effective non-perturbative expansion parameter $(n\Lambda_{\rm QCD}/m_b)$ based on the results of the leading dimension four condensate corrections, the partial NLO dimension four condensate corrections and the dimension six condensate corrections. See text for further explanations.

moments, rising from about 80% for $n = 10$ to above 95% for the 24th moment. It is somewhat puzzling that this nice agreement is completely spoiled by the leading dimension four condensate contribution, which is more than twice as large as the perturbative part for the estimate (8.43) and our central scale choice. It is, however, almost entirely canceled by the condensate contribution to the rest, which exceeds the perturbative estimate for the rest by an even larger factor. The degree of cancellation is up to 1 part in 1000 for $n = 8$ and still effective at the 1% level for $n = 24$. Therefore, the overall dimension four condensate contribution is very small, only about 2% for $n = 24$ where power counting arguments clearly predict a breakdown of the OPE.

While the exact size of the condensate terms is rather ambiguous, as discussed above, this cancellation and the smallness of the total contribution is intrinsic. Although the moments were designed precisely for that reason, the extend of the cancellations is astonishing, as this behaviour is even enhanced for the partial NLO corrections to the dimension four contribution and the dimension six part. The $\Upsilon(1S)$ contribution from both is even larger than the leading order dimension four part, but cancels to a still larger degree with the remaining contribution. Unless the cancellation is much less effective for the missing ultrasoft correction to the dimension four part, it therefore naively appears that the condensate expansion is converging well up to very high values of at least $n \sim 20 - 24$.

The overall smallness of the condensate contributions is, however, partially due to the suppression of the dipole operator (8.3) by $v \sim \alpha_s$, which manifests as an additional suppression by $1/n$ in the condensate corrections to the moments. We can therefore use

$$(n\Lambda_{\rm QCD}/m_b)_{\text{eff, dim 4}} = \left|\frac{n\,\delta^{(0)}_{\Lambda^4}\widetilde{\mathcal{M}}_n}{\widetilde{\mathcal{M}}_n^{\text{pert, LO}}}\right|^{\frac{1}{4}} \tag{8.44}$$

$$(n\Lambda_{\rm QCD}/m_b)_{\text{eff, dim 4}^*} = \left|\frac{n\,\delta^{(1*)}_{\Lambda^4}\widetilde{\mathcal{M}}_n}{\widetilde{\mathcal{M}}_n^{\text{pert, NLO}}}\right|^{\frac{1}{4}} \tag{8.45}$$

$$(n\Lambda_{\rm QCD}/m_b)_{\text{eff, dim 6}} = \left|\frac{n\,\delta^{(0)}_{\Lambda^6}\widetilde{\mathcal{M}}_n}{\widetilde{\mathcal{M}}_n^{\text{pert, LO}}}\right|^{\frac{1}{6}} \tag{8.46}$$

to estimate the size of the expansion parameter $(n\Lambda_{\rm QCD}/m_b)$ based on our results for the condensate corrections. The results are shown in Table 8.2. We observe that the estimate for the effective expansion parameter based on the dimension four results becomes order one in the ballpark of $n = 20$. This hints that a breakdown of the OPE indeed happens around this region, which implies that the perturbative treatment of the ultrasoft correction is no longer appropriate. We refer to [61] for a review of EFTs, that can be constructed for heavy quarkonium with different hierarchies between the soft, ultrasoft and QCD scale.

The dimension six contribution is smaller, than a naive estimate based on the effective expansion parameter from the dimension four terms would predict. This might indicate that the expansion is better behaved, which is reflected by lower estimates for the expansion parameters from dimension six. It was however pointed out in [193] that the dimension six contribution is numerically suppressed by a factor 1/15, which is not present at dimension eight. Intriguingly, if we compensate for this factor, the estimates for the expansion parameters are nearly identical to dimension four as shown in the lowest row of Table 8.2. Thus, it might be interesting to consider the dimension eight terms, which should provide further insight on the convergence of the condensate expansion. It is a straightforward exercise to determine the relevant coefficients along the lines of Section 8.2, but reliable information on the corresponding condensate is practically non-existent.

The results in Table 8.1 and 8.2 clearly demonstrate that condensate contributions are insignificant for our analysis based on the tenth moment. They affect the extracted bottom-quark mass by less than 1 MeV and are therefore neglected. To be on the safe side, we refrain from using $n \geq 16$ in our analysis for the bottom-quark mass because we can presently not exclude that the breakdown of the OPE, although veiled by the $1/n$ suppression and the numerical suppression of the dimension six contribution, indeed occurs in this region.

8.4.2. Upsilon resonances

We illustrate the perturbative and non-perturbative contribution to the mass of the $\Upsilon(1S)$ resonance in Figure 8.5. Similar to the non-relativistic moments, we observe that perturbation theory does not converge well for small renormalization scales, roughly $\mu \leq 2.5\,\text{GeV}$. However, near $\mu = m_b$ the behaviour of the perturbative series is excellent. The reverse happens for the condensate corrections. They exceed the perturbative corrections for scales larger than about 2 GeV and show no convergence neither in the power series nor for the preliminary α_s corrections (although the latter could possibly be remedied by the missing ultrasoft correction). For very small scales near 1 GeV, the condensate corrections are tiny and the results indicate that the expansion is convergent.

The combined result for the $\Upsilon(1S)$ mass does not behave satisfactory for any given scale. It must therefore be doubted that the hierarchy $\Lambda_{\rm QCD} \ll E_{\Upsilon(1S)}$ provides an adequate description of the $1S$ system. It seems however possible that the resummation of threshold logarithms stabilizes the scale behaviour and yields a small intermediate region of the renormalization scale, where the perturbative and condensate expansions converge. Also here, it would be interesting to consider the dimension eight condensate to probe the

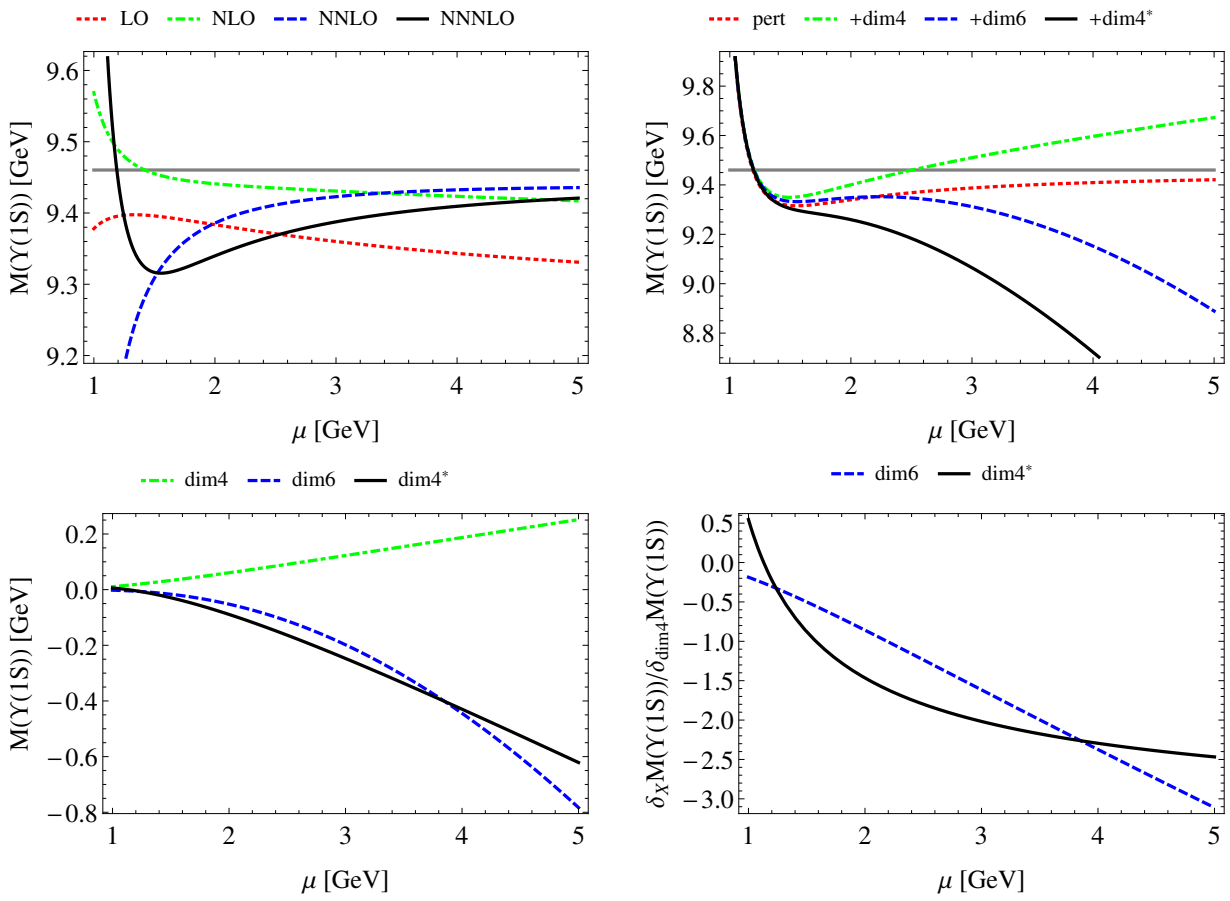

Figure 8.5.: Mass of the $\Upsilon(1S)$ resonance. We show the perturbative results up to NNNLO (upper left), the condensate corrections on top of the NNNLO perturbative result (upper right), the absolute condensate corrections (lower left) and the relative dimension six and NLO dimension four corrections with respect to the leading dimension four contribution (lower right). The gray horizontal line in the upper panel corresponds to the experimental value.

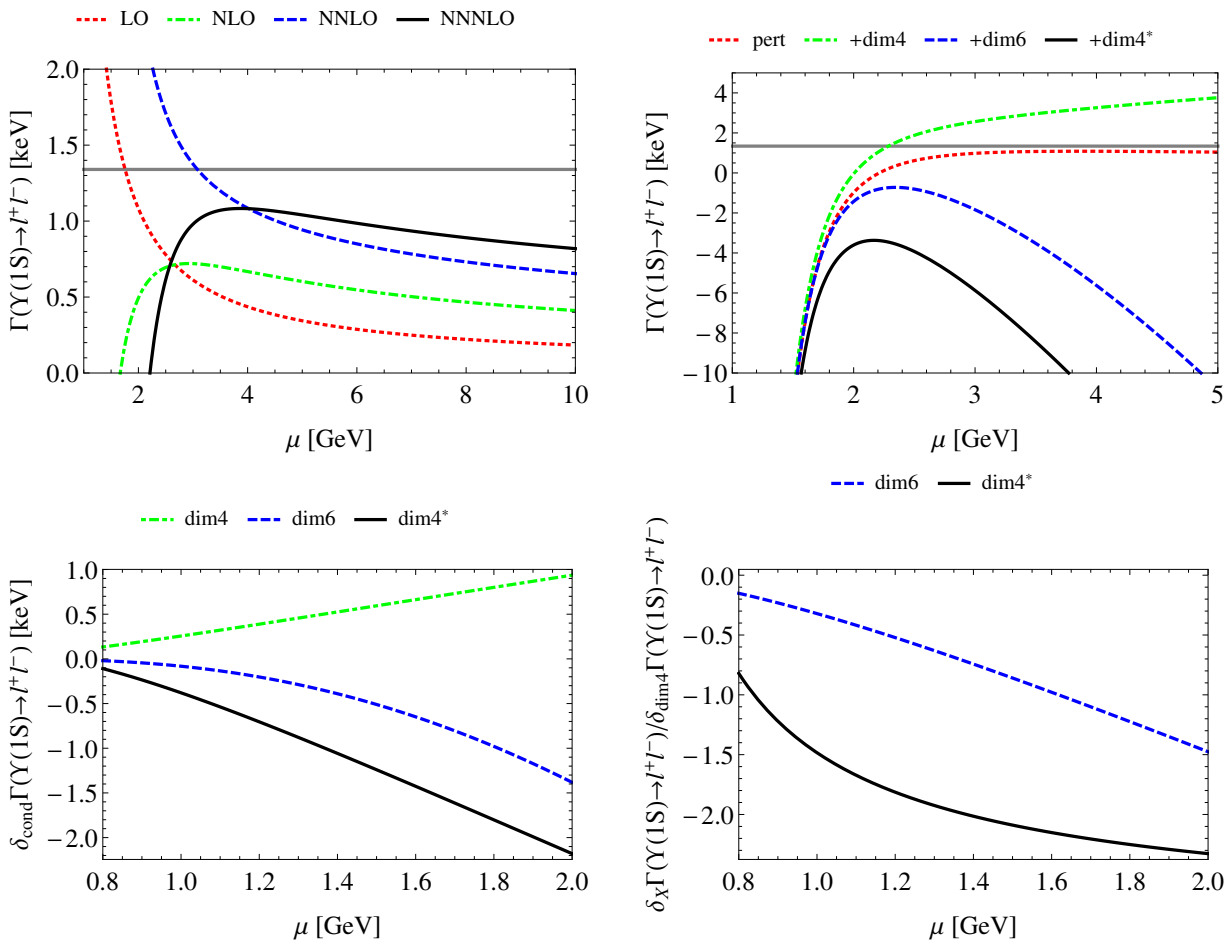

Figure 8.6.: Leptonic decay rate of the $\Upsilon(1S)$ resonance. See Figure 8.5 for details.

hypothesis of the dimension six contribution being numerically small (cf. [193]), in which case the breakdown of the condensate expansion would be unambiguous.

In Figure 8.6 and 8.7 we show the same results for the leptonic decay width of the $\Upsilon(1S)$ resonance and the $\Upsilon(2S)$ mass, respectively. The condensate contributions may be converging for the leptonic $\Upsilon(1S)$ decay rate in the region around $\mu = 1\,\text{GeV}$, if the missing ultrasoft corrections partially compensate the large other NLO dimension four corrections, but the perturbative part is clearly not convergent below roughly $\mu = 3\,\text{GeV}$ and no stable overall result can be expected. The condensate corrections to the $\Upsilon(2S)$ mass do not even converge for scales as low as 800 MeV, which clearly invalidates the approach for the $2S$ state. This may not be so surprising after all, since even expansions in $\Lambda_{\rm QCD}/m_c$ of fully inclusive quantities like D-meson mixing and lifetimes [7,8,207] only converge rather slowly and the charm-quark mass is significantly larger than the binding energies of the $\Upsilon(NS)$ resonances.

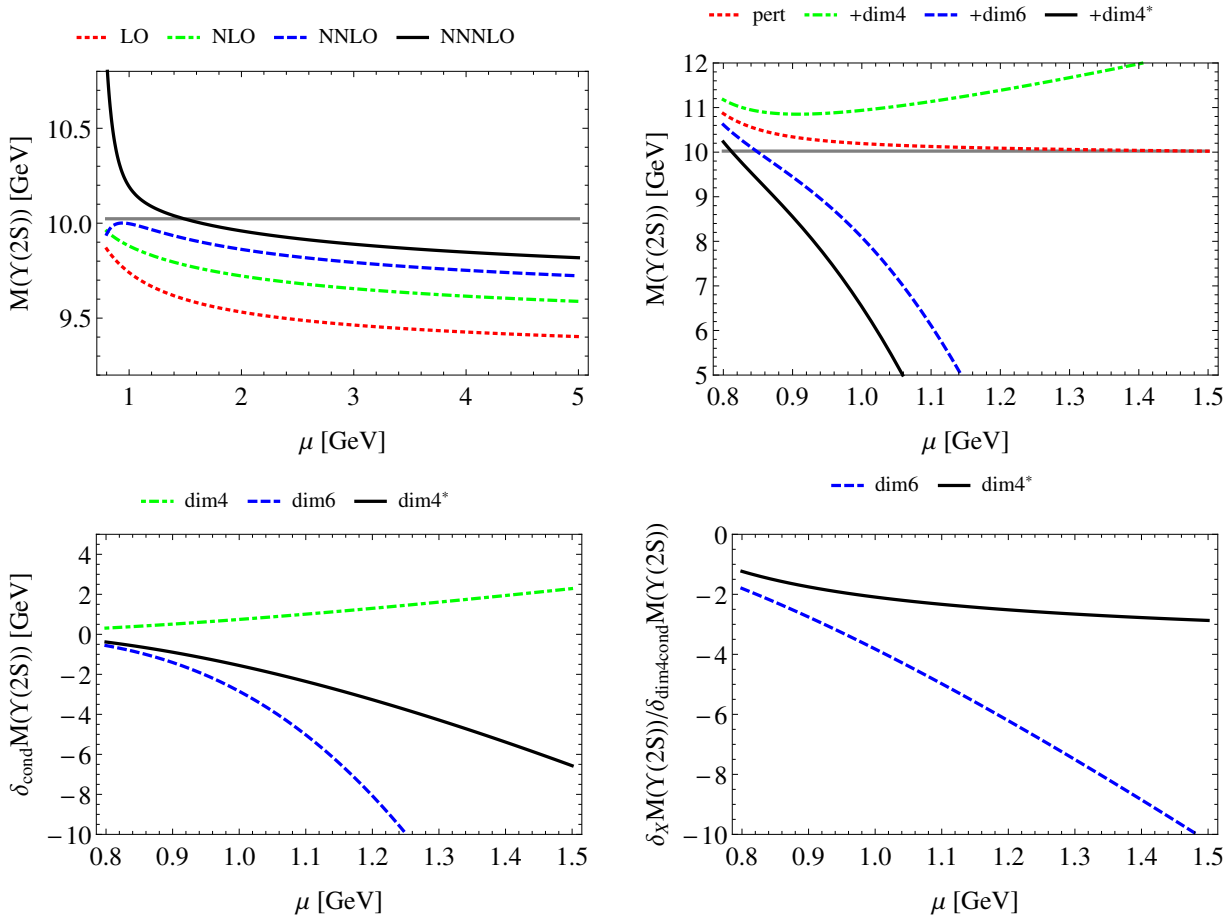

Figure 8.7.: Mass of the $\Upsilon(2S)$ resonance. See Figure 8.5 for details.

9. Conclusions and Outlook

Precision determinations of SM parameters offer a direct way to improve theory predictions for a large number of observables. Since the parameters are, in general, not observables themselves, they cannot be measured directly. They can only be extracted from the comparison of experimental data with theory predictions. In this dissertation we have studied the production of heavy-quark pairs in electron-positron collisions in the particularly interesting energy region near the heavy-quark production threshold. In this region the cross section is highly sensitive to the heavy-quark mass, which facilitates the determination of the top and bottom masses with a very small uncertainty. In addition, one can extract precise values for the strong coupling constant, the top-quark width and the top-quark Yukawa coupling.

Near the production threshold conventional perturbation theory in the strong coupling breaks down due to the non-perturbatively strong Coulomb interaction between the non-relativistic heavy quark and anti-quark. A meaningful prediction for the cross section can only be obtained by resumming the Coulomb effects to all orders. A systematic approach based on non-relativistic effective field theories has been developed, generalized for unstable particles, and applied in the last 20 years. The recent completion of the NNNLO QCD result for top-pair production [28] has resolved the long-standing problem with the large perturbative uncertainty of NNLO predictions [27]. Based on variation of the renormalization scale the estimated size of missing higher-order QCD contributions is $\pm 3\%$.

The first major result of this work is the computation of the full NNLO and partial NNNLO non-QCD corrections to the top-quark pair production cross section. Our results show that these corrections are significantly larger than the remaining QCD uncertainty, reaching up to more than 20% below the characteristic peak of the cross section. This demonstrates the importance of the non-QCD contributions for a threshold scan of top-pair production at a future linear collider. Neglecting the non-QCD effects would distort the extracted value of the top-quark mass by an amount that is comparable to the overall uncertainty of the determination.

The large correction below the peak is mostly due to the non-resonant production of the top-pair decay products $W^+W^-b\bar{b}$ and its interference with the production of resonant top pairs. The resonant cross section by itself is ill-defined for unstable top quarks, which manifests through a divergence that only cancels once the non-resonant contribution is taken into account as well. Special care was taken that the divergences and the respective scheme dependences are treated consistently in both parts. On top of the full NNLO treatment of electroweak effects, we include NNNLO P-wave and Higgs corrections. The latter is especially interesting because the top threshold scan is sensitive to deviations of the top-quark Yukawa coupling y_t from its SM value and can therefore probe a large

number of possible extensions to the SM that predict a non-standard coupling. A realistic result for the modification of the shape of the cross section under variation of y_t is only obtained at NNNLO, where the effects of the Higgs potential appear.

To estimate the physics potential of a top threshold scan we have compared the size of the modifications of the cross section under variation of the input parameters to the theory uncertainty. Based on this approach we expect the theory uncertainties to be about or below 50 MeV for the top-quark $\overline{\text{MS}}$ or PS mass and below 100 MeV for the top-quark width. Adopting the same approach for the top Yukawa coupling and the strong coupling constant we expect the threshold scan to be sensitive to variations of the order $^{+20}_{-50}\%$ and 0.0015, respectively. Their determination in a simultaneous fit however suffers from a strong correlation and it is presently not clear to which degree this affects the results. This question will be settled by a simulation based on the theory prediction of `QQbar_Threshold` [29], that is currently being performed. First results for the top-quark mass [140] are in very good agreement with our estimate. Furthermore statistical and experimental systematic uncertainties are expected to be at the level of only 20 MeV and a few 10 MeV, respectively, which implies that the total uncertainty should be well below 100 MeV.

The other major result presented in this dissertation is the first complete NNNLO determination of the bottom-quark mass from non-relativistic moments of the pair production cross section. In addition to the NNNLO QCD corrections (cf. [28]) we consider NNLO charm-quark mass effects, NLO QED corrections and dimension four condensate corrections, which are all tiny. Just as for the top-pair production cross section [28], the NNNLO corrections lead to a substantial stabilization and to better insight into the scale behaviour of the result. Consequently, we observe a significant reduction of the uncertainty compared to previous NNLO results. The masses obtained from perturbative moments with $8 \leq n \leq 15$ are in good agreement with each other. We adopt $n = 10$ for our central value and find $m_b^{\text{PS}}(2\,\text{GeV}) = 4.532^{+0.013}_{-0.039}$ and $m_b^{\overline{\text{MS}}}(m_b^{\overline{\text{MS}}}) = 4.203^{+0.016}_{-0.034}$ in the PS and $\overline{\text{MS}}$ schemes, respectively. Our values are in good agreement with the current PDG average and other recent sum rule results.

We have studied the impact of subleading condensate corrections on the non-relativistic moments and the $\Upsilon(NS)$ properties. The results of [189] for the dimension six contributions to the Upsilon resonances are extended and applied to the moments. Furthermore, we computed the potential NLO QCD corrections to the dimension four contribution. To obtain complete NLO QCD accuracy, the contributions from ultrasoft gluons must still be determined. Due to the numerical uncertainty of the condensates and the strong scale dependence, we only focus on the convergence properties. The results clearly show that the moments with $n \sim 10$ receive only minuscule non-perturbative corrections. Because of a possible numerical suppression of the dimension six contribution (cf. [193]), it remains unclear for which values of n the breakdown of the OPE occurs. A future calculation of the dimension eight contribution should settle this question. Our results for the mass of the $\Upsilon(1S)$ resonance show that the condensate expansion is questionable even here since there is no value of the renormalization scale where the perturbative and condensate expansion both converge. If an analysis of the dimension eight correction substantiates the numerical

smallness of the dimension six contribution, the breakdown of the OPE would be obvious. The condensate expansion doesn't show any sign of convergence for either the leptonic decay rate of the $\Upsilon(1S)$ or the masses of the exited resonances.

In the future the results discussed in this work could be further improved in a number of ways. Firstly, both the top threshold scan and the determination of the bottom-quark mass would benefit from a NNNLO plus NNLL QCD prediction for the cross section, which could by achieved by a combination of the results of [28,208,209]. This could further reduce the perturbative uncertainty and stabilize the scale behaviour. The resummation of ISR at NLL accuracy is of integral importance for the top threshold scan as shown by the substantial modification of the cross section from ISR at the LL level. Since this effect is universal, it is of similar relevance for a future linear collider as precise parton distribution functions are for the LHC. The full treatment of NNNLO electroweak corrections in the resonant contribution would be desirable. Partial results for the hard matching coefficients are already available [118, 119]. However, the determination of the full NNNLO non-resonant contributions is not feasible with present methods. Last but not least, it would be interesting to extend the formalism beyond the total cross section to other observables like the forward-backward asymmetry [92] to fully exploit the physics opportunities of the top threshold scan.

A. Details on the computation of the NLO P-wave Green function

We show how the results (5.52) and (5.53) can be obtained. To get rid of the prefactor in (5.50), we define $\tilde{j}_{\mathrm{P}}(u) = [\Gamma(1+2u)\cos(\pi u)/\Gamma(4+2u)]j_{\mathrm{P}}(u)$. Setting $z = (1+t_1+t_2)/(t_1t_2)$ and $y = t_1/(1+t_1+t_2)$, the Jacobian is $(1+yz/(y^2(1-y)^2z^3))$ and we obtain

$$\tilde{j}_{\mathrm{P}}(u) = \int_0^\infty dz \int_0^1 dy \frac{y^{2u}(1-y)^{2u}(1+z)}{z^{3-2u}(1+yz)^{1+2u}} \left[(1+z)^\lambda - 1 - \lambda \log(1+z) - \frac{\lambda^2}{2}\log^2(1+z) \right]. \tag{A.1}$$

In the case of $\tilde{j}_{\mathrm{P}}(0)$, the y-integration is straightforward. For the z-integration we introduce an analytic regulator $z^{-\alpha}$ and rewrite the logarithms in the following way:

$$\log(1+z)^n = \left(\frac{d}{d\beta}\right)(1+z)^\beta|_{\beta=0}. \tag{A.2}$$

This way, the individual integrals can be solved

$$\begin{aligned}\tilde{j}_{\mathrm{P}}(0) = \lim_{\alpha\to 0} \Bigg[&\frac{d}{d\beta}B(-3-\alpha, 2+\alpha-\beta-\lambda) - \frac{d}{d\beta}B(-3-\alpha, 2+\alpha-\beta) \\ &-\lambda\frac{d^2}{d\beta^2}B(-3-\alpha, 2+\alpha-\beta-) - \frac{\lambda^2}{2}\frac{d^3}{d\beta^3}B(-3-\alpha, 2+\alpha-\beta)\Bigg]_{\beta=0}\end{aligned} \tag{A.3}$$

in terms of the Euler Beta function

$$B(a,b) = \frac{\Gamma(a)\Gamma(b)}{\Gamma(a+b)} = \int_0^\infty dz \frac{z^{a-1}}{(1+z)^{a+b}}. \tag{A.4}$$

It is now straightforward to obtain

$$\tilde{j}_{\mathrm{P}}(0) = \frac{1}{6}\left[-1 + \left(\frac{\pi^2}{3} - 2\right)\lambda + 3\zeta(3)\lambda^2 + \left(1-3\lambda^2\right)\hat{\psi}(2-\lambda) + \left(\lambda^3-\lambda\right)\psi'(2-\lambda)\right]. \tag{A.5}$$

The computation of the derivative at zero proceeds similarly

$$\begin{aligned}\tilde{j}'_{\mathrm{P}}(0) =& 2\int_0^\infty dz \int_0^1 dy \frac{1+z}{z^3(1+yz)} \log\left(\frac{yz(1-y)}{1+yz}\right) \\ & \times \left[(1+z)^\lambda - 1 - \lambda \log(1+z) - \frac{\lambda^2}{2}\log^2(1+z)\right] \\ =& \int_0^\infty dz \frac{1+z}{z^4}\left[2\log(z)\log(1+z) - 2\log^2(1+z) - 4\mathrm{Li}_2\left(\frac{z}{1+z}\right)\right] \\ & \times \left[(1+z)^\lambda - 1 - \lambda \log(1+z) - \frac{\lambda^2}{2}\log^2(1+z)\right]\end{aligned} \tag{A.6}$$

We set $t = \frac{z}{1+z}$:

$$\begin{aligned}\tilde{j}'_{\mathrm{P}}(0) =& \int_0^1 dt \frac{1-t}{t^4}\left[-2\ln(t)\ln(1-t) - 4\mathrm{Li}_2(t)\right]\left[(1-t)^{-\lambda} - 1 + \lambda\ln(1-t) - \frac{\lambda^2}{2}\ln(1-t)^2\right] \\ =& -2\partial_\delta\partial_\epsilon \int_0^1 dt t^{\delta-4}(1-t)^{1+\epsilon-\lambda}\Big|_{\delta=\epsilon=0} + 2\partial_\delta\left(\partial_\epsilon - \lambda\partial_\epsilon^2 + \frac{\lambda^2}{2}\partial_\epsilon^3\right)\int_0^1 dt t^{\delta-4}(1-t)^{1+\epsilon}\Big|_{\delta=\epsilon=0} \\ & - 4\sum_{n=1}^\infty \frac{1}{n^2}\int_0^1 dt t^{n-4}(1-t)^{1-\lambda} + 4\sum_{n=1}^\infty \frac{1}{n^2}\left(1 - \lambda\partial_\epsilon + \frac{\lambda^2}{2}\partial_\epsilon^2\right)\int_0^1 dt t^{n-4}(1-t)^{1+\epsilon}\Big|_{\epsilon=0} \\ =& -2\partial_\delta\partial_\epsilon \frac{\Gamma(\delta-3)\Gamma(2+\epsilon-\lambda)}{\Gamma(-1+\epsilon+\delta-\lambda)}\Big|_{\delta=\epsilon=0} + 2\partial_\delta\left(\partial_\epsilon - \lambda\partial_\epsilon^2 + \frac{\lambda^2}{2}\partial_\epsilon^3\right)\frac{\Gamma(\delta-3)\Gamma(2+\epsilon)}{\Gamma(-1+\epsilon+\delta)}\Big|_{\delta=\epsilon=0} \\ & - 4\sum_{n=1}^\infty \frac{1}{n^2}\frac{\Gamma(n-3)\Gamma(2-\lambda)}{\Gamma(-1+n-\lambda)} + 4\sum_{n=1}^\infty \frac{1}{n^2}\left(1 - \lambda\partial_\epsilon + \frac{\lambda^2}{2}\partial_\epsilon^2\right)\frac{\Gamma(n-3)\Gamma(2+\epsilon)}{\Gamma(-1+n+\epsilon)}\Big|_{\epsilon=0} \\ =& \frac{1}{108}\left(3\pi^2 - 34\right) + \frac{\lambda}{54}\left[30 - 5\pi^2 - 36\zeta(3)\right] + \frac{\lambda^2}{1080}\left[2040 + 30\pi^2 - \pi^4 - 900\zeta(3)\right] \\ & + \frac{1}{18}\left[1 + 18\lambda + 3\lambda^2\right]\hat{\psi}(2-\lambda) + \frac{1}{6}\left(3\lambda^2 - 1\right)\hat{\psi}(2-\lambda)^2 \\ & + \left[\frac{1}{2} - \frac{11}{18}\lambda - \frac{3}{2}\lambda^2 + \frac{11}{18}\lambda^3 + \frac{1}{3}\left(\lambda - \lambda^3\right)\hat{\psi}(2-\lambda)\right]\psi'(2-\lambda) \\ & - \frac{1}{6}\left(\lambda - \lambda^3\right)\psi''(2-\lambda) + \frac{1}{4(\lambda-2)}\,{}_4F_3(1,1,4,4;5,5,3-\lambda;1).\end{aligned} \tag{A.7}$$

The remainder of this section describes the computation of part (a), the divergent contribution of the single-insertion function (5.54), which is performed in momentum space. After the integrations over the zero-components of the loop momenta are performed, the

product of the top and antitop propagators reduces to the simple form $1/(\mathbf{p}^2 - mE)$ and the "mass" mE of the non-relativistic heavy quark propagators is the only scale in the integrals. It is convenient to rescale the loop momenta by $\mathbf{p} \to \sqrt{-mE}\,\mathbf{k}$, which reveals that the loop integrals only depend on the dimension d and the non-integer power $1+u$ from the NLO Coulomb insertion. We have used FIRE [133, 134] to reduce the diagrams to a small set of master integrals. We use solid lines to denote the rescaled massive propagators of the form $1/(\mathbf{k}^2+1)$, dashed lines for potential gluons and a wavy line for the insertion of the NLO Coulomb potential, i.e. the gluon propagator with an index $1+u$. At first, we assign μ_r to all μ with an exponent proportional to u and μ_w to all μ with an exponent proportional to ϵ, since the former are related to the running of the strong coupling in the NLO Coulomb potential. We note, however, that this introduces some spurious terms, which will be addressed in more detail below. We find

$$I_{\mathrm{P}}^{00}[1+u] = m^3 E \left(\frac{-mE}{\mu_r^2}\right)^{-u} \left(\frac{-mE}{\tilde{\mu}_w^2}\right)^{-2\epsilon} \left[\frac{1+u}{1-u-2\epsilon}\right. \left.\right], \tag{A.8}$$

$$\begin{aligned} I_{\mathrm{P}}^{10}[1+u] &= m^3 E\lambda \left(\frac{-mE}{\mu_r^2}\right)^{-u} \left(\frac{-mE}{\tilde{\mu}_w^2}\right)^{-3\epsilon} (8\pi) \\ &\times \left[\frac{1+u}{4\epsilon(1-u-2\epsilon)} \right. \left. - \frac{1-u-4\epsilon-2u^2-6u\epsilon-4\epsilon^2}{8\epsilon(1-u-2\epsilon)} \right], \end{aligned} \tag{A.9}$$

$$\begin{aligned} I_{\mathrm{P}}^{20}[1+u] &= -m^3 E\lambda^2 \left(\frac{-mE}{\mu_r^2}\right)^{-u} \left(\frac{-mE}{\tilde{\mu}_w^2}\right)^{-4\epsilon} \frac{(8\pi)^2}{64\epsilon^2(2\epsilon-1)(u+2\epsilon-1)(u+3\epsilon)} \\ &\times \Big\{ (u+2\epsilon)(u+4\epsilon-1)\Big[u^2(4\epsilon-2) + u(4\epsilon(7\epsilon-1)-1) \\ &\qquad + 4\epsilon\left(12\epsilon^2+\epsilon-1\right)+1\Big] \\ &\quad + 2(u+3\epsilon)\Big[(2\epsilon-1)\left(2u^2+6u\epsilon+u+4\epsilon(\epsilon+1)-1\right) \\ &\quad + 2(1+u)\Big[-2\epsilon(4\epsilon(\epsilon+1)-1) + (2\epsilon-1) \Big(\Big)^2\Big]\Big]\Big\}, \end{aligned} \tag{A.10}$$

$$\begin{aligned} I_{\mathrm{P}}^{11}[1+u] &= -m^3 E\lambda^2 \left(\frac{-mE}{\mu_r^2}\right)^{-u} \left(\frac{-mE}{\tilde{\mu}_w^2}\right)^{-4\epsilon} \frac{(8\pi)^2}{32\epsilon^2(u+2\epsilon-1)(u+3\epsilon)} \\ &\times \Big\{ (u+4\epsilon-1)\left[u\left(2u^2+u-1\right)+8(4u+1)\epsilon^2+2(u(7u+3)-2)\epsilon+24\epsilon^3\right] \end{aligned}$$

$$+2(u+3\epsilon)\Bigg[\left(2u^2+6u\epsilon+u+4\epsilon(\epsilon+1)-1\right)$$ 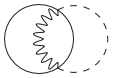 $$+(u+1)$$ 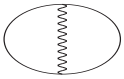 $$\left(\quad\right)^2\Bigg]\Bigg\}. \tag{A.11}$$

With the exception of the diagram with three massive lines, all master integral have been computed with standard methods. We obtain

$$\equiv \int \frac{d^{d-1}\mathbf{k}}{(2\pi)^{d-1}}\frac{1}{\mathbf{k}^2+1} = \frac{1}{(4\pi)^{\frac{3}{2}-\epsilon}}\Gamma\left(-\frac{1}{2}+\epsilon\right), \tag{A.12}$$

$$\begin{aligned}\equiv&\int \frac{d^{d-1}\mathbf{k}_1}{(2\pi)^{d-1}}\int \frac{d^{d-1}\mathbf{k}_1}{(2\pi)^{d-1}}\frac{1}{[\mathbf{k}_1^2+1][\mathbf{k}_2^2+1][(\mathbf{k}_1-\mathbf{k}_2)^2]^{1+u}}\\ =&\frac{1}{(4\pi)^{3-2\epsilon}}(-2\pi)\frac{\Gamma(-2u-2\epsilon)\Gamma(1/2+u+\epsilon)\sin[\pi(u+\epsilon)]}{\Gamma(1-u-2\epsilon)\Gamma(3/2-\epsilon)\sin[\pi(u+2\epsilon)]},\end{aligned} \tag{A.13}$$

$$\begin{aligned}\equiv&\int\left[\prod_{j=1}^{3}\frac{d^{d-1}\mathbf{k}_j}{(2\pi)^{d-1}}\right]\frac{1}{[\mathbf{k}_1^2+1][\mathbf{k}_3^2+1][(\mathbf{k}_1-\mathbf{k}_2)^2]^{1+u}(\mathbf{k}_2-\mathbf{k}_3)^2}\\ =&\frac{1}{(4\pi)^{\frac{9}{2}-3\epsilon}}\frac{-2^{1-2u-4\epsilon}\pi^{3/2}\Gamma\left(1/2-u-2\epsilon\right)\Gamma(u+2\epsilon)}{(1-2\epsilon)\Gamma(1+u)\Gamma\left(3/2-u-3\epsilon\right)\cos(\pi\epsilon)}\\ &\times\left(\frac{1}{\cos[\pi(u+\epsilon)]}+\frac{1}{\cos[\pi(u+3\epsilon)]}\right),\end{aligned} \tag{A.14}$$

$$\begin{aligned}\equiv&\int\left[\prod_{j=1}^{4}\frac{d^{d-1}\mathbf{k}_j}{(2\pi)^{d-1}}\right]\frac{1}{[\mathbf{k}_1^2+1][\mathbf{k}_4^2+1][(\mathbf{k}_1-\mathbf{k}_2)^2]^{1+u}(\mathbf{k}_2-\mathbf{k}_3)^2(\mathbf{k}_3-\mathbf{k}_4)^2}\\ =&\frac{1}{(4\pi)^{6-4\epsilon}}\left(\frac{1}{\sin[\pi(u+2\epsilon)]}+\frac{1}{\sin[\pi(u+4\epsilon)]}\right)\left(-2^{2-2u-6\epsilon}\pi^{3/2}\right)\\ &\times\frac{\Gamma\left(1/2-\epsilon\right)\Gamma(1-u-3\epsilon)\Gamma\left(1/2-u-\epsilon\right)\Gamma\left(-1/2+u+3\epsilon\right)}{(1-2\epsilon)\Gamma(1+u)\Gamma(2-u-4\epsilon)\Gamma(1-u-2\epsilon)\cos(\pi\epsilon)}.\end{aligned} \tag{A.15}$$

The remaining master integral is more difficult:

$$\equiv\int\left[\prod_{j=1}^{4}\frac{d^{d-1}\mathbf{k}_j}{(2\pi)^{d-1}}\right]\frac{1}{[\mathbf{k}_1^2+1][\mathbf{k}_2^2+1][\mathbf{k}_4^2+1][(\mathbf{k}_1-\mathbf{k}_2)^2]^{1+u}(\mathbf{k}_2-\mathbf{k}_3)^2(\mathbf{k}_3-\mathbf{k}_4)^2}. \tag{A.16}$$

For $u=0$ one can reduce the integral with FIRE and obtain a result in terms of the other master integrals. The result agrees with the one in [135]. For $u=\epsilon$ we only compute the

solution in expanded form, where terms up to order ϵ^2 are required because the coefficient of this master integral in (A.10) and the NLO potential each contain a factor $1/\epsilon$. We derive a Mellin-Barnes representation and perform an analytic continuation of the integrals with the mathematica package `MB` [210]. The result can be rewritten in terms of single and double infinite sums over the residues in the integration variables by closing the contours. Through algebraic manipulations like partial fractioning these sums can be transformed to cyclotomic harmonic sums. This step was achieved in a semi-automatic fashion with a private mathematica code. After the work was completed, the fully automated package `MBsums` [218] has appeared, that should considerably simplify similar tasks. We use the `Harmonic Sums` package [211–217] to reduce the cyclotomic harmonic sums to a set of known basis sums. Our result is given by

$$\begin{aligned}\Big|_{u=\epsilon} = \frac{\exp(-4\epsilon\gamma_E)}{(4\pi)^{6-4\epsilon}}\Bigg[&\frac{2\pi^2}{5\epsilon^2}+\frac{4\pi^2}{5\epsilon}(4-5\ln 2)+\frac{4\pi^2}{5}\left(26-40\ln 2+25\ln^2 2\right)\\&+\frac{8\pi^2}{15}\epsilon\left(240-390\ln 2+300\ln^2 2-125\ln^3 2+32\zeta(3)\right)\\&+\frac{4\pi^2}{225}\epsilon^2\Big(43560-326\pi^4-72000\ln 2+58500\ln^2 2\\&-30000\ln^3 2+9375\ln^4 2+1920(4-5\ln 2)\zeta(3)\Big)+\mathcal{O}(\epsilon^3)\Bigg].\end{aligned} \tag{A.17}$$

Inserting the results for the master integrals into (A.8)–(A.11) yields the results for the diagrams of part (a). We observe, however, that using $u=\epsilon$ in (A.8)–(A.11) produces in spurious logarithms $\ln(\mu_r/\mu_w)$ through terms of the form

$$\frac{1}{n\epsilon+u}\mu_r^u\mu_w^{n\epsilon}\overset{u=\epsilon}{=}\frac{1}{(n+1)\epsilon}+\ln(\mu_w)+\frac{1}{n+1}\ln\left(\frac{\mu_r}{\mu_w}\right)+\mathcal{O}(\epsilon). \tag{A.18}$$

This signifies the fact that, in general, the origin of poles cannot be unambiguously identified in dimensional regularization. We derive the correct scale assignment by subtracting the scale dependent logarithms from the results of (A.8)–(A.11) and then adding back the respective terms obtained with the Coulomb potential expanded in ϵ, i.e without the identification $u=\epsilon$. Furthermore, we set the scales μ_r and μ_w equal in the singular terms $\ln(\mu_r/\mu_w)/\epsilon$ to render the pole terms scale independent. Our results for the individual diagrams are given by:

$$\begin{aligned}I_{\rm P}^{00}[1] &= \frac{m^3E}{(4\pi)^2}\left[\frac{1}{4\epsilon}+1+L_\lambda^w\right],\\ I_{\rm P}^{00}[1+\epsilon] &= \frac{m^3E}{(4\pi)^2}\left[\frac{1}{6\epsilon}+1+L_\lambda^w\right],\\ \frac{1}{\epsilon}\left[I_{\rm P}^{00}[1+\epsilon]-I_{\rm P}^{00}[1]\right] &= \frac{m^3E}{(4\pi)^2}\left[-\frac{1}{12\epsilon^2}+1+\frac{17\pi^2}{72}+2L_\lambda^r+2L_\lambda^rL_\lambda^w-(L_\lambda^w)^2\right].\end{aligned} \tag{A.19}$$

$$
\begin{aligned}
I_{\mathrm{P}}^{10}[1] = I_{\mathrm{P}}^{10}[1+\epsilon] &= \frac{m^3 E}{(4\pi)^2}\lambda\left[\frac{1}{2}+\frac{\pi^2}{6}\right], \\
\frac{1}{\epsilon}\left[I_{\mathrm{P}}^{10}[1+\epsilon]-I_{\mathrm{P}}^{10}[1]\right] &= \frac{m^3 E}{(4\pi)^2}\lambda\left[\frac{5}{2}+\frac{\pi^2}{3}-2\zeta(3)+\left(1+\frac{\pi^2}{3}\right)L_\lambda^r\right]. \qquad \text{(A.20)} \\
I_{\mathrm{P}}^{20}[1] = I_{\mathrm{P}}^{11}[1] &= \frac{m^3 E}{(4\pi)^2}\lambda^2\left[-\frac{1}{8\epsilon}-\frac{7}{4}+\zeta(3)-L_\lambda^w\right], \\
I_{\mathrm{P}}^{20}[1+\epsilon] &= \frac{m^3 E}{(4\pi)^2}\lambda^2\left[-\frac{1}{10\epsilon}-\frac{17}{10}+\zeta(3)-L_\lambda^w\right], \\
\frac{1}{\epsilon}\left[I_{\mathrm{P}}^{20}[1+\epsilon]-I_{\mathrm{P}}^{20}[1]\right] &= \frac{m^3 E}{(4\pi)^2}\lambda^2\Bigg[\frac{1}{40\epsilon^2}+\frac{1}{20\epsilon}-\frac{29}{10}-\frac{\pi^2}{24}-\frac{\pi^4}{180}+2\zeta(3)+\frac{1}{2}L_\lambda^w \\
&\qquad -\left(\frac{7}{2}-2\zeta(3)\right)L_\lambda^r+\left(L_\lambda^w\right)^2-2L_\lambda^w L_\lambda^r\Bigg]. \qquad \text{(A.21)} \\
I_{\mathrm{P}}^{11}[1+\epsilon] &= \frac{m^3 E}{(4\pi)^2}\lambda^2\left[-\frac{1}{10\epsilon}-\frac{9}{5}+\zeta(3)-L_\lambda^w\right], \\
\frac{1}{\epsilon}\left[I_{\mathrm{P}}^{11}[1+\epsilon]-I_{\mathrm{P}}^{11}[1]\right] &= \frac{m^3 E}{(4\pi)^2}\lambda^2\Bigg[\frac{1}{40\epsilon^2}-\frac{1}{20\epsilon}-\frac{29}{5}+\frac{\pi^2}{8}+\frac{\pi^4}{180}+2\zeta(3)-\frac{1}{2}L_\lambda^w \\
&\qquad -\left(\frac{7}{2}-2\zeta(3)\right)L_\lambda^r+\left(L_\lambda^w\right)^2-2L_\lambda^w L_\lambda^r\Bigg]. \qquad \text{(A.22)}
\end{aligned}
$$

B. Evaluation of the hypergeometric function

The series defining the generalized hypergeometric function in the NLO P-wave Green function (5.55) only converges for $\mathrm{Re}\,(\lambda) < 3$. Values of λ with a large positive real part may however occur for particles with vanishing or very small width when the energy approaches the threshold from below. Therefore, we perform an analytic continuation for the generalized hypergeometric function by expressing it in terms of harmonic sums for which the analytic continuation can be easily done, see for example [215, 219]. In a first step we perform a change of arguments to more suitable values

$$
\begin{aligned}
{}_4F_3(1,1,4,4;5,5,3-\lambda;1) = 4(\lambda-2)(\lambda-1)\lambda(\lambda+1)\Bigg[&\frac{2}{3(1+\lambda)}\,{}_4F_3(1,1,1,1;2,2,-\lambda;1)\\
&+\frac{1}{27}\left(\frac{\lambda(\lambda(3(8-17\lambda)\lambda-20)+11)-18}{(\lambda-1)^2\lambda^2(\lambda+1)}-33\psi_1(2-\lambda)\right)\Bigg].
\end{aligned}
\tag{B.1}
$$

The remaining hypergeometric function has been rewritten in terms of harmonic sums in Appendix A.1 of [220]. This was achieved by rewriting it as the Mellin transform of a dilogarithm, which can then be expressed as

$$
\begin{aligned}
&\frac{1}{(1+\lambda)}\,{}_4F_3(1,1,1,1;2,2,-\lambda;1) = -\mathbf{M}\left[\frac{\mathrm{Li}_2(1-x)}{1-x}\right](-2-\lambda)\\
&= -\left[S_1(-2-\lambda)S_2(-2-\lambda)-\zeta(2)S_1(-2-\lambda)+S_3(-2-\lambda)-S_{2,1}(-2-\lambda)+\zeta(3)\right].
\end{aligned}
\tag{B.2}
$$

We have used the `FORM` [221] program `HARMPOL` [216] for the latter step. The (nested) harmonic sums are defined in the usual way as $S_a(N) = \sum_{i=1}^{N} \frac{1}{i^a}$ and $S_{a,b}(N) = \sum_{i=1}^{N} \frac{1}{i^a} S_b(i)$.

C. Charm-quark mass effects in the bottom-quark pair production cross section

C.1. Charm effects in the Coulomb potential

We consider the Coulomb potential in the presence of n_l light quarks, one of which has a non-zero mass, denoted by m_c. The Coulomb potential can be split into a part containing the contributions from n_l massless quarks and the charm-quark mass correction:

$$\tilde{V} = \tilde{V}_{\text{massless}} + \tilde{V}_{m_c}\,, \tag{C.1}$$

where the charm-quark mass correction $\tilde{V}_{m_c}$ vanishes for $m_c = 0$.

The charm-quark mass corrections to the Coulomb potential have been determined at NNLO in [169,170]. We employ convenient dispersion relation representations from [168], which simplify the computations of the corrections to the cross section. The momentum space potential is given by

$$\tilde{V}_{m_c}(\mathbf{q}) = \sum_{i=1}^{\infty} \delta\tilde{V}_{m_c}^{(i)}(\mathbf{q})\,, \tag{C.2}$$

$$\delta\tilde{V}_{m_c}^{(1)}(\mathbf{q}) = -\frac{4\pi\alpha_s C_F}{\mathbf{q}^2}\frac{\alpha_s}{3\pi}T_F\left[\Pi(\mathbf{q}^2) - \left(\ln\frac{\mathbf{q}^2}{m_c^2} - \frac{5}{3}\right)\right]\,, \tag{C.3}$$

$$\begin{aligned}\delta\tilde{V}_{m_c}^{(2)}(\mathbf{q}) = -\frac{4\pi\alpha_s C_F}{\mathbf{q}^2}\left(\frac{\alpha_s}{4\pi}\right)^2 \Bigg\{ &\frac{8T_F}{3}\left[\Pi(\mathbf{q}^2) - \left(\ln\frac{\mathbf{q}^2}{m_c^2} - \frac{5}{3}\right)\right]\left(a_1 - \beta_0 \ln\frac{\mathbf{q}^2}{\mu^2}\right) \\ &+ \left(\frac{4T_F}{3}\right)^2\left[\Pi(\mathbf{q}^2) - \left(\ln\frac{\mathbf{q}^2}{m_c^2} - \frac{5}{3}\right)\right]^2 \\ &+ \frac{76T_F}{3}\left[\Xi(\mathbf{q}^2) - \left(\ln\frac{\mathbf{q}^2}{m_c^2} - \frac{161}{114} - \frac{26}{19}\zeta_3\right)\right]\Bigg\}\,,\end{aligned} \tag{C.4}$$

with

$$a_1 = \frac{31}{9}C_A - \frac{20}{9}T_F n_l\,, \tag{C.5}$$

$$\beta_0 = \frac{11}{3}C_A - \frac{4}{3}T_F n_l\,, \tag{C.6}$$

$$\Pi(\mathbf{q}^2) = 2\mathbf{q}^2 \int\limits_1^\infty dx \frac{f(x)}{\mathbf{q}^2 + 4x^2 m_c^2}, \tag{C.7}$$

$$\Xi(\mathbf{q}^2) = 2c_1\mathbf{q}^2 \int\limits_{c_2}^\infty \frac{dx}{x} \frac{1}{\mathbf{q}^2 + 4x^2 m_c^2} + 2d_1\mathbf{q}^2 \int\limits_{d_2}^\infty \frac{dx}{x} \frac{1}{\mathbf{q}^2 + 4x^2 m_c^2}, \tag{C.8}$$

$$f(x) = \frac{\sqrt{x^2-1}}{x^2}\left(1 + \frac{1}{2x^2}\right). \tag{C.9}$$

We take the parameters c_1, c_2, d_1, d_2 from [168]

$$c_1 = \frac{\ln\frac{A}{d2}}{\ln\frac{c2}{d2}}, \qquad d_1 = \frac{\ln\frac{c2}{A}}{\ln\frac{c2}{d2}}, \tag{C.10}$$

$$c_2 = 0.470, \qquad d_2 = 1.120, \tag{C.11}$$

$$A = \exp\left(\frac{161}{228} + \frac{13}{19}\zeta_3 - \ln 2\right), \tag{C.12}$$

and neglect the tiny uncertainties, which were found to be numerically insignificant. The potential in configuration space follows from a Fourier transformation. We find

$$\delta V_{m_c}^{(1)}(r) = -\frac{C_F\alpha_s}{r}\frac{\alpha_s}{3\pi}\left[\int\limits_1^\infty dx f(x) e^{-2m_c r x} + \left(\ln(\tilde{m}_c r) + \frac{5}{6}\right)\right], \tag{C.13}$$

$$\begin{aligned}
\delta V_{m_c}^{(2)}(r) = & -\frac{C_F\alpha_s}{r}\left(\frac{\alpha_s}{3\pi}\right)^2 \left\{\left[-\frac{3}{2}\int\limits_1^\infty dx f(x) e^{-2xm_c r}\right.\right. \\
& \times \left(\beta_0\left[\ln\frac{4x^2m_c^2}{\mu^2} - \mathrm{Ei}(2xm_cr) - e^{4xm_cr}\mathrm{Ei}(-2xm_cr)\right] - a_1\right) \\
& + 3\left(\ln(\tilde{m}_c r) + \frac{5}{6}\right)\left(\beta_0\ln(\tilde{\mu}r) + \frac{a_1}{2}\right) + \beta_0\frac{\pi^2}{4}\Bigg] \\
& - \left[\int\limits_1^\infty dx f(x) e^{-2xm_c r}\left(\frac{5}{3} + \frac{1}{x^2} + \frac{\sqrt{x^2-1}(1+2x^2)}{2x^3}\ln\left(\frac{x-\sqrt{x^2-1}}{x+\sqrt{x^2-1}}\right)\right)\right. \\
& + \int\limits_1^\infty dx f(x) e^{-2xm_c r}\left(\ln(4x^2) - \mathrm{Ei}(2xm_cr) - e^{4xm_cr}\mathrm{Ei}(-2xm_cr) - \frac{5}{3}\right) \\
& \left.\left. - \left(\ln(\tilde{m}_c r) + \frac{5}{6}\right)^2 - \frac{\pi^2}{12}\right] \right. \\
& \left. + \frac{57}{4}\left[c_1\Gamma(0, 2c_2m_cr) + d_1\Gamma(0, 2d_2m_cr) + \ln(\tilde{m}_c r) + \frac{161}{228} + \frac{13}{19}\zeta_3\right]\right\},
\end{aligned} \tag{C.14}$$

where

$$\tilde{m}_c = m_c e^{\gamma_E}, \qquad \tilde{\mu} = \mu e^{\gamma_E}. \tag{C.15}$$

We have found some typos in Eq. (30) of [168] and corrected them in (C.14). We also correct an integral representation in [168] that should read

$$e^{-x}\,\mathrm{Ei}(x) + e^{x}\,\mathrm{Ei}(-x) = \mathcal{P}\int\limits_0^\infty dt \frac{2te^{-xt}}{1-t^2}. \tag{C.16}$$

However, to our understanding the computations in [168] were performed with the correct potential.

C.2. Charm effects in the relation between PS and pole mass

We recall the definition of the PS mass at the subtraction scale μ_f [51]:

$$m_b = m_b^{\rm PS}(\mu_f) - \frac{1}{2}\int_{|\mathbf{q}|<\mu_f} \frac{d^3\mathbf{q}}{(2\pi)^3}\,\tilde{V}(|\mathbf{q}|) = m_b^{\rm PS}(\mu_f) + \sum_{i=0}^{\infty}\delta m_i^{\rm PS}\,. \tag{C.17}$$

The charm-quark mass corrections to the PS-pole relation will be denoted by

$$\sum_{i=1}^{\infty}\delta m_{i,m_c}^{\rm PS} = -\frac{1}{2}\int_{|\mathbf{q}|<\mu_f} \frac{d^3\mathbf{q}}{(2\pi)^3}\,\tilde{V}_{m_c}(|\mathbf{q}|)\,, \tag{C.18}$$

and vanishes for $m_c = 0$. We obtain

$$\delta m_{1,m_c}^{\rm PS} = \frac{\alpha_s}{\pi}C_F\mu_f\frac{\alpha_s}{4\pi}\frac{4}{3}T_F\left(I_\Pi(z) + I_{\ln}(m_c) + \frac{5}{3}\right), \tag{C.19}$$

$$\begin{aligned}
\delta m_{2,m_c}^{\rm PS} = \frac{\alpha_s}{\pi}C_F\mu_f\left(\frac{\alpha_s}{4\pi}\right)^2\frac{4}{3}T_F\Bigg[& \\
&+ \frac{4}{3}T_F\left(I_{\Pi^2}(z) + 2I_{\Pi,\ln}(z,m_c) + I_{\ln,\ln}(m_c,m_c) + \frac{10}{3}\big(I_\Pi(z) + I_{\ln}(m_c)\big) + \frac{25}{9}\right)\\
&+ 2\beta_0\left(I_{\Pi,\ln}(z,\mu) + I_{\ln,\ln}(m_c,\mu) + \frac{5}{3}I_{\ln}(\mu)\right)\\
&+ 19\left(c_1 I_\Xi\left(\frac{z}{c_2^2}\right) + d_1 I_\Xi\left(\frac{z}{d_2^2}\right) + I_{\ln}(m_c)\right)\\
&+ 2a_1\left(I_\Pi(z) + I_{\ln}(m_c) + \frac{5}{3}\right) + \frac{161}{6} + 26\zeta_3\Bigg]
\end{aligned} \tag{C.20}$$

where

$$z = \left(\frac{\mu_f}{2m_c}\right)^2, \tag{C.21}$$

$$I_{\ln}(m) = \ln\frac{m^2}{\mu_f^2} + 2\,, \tag{C.22}$$

$$I_{\ln,\ln}(m_0,m_1) = \ln\frac{m_0^2}{\mu_f^2}\ln\frac{m_1^2}{\mu_f^2} + 2\ln\frac{m_0^2}{\mu_f^2} + 2\ln\frac{m_1^2}{\mu_f^2} + 8\,, \tag{C.23}$$

$$I_\Xi(\hat{z}) = 2\,\frac{\arctan\sqrt{\hat{z}}}{\sqrt{\hat{z}}} + \ln(1+\hat{z}) - 2\,, \tag{C.24}$$

$$I_\Pi(z) = \frac{z}{5}\left[{}_2F_1\left(\begin{matrix}1 & 1\\ \frac{7}{2}\end{matrix}\,\middle|\, -z\right) + \frac{1}{3}\,{}_3F_2\left(\begin{matrix}1 & 1 & \frac{3}{2}\\ \frac{5}{2} & \frac{7}{2}\end{matrix}\,\middle|\, -z\right)\right], \tag{C.25}$$

$$I_{\Pi,\ln}(z,m) = I_\Pi(z)\ln\frac{m^2}{\mu_f^2} + \frac{2}{15}z\left[{}_3F_2\left(\begin{matrix}1 & 1 & \frac{3}{2}\\ \frac{5}{2} & \frac{7}{2}\end{matrix}\,\middle|\, -z\right) + \frac{1}{3}\,{}_4F_3\left(\begin{matrix}1 & 1 & \frac{3}{2} & \frac{3}{2}\\ \frac{5}{2} & \frac{5}{2} & \frac{7}{2}\end{matrix}\,\middle|\, -z\right)\right], \tag{C.26}$$

$$\begin{aligned} I_{\Pi^2}(z) = \frac{1}{45z^3}\Big\{ & z\big(-9 + z(48+785z)\big) \\ & - 6\sqrt{z(1+z)}\big(-3 + z(17+110z)\big)\,\mathrm{arsinh}(\sqrt{z}) \\ & + 9\,(-1+5z+20z^3)\,\mathrm{arsinh}(\sqrt{z})^2 \\ & + z^{\frac{5}{2}}\Big[-18\pi^2 + 36\,\mathrm{arsinh}(\sqrt{z})\big(\ln(z) - 2\ln(-1+\sqrt{1+z})\big) \\ & \quad - 36\,\mathrm{Li}_2\left((\sqrt{z}+\sqrt{1+z})^{-2}\right) + 144\,\mathrm{Li}_2\left((\sqrt{z}+\sqrt{1+z})^{-1}\right)\Big]\Big\}. \end{aligned} \tag{C.27}$$

The parameters c_1, c_2, d_1, d_2 are given in (C.10)–(C.12). $\mathrm{Li}_2(x) = \sum_{i=1}^{\infty} x^i/i^2$ is the dilogarithm function and ${}_PF_{P-1}$ denotes (generalized) hypergeometric functions. We refrain from expressing the ${}_2F_1$ and ${}_3F_2$ functions in (C.25) and (C.26) through elementary functions because of the length of the resulting expressions. The strong coupling α_s is defined assuming $n_l = 4$ active flavours, i.e. $\alpha_s = \alpha_s^{(n_l)}(\mu)$.

The Eqs. (C.19)–(C.21) are given in the pole-mass scheme for the charm quark. In the $\overline{\mathrm{MS}}$ mass scheme, (C.20) must be modified by

$$\delta m_{2,m_c}^{\mathrm{PS}} \to \delta m_{2,m_c}^{\mathrm{PS}} + \frac{\alpha_s}{\pi}C_F\mu_f\left(\frac{\alpha_s}{4\pi}\right)^2\frac{16}{3}T_F C_F\left(2 + 3\ln\frac{\mu_c}{m_c^{\overline{\mathrm{MS}}}(\mu_c)}\right)\big(1 - zI'_\Pi(z)\big) \tag{C.28}$$

where $m_c^{\overline{\mathrm{MS}}}(\mu_c)$ is the charm-quark $\overline{\mathrm{MS}}$ mass and

$$I'_\Pi(z) = \frac{1}{2(z+1)} + \frac{z-2}{10(z+1)}\,{}_2F_1\left(\begin{matrix}1 & 1\\ \frac{7}{2}\end{matrix}\,\middle|\, -z\right) - \frac{1}{30}\,{}_3F_2\left(\begin{matrix}1 & 1 & \frac{3}{2}\\ \frac{5}{2} & \frac{7}{2}\end{matrix}\,\middle|\, -z\right). \tag{C.29}$$

In the numerical analysis, we set the scale μ_c to the renormalization scale μ.

C.3. NLO charm effects in the non-relativistic current correlator

We describe the calculation of the NLO corrections to the non-relativistic vector-current correlator in detail. We parametrize the perturbative expansion of the Green function $G(E)$ defined in (3.22) as

$$G(E) = G_0(E) + \sum_{i=1}^{\infty} \delta_i G(E)\,. \tag{C.30}$$

Again, the charm-quark mass corrections $\delta_i G_{m_c}(E)$ are defined such that they vanish for $m_c = 0$. We then have

$$\delta_i G(E) = \delta_i G_{\text{massless}}(E) + \delta_i G_{m_c}(E). \tag{C.31}$$

The NLO contribution $\delta_1 G_{m_c}(E)$ is given by the single insertions of the potential (C.13). We find it convenient to split the correction into a part A given by the two loop diagram, i.e. with no additional Coulomb exchange between the quark and the anti-quark, and a part B, which contains the remainder, i.e. all ladder diagrams with at least one Coulomb exchange. This distinction follows [89] (see also Section 5.2), although here both parts are finite.

We first compute the two-loop diagram of part A in momentum space

$$\begin{aligned}\delta_1 G_{m_c,A}(E) &= -\int \left[\prod_{i=1}^{4} \frac{d^3\mathbf{p}_i}{(2\pi)^3}\right] \tilde{G}_0^{(0\text{ex})}(\mathbf{p}_1,\mathbf{p}_2;E)\delta\tilde{V}_{m_c}^{(1)}(\mathbf{p}_3-\mathbf{p}_2)\tilde{G}_0^{(0\text{ex})}(\mathbf{p}_3,\mathbf{p}_4;E) \\ &= m_b^2 \frac{4T_f C_f \alpha_s^2}{3}\left[2I_A[\Pi] + \frac{d}{du} I_A[1+u]\Big|_{u=0,\mu_r\to m_c} + \frac{5}{3} I_A[1]\right], \end{aligned} \tag{C.32}$$

where $\tilde{G}_0^{(0\text{ex})}$ is the zero-gluon exchange part of the Green function, the single insertion function $I_A[1+u]$ is defined as in [89], and

$$I_A[\Pi] = \tilde{\mu}^{4\epsilon} \int_1^{\infty} dx f(x) \int \frac{d^{d-1}\vec{p}}{(2\pi)^{d-1}} \int \frac{d^{d-1}\vec{p}'}{(2\pi)^{d-1}} \frac{1}{\vec{p}^2 - m_b E} \frac{1}{(\vec{p}-\vec{p}')^2 + 4x^2 m_c^2} \frac{1}{\vec{p}'^2 - m_b E}, \tag{C.33}$$

is the single insertion function associated with the contribution of a massive charm quark, without the subtraction of the massless contribution. We employ the Mellin-Barnes representation (see e.g. [132])

$$\frac{1}{(X+Y)^{\eta}} = \frac{1}{\Gamma(\eta)} \frac{1}{2\pi i} \int_{-i\infty}^{+i\infty} dz \Gamma(\eta+z)\Gamma(-z) \frac{Y^z}{X^{\eta+z}}, \tag{C.34}$$

where the contour must be chosen to the left of all poles from $\Gamma(-z)$ and to the right of all poles from $\Gamma(\eta+z)$, to simplify the denominator from the potential. The expression under

the Mellin-Barnes integral then corresponds to part A of the single insertion function of the massless potential known from [89]. We find

$$\begin{aligned}
I_A[\Pi] &= \tilde{\mu}^{4\epsilon}\frac{1}{2\pi i}\int\limits_{-i\infty}^{i\infty} du\Gamma(1+u)\Gamma(-u)\int\limits_1^\infty dx f(x)(4x^2m_c^2)^u \\
&\quad\times\int\frac{d^{d-1}\vec{p}}{(2\pi)^{d-1}}\int\frac{d^{d-1}\vec{p}'}{(2\pi)^{d-1}}\frac{1}{\vec{p}^2-m_bE}\frac{1}{[(\vec{p}-\vec{p}')^2]^{1+u}}\frac{1}{\vec{p}'^2-m_bE} \\
&= \frac{\Gamma(3/2)}{2(4\pi)^{d-1}}\left(\frac{\tilde{\mu}^2}{-m_bE}\right)^{2\epsilon}\frac{1}{2\pi i}\int\limits_{-i\infty}^{i\infty} du\Gamma(1+u)\Gamma(-u)\left(\xi^2/4\right)^{-u} \\
&\quad\times\left[\frac{\Gamma(-u)}{\Gamma(3/2-u)}+\frac{\Gamma(1-u)}{2\Gamma(5/2-u)}\right]\frac{\Gamma(1/2-\epsilon-u)\Gamma(1/2+\epsilon+u)^2\Gamma(u+2\epsilon)}{\Gamma(3/2-\epsilon)\Gamma(1+2\epsilon+2u)} \\
&= \frac{\Gamma(3/2)}{128\pi^2}\left[\frac{\Gamma(1-2\epsilon)\Gamma(2\epsilon)\Gamma(1/2+\epsilon)\Gamma(1/2-\epsilon)^2}{\Gamma(3/2-\epsilon)\Gamma(1-2\epsilon)}\frac{3(1+2\epsilon)\Gamma(2\epsilon)}{2\Gamma(5/2+2\epsilon)}\left(\frac{\mu e^{\frac{\gamma_E}{2}}}{2m_c}\right)^{4\epsilon}\right. \\
&\quad\left.+\frac{1}{2\pi i}\int\limits_{-\frac{1}{4}-i\infty}^{-\frac{1}{4}+i\infty} du\frac{3u(1-u)\Gamma(-u)^2\Gamma(1/2-u)\Gamma(1/2+u)^2\Gamma(u)^2}{2\pi\Gamma(3/2)\Gamma(1+2u)\Gamma(5/2-u)}\left(\frac{4m_c\lambda}{m_b\alpha_sC_F}\right)^{2u}\right].
\end{aligned} \tag{C.35}$$

The $1/\epsilon$ poles cancel with those of the massless part in (C.32) and we obtain

$$\begin{aligned}
\delta_1 G_{m_c,A}(E) &= \frac{m_b^2\alpha_s^2C_F}{96\pi^2}\left[4L_\lambda^{(m_c)}\left(L_\lambda^{(m_c)}+\frac{5}{3}\right)+\pi^2+\frac{56}{9}\right. \\
&\quad\left.+\frac{1}{2\pi i}\int\limits_{-\frac{1}{4}-i\infty}^{-\frac{1}{4}+i\infty} du\left(\frac{2}{\xi}\right)^{2u}\frac{3u(1-u)\Gamma(-u)^2\Gamma(1/2-u)\Gamma(1/2+u)^2\Gamma(u)^2}{2\pi\Gamma(1+2u)\Gamma(5/2-u)}\right],
\end{aligned} \tag{C.36}$$

where

$$\xi=\frac{\sqrt{-m_bE}}{m_c},\qquad L_\lambda^{(m_c)}=\log\frac{m_c\lambda}{m_b\alpha_sC_F}. \tag{C.37}$$

The first line in Eq. (C.36) is equivalent to the subtraction of the contribution from a massless light quark and the Mellin-Barnes integral in the second line to the contribution from a massive charm quark. One can deform the contour across the pole at $u=0$ to simplify the result

$$\delta_1 G_{m_c,A}(E) = \frac{m_b^2\alpha_sC_F}{4\pi}\frac{\alpha_s}{4\pi}\frac{1}{2\pi i}\int\limits_{-i\infty}^{i\infty} du\,\frac{u(1-u)\Gamma(-u)^2\Gamma(1/2-u)\Gamma(1/2+u)^2\Gamma(u)^2}{4\pi(\xi/2)^{2u}\Gamma(1+2u)\Gamma(5/2-u)}, \tag{C.38}$$

where the contour now must be chosen to the right of the pole at $u = 0$, i.e. such that $0 < \mathrm{Re}(u) < 1/2$ on the real axis. The integral can be performed numerically.

Now we consider part B, i.e. the contributions with more than two loops. It can be computed in configuration space

$$\begin{aligned}
\delta_1 G_{m_c,B}(E) &= -\int d^3\mathbf{r}\delta V_{m_c}^{(1)}(\mathbf{r})\left[G_0(0,\mathbf{r};E)^2 - G_0^{(0\mathrm{ex})}(0,\mathbf{r};E)^2\right] \\
&= \frac{m_b^2 C_F \alpha_s^2}{12\pi^2}\int\limits_0^\infty dz \int\limits_0^1 dy \frac{(1+z)^\lambda - 1}{z(1+yz)}\left[\int\limits_1^\infty dx \frac{f(x)}{\left(1+\frac{y(1-y)z}{1+yz}\frac{x}{\xi}\right)^2}\right. \\
&\quad \left. + \frac{11}{6} + \log\frac{m_c}{2p} - \log\left(\frac{1+yz}{y(1-y)z}\right)\right] \\
&= \frac{m_b^2 C_F \alpha_s^2}{12\pi^2}\left[\delta J_c^{(1)} + \left(\frac{5}{6} + L_\lambda^{(m_c)}\right) j_0 + \frac{1}{2} j_1\right],
\end{aligned} \tag{C.39}$$

where $p = \sqrt{-mE}$, we have used the integral representation (3.34) for the LO Green function and applied the integral transformations described in [89] and Appendix A. The $j_{0,1}$ can be taken from [89] and

$$\delta J_c^{(1)} = \int\limits_1^\infty dx f(x) \int\limits_0^\infty dz \int\limits_0^1 dy \frac{1+yz}{y^2(1-y)^2 z^3} \frac{(1+z)^\lambda - 1}{\left[\frac{1+yz}{y(1-y)z} + \frac{x}{\xi}\right]^2}. \tag{C.40}$$

A convenient strategy to simplify (C.40) is to introduce the following Mellin-Barnes-type representation[1]

$$\begin{aligned}
&\frac{\lambda}{\Gamma(1-\lambda)} \frac{1}{2\pi i} \int\limits_{-i\infty}^{i\infty} dw \frac{\Gamma(-\lambda+w)\Gamma(w)\Gamma(1-w)}{\Gamma(1+w)} z^w \qquad (C.41) \\
&= -\frac{\lambda}{\Gamma(1-\lambda)} \sum_{n=1}^\infty \frac{(-1)^n}{n!}\Gamma(-\lambda+n) z^n \\
&= (1+z)^\lambda - 1.
\end{aligned}$$

[1] This applies in more generality to situations, where one would like to use a series representations to simplify an integrand, but the individual terms in the series are singular after integration. A Mellin-Barnes-type representation, if it can be found, naturally provides an analytical regulator and yields extra or higher order poles in the Mellin-Barnes integral instead of singular terms in the sum.

Applying (C.42) and (C.34) to (C.40), we find

$$\begin{aligned}
\delta J_c^{(1)} &= \frac{\lambda}{\Gamma(1-\lambda)}\frac{1}{(2\pi i)^2}\int\limits_{-i\infty}^{i\infty} du\Gamma(2+u)\Gamma(-u)\int\limits_{-i\infty}^{i\infty} dw\frac{\Gamma(-\lambda+w)\Gamma(w)\Gamma(1-w)}{\Gamma(1+w)} \\
&\quad\times\int\limits_1^\infty dx f(x)\left(\frac{x}{\xi}\right)^u\int\limits_0^\infty dz\int\limits_0^1 dy\frac{z^{w+u-1}}{(1+yz)^{u+1}}y^u(1-y)^u \\
&\overset{z\to z/y}{=} \frac{\lambda\Gamma(3/2)}{2\Gamma(1-\lambda)}\frac{1}{(2\pi i)^2}\int\limits_{-i\infty}^{i\infty} du\frac{\Gamma(2+u)\Gamma(-u)}{\xi^u}\int\limits_{-i\infty}^{i\infty} dw\frac{\Gamma(-\lambda+w)\Gamma(w)\Gamma(1-w)}{\Gamma(1+w)} \\
&\quad\times\left[\frac{\Gamma(-u/2)}{\Gamma(3/2-u/2)}+\frac{\Gamma(1-u/2)}{2\Gamma(5/2-u/2)}\right]\int\limits_0^\infty dz\int\limits_0^1 dy\frac{z^{w+u-1}}{(1+z)^{u+1}}y^{-w}(1-y)^u \\
&= \frac{\lambda\Gamma(3/2)}{2\Gamma(1-\lambda)}\frac{1}{(2\pi i)^2}\int\limits_{-i\infty}^{i\infty} du\frac{\Gamma(2+u)\Gamma(-u)}{\xi^u}\int\limits_{-i\infty}^{i\infty} dw\frac{\Gamma(-\lambda+w)\Gamma(w)\Gamma(1-w)^3}{\Gamma(1+w)} \\
&\quad\times\left[\frac{\Gamma(-u/2)}{\Gamma(3/2-u/2)}+\frac{\Gamma(1-u/2)}{2\Gamma(5/2-u/2)}\right]\frac{\Gamma(u+w)}{\Gamma(2+u-w)},
\end{aligned} \tag{C.42}$$

which can be evaluated numerically. The contours must be chosen such that Re $u \in (-1,0)$, Re $w \in (0,1)$ and Re $u+w>0$ on the real axis. After the contour of the u-integral is pushed across the pole at $u=0$ and the corresponding residue has canceled the massless $j_{0,1}$ terms in (C.39), the result for part B can be written as a two-dimensional Mellin-Barnes integral

$$\begin{aligned}
\delta_1 G_{m_c,B}(E) &= \frac{m_b^2\alpha_s C_F}{4\pi}\frac{\alpha_s}{4\pi}\left(-\frac{\sqrt{\pi}}{\Gamma(-\lambda)}\right)\frac{1}{(2\pi i)^2}\int\limits_{-i\infty}^{i\infty} dw\,\Gamma(w+1-\lambda)\Gamma^*(-w-1)\Gamma(-w)^2 \\
&\quad\times\int\limits_{-i\infty}^{i\infty} du\,I^{(1)}(u)\xi^{-u}\frac{\Gamma(2+u)\Gamma(-u)\Gamma(1+u+w)}{\Gamma(1+u-w)},
\end{aligned} \tag{C.43}$$

where

$$I^{(1)}(u) = \frac{\Gamma(2-\frac{u}{2})}{u\,\Gamma(\frac{5-u}{2})}\,. \tag{C.44}$$

The contour for the integral over the variable u should now be chosen such that $0 < \mathrm{Re}(u) < 1$ on the real axis. In going from (C.42) to (C.43) we have furthermore redefined w. Following [132], the notation $\Gamma^*(-w-1)$ implies that the contour should be fixed to the right of the first pole at $w=-1$. Above threshold, i.e. for $E>0$, λ is purely imaginary and left and right poles are separated. Thus, the natural choice for the contour is parallel to the imaginary axis with $-1 < \mathrm{Re}(w) < 0$ and the integration can be performed numerically.

For positive integer values N of λ, i.e. below threshold, part B (C.43) contains poles in $N-\lambda$ because of the pinching of the contour in the complex w plane by left and right poles. We recall from Section 5.2.3 that the singular terms in an expansion of the Green function for λ near N determine the corrections to the energy levels and wave functions of the resonances. It is now straightforward to extract the expressions for the NLO charm-mass corrections to the resonances, that are given in Appendix C.4.

The calculation of the NNLO charm-quark effects for the resonances was performed in the same way, i.e. applying the representation (C.34) to the potentials and (C.42) for the term $(1+z)^\lambda - 1$, and proceeding otherwise as for the conventional Coulomb corrections described in [89]. We refrain from showing the details of this lengthy computation and only present the results in Appendix C.4.

C.4. Charm corrections to bound-state energies and wave functions

We parametrize the energies and wave functions of the bound states by

$$E_N = E_N^{(0)}\left(1+\sum_{i=1}^{\infty} e_N^{(i)}\right), \tag{C.45}$$

$$|\psi_N(0)|^2 = |\psi_N^{(0)}(0)|^2\left(1+\sum_{i=1}^{\infty} f_N^{(i)}\right), \tag{C.46}$$

with $E_N = -m_b(\alpha_s C_F/(2n))^2$ and $|\psi_N(0)|^2 = (m_b\alpha_s C_F/(2n))^3/\pi$. The higher-order terms $e_N^{(i)}, f_N^{(i)}$ are again split into two parts

$$e_N^{(i)} = e_{N,\text{massless}}^{(i)} + e_{N,m_c}^{(i)}\,, \tag{C.47}$$

$$f_N^{(i)} = f_{N,\text{massless}}^{(i)} + f_{N,m_c}^{(i)}\,, \tag{C.48}$$

where $e_{N,\text{massless}}^{(i)}, f_{N,\text{massless}}^{(i)}$ are the known corrections with massless charm quarks and $e_{N,m_c}^{(i)}, f_{N,m_c}^{(i)}$ vanish for $m_c = 0$. The NLO ($i = 1$) mass corrections are due to the single insertion of the NLO Coulomb potential in the Green function. The NNLO ($i = 2$) contributions are further split into three parts

$$e_{N,m_c}^{(2)} = e_{N,\{m_c\}}^{(2)} + e_{N,\{m_c,m_c\}}^{(2)} + e_{N,\{m_c,\text{massless}\}}^{(2)}\,, \tag{C.49}$$

$$f_{N,m_c}^{(2)} = f_{N,\{m_c\}}^{(2)} + f_{N,\{m_c,m_c\}}^{(2)} + f_{N,\{m_c,\text{massless}\}}^{(2)}\,, \tag{C.50}$$

where the subscript $\{m_c\}$ denotes the single insertions of the NNLO potential $V_{m_c}^{(2)}$, $\{m_c, m_c\}$ denotes the double insertion of the NLO potential $V_{m_c}^{(1)}$ and $\{m_c, \text{massless}\}$ denotes the mixed double insertion of the charm-correction V_{m_c} and the massless potential V_{massless}. Our results for these contributions are given below.

The single insertion corrections to the energy levels and wave functions read

$$e^{(1)}_{N,m_c} = -2\,\Gamma(1/2)\Gamma(N)\frac{\alpha_s}{4\pi}\frac{1}{2\pi i}\int_{-i\infty}^{i\infty} du\,\xi_N^{-u}\,I^{(1)}(u)\sum_{i=1}^{N}\eta_c(u,i,N)\,, \tag{C.51}$$

$$e^{(2)}_{N,\{m_c\}} = \frac{4}{3}\,\Gamma(1/2)\Gamma(N)\left(\frac{\alpha_s}{4\pi}\right)^2\frac{1}{2\pi i}\int_{-i\infty}^{i\infty} du\,\xi_N^{-u}\,I^{(2)}(u)\sum_{i=1}^{N}\eta_c(u,i,N)\,, \tag{C.52}$$

$$f^{(1)}_{N,m_c} = -\Gamma(1/2)\Gamma(N+1)\frac{\alpha_s}{4\pi}\frac{1}{2\pi i}\int_{-i\infty}^{i\infty} du\,\xi_N^{-u}\,I^{(1)}(u)\sum_{i=1}^{N}\phi_c(u,i,N)\,, \tag{C.53}$$

$$f^{(2)}_{N,\{m_c\}} = \frac{2}{3}\Gamma(1/2)\Gamma(N+1)\left(\frac{\alpha_s}{4\pi}\right)^2\frac{1}{2\pi i}\int_{-i\infty}^{i\infty} du\,\xi_N^{-u}\,I^{(2)}(u)\sum_{i=1}^{N}\phi_c(u,i,N)\,, \tag{C.54}$$

where

$$\xi_N = \frac{\alpha_s C_F m_b}{2N m_c}\,, \tag{C.55}$$

$$\eta_c(u,i,N) = \frac{\Gamma(-u)\Gamma(u+2)}{\Gamma(N-i+1)\Gamma(i)^2\Gamma(i+1)}\frac{\Gamma(u+i)}{\Gamma(u-i+2)}\,, \tag{C.56}$$

$$\begin{aligned}\phi_c(u,i,N) = \eta_c(u,i,N)\,\Bigg(&\frac{3-u}{N} - \psi(N+1) + 2\,\psi(i) + \psi(i+1)\\ &- \psi(u+i) - \psi(u-i+2)\Bigg)\,,\end{aligned} \tag{C.57}$$

$$\begin{aligned}I^{(2)}(u) = {}& \frac{2\,\Gamma(3-\frac{u}{2})}{(u-2)\Gamma(\frac{7-u}{2})} - \frac{\Gamma(2-\frac{u}{2})}{u\,\Gamma(\frac{5-u}{2})}\Bigg(3a_1 - 3\beta_0\ln\left(\frac{m_c^2}{\mu^2}\right)\\ &+ (2+3\beta_0)\left[\frac{2}{u} + \psi\left(2-\frac{u}{2}\right) - \psi\left(\frac{5-u}{2}\right) - \ln(4) + \pi\cot\left(\frac{\pi}{2}u\right)\right]\Bigg)\\ &+ \left(-\frac{2}{3}\frac{\Gamma(\frac{u-5}{2})}{(u-6)\Gamma(\frac{u}{2}-2)} - 2\frac{\Gamma(\frac{u-3}{2})}{(u-4)\Gamma(\frac{u}{2}-1)} + \frac{8}{3}\frac{\Gamma(\frac{u+1}{2})}{u\,\Gamma(\frac{u}{2}+1)}\right)\cot\left(\frac{\pi}{2}u\right)\\ &- \frac{38}{\sqrt{\pi}}\frac{1}{u}\big(c_1 c_2^u + d_1 d_2^u\big)\,,\end{aligned} \tag{C.58}$$

and $I^{(1)}(u)$ given in (C.44). The integration contour must be chosen such that $0 < \mathrm{Re}(u) < 1$ on the real axis as discussed in Appendix C.3.[2]

The above expressions are given in the pole-mass scheme for the charm quark. In terms

[2] We recall that the corrections due to a massive charm quark are actually recovered by choosing $-1 < \mathrm{Re}(u) < 0$. The pole at $u = 0$ amounts to the contribution for massless charm quarks and is absorbed into the massless part. Our contour choice $0 < \mathrm{Re}(u) < 1$ thus corresponds to the definitions (C.47), (C.48) of $e^{(i)}_{N,m_c}$ and $f^{(i)}_{N,m_c}$, where the massless part is subtracted.

of the $\overline{\rm MS}$ mass $m_c^{\overline{\rm MS}}(\mu_c)$, the results receive an additional contribution

$$e^{(2)}_{N,\{m_c\}} \to e^{(2)}_{N,\{m_c\}} + \left(\frac{\alpha_s}{4\pi}\right)^2 \left[\frac{4}{3} + 2\ln\left(\frac{\mu_c}{m_c^{\overline{\rm MS}}(\mu_c)}\right)\right] \times \left(-8\Gamma(1/2)\Gamma(N)\frac{1}{2\pi i}\int_{-i\infty}^{i\infty} du\, u\, \xi_N^{-u}\, I^{(1)}(u) \sum_{i=1}^{N} \eta_c(u,i,N)\right), \tag{C.59}$$

$$f^{(2)}_{N,\{m_c\}} \to f^{(2)}_{N,\{m_c\}} + \left(\frac{\alpha_s}{4\pi}\right)^2 \left[\frac{4}{3} + 2\ln\left(\frac{\mu_c}{m_c^{\overline{\rm MS}}(\mu_c)}\right)\right] \times \left(-4\Gamma(1/2)\Gamma(N+1)\frac{1}{2\pi i}\int_{-i\infty}^{i\infty} du\, u\, \xi_N^{-u}\, I^{(1)}(u) \sum_{i=1}^{N} \phi_c(u,i,N)\right). \tag{C.60}$$

We find numerical agreement between our results for the binding energy of the $\Upsilon(1S)$ resonance up to NNLO with [168]. In addition, the NLO energy levels $e^{(1)}_{N,m_c}$ and wave functions $f^{(1)}_{1,m_c}$ agree numerically with [171].

The results for the contribution of the double insertion of the NLO potential $V^{(1)}_{m_c}$ to the binding energies and the wave functions are as follows:

$$e^{(2)}_{N,\{m_c,m_c\}} = \left(\frac{\alpha_s}{4\pi}\right)^2 \frac{\pi}{\Gamma(N)^2} \left\{ \frac{h^{(0)}_{m_c}(N)}{N^2}\left[h^{(0)}_{m_c}(N)\big(7+4N\psi(N)\big) - 4h^{(1)}_{m_c}(N)\right] + 2\sum_{\substack{s=1\\ s\neq N}}^{\infty} \frac{h^{(0)}_{m_c}(s)^2}{s(s-N)}\right\} - e^{(1)}_{N,m_c} f^{(1)}_{N,m_c}\,, \tag{C.61}$$

$$f^{(2)}_{N,\{m_c,m_c\}} = \left(\frac{\alpha_s}{4\pi}\right)^2 \frac{\pi}{\Gamma(N)^2} \left\{ \frac{1}{N^2}\left[h^{(1)}_{m_c}(N)^2 + h^{(0)}_{m_c}(N)\left(3h^{(0)}_{m_c}(N) - 4h^{(1)}_{m_c}(N)[1+N\psi(N)] + h^{(2)}_{m_c}(N) + Nh^{(0)}_{m_c}(N)\Big[4\psi(N) + N\big(2\zeta_2 + 2\psi(N)^2 - \psi^{(1)}(N)\big)\Big]\right)\right] - \sum_{\substack{s=1\\ s\neq N}}^{\infty} \frac{h^{(0)}_{m_c}(s)}{s(s-N)}\left[2h^{(1)}_{m_c}(s) - h^{(0)}_{m_c}(s)\left(2 + 2N\psi(N) + \frac{N}{N-s}\right)\right]\right\}. \tag{C.62}$$

The coefficients $h^{(j)}_{m_c}$ can be expressed as single Mellin-Barnes integrals

$$h^{(j)}_{m_c}(s) = \sum_{k=1}^{s} \frac{(-1)^k\Gamma(s+1)}{k\,\Gamma(k)^2\Gamma(s-k+1)} \times \frac{1}{2\pi i}\int_{-i\infty}^{i\infty} du\, \xi_N^{-u}\, I^{(1)}(u)\, \frac{(k+u)\Gamma(k+u)^2\Gamma(-u)}{\Gamma(1+k+u-N)}\kappa^{(j)}(u, 1+k+u-N)\,, \tag{C.63}$$

where

$$\kappa^{(0)}(u,x) = 1\,, \tag{C.64}$$
$$\kappa^{(1)}(u,x) = u + N\psi(x)\,, \tag{C.65}$$
$$\kappa^{(2)}(u,x) = u(u-1) + N\psi(x)\big(2u + N\psi(x)\big) - N^2\psi^{(1)}(x)\,, \tag{C.66}$$

and ξ_N and $I^{(1)}(u)$ have been defined in (C.55), (C.44). The contour should again be fixed such that $0 < \mathrm{Re}(u) < 1$. The infinite sums in (C.61) and (C.62) converge quickly and can be truncated after the tenth term for all six resonances considered in the sum rule. There are however large cancellations in the finite sum in (C.63), which makes the evaluation rather time consuming.

The results for the contribution of the mixed double insertion of the NLO potentials $V_{m_c}^{(1)}$ and V_{massless} to the binding energies and the wave functions are as follows:

$$\begin{aligned} e^{(2)}_{N,\{m_c,\text{massless}\}} = \left(\frac{\alpha_s}{4\pi}\right)^2 \frac{4\sqrt{\pi}}{\Gamma(N)}(-1)^{N+1}\Bigg\{ & \frac{h^{(0)}_{\text{massless}}(N) h^{(0)}_{m_c}(N)}{N} \\ & + \frac{h^{(-1)}_{\text{massless}}(N)}{N^2}\left[h^{(1)}_{m_c}(N) - h^{(0)}_{m_c}(N)\left(\frac{7}{2} + N\psi(N)\right)\right] \\ & + \sum_{\substack{s=1\\ s\neq N}}^{\infty} \frac{h^{(-1)}_{\text{massless}}(s) h^{(0)}_{m_c}(s)}{s(N-s)}\Bigg\} - e^{(1)}_{N,m_c} f^{(1)}_{N,\text{massless}} - e^{(1)}_{N,\text{massless}} f^{(1)}_{N,m_c}\,, \end{aligned} \tag{C.67}$$

$$\begin{aligned} f^{(2)}_{N,\{m_c,\text{massless}\}} = \left(\frac{\alpha_s}{4\pi}\right)^2 \frac{2\sqrt{\pi}}{\Gamma(N)}(-1)^{N+1}\Bigg\{ & \frac{1}{2N^2}\Big[2N\Big(- N h^{(1)}_{\text{massless}}(N) h^{(0)}_{m_c}(N) \\ & + h^{(0)}_{\text{massless}}(N)\big[- h^{(1)}_{m_c}(N) + h^{(0)}_{m_c}(N)\big(2 + N\psi(N)\big)\big]\Big) \\ & - h^{(-1)}_{\text{massless}}(N)\Big(h^{(2)}_{m_c}(N) - 2h^{(1)}_{m_c}(N)\big(2 + N\psi(N)\big) \\ & + h^{(0)}_{m_c}(N)\big[6 + 4N\psi(N) + N^2\big(\psi(N)^2 - \psi^{(1)}(N) + 2\zeta_2\big)\big]\Big)\Big] \\ & + \sum_{\substack{s=1\\ s\neq N}}^{\infty} \frac{1}{s(N-s)}\Big[- h^{(-1)}_{\text{massless}}(s) h^{(1)}_{m_c}(s) - N h^{(0)}_{\text{massless}}(s) h^{(0)}_{m_c}(s) \\ & + h^{(-1)}_{\text{massless}}(s) h^{(0)}_{m_c}(s)\left(\frac{N}{N-s} + 2 + N\psi(N)\right)\Big]\Bigg\}\,, \end{aligned} \tag{C.68}$$

with the coefficients $h^{(j)}_{m_c}$ from (C.63) and

$$h^{(-1)}_{\text{massless}}(s) \overset{s\leq N}{=} 2\beta_0 \frac{s}{N-s}\,, \tag{C.69}$$
$$h^{(-1)}_{\text{massless}}(N) = -N\big[a_1 + 2\beta_0\big(L_N + S_1(N)\big)\big]\,, \tag{C.70}$$
$$h^{(-1)}_{\text{massless}}(s) \overset{s\geq N}{=} 2\beta_0 \frac{N}{s-N}\,, \tag{C.71}$$

$$h^{(0)}_{\rm massless}(s) \overset{s<N}{=} \frac{1}{N-s}\Big\{ - h^{(-1)}_{\rm massless}(s) - a_1 s + 2\beta_0\Big[N\Big(\psi(N-s)-\psi(N)\Big) + s\Big(S_1(N-s) - L_N\Big)\Big]\Big\}, \tag{C.72}$$

$$h^{(0)}_{\rm massless}(N) = -2\beta_0\Big(1 + S_1(N-1) + N\psi^{(1)}(N)\Big), \tag{C.73}$$

$$h^{(0)}_{\rm massless}(s) \overset{s>N}{=} \frac{1}{s-N}\Big\{h^{(-1)}_{\rm massless}(s) + a_1 s - 2\beta_0\Big[N\Big(\psi(s-N)-\psi(N)\Big) + s\Big(S_1(s-N) - L_N\Big) - 2\Big]\Big\}, \tag{C.74}$$

$$h^{(1)}_{\rm massless}(N) = \beta_0\Big[\frac{1}{N} + 2S_2(N-1) - N\Big(\psi^{(2)}(N) + 4\zeta_3\Big)\Big]. \tag{C.75}$$

The $S_i(n) = \sum_{k=1}^{n} k^{-i}$ are generalized harmonic numbers of rank i.

D. Mixed QCD-condensate corrections to the energy levels and wave functions: Potential contributions

We give the lengthy expressions for the potential contributions to the energy levels (8.40) and wave functions at the origin (8.42):

$$\widetilde{e}_{,N}^{\,\mathrm{GVG}} = \frac{128N^6}{9\left(6561N^4-25920N^2+16384\right)^2}\Bigg\{2\left[a_1+2\beta_0\left(S_1+L_N\right)\right]$$
$$\times\Big(167403915N^{10}-1486558575N^8+4690934208N^6-6303780864N^4$$
$$+3483631616N^2-536870912\Big)+\beta_0(9N-8)\Big(94419351N^9+46727442N^8$$
$$-800382951N^7-381105162N^6+2367378684N^5+1061906784N^4$$
$$-2883647232N^3-1162401792N^2+1320550400N+405274624\Big)\Bigg\}, \qquad \text{(D.1)}$$

$$\widetilde{e}_{,N}^{\,\mathrm{GGV}} = \left[a_1+2\beta_0\left(S_1+L_N\right)\right]\frac{32N^6}{9\left(6561N^4-25920N^2+16384\right)^2}\Big(5859137025N^{10}$$
$$-48288205485N^8+136847786688N^6-159273676800N^4+81059381248N^2$$
$$-15166603264\Big)-\beta_0\frac{32N^6}{3\left(6561N^4-25920N^2+16384\right)}\Big(451332N^6-161595N^5$$
$$-1797839N^4+646725N^3+1160272N^2-425280N+7168\Big), \qquad \text{(D.2)}$$

$$\widetilde{f}_{,N}^{\,\mathrm{GVG}} = \left(a_1+2\beta_0 L_N\right)\frac{256N^6}{81\left(6561N^4-25920N^2+16384\right)^3}\Big(-29655101330505N^{14}$$
$$+370819521046350N^{12}-1836925493383872N^{10}+4598115283537920N^8$$
$$-6194386829574144N^6+4467901285269504N^4-1563638678683648N^2$$
$$+189115999977472\Big)+\beta_0\frac{128N^5}{81\left(6561N^4-25920N^2+16384\right)^2}\Bigg\{$$
$$\frac{1}{9\left(6561N^4-25920N^2+16384\right)^2}\Big(-8888937845922281277N^{19}$$

$$
\begin{aligned}
&+2334805437953319660N^{18}+14667993087120936733 5N^{17}\\
&-38038386654486402750N^{16}-10196969173230837709 98N^{15}\\
&+260020266583548188160N^{14}+389374991164904358297 6N^{13}\\
&-970389752080885235712N^{12}-895474960063956570931 2N^{11}\\
&+216112284501060825907 2N^{10}+128473150959443100303 36N^{9}\\
&-29558695971866290421 76N^{8}-11551005743863723720704N^{7}\\
&+243688307882479268659 2N^{6}+629057700866626368307 2N^{5}\\
&-106504345447175710310 4N^{4}-182931305345348272128 0N^{3}\\
&+131764347572768997376N^{2}+18226912116898529280 0N\\
&+36893488147419103232\Big)+\frac{36NS_1}{6561N^4-25920N^2+16384}\\
&\times\Big(-3295011258945N^{14}+41202169005150N^{12}-204102832598208N^{10}\\
&+510901698170880N^{8}-688295779762176N^{6}+498462848188416N^{4}\\
&-178391466639360N^{2}+21990232555520\Big)-\frac{33554432N}{6561N^4-25920N^2+16384}\\
&\times\Bigg[\left(-32805N^6+2177280N^4-4993024N^2+1048576\right)S_1\left(\frac{N}{8}\right)\\
&+\left(-111537N^6+124416N^4-5386240N^2+7340032\right)S_1\left(\frac{9N}{8}\right)\Bigg]\\
&-36N^2\left(S_2-\frac{\pi^2}{6}\right)\Big(-167403915N^{10}+1486558575N^{8}-4690934208N^{6}\\
&+6303780864N^{4}-3483631616N^{2}+536870912\Big)\Bigg\},
\end{aligned}
\tag{D.3}
$$

$$
\begin{aligned}
\widetilde{f}_{,N}^{\,\mathrm{GGV}}=&\left(a_1+2\beta_0L_N\right)\frac{64N^6}{81\left(6561N^4-25920N^2+16384\right)^3}\Big(-385516317296565N^{14}\\
&+4654961778867030N^{12}-21965572921731408N^{10}+51360436390947840N^{8}\\
&-63132424989769728N^{6}+41064256744980480N^{4}-13147993330941952N^{2}\\
&+1582746988183552\Big)+\beta_0\frac{32N^5}{81\left(6561N^4-25920N^2+16384\right)^2}\Big\{\\
&\frac{1}{9\left(6561N^4-25920N^2+16384\right)^2}\Big(614053830181723070 58N^{19}\\
&-22180651660556536770N^{18}-96583756545845150013 9N^{17}\\
&+35108041116949310857 5N^{16}+62895218841715127831 28N^{15}\\
&-23076757989436648435 20N^{14}-21902675740289714221056N^{13}\\
&+81539966872334886912 00N^{12}+44045654765398681780224N^{11}
\end{aligned}
$$

$$
\begin{aligned}
&-167993712816758949150 72N^{10} - 516851212853325154222 08N^{9} \\
&+206212425597170724372 48N^{8} + 339747357194196552253 44N^{7} \\
&-149444376082416528261 12N^{6} - 106799232780400066560 00N^{5} \\
&+603667732455989497036 8N^{4} + 609631074176867500032N^{3} \\
&-105464339058841459097 6N^{2} + 220638101144321654784N \\
&-18446744073709551616\Big) + \frac{4NS_1}{6561N^4 - 25920N^2 + 16384} \\
&\times\Big(- 652412229271110N^{14} + 7881876138460500N^{12} - 37221596700680304N^{10} \\
&+87133432412759040N^{8} - 107286357009825792N^{6} + 69985956437950464N^{4} \\
&-22538834096947200N^{2} + 2696552267120640\Big) + \frac{16777216N}{6561N^4 - 25920N^2 + 16384} \\
&\Big(\left(203391N^6 - 13405824N^4 + 24866816N^2 + 1048576\right) S_1\left(\frac{N}{8}\right) \\
&+ \left(-465831N^6 + 30824064N^4 - 64811008N^2 + 7340032\right) S_1\left(\frac{9N}{8}\right)\Big) \\
&-18N^2\left(S_2 - \frac{\pi^2}{6}\right)\Big(- 5859137025N^{10} + 48288205485N^{8} - 136847786688N^{6} \\
&+159273676800N^4 - 81050992640N^2 + 14629732352\Big)\Bigg\}, \qquad \text{(D.4)}
\end{aligned}
$$

where $L_N = \ln(N\mu/(m\alpha_s C_F))$, $S_1(x) = \sum_{k=1}^{x} k^{-1}$ is the analytic continuation of the harmonic number to non-integer values and $S_i = \sum_{k=1}^{N} k^{-i}$ without an explicit argument is the Nth harmonic number of rank i.

Bibliography

[1] M. Beneke, J. Piclum and T. Rauh, *P-wave contribution to third-order top-quark pair production near threshold*, Nucl. Phys. B **880** (2014) 414 [arXiv:1312.4792 [hep-ph]].

[2] M. Beneke, A. Maier, J. Piclum and T. Rauh, *The bottom-quark mass from non-relativistic sum rules at NNNLO*, Nucl. Phys. B **891** (2015) 42 [arXiv:1411.3132 [hep-ph]].

[3] T. Rauh, *The bottom-quark mass from Υ sum rules at NNNLO*, PoS FWNP (2014) 017.

[4] M. Beneke, A. Maier, J. Piclum and T. Rauh, *Higgs effects in top anti-top production near threshold in e^+e annihilation*, Nucl. Phys. B **899** (2015) 180 [arXiv:1506.06865 [hep-ph]].

[5] M. Beneke, A. Maier, J. Piclum and T. Rauh, *Non-QCD contributions to top-pair production near threshold*, PoS EPS-HEP2015 (2015) 315 [arXiv:1511.00801 [hep-ph]].

[6] M. Beneke, A. Maier, J. Piclum and T. Rauh, *NNNLO determination of the bottom-quark mass from non-relativistic sum rules*, arXiv:1601.02949 [hep-ph].

[7] M. Bobrowski, A. Lenz and T. Rauh, *Short distance D-Dbar mixing*, arXiv:1208.6438 [hep-ph].

[8] A. Lenz and T. Rauh, *D-meson lifetimes within the heavy quark expansion*, Phys. Rev. D **88** (2013) 034004 [arXiv:1305.3588 [hep-ph]].

[9] F. Krinner, A. Lenz and T. Rauh, *The inclusive decay $b \to c\bar{c}s$ revisited*, Nucl. Phys. B **876** (2013) 31 [arXiv:1305.5390 [hep-ph]].

[10] G. Aad *et al.* [ATLAS Collaboration], *Observation of a new particle in the search for the Standard Model Higgs boson with the ATLAS detector at the LHC*, Phys. Lett. B **716** (2012) 1 [arXiv:1207.7214 [hep-ex]].

[11] S. Chatrchyan *et al.* [CMS Collaboration], *Observation of a new boson at a mass of 125 GeV with the CMS experiment at the LHC*, Phys. Lett. B **716** (2012) 30 [arXiv:1207.7235 [hep-ex]].

[12] J. Alwall *et al.*, *The automated computation of tree-level and next-to-leading order differential cross sections, and their matching to parton shower simulations*, JHEP **1407** (2014) 079 [arXiv:1405.0301 [hep-ph]].

[13] M. Czakon, P. Fiedler and A. Mitov, *Total Top-Quark Pair-Production Cross Section at Hadron Colliders Through $\mathcal{O}(\alpha_s^4)$*, Phys. Rev. Lett. **110** (2013) 252004 [arXiv:1303.6254 [hep-ph]].

[14] M. Czakon, P. Fiedler and A. Mitov, *Resolving the Tevatron Top Quark Forward-Backward Asymmetry Puzzle: Fully Differential Next-to-Next-to-Leading-Order Calculation*, Phys. Rev. Lett. **115** (2015) 5, 052001 [arXiv:1411.3007 [hep-ph]].

[15] M. Czakon, D. Heymes and A. Mitov, *Dynamical scales for multi-TeV top-pair production at the LHC*, arXiv:1606.03350 [hep-ph].

[16] C. Anastasiou, C. Duhr, F. Dulat, E. Furlan, T. Gehrmann, F. Herzog, A. Lazopoulos and B. Mistlberger, *High precision determination of the gluon fusion Higgs boson cross-section at the LHC*, JHEP **1605** (2016) 058 [arXiv:1602.00695 [hep-ph]].

[17] [ATLAS and CDF and CMS and D0 Collaborations], *First combination of Tevatron and LHC measurements of the top-quark mass*, arXiv:1403.4427 [hep-ex].

[18] A. H. Hoang, *The Top Mass: Interpretation and Theoretical Uncertainties*, arXiv:1412.3649 [hep-ph].

[19] CMS Collaboration, *Determination of the top-quark pole mass and strong coupling constant from the $t\bar{t}$ production cross section in pp collisions at $\sqrt{s} = 7$ TeV*, Phys. Lett. B **728** (2014) 496, Corrigendum-ibid. B **728** (2014) 526, [arXiv:1307.1907 [hep-ex]].

[20] ATLAS Collaboration, *Measurement of the $t\bar{t}$ production cross-section using $e\mu$ events with b -tagged jets in pp collisions at $\sqrt{s} = 7$ and 8 TeV with the ATLAS detector*, Eur. Phys. J. C **74** (2014) 10, 3109 [arXiv:1406.5375 [hep-ex]].

[21] V. Khachatryan *et al.* [CMS Collaboration], *Measurement of the t-tbar production cross section in the e-mu channel in proton-proton collisions at $\sqrt{s} = 7$ and 8 TeV*, arXiv:1603.02303 [hep-ex].

[22] G. F. Giudice, P. Paradisi and A. Strumia, *Indirect determinations of the top quark mass*, JHEP **1511** (2015) 192 [arXiv:1508.05332 [hep-ph]].

[23] A. V. Bednyakov, B. A. Kniehl, A. F. Pikelner and O. L. Veretin, *Stability of the Electroweak Vacuum: Gauge Independence and Advanced Precision*, Phys. Rev. Lett. **115** (2015) 20, 201802 [arXiv:1507.08833 [hep-ph]].

[24] K. A. Olive *et al.* [Particle Data Group Collaboration], *Review of Particle Physics*, Chin. Phys. C **38** (2014) 090001.

[25] L. G. Almeida, S. J. Lee, S. Pokorski and J. D. Wells, *Study of the standard model Higgs boson partial widths and branching fractions*, Phys. Rev. D **89** (2014) 3, 033006 [arXiv:1311.6721 [hep-ph]].

[26] K. Seidel, F. Simon, M. Tesar and S. Poss, *Top quark mass measurements at and above threshold at CLIC*, Eur. Phys. J. C **73** (2013) 8, 2530 [arXiv:1303.3758 [hep-ex]].

[27] A. H. Hoang *et al.*, *Top - anti-top pair production close to threshold: Synopsis of recent NNLO results*, Eur. Phys. J. direct C **3** (2000) 1 [hep-ph/0001286].

[28] M. Beneke, Y. Kiyo, P. Marquard, A. Penin, J. Piclum and M. Steinhauser, *Next-to-Next-to-Next-to-Leading Order QCD Prediction for the Top Antitop S-Wave Pair Production Cross Section Near Threshold in e^+e^- Annihilation*, Phys. Rev. Lett. **115** (2015) 19, 192001 [arXiv:1506.06864 [hep-ph]].

[29] M. Beneke, Y. Kiyo, A. Maier and J. Piclum, *Near-threshold production of heavy quarks with QQbar_threshold*, arXiv:1605.03010 [hep-ph].

[30] V. A. Novikov, L. B. Okun, M. A. Shifman, A. I. Vainshtein, M. B. Voloshin and V. I. Zakharov, *Sum Rules for Charmonium and Charmed Mesons Decay Rates in Quantum Chromodynamics*, Phys. Rev. Lett. **38** (1977) 626 [Phys. Rev. Lett. **38** (1977) 791].

[31] V. A. Novikov, L. B. Okun, M. A. Shifman, A. I. Vainshtein, M. B. Voloshin and V. I. Zakharov, *Charmonium and Gluons: Basic Experimental Facts and Theoretical Introduction*, Phys. Rept. **41** (1978) 1.

[32] B. Aubert *et al.* [BaBar Collaboration], *Measurement of the $e^+e^- \to b\bar{b}$ cross section between $\sqrt{s}$ = 10.54 GeV and 11.20 GeV*, Phys. Rev. Lett. **102** (2009) 012001 [arXiv:0809.4120 [hep-ex]].

[33] K. G. Chetyrkin, J. H. Kühn, A. Maier, P. Maierhofer, P. Marquard, M. Steinhauser and C. Sturm, *Charm and Bottom Quark Masses: An Update*, Phys. Rev. D **80** (2009) 074010 [arXiv:0907.2110 [hep-ph]].

[34] A. Pineda and J. Soto, *Effective field theory for ultrasoft momenta in NRQCD and NRQED*, Nucl. Phys. Proc. Suppl. **64** (1998) 428 [hep-ph/9707481].

[35] A. Pineda and J. Soto, *The Lamb shift in dimensional regularization*, Phys. Lett. B **420** (1998) 391 [hep-ph/9711292].

[36] M. Beneke, *New results on heavy quarks near threshold*, hep-ph/9806429.

[37] M. Beneke, A. Signer and V. A. Smirnov, *Top quark production near threshold and the top quark mass*, Phys. Lett. B **454** (1999) 137 [hep-ph/9903260].

[38] N. Brambilla, A. Pineda, J. Soto and A. Vairo, *Potential NRQCD: An Effective theory for heavy quarkonium*, Nucl. Phys. B **566** (2000) 275 [hep-ph/9907240].

[39] M. Beneke, A. P. Chapovsky, A. Signer and G. Zanderighi, *Effective theory approach to unstable particle production*, Phys. Rev. Lett. **93** (2004) 011602 [hep-ph/0312331].

[40] M. Beneke, A. P. Chapovsky, A. Signer and G. Zanderighi, *Effective theory calculation of resonant high-energy scattering*, Nucl. Phys. B **686** (2004) 205 [hep-ph/0401002].

[41] A. S. Kronfeld, *The Perturbative pole mass in QCD*, Phys. Rev. D **58** (1998) 051501 [hep-ph/9805215].

[42] M. Beneke and V. M. Braun, *Heavy quark effective theory beyond perturbation theory: Renormalons, the pole mass and the residual mass term*, Nucl. Phys. B **426** (1994) 301 [hep-ph/9402364].

[43] I. I. Y. Bigi, M. A. Shifman, N. G. Uraltsev and A. I. Vainshtein, *The Pole mass of the heavy quark. Perturbation theory and beyond*, Phys. Rev. D **50** (1994) 2234 [hep-ph/9402360].

[44] M. Beneke, *More on ambiguities in the pole mass*, Phys. Lett. B **344** (1995) 341 [hep-ph/9408380].

[45] M. Beneke, *Renormalons*, Phys. Rept. **317** (1999) 1 [hep-ph/9807443].

[46] M. Beneke and V. M. Braun, *Naive nonAbelianization and resummation of fermion bubble chains*, Phys. Lett. B **348** (1995) 513 [hep-ph/9411229].

[47] A. D. Sokal, *An Improvement Of Watson's Theorem On Borel Summability*, J. Math. Phys. **21** (1980) 261.

[48] P. Ball, M. Beneke and V. M. Braun, *Resummation of $(\beta_0\alpha_s)^n$ corrections in QCD: Techniques and applications to the tau hadronic width and the heavy quark pole mass*, Nucl. Phys. B **452** (1995) 563 [hep-ph/9502300].

[49] P. Marquard, A. V. Smirnov, V. A. Smirnov and M. Steinhauser, *Quark Mass Relations to Four-Loop Order in Perturbative QCD*, Phys. Rev. Lett. **114** (2015) no.14, 142002 [arXiv:1502.01030 [hep-ph]].

[50] M. Beneke, P. Marquard, P. Nason and M. Steinhauser, *On the ultimate uncertainty of the top quark pole mass*, arXiv:1605.03609 [hep-ph].

[51] M. Beneke, *A Quark mass definition adequate for threshold problems*, Phys. Lett. B **434** (1998) 115 [hep-ph/9804241].

[52] A. H. Hoang and T. Teubner, *Top quark pair production close to threshold: Top mass, width and momentum distribution*, Phys. Rev. D **60** (1999) 114027 [hep-ph/9904468].

[53] I. I. Y. Bigi, M. A. Shifman, N. Uraltsev and A. I. Vainshtein, *High power n of m_b in beauty widths and $n = 5 \to \infty$ limit*, Phys. Rev. D **56** (1997) 4017 [hep-ph/9704245].

[54] A. Pineda, *Determination of the bottom quark mass from the $\Upsilon(1S)$ system*, JHEP **0106** (2001) 022 [hep-ph/0105008].

[55] A. H. Hoang, M. C. Smith, T. Stelzer and S. Willenbrock, *Quarkonia and the pole mass*, Phys. Rev. D **59** (1999) 114014 [hep-ph/9804227].

[56] M. Beneke, *Perturbative heavy quark - anti-quark systems*, PoS hf **8** (1999) 009 [hep-ph/9911490].

[57] M. Beneke and V. A. Smirnov, *Asymptotic expansion of Feynman integrals near threshold*, Nucl. Phys. B **522** (1998) 321 [hep-ph/9711391].

[58] V. A. Smirnov, *Problems of the strategy of regions*, Phys. Lett. B **465** (1999) 226 [hep-ph/9907471].

[59] B. Jantzen, *Foundation and generalization of the expansion by regions,* JHEP **1112** (2011) 076 [arXiv:1111.2589 [hep-ph]].

[60] M. Beneke, Y. Kiyo and K. Schuller, *Third-order correction to top-quark pair production near threshold I. Effective theory set-up and matching coefficients*, arXiv:1312.4791 [hep-ph].

[61] N. Brambilla, A. Pineda, J. Soto and A. Vairo, *Effective field theories for heavy quarkonium*, Rev. Mod. Phys. **77** (2005) 1423 [hep-ph/0410047].

[62] A. Pineda, *Review of Heavy Quarkonium at weak coupling*, Prog. Part. Nucl. Phys. **67** (2012) 735 [arXiv:1111.0165 [hep-ph]].

[63] B. A. Thacker and G. P. Lepage, *Heavy quark bound states in lattice QCD*, Phys. Rev. D **43** (1991) 196.

[64] G. P. Lepage, L. Magnea, C. Nakhleh, U. Magnea and K. Hornbostel, *Improved nonrelativistic QCD for heavy quark physics*, Phys. Rev. D **46** (1992) 4052 [hep-lat/9205007].

[65] G. T. Bodwin, E. Braaten and G. P. Lepage, *Rigorous QCD analysis of inclusive annihilation and production of heavy quarkonium*, Phys. Rev. D **51** (1995) 1125 Erratum: [Phys. Rev. D **55** (1997) 5853] [hep-ph/9407339].

[66] M. Beneke, A. Signer and V. A. Smirnov, *Two loop correction to the leptonic decay of quarkonium*, Phys. Rev. Lett. **80** (1998) 2535 [hep-ph/9712302].

[67] A. Czarnecki and K. Melnikov, *Two loop QCD corrections to the heavy quark pair production cross-section in e^+e^- annihilation near the threshold*, Phys. Rev. Lett. **80** (1998) 2531 [hep-ph/9712222].

[68] P. Marquard, J. H. Piclum, D. Seidel and M. Steinhauser, *Three-loop matching of the vector current*, Phys. Rev. D **89** (2014) no.3, 034027 [arXiv:1401.3004 [hep-ph]].

[69] P. Marquard, J. H. Piclum, D. Seidel and M. Steinhauser, *Completely automated computation of the heavy-fermion corrections to the three-loop matching coefficient of the vector current,* Phys. Lett. B **678** (2009) 269 [arXiv:0904.0920 [hep-ph]].

[70] P. Marquard, J. H. Piclum, D. Seidel and M. Steinhauser, *Fermionic corrections to the three-loop matching coefficient of the vector current*, Nucl. Phys. B **758** (2006) 144 [hep-ph/0607168].

[71] K. G. Wilson, *Nonlagrangian models of current algebra*, Phys. Rev. **179** (1969) 1499.

[72] M. Beneke, P. Falgari and C. Schwinn, *Threshold resummation for pair production of coloured heavy (s)particles at hadron colliders*, Nucl. Phys. B **842** (2011) 414 [arXiv:1007.5414 [hep-ph]].

[73] M. Beneke, Y. Kiyo and A. A. Penin, *Ultrasoft contribution to quarkonium production and annihilation*, Phys. Lett. B **653** (2007) 53 [arXiv:0706.2733 [hep-ph]].

[74] M. Beneke and Y. Kiyo, *Ultrasoft contribution to heavy-quark pair production near threshold*, Phys. Lett. B **668** (2008) 143 [arXiv:0804.4004 [hep-ph]].

[75] S. Weinberg, *The Quantum theory of fields. Vol. 1: Foundations*, Cambridge University Press, 1995.

[76] M. Baker, P. Marquard, A. Penin, J. Piclum and M. Steinhauser, *Hyperfine Splitting in Positronium to $\mathcal{O}(\alpha^7 m_e)$: One Photon Annihilation Contribution*, Phys. Rev. Lett. **112** (2014) no.12, 120407 [arXiv:1402.0876 [hep-ph]].

[77] E. Wichmann and C. Woo, *Integral Representation for the Nonrelativistic Coulomb Green's Function*, J. Math. Ph. **2** (1961) 178.

[78] J. Schwinger, *Coulomb Green's Function*, J. Math. Phys. **5** (1964) 1606.

[79] M. B. Voloshin, *Nonperturbative Effects In Hadronic Annihilation Of Heavy Quarkonium*, Sov. J. Nucl. Phys. **40** (1984) 662 [Yad. Fiz. **40** (1984) 1039].

[80] M. B. Voloshin, *Precoulombic Asymptotics for Energy Levels of Heavy Quarkonium*, Sov. J. Nucl. Phys. **36** (1982) 143 [Yad. Fiz. **36** (1982) 247].

[81] Y. Schröder, *The Static potential in QCD to two loops*, Phys. Lett. B **447** (1999) 321 [hep-ph/9812205].

[82] Y. Schröder, *The Static potential in QCD*, DESY-THESIS-1999-021.

[83] C. Anzai, Y. Kiyo and Y. Sumino, *Static QCD potential at three-loop order*, Phys. Rev. Lett. **104** (2010) 112003 [arXiv:0911.4335 [hep-ph]].

[84] A. V. Smirnov, V. A. Smirnov and M. Steinhauser, *Three-loop static potential*, Phys. Rev. Lett. **104** (2010) 112002 [arXiv:0911.4742 [hep-ph]].

[85] B. A. Kniehl, A. A. Penin, M. Steinhauser and V. A. Smirnov, *NonAbelian $\alpha_s^3/(m_q r^2)$ heavy quark anti-quark potential*, Phys. Rev. D **65** (2002) 091503 [hep-ph/0106135].

[86] M. Beneke, Y. Kiyo, P. Marquard, A. Penin, J. Piclum, D. Seidel and M. Steinhauser, *Leptonic decay of the $\Upsilon(1S)$ meson at third order in QCD*, Phys. Rev. Lett. **112** (2014) no.15, 151801 [arXiv:1401.3005 [hep-ph]].

[87] S. Wüster, *Heavy quark potential at order α_s^2/m^2 [in German]*, *Diploma Thesis* (Aachen 2003) .

[88] M. Beneke, Y. Kiyo and K. Schuller, *Third-order Coulomb corrections to the S-wave Green function, energy levels and wave functions at the origin*, Nucl. Phys. B **714** (2005) 67 [hep-ph/0501289].

[89] M. Beneke, Y. Kiyo and K. Schuller, *Third-order correction to top-quark pair production near threshold II. Potential contributions*, to appear.

[90] I. I. Y. Bigi, V. S. Fadin and V. A. Khoze, *Stop near threshold*, Nucl. Phys. B **377** (1992) 461.

[91] A. A. Penin and A. A. Pivovarov, *Top quark threshold production in $\gamma\gamma$ collision in the next-to-leading order*, Nucl. Phys. B **550** (1999) 375 [hep-ph/9810496].

[92] A. A. Penin and A. A. Pivovarov, *Analytical results for $e^+e^- \to t\bar{t}$ and $\gamma\gamma \to t\bar{t}$ observables near the threshold up to the next-to-next-to leading order of NRQCD*, Phys. Atom. Nucl. **64** (2001) 275 [Yad. Fiz. **64** (2001) 323] [hep-ph/9904278].

[93] J. H. Kühn and T. Teubner, *Axial contributions at the top threshold*, Eur. Phys. J. C **9** (1999) 221 [hep-ph/9903322].

[94] M. Beneke, P. Falgari, C. Schwinn, A. Signer and G. Zanderighi, *Four-fermion production near the W pair production threshold*, Nucl. Phys. B **792** (2008) 89 [arXiv:0707.0773 [hep-ph]].

[95] P. Falgari, *W-pair production near threshold in unstable-particle effective theory*, PhD thesis, 2008.

[96] S. Actis, M. Beneke, P. Falgari and C. Schwinn, *Dominant NNLO corrections to four-fermion production near the W-pair production threshold*, Nucl. Phys. B **807** (2009) 1 [arXiv:0807.0102 [hep-ph]].

[97] M. Beneke, B. Jantzen and P. Ruiz-Femenía, *Electroweak non-resonant NLO corrections to $e^+e^- \to W^+W^-b\bar{b}$ in the $t\bar{t}$ resonance region*, Nucl. Phys. B **840** (2010) 186 [arXiv:1004.2188 [hep-ph]].

[98] B. Jantzen and P. Ruiz-Femenía, *Next-to-next-to-leading order nonresonant corrections to threshold top-pair production from e^+e^- collisions: Endpoint-singular terms*, Phys. Rev. D **88** (2013) no.5, 054011 [arXiv:1307.4337].

[99] P. Ruiz-Femenía, *First estimate of the NNLO nonresonant corrections to top-antitop threshold production at lepton colliders*, Phys. Rev. D **89** (2014) no.9, 097501 [arXiv:1402.1123 [hep-ph]].

[100] A. A. Penin and J. H. Piclum, *Threshold production of unstable top*, JHEP **1201** (2012) 034 [arXiv:1110.1970 [hep-ph]].

[101] M. Beneke, *Unstable-particle effective field theory*, Nucl. Part. Phys. Proc. **261-262** (2015) 218 [arXiv:1501.07370 [hep-ph]].

[102] C. W. Bauer, S. Fleming and M. E. Luke, *Summing Sudakov logarithms in $B \to X_s\gamma$ in effective field theory*, Phys. Rev. D **63** (2000) 014006 [hep-ph/0005275].

[103] C. W. Bauer, S. Fleming, D. Pirjol and I. W. Stewart, *An Effective field theory for collinear and soft gluons: Heavy to light decays*, Phys. Rev. D **63** (2001) 114020 [hep-ph/0011336].

[104] C. W. Bauer, D. Pirjol and I. W. Stewart, *Soft collinear factorization in effective field theory*, Phys. Rev. D **65** (2002) 054022 [hep-ph/0109045].

[105] M. Beneke, A. P. Chapovsky, M. Diehl and T. Feldmann, *Soft collinear effective theory and heavy to light currents beyond leading power*, Nucl. Phys. B **643** (2002) 431 [hep-ph/0206152].

[106] M. Beneke and T. Feldmann, *Multipole expanded soft collinear effective theory with nonAbelian gauge symmetry*, Phys. Lett. B **553** (2003) 267 [hep-ph/0211358].

[107] T. Becher, A. Broggio and A. Ferroglia, *Introduction to Soft-Collinear Effective Theory*, Lect. Notes Phys. **896** (2015) [arXiv:1410.1892 [hep-ph]].

[108] A. Denner, *Techniques for calculation of electroweak radiative corrections at the one loop level and results for W physics at LEP-200*, Fortsch. Phys. **41** (1993) 307 [arXiv:0709.1075 [hep-ph]].

[109] B. A. Kniehl and A. Sirlin, *Pole Mass, Width, and Propagators of Unstable Fermions*, Phys. Rev. D **77** (2008) 116012 [arXiv:0801.0669 [hep-th]].

[110] J. Reuter, F. Bach, B. Chokoufé Nejad, A. Hoang, W. Kilian, M. Stahlhofen, T. Teubner and C. Weiss, *Top Physics in WHIZARD*, arXiv:1602.08035 [hep-ph].

[111] S. Frixione, Z. Kunszt and A. Signer, *Three jet cross-sections to next-to-leading order*, Nucl. Phys. B **467** (1996) 399 [hep-ph/9512328].

[112] R. Frederix, S. Frixione, F. Maltoni and T. Stelzer, *Automation of next-to-leading order computations in QCD: The FKS subtraction*, JHEP **0910** (2009) 003 [arXiv:0908.4272 [hep-ph]].

[113] G. Ossola, C. G. Papadopoulos and R. Pittau, *On the Rational Terms of the one-loop amplitudes*, JHEP **0805** (2008) 004 [arXiv:0802.1876 [hep-ph]].

[114] G. 't Hooft and M. J. G. Veltman, *Regularization and Renormalization of Gauge Fields*, Nucl. Phys. B **44** (1972) 189.

[115] R. Frederix, *private communications*

[116] J. Bluemlein, K. H. Phan and T. Riemann, *General ε-representation for scalar one-loop Feynman integrals*, Nucl. Part. Phys. Proc. **270-272** (2016) 227 [arXiv:1510.01063 [hep-ph]].

[117] A. H. Hoang and C. J. Reißer, *Electroweak absorptive parts in NRQCD matching conditions*, Phys. Rev. D **71** (2005) 074022 [hep-ph/0412258].

[118] D. Eiras and M. Steinhauser, *Complete Higgs mass dependence of top quark pair threshold production to order $\alpha\alpha_s$*, Nucl. Phys. B **757** (2006) 197 [hep-ph/0605227].

[119] Y. Kiyo, D. Seidel and M. Steinhauser, *$\mathcal{O}(\alpha\alpha_s)$ corrections to the $\gamma t\bar{t}$ vertex at the top quark threshold*, JHEP **0901** (2009) 038 [arXiv:0810.1597 [hep-ph]].

[120] A. Czarnecki and K. Melnikov, *Two loop QCD corrections to top quark width*, Nucl. Phys. B **544** (1999) 520 [hep-ph/9806244].

[121] K. G. Chetyrkin, R. Harlander, T. Seidensticker and M. Steinhauser, *Second order QCD corrections to $\Gamma(t \to Wb)$*, Phys. Rev. D **60** (1999) 114015 [hep-ph/9906273].

[122] B. Grzadkowski, J. H. Kühn, P. Krawczyk and R. G. Stuart, *Electroweak Corrections on the Toponium Resonance*, Nucl. Phys. B **281** (1987) 18.

[123] R. J. Guth and J. H. Kühn, *Top quark threshold and radiative corrections*, Nucl. Phys. B **368** (1992) 38.

[124] A. H. Hoang and C. J. Reißer, *On electroweak matching conditions for top pair production at threshold*, Phys. Rev. D **74** (2006) 034002 [hep-ph/0604104].

[125] W. H. Furry, *A Symmetry Theorem in the Positron Theory*, Phys. Rev. **51** (1937) 125.

[126] F. Jegerlehner, *Electroweak effective couplings for future precision experiments*, Nuovo Cim. C **034S1** (2011) 31 [arXiv:1107.4683 [hep-ph]].

[127] E. A. Kuraev and V. S. Fadin, *On Radiative Corrections to e^+e^- Single Photon Annihilation at High-Energy*, Sov. J. Nucl. Phys. **41** (1985) 466 [Yad. Fiz. **41** (1985) 733].

[128] M. Skrzypek, *Leading logarithmic calculations of QED corrections at LEP*, Acta Phys. Polon. B **23** (1992) 135.

[129] W. Beenakker and A. Denner, *Standard model predictions for W pair production in electron - positron collisions*, Int. J. Mod. Phys. A **9** (1994) 4837.

[130] W. Beenakker *et al.*, *WW cross-sections and distributions*, hep-ph/9602351.

[131] B. A. Kniehl, A. Onishchenko, J. H. Piclum and M. Steinhauser, *Two-loop matching coefficients for heavy quark currents*, Phys. Lett. B **638** (2006) 209 [hep-ph/0604072].

[132] V. A. Smirnov, *Feynman integral calculus*, Berlin, Germany: Springer (2006) 283 p.

[133] A. V. Smirnov, *Algorithm FIRE – Feynman Integral REduction*, JHEP **0810** (2008) 107 [arXiv:0807.3243 [hep-ph]].

[134] A. V. Smirnov and V. A. Smirnov, *FIRE4, LiteRed and accompanying tools to solve integration by parts relations*, Comput. Phys. Commun. **184** (2013) 2820 [arXiv:1302.5885 [hep-ph]].

[135] Y. Schröder and A. Vuorinen, *High-precision epsilon expansions of single-mass-scale four-loop vacuum bubbles*, JHEP **0506** (2005) 051 [hep-ph/0503209].

[136] A. H. Hoang, A. V. Manohar, I. W. Stewart and T. Teubner, *The Threshold $t\bar{t}$ cross-section at NNLL order*, Phys. Rev. D **65** (2002) 014014 [hep-ph/0107144].

[137] M. J. Strassler and M. E. Peskin, *The Heavy top quark threshold: QCD and the Higgs*, Phys. Rev. D **43** (1991) 1500.

[138] M. Martinez and R. Miquel, *Multiparameter fits to the t anti-t threshold observables at a future e^+e^- linear collider*, Eur. Phys. J. C **27** (2003) 49 [hep-ph/0207315].

[139] T. Horiguchi, A. Ishikawa, T. Suehara, K. Fujii, Y. Sumino, Y. Kiyo and H. Yamamoto, *Study of top quark pair production near threshold at the ILC*, arXiv:1310.0563 [hep-ex].

[140] F. Simon, *A First Look at the Impact of NNNLO Theory Uncertainties on Top Mass Measurements at the ILC*, arXiv:1603.04764 [hep-ex].

[141] W. Buchmüller and D. Wyler, *Effective Lagrangian Analysis of New Interactions and Flavor Conservation*, Nucl. Phys. B **268** (1986) 621.

[142] B. Grzadkowski, M. Iskrzynski, M. Misiak and J. Rosiek, *Dimension-Six Terms in the Standard Model Lagrangian*, JHEP **1010** (2010) 085 [arXiv:1008.4884 [hep-ph]].

[143] G. Buchalla, O. Cata, A. Celis and C. Krause, *Note on Anomalous Higgs-Boson Couplings in Effective Field Theory*, Phys. Lett. B **750** (2015) 298 [arXiv:1504.01707 [hep-ph]].

[144] H. Baer *et al.*, *The International Linear Collider Technical Design Report - Volume 2: Physics*, arXiv:1306.6352 [hep-ph].

[145] I. F. Ginzburg, G. L. Kotkin, S. L. Panfil, V. G. Serbo and V. I. Telnov, *Colliding γe and $\gamma\gamma$ Beams Based on the Single Pass e^+e^- Accelerators. 2. Polarization Effects. Monochromatization Improvement*, Nucl. Instrum. Meth. A **219** (1984) 5.

[146] B. Badelek *et al.* [ECFA/DESY Photon Collider Working Group Collaboration], *TESLA: The Superconducting electron positron linear collider with an integrated X-ray laser laboratory. Technical design report. Part 6. Appendices. Chapter 1. Photon collider at TESLA*, Int. J. Mod. Phys. A **19** (2004) 5097 [hep-ex/0108012].

[147] C. Adolphsen *et al.*, *The International Linear Collider Technical Design Report - Volume 3.II: Accelerator Baseline Design*, arXiv:1306.6328 [physics.acc-ph].

[148] A. H. Hoang and P. Ruiz-Femenía, *Renormalization group analysis in NRQCD for colored scalars*, Phys. Rev. D **73** (2006) 014015 [hep-ph/0511102].

[149] M. Beneke, J. Piclum, C. Schwinn and C. Wever, *NNLL soft and Coulomb resummation for squark and gluino production at the LHC*, [arXiv:1607.07574 [hep-ph]].

[150] P. Falgari, C. Schwinn and C. Wever, *NLL soft and Coulomb resummation for squark and gluino production at the LHC*, JHEP **1206** (2012) 052 [arXiv:1202.2260 [hep-ph]].

[151] P. Falgari, C. Schwinn and C. Wever, *Finite-width effects on threshold corrections to squark and gluino production*, JHEP **1301** (2013) 085 [arXiv:1211.3408 [hep-ph]].

[152] M. Beneke, P. Falgari, J. Piclum, C. Schwinn and C. Wever, *Higher-order soft and Coulomb corrections to squark and gluino production at the LHC*, PoS RADCOR **2013** (2013) 051 [arXiv:1312.0837 [hep-ph]].

[153] E. C. Poggio, H. R. Quinn and S. Weinberg, *Smearing the Quark Model*, Phys. Rev. D **13** (1976) 1958.

[154] J. Portoles and P. D. Ruiz-Femenía, *New contributions to heavy quark sum rules*, Eur. Phys. J. C **24** (2002) 439 [hep-ph/0202114].

[155] R. Boughezal, M. Czakon and T. Schutzmeier, *Four-Loop Tadpoles: Applications in QCD*, Nucl. Phys. Proc. Suppl. **160** (2006) 160 [hep-ph/0607141].

[156] A. Maier, P. Maierhofer and P. Marquard, *Higher Moments of Heavy Quark Correlators in the Low Energy Limit at $\mathcal{O}(\alpha_s^2)$*, Nucl. Phys. B **797** (2008) 218 [arXiv:0711.2636 [hep-ph]].

[157] M. B. Voloshin and Y. M. Zaitsev, *Physics of upsilon resonances: Ten years later*, Sov. Phys. Usp. **30** (1987) 553 [Usp. Fiz. Nauk **152** (1987) 361].

[158] M. B. Voloshin, *Precision determination of α_s and m_b from QCD sum rules for b anti-b*, Int. J. Mod. Phys. A **10** (1995) 2865 [hep-ph/9502224].

[159] J. Beringer *et al.* [Particle Data Group Collaboration], *Review of Particle Physics (RPP)*, Phys. Rev. D **86** (2012) 010001.

[160] K. Chetyrkin, J. H. Kühn, A. Maier, P. Maierhofer, P. Marquard, M. Steinhauser and C. Sturm, *Precise Charm- and Bottom-Quark Masses: Theoretical and Experimental Uncertainties*, Theor. Math. Phys. **170** (2012) 217 [arXiv:1010.6157 [hep-ph]].

[161] M. E. Luke and M. J. Savage, *Power counting in dimensionally regularized NRQCD*, Phys. Rev. D **57** (1998) 413 [hep-ph/9707313].

[162] B. A. Kniehl, A. A. Penin, V. A. Smirnov and M. Steinhauser, *Potential NRQCD and heavy quarkonium spectrum at next-to-next-to-next-to-leading order*, Nucl. Phys. B **635** (2002) 357 [hep-ph/0203166].

[163] A. A. Penin, V. A. Smirnov and M. Steinhauser, *Heavy quarkonium spectrum and production/annihilation rates to order $\beta_0^3\alpha_s^3$*, Nucl. Phys. B **716** (2005) 303 [hep-ph/0501042].

[164] M. Beneke, Y. Kiyo and K. Schuller, *Third-order non-Coulomb correction to the S-wave quarkonium wave functions at the origin*, Phys. Lett. B **658** (2008) 222 [arXiv:0705.4518 [hep-ph]].

[165] B. A. Kniehl and A. A. Penin, *Ultrasoft effects in heavy quarkonium physics*, Nucl. Phys. B **563** (1999) 200 [hep-ph/9907489].

[166] K. G. Chetyrkin and M. Steinhauser, *The Relation between the MS-bar and the on-shell quark mass at order α_s^3*, Nucl. Phys. B **573** (2000) 617 [hep-ph/9911434].

[167] K. Melnikov and T. v. Ritbergen, *The Three loop relation between the MS-bar and the pole quark masses*, Phys. Lett. B **482** (2000) 99 [hep-ph/9912391].

[168] A. H. Hoang, *Bottom quark mass from Upsilon mesons: Charm mass effects*, hep-ph/0008102.

[169] M. Melles, *Massive fermionic corrections to the heavy quark potential through two loops*, Phys. Rev. D **58** (1998) 114004 [hep-ph/9805216].

[170] M. Melles, *The Static QCD potential in coordinate space with quark masses through two loops*, Phys. Rev. D **62** (2000) 074019 [hep-ph/0001295].

[171] D. Eiras and J. Soto, *Light fermion finite mass effects in non-relativistic bound states*, Phys. Lett. B **491** (2000) 101 [hep-ph/0005066].

[172] S. Bekavac, A. Grozin, D. Seidel and M. Steinhauser, *Light quark mass effects in the on-shell renormalization constants*, JHEP **0710** (2007) 006 [arXiv:0708.1729 [hep-ph]].

[173] K. G. Chetyrkin, J. H. Kühn and M. Steinhauser, *RunDec: A Mathematica package for running and decoupling of the strong coupling and quark masses*, Comput. Phys. Commun. **133** (2000) 43 [hep-ph/0004189].

[174] M. Beneke and A. Signer, *The Bottom MS-bar quark mass from sum rules at next-to-next-to-leading order*, Phys. Lett. B **471** (1999) 233 [hep-ph/9906475].

[175] A. Hoang, P. Ruiz-Femenía and M. Stahlhofen, *Renormalization Group Improved Bottom Mass from Upsilon Sum Rules at NNLL Order*, JHEP **1210** (2012) 188 [arXiv:1209.0450 [hep-ph]].

[176] A. Pineda and A. Signer, *Renormalization group improved sum rule analysis for the bottom quark mass*, Phys. Rev. D **73** (2006) 111501 [hep-ph/0601185].

[177] A. O. G. Källén and A. Sabry, *Fourth order vacuum polarization*, Kong. Dan. Vid. Sel. Mat. Fys. Med. **29** (1955) no.17, 1.

[178] K. G. Chetyrkin, J. H. Kühn and M. Steinhauser, *Three loop polarization function and $\mathcal{O}(\alpha_s^2)$ corrections to the production of heavy quarks*, Nucl. Phys. B **482** (1996) 213 [hep-ph/9606230].

[179] A. H. Hoang, V. Mateu and S. Mohammad Zebarjad, *Heavy Quark Vacuum Polarization Function at $\mathcal{O}(\alpha_s^2)$ and $\mathcal{O}(\alpha_s^3)$*, Nucl. Phys. B **813** (2009) 349 [arXiv:0807.4173 [hep-ph]].

[180] Y. Kiyo, A. Maier, P. Maierhofer and P. Marquard, *Reconstruction of heavy quark current correlators at $\mathcal{O}(\alpha_s^3)$*, Nucl. Phys. B **823** (2009) 269 [arXiv:0907.2120 [hep-ph]].

[181] A. Maier, *private communications.*

[182] D. Greynat and S. Peris, *Resummation of Threshold, Low- and High-Energy Expansions for Heavy-Quark Correlators*, Phys. Rev. D **82** (2010) 034030 Erratum: [Phys. Rev. D **82** (2010) 119907] [arXiv:1006.0643 [hep-ph]].

[183] D. Greynat, P. Masjuan and S. Peris, *Analytic Reconstruction of heavy-quark two-point functions at $O(\alpha_s^3)$*, Phys. Rev. D **85** (2012) 054008 [arXiv:1104.3425 [hep-ph]].

[184] A. I. Onishchenko, *B_c meson sum rules at next-to-leading order*, hep-ph/0005127.

[185] B. Dehnadi, A. H. Hoang and V. Mateu, *Bottom and Charm Mass Determinations with a Convergence Test*, JHEP **1508** (2015) 155 [arXiv:1504.07638 [hep-ph]].

[186] A. A. Penin and N. Zerf, *Bottom Quark Mass from Υ Sum Rules to $\mathcal{O}(\alpha_s^3)$*, JHEP **1404** (2014) 120 [arXiv:1401.7035 [hep-ph]].

[187] M. E. Luke, A. V. Manohar and I. Z. Rothstein, *Renormalization group scaling in nonrelativistic QCD*, Phys. Rev. D **61** (2000) 074025 [hep-ph/9910209].

[188] H. Leutwyler, *How to Use Heavy Quarks to Probe the QCD Vacuum*, Phys. Lett. B **98** (1981) 447.

[189] A. Pineda, *Next-to-leading nonperturbative calculation in heavy quarkonium*, Nucl. Phys. B **494** (1997) 213 [hep-ph/9611388].

[190] K. G. Chetyrkin, V. A. Ilyin, V. A. Smirnov and A. Y. Taranov, *Two Loop Calculations in the Large Quark Mass Expansion in the Framework of the QCD Sum Rules Method*, Phys. Lett. B **225** (1989) 411.

[191] D. J. Broadhurst, P. A. Baikov, V. A. Ilyin, J. Fleischer, O. V. Tarasov and V. A. Smirnov, *Two loop gluon condensate contributions to heavy quark current correlators: Exact results and approximations*, Phys. Lett. B **329** (1994) 103 [hep-ph/9403274].

[192] S. N. Nikolaev and A. V. Radyushkin, *Vacuum Corrections to QCD Charmonium Sum Rules: Basic Formalism and O (G^3) Results*, Nucl. Phys. B **213** (1983) 285.

[193] S. N. Nikolaev and A. V. Radyushkin, *Qcd Charmonium Sum Rules Up To O (G^4) Order.*, Phys. Lett. B **124** (1983) 243.

[194] V. A. Novikov, M. A. Shifman, A. I. Vainshtein and V. I. Zakharov, *Calculations in External Fields in Quantum Chromodynamics. Technical Review*, Fortsch. Phys. **32** (1984) 585.

[195] L. J. Reinders, H. Rubinstein and S. Yazaki, *Hadron Properties from QCD Sum Rules*, Phys. Rept. **127** (1985) 1.

[196] F. V. Gubarev, M. I. Polikarpov and V. I. Zakharov, *Physics of the power corrections in QCD*, Surveys High Energ. Phys. **15** (2000) 89 [hep-ph/9908292].

[197] S. L. Nyeo, *Gluon propagator and selfenergy in the temporal gauge*, Z. Phys. C **52** (1991) 685.

[198] A. Pineda and M. Stahlhofen, *The static hybrid potential in D dimensions at short distances*, Phys. Rev. D **84** (2011) 034016 [arXiv:1105.4356 [hep-ph]].

[199] N. Brambilla, X. Garcia i Tormo, J. Soto and A. Vairo, *The Logarithmic contribution to the QCD static energy at N^4LO*, Phys. Lett. B **647** (2007) 185 [hep-ph/0610143].

[200] N. Brambilla, D. Gromes and A. Vairo, *Poincare invariance constraints on NRQCD and potential NRQCD*, Phys. Lett. B **576** (2003) 314 [hep-ph/0306107].

[201] B. A. Kniehl, A. A. Penin, Y. Schröder, V. A. Smirnov and M. Steinhauser, *Two-loop static QCD potential for general colour state*, Phys. Lett. B **607** (2005) 96 [hep-ph/0412083].

[202] C. Anzai, M. Prausa, A. V. Smirnov, V. A. Smirnov and M. Steinhauser, *Color octet potential to three loops*, Phys. Rev. D **88** (2013) no.5, 054030 [arXiv:1308.1202 [hep-ph]].

[203] C. Ayala, G. Cveti and A. Pineda, *The bottom quark mass from the $\Upsilon(1S)$ system at NNNLO*, JHEP **1409** (2014) 045 [arXiv:1407.2128 [hep-ph]].

[204] C. Ayala, G. Cvetic and A. Pineda, *Mass of the bottom quark from $\Upsilon(1S)$ at NNNLO: an update*, arXiv:1606.01741 [hep-ph].

[205] Y. Kiyo, G. Mishima and Y. Sumino, *Determination of m_c and m_b from quarkonium $1S$ energy levels in perturbative QCD*, Phys. Lett. B **752** (2016) 122 [arXiv:1510.07072 [hep-ph]].

[206] M. A. Shifman, A. I. Vainshtein and V. I. Zakharov, *QCD and Resonance Physics: Applications*, Nucl. Phys. B **147** (1979) 448.

[207] M. Bobrowski, A. Lenz, J. Riedl and J. Rohrwild, *How Large Can the SM Contribution to CP Violation in $D^0-\bar{D}^0$ Mixing Be?*, JHEP **1003** (2010) 009 [arXiv:1002.4794 [hep-ph]].

[208] A. H. Hoang and M. Stahlhofen, *The Top-Antitop Threshold at the ILC: NNLL QCD Uncertainties*, JHEP **1405** (2014) 121 [arXiv:1309.6323 [hep-ph]].

[209] A. Pineda and A. Signer, *Heavy Quark Pair Production near Threshold with Potential Non-Relativistic QCD*, Nucl. Phys. B **762** (2007) 67 [hep-ph/0607239].

[210] M. Czakon, *Automatized analytic continuation of Mellin-Barnes integrals*, Comput. Phys. Commun. **175** (2006) 559 [hep-ph/0511200].

[211] J. Ablinger, *A Computer Algebra Toolbox for Harmonic Sums Related to Particle Physics*, arXiv:1011.1176 [math-ph].

[212] J. Ablinger, *Computer Algebra Algorithms for Special Functions in Particle Physics*, arXiv:1305.0687 [math-ph].

[213] J. Ablinger, J. Blümlein and C. Schneider, *Analytic and Algorithmic Aspects of Generalized Harmonic Sums and Polylogarithms*, J. Math. Phys. **54** (2013) 082301 [arXiv:1302.0378 [math-ph]].

[214] J. Ablinger, J. Blümlein and C. Schneider, *Harmonic Sums and Polylogarithms Generated by Cyclotomic Polynomials*, J. Math. Phys. **52** (2011) 102301 [arXiv:1105.6063 [math-ph]].

[215] J. Blümlein, *Structural Relations of Harmonic Sums and Mellin Transforms up to Weight $w = 5$*, Comput. Phys. Commun. **180** (2009) 2218 [arXiv:0901.3106 [hep-ph]].

[216] E. Remiddi and J. A. M. Vermaseren, *Harmonic polylogarithms*, Int. J. Mod. Phys. A **15** (2000) 725 [hep-ph/9905237].

[217] J. A. M. Vermaseren, *Harmonic sums, Mellin transforms and integrals*, Int. J. Mod. Phys. A **14** (1999) 2037 [hep-ph/9806280].

[218] M. Ochman and T. Riemann, *MBsums - a Mathematica package for the representation of Mellin-Barnes integrals by multiple sums*, Acta Phys. Polon. B **46** (2015) no.11, 2117 [arXiv:1511.01323 [hep-ph]].

[219] S. Albino, *Analytic Continuation of Harmonic Sums*, Phys. Lett. B **674** (2009) 41 [arXiv:0902.2148 [hep-ph]].

[220] M. Beneke, P. Falgari, S. Klein and C. Schwinn, *Hadronic top-quark pair production with NNLL threshold resummation*, Nucl. Phys. B **855** (2012) 695 [arXiv:1109.1536 [hep-ph]].

[221] J. A. M. Vermaseren, *New features of FORM*, math-ph/0010025.

[222] H. H. Patel, *Package-X: A Mathematica package for the analytic calculation of one-loop integrals*, Comput. Phys. Commun. **197** (2015) 276 [arXiv:1503.01469 [hep-ph]].

[223] R. Mertig, M. Böhm and A. Denner, *FEYN CALC: Computer algebraic calculation of Feynman amplitudes*, Comput. Phys. Commun. **64** (1991) 345.

[224] V. Shtabovenko, R. Mertig and F. Orellana, *New Developments in FeynCalc 9.0*, arXiv:1601.01167 [hep-ph].

[225] T. Hahn and M. Pérez-Victoria, *Automatized one loop calculations in four-dimensions and D-dimensions*, Comput. Phys. Commun. **118** (1999) 153 [hep-ph/9807565].

[226] T. Huber and D. Maître, *HypExp: A Mathematica package for expanding hypergeometric functions around integer-valued parameters*, Comput. Phys. Commun. **175** (2006) 122 [hep-ph/0507094].

[227] T. Huber and D. Maître, *HypExp 2, Expanding Hypergeometric Functions about Half-Integer Parameters*, Comput. Phys. Commun. **178** (2008) 755 [arXiv:0708.2443 [hep-ph]].

[228] W. Beenakker, S. Dittmaier, M. Krämer, B. Plümper, M. Spira and P. M. Zerwas, *NLO QCD corrections to t anti-t H production in hadron collisions*, Nucl. Phys. B **653** (2003) 151 [hep-ph/0211352].

[229] J. A. M. Vermaseren, *Axodraw*, Comput. Phys. Commun. **83** (1994) 45.

[230] D. Binosi, J. Collins, C. Kaufhold and L. Theussl, *JaxoDraw: A Graphical user interface for drawing Feynman diagrams. Version 2.0 release notes*, Comput. Phys. Commun. **180** (2009) 1709 [arXiv:0811.4113 [hep-ph]].

Acknowledgements

First of all, I am grateful to Prof. Martin Beneke for his advice, many inspiring discussions and for giving me the opportunity to work on this very interesting topic. I am very much indebted to Jan Piclum, Andreas Maier and Pedro Ruiz-Femenía for the fruitful collaboration, numerous enlightening discussions and their comments on the manuscript. I wish to thank Prof. Stephan Paul, Priv.-Doz. Antonio Vairo and Prof. Andrzej Czarnecki for agreeing to be the chairman of the committee and the second and third referees.

I am thankful to Prof. Matthias Steinhauser, Rikkert Frederix, Yuichiro Kiyo, B. Chokoufé Nejad and J.F. von Soden-Fraunhofen for helpful correspondence and discussions about the work presented in this thesis. I am grateful to Alexander Lenz, Fabian Krinner and Markus Bobrowski for the collaboration on the works [7–9] and to everyone who helped me to widen my scientific horizon through discussions of other subjects.

I wish to thank my family and friends for their continuous encouragement and support throughout the completion of this dissertation.

The computer programs `QQbar_Threshold` [29], `MadGraph5_aMC@NLO` [12], `Package-X` [222], `FeynCalc` [223,224], `LoopTools` [225], `HypExp` [226,227], `RunDec` [173], `FIRE` [133,134], `MB` [210], `Harmonic Sums` [211–217], `FORM` [221] and `HARMPOL` [216], as well as a number of private codes by Jan Piclum and Andreas Maier have been employed within the work presented in this dissertation. The result for the scalar four-point integral in the diagram h_{1b} of Figure 3.8 was taken from [228]. We have used `Axodraw` [229] and `JaxoDraw` [230] to draw Feynman diagrams.